Performance Studies of Gas Electron Multiplier Detector for the Muon Chamber of High Rate CBM Experiment at FAIR

Thesis submitted for the degree of
Doctor of Philosophy (Science)
of the
University of Calcutta

By
Sayak Chatterjee

Department of Physics
University of Calcutta

2022

Dedicated to my parents

Ms. Rinku Chatterjee

&

Mr. Chandra Sekhar Chatterjee

For their endless support in every aspect of my life

Acknowledgment

This thesis is the outcome of my last four years of work at the Department of Physics, Bose Institute, Kolkata. During this period, I got the opportunity to work and discuss with great people. Many individuals have helped me to complete my thesis work. I take this opportunity to thank them all for their continuous support and help.

First, I would like to express my sincere gratitude to my supervisor Dr. Saikat Biswas. I am grateful for his constant and invaluable academic and personal support throughout my research period. I am thankful and indebted to him for being the advisor everyone would like to have. Without his continuous mentorship and support, it would have never been possible to complete my thesis.

I would like to thank Prof. Supriya Das for his clear guidance and enthusiastic discussion and valuable suggestions. He has constantly supported me in my research work and also in writing research articles.

I am very much thankful to Dr. Sidharth Kumar Prasad for helping me to learn the CERN-ROOT framework and also for the discussions we have during our group meetings.

I am thankful to Prof. Sibaji Raha, Prof. Sanjay Kumar Ghosh, Prof. Rajarshi Ray, Prof. Somshubhro Bandyopadhyay, Prof. Dhurba Gupta, Prof. Achintya Singha, Prof. Soumen Roy, Prof. Sushanta Duttagupta, Prof. Swapan Saha, Prof. Debapriyo Syam, Prof. Mahendra Sinha Roy, Prof. Shibshankar Bhattacharyya, Prof. Soumya Mitra, Prof. Gopinath Laha, Prof. Sankhasubhra Nag and Prof. Sankar De for their invaluable classes on basic physics courses during my M.Sc and post M.Sc. courses at Bose Institute.

I would like to convey my sincere thanks to Prof. Probir Roy, Guest Scientist, at Bose Institute for discussing and helping me in writing my thesis and also to improve my understanding of basic Physics.

I am thankful to Dr. Subhasis Chattopadhyay, Variable Energy Cyclotron Center (VECC) for allowing me to work on the Compressed Baryonic Matter (CBM) experiment in collaboration with Dr. Partha Pratim Bhaduri, Dr. Anand Kumar Dubey, Dr. Zubayer Ahammed, Dr. Vikas Singhal, Dr. Ajit Kumar, Mr. Joginder Saini, Mr. Chandra Sekhar Ghosh, Ms. Ekata Nandy of VECC.

I would like to especially thank Dr. Partha Pratim Bhaduri for discussing several phenomenological aspects of Heavy-Ion experiments. He has helped me in doing the simulation studies for the CBM Muon Chamber.

I am thankful to Mr. Omveer Singh of Aligarh Muslim University and Ms. Ekata Nandy of VECC for helping me to learn the CBMROOT framework for doing the physics simulation studies of the di-muon detection with the CBM Muon Chamber detector sub-system.

I would like to thank Mr. Probir Roy of Bose Institute, Mr. Abhishek Seal and Mr. Prasun Singh Roy of VECC for their invaluable technical support.

I would like to thank my seniors Dr. Rama Prasad Adak, Dr. Deeptak Biswas, Mr. Pratik Ghosal, and Ms. Shreya Roy, for their valuable discussions and suggestions on different aspects of my studies.

I would like to especially thank Ms. Shreya Roy for helping me to develop several analysis codes/techniques for the course of my studies.

I would like to thank my colleagues Mr. Arindam Sen, Mr. Abhi Modak, Mr. Prottoy Das, Mr. Tanmay Saha, Mr. Prateek Chawla, Md. Asif Bhat, Mr. Arun Kumar Das, Ms. Debjani Banerjee for being there and making my PhD journey non-monotonic and exciting.

I would also like to thank my juniors, visiting students, project students and summer students Ms. Rudrapriya Das, Mr. Akash Pandey, Mr. Rajat Paul, Mr. Shreesh Sahai, Mr. Pranjal Barik, Mr. Ayan Dandapath, Mr. Shivshant Chauhan, Mr. Shubham Jaiswal, Mr. Abhishek Roy, Mr. Shibnath Shaw, Ms. Krishna Nivedita G, Ms. Debonita Saha, Ms. Rituparna Banerjee and Ms. Ayushi Paul.

I would also like to thank Dr. Ajit Kumar, Mr. Gitesh Sikdar, Ms. Shaifali Mehta, Ms. Kanika Wadhwa, Ms. Ekata Nandy, Mr. Vinod Negi, Mr. Joginder Saini, Dr. Anand Kumar Dubey for helping me during the mini-CBM (mCBM) beam time campaign at GSI, Germany.

I would like to thank the following persons for their support during the CERN-SPS test beam. Dr. Ulrich Frankenfeld, Dr. Chilo Jose Garabatos, Dr. Joerg Hehner, Dr. Thomas Morhardt, Dr. Christian Joachim Schmidt, Dr. Hans Rudolf Schmidt, Dr. Anton Lymanets, Dr. Leszek Ropelewski, Dr. Serge Duarte Pinto, Dr. Ingo Fröhlich, Prof. Dr. Peter Fischer, Jorrit C. L. Widder, Dr. Anna Senger, Prof. Dr. Peter Senger and Dr. Subhasis Chattopadhyay.

I would like to thank Prof. Tetyana Galatyuk, Dr. Anna Senger, Dr. Ilya Selyuzhenkov and all the other members of the CBM dilepton physics working group for their valuable discussions and suggestions on my simulation studies of di-muon reconstruction at CBM energies with MuCh detector sub-system.

I would like to express my sincere gratitude to Dr. Vladimir Nikulin for giving ideas to simulate the realistic absorber configurations for the MuCh detector sub-system.

I would also like to express my sincere gratitude to the following staff of Bose Institute for their various support during my stay at Bose Institute. Mr. Subrata Das, Mr. Kanak Baran Hazra, Mr. Manoj Shee, Mr. Sumanta Ghosh, Mr. Pratap Pakray, Mr. Mohon Das, Suraj da, Anand da, Satyajit da, Nimai da and Dipankar da.

I would like to thank Ms. Ananya Raha and Ms. Sumita Dey of Bose Institute library for their help and support.

I would also like to thank the following people from the Department of Life Sciences, Bose Institute for allowing me to use their instrumentation facilities in the course of my studies. Ms. Ruby Biswas, Ms. Sonal Sachdev, Mr. Dibakar Sarkar, Mr. Pritam Naskar, Prof. Shubho Chaudhuri and Prof. Anirban Bhunia.

I would like to thank the Helmholtz Graduate School for Hadron and Ion Research "HGS-HIRe for FAIR" for providing me with the financial support to attain the HSG-HIRe summer student program at GSI, Germany in 2018. I would like to thank the Bose Institute-Indo FAIR Coordination Center and Federal Ministry for Education and Research in Germany for providing me financial support to attain the 6^{th} International FAIR School in Italy, 2019. Special thanks to the organizing committee of the 15^{th} PISA Meeting on Advanced Detector, Italy, 2022 for providing me with the Young Research Grant to participate in the conference. Special thanks to the organizing committee of XXIXth International Conference on Ultra-relativistic Nucleus-Nucleus Collisions (QM2022) and the committee members of the CBM Juniors Travel Grant for providing financial support to attain the QM2022 in Poland, 2022.

I would like to thank Prof. Srimonti Sarkar, the Dean of Students, Bose Institute for allowing me to adjudicate the Senior School Science Exhibition at La Martiniere for Boys, Kolkata, 2022. I would like to thank Prof. Uday Bandyopadhyay, Director of Bose Institute for providing me with the infrastructure and necessary facilities to carry out my research uninterruptedly. I would like to acknowledge my institutional fellowship for carrying out my research.

I would like to thank Ms. Sunipa Roy and Ms. Sahana Roy for helping me in writing my thesis.

Last but not the least, I would like to thank my parents, Ms. Rinku Chatterjee and Mr. Chandra Sekhar Chatterjee for keeping faith in me and also for motivating me during the roller-coaster ride of finishing my thesis works. I would also like to thank my sister Ms. Ritashree Bhattacharjee, my niece Rajarsi Bhattacharjee and my nephew Saptarsi Bhattacharjee for always bringing smile on my face.

Sayak Chatterjee

Kolkata, India

Abstract of The Thesis

Compressed Baryonic Matter (CBM) experiment at the Facility for Antiproton and Ion Research (FAIR) in Darmstadt, Germany, will try to probe the QCD phase diagram at low temperatures and moderate to high baryon densities by colliding protons and heavy ions to a fixed target at relativistic energies [1]. A particular challenging feature of CBM is its capacity for heavy-ion collisions at very high interaction rates (10^7 collisions per second), which is orders of magnitude higher than the rates reached in other high energy heavy-ion experiments till date. The unprecedented high rate capability of CBM combined with the high-intensity beams of FAIR will allow to overcome the limitations in statistics of the rare probes suffered by other past and present experiments. These features will provide unique conditions for performing high-precision measurements of multi-differential observables and getting the signatures of extremely rare diagnostic probes by their decay channels such as Charmonium ($J/\psi \rightarrow \mu^+\mu^-$) and Low Mass Vector Mesons (LMVM) ($\rho^0 \rightarrow \mu^+\mu^-$, $\omega^0 \rightarrow \mu^+\mu^-$, $\phi^0 \rightarrow \mu^+\mu^-$), which will give us the indication of in-medium modification of hadrons, chiral symmetry restoration and deconfinement at high baryon densities. Several detector sub-systems will be used in the CBM experiment for the detection of different kinds of particles at different momentum ranges. Muon Chamber (MuCh) is the detector sub-system that will be dedicatedly used for the detection of muons produced in the decay of Charmonium and LMVM.

The MuCh detector will consist of several hadron absorbers made of Graphite, Carbon and Iron segments with the detector stations, placed between two consecutive absorbers. The optimisation of the MuCh absorber configuration and detector stations are performed using the Monte Carlo (MC) based simulation for the CBM SIS100 energy range and the feasibility of muon measurement at CBM SIS100 energies with the optimised MuCh detector sub-system are discussed in this thesis.

The foreseen high interaction rate at CBM requires extensive R&D on innovative technologies for detectors, electronics, and data acquisition systems. Due to the good rate handling capability and spatial resolution, Gas Electron Multiplier (GEM) detectors will be used in the first two stations of CBM-MuCh and for the rest of the stations, Straw tube or Resistive Plate Chambers (RPC) may be considered. This thesis reports the detailed R&D on the GEM detector. GEM chambers are operated just above the atmospheric pressure and in a continuous flow mode with Ar/CO_2 gas mixtures in different volume ratios. The R&D is initiated with the investigation of uniformity in performance over the active area of the chambers using Fe^{55} X-ray source. A novel technique is used to irradiate the GEM chambers and also to record the spectra using the same Fe^{55} source to investigate the long-term stability of the chambers. To understand the radiation induced effects on the performance of the chambers, the charging-up phenomena is investigated for different X-ray irradiation rates and gain of the chambers. Investigation of the discharge probability of a GEM chamber prototype is performed at the CERN SPS beam line facility with pion beam of momentum 150 GeV/c and also in the shower environment.

[1] The SIS100 accelerator at FAIR will deliver accelerated proton beams with beam energy up to 30 GeV ($\sqrt{s_{NN}} \sim 7.6$ GeV), while for heavy ions (Z/A $\sim$ 0.4) the foreseen beam energy ranges between 3.4 - 12.0 A GeV and for light ions (Z/A $\sim$ 0.5) 3.4 - 15.0 A GeV, corresponding to the centre of mass energy $\sqrt{s_{NN}} \sim 2.7$ - 5.5 GeV.

Declaration

I do hereby declare that the investigation presented in the thesis has been carried out by me under the supervision of Dr. Saikat Biswas. The work is original and has not been submitted earlier as a whole or in part for a degree/diploma at this or any other Institution/University.

Sayak Chatterjee

List of publications

Thesis is based on the following publications

Journals

- **Study of charging-up effect for a single mask triple GEM detector**
  S. Chatterjee, A. Sen, S. Das, S. K. Ghosh, S. Biswas
  Nuclear Inst. and Methods in Physics Research, A 1014 (2021) 165749 [arXiv:2107.00890]

- **Study of charging up effect in a triple GEM detector**
  S. Chatterjee, A. Sen, S. Roy, K. Nivedita G, A. Paul, S. Das, S. Biswas
  Journal of Instrumentation 15 (2020) T09011 [arXiv:2007.11444]

- **Spark probability measurement of a single mask triple GEM detector**
  S. Chatterjee, U. Frankenfeld, C. Garabatos, J. Hehner, T. Morhardt, C. J. Schmidt, H. R. Schmidt, A. Lymanets, S. Biswas
  Nuclear Inst. and Methods in Physics Research, A 977 (2020) 164334 [arXiv:2107.00883]

- **Long term stability study of triple GEM detector using different Argon based gas mixtures: an update**
  S. Chatterjee, S. Roy, A. Sen, S. Chakraborty, S. Biswas, S. Das, S. K. Ghosh, S. K. Prasad and S. Raha

Journal of Physics: Conference Series, 1498 (2020) 012037 [**arXiv:2107.00858**]

- **Study of uniformity of characteristics over the surface for triple GEM detector**
  S. Chatterjee, S. Chakraborty, S. Roy, S. Biswas, S. Das, S.K. Ghosh, S.K. Prasad, S. Raha
  Nuclear Inst. and Methods in Physics Research, A 936 (2019) 491
  [**arXiv:1807.04961**]

- **Commissioning and testing of pre-series triple GEM prototypes for CBM MuCh in the mCBM experiment at the SIS18 facility of GSI**
  A. Kumar, A. Agarwal, **S. Chatterjee**, S. Chattopadhyay, A.K. Dubey, C. Ghosh, E. Nandy, V. Negi, S. K. Prasad, J. Saini, V. Singhal, O. Singh, G. Sikder, J. de Cuveland, I. Deppner, D. Emschermann, V. Friese, J. Frühauf, M. Gumiński, N. Herrmann, D. Hutter, M. Kis, J. Lehnert, P. A. Loizeau, C.J. Schmidt, C. Sturm, F. Uhlig and W. Zabołotny
  Journal of Instrumentation 16 (2021) P09002

- **Testing of triple GEM prototypes for the CBM Muon Chamber system in the mCBM experiment at the SIS18 facility of GSI**
  A. Kumar, C. Ghosh, **S. Chatterjee**, G. Sikder, A. K. Dubey, J. Saini, E. Nandy, V. Singhal, V. S. Negi, S. Chattopadhyay, and S.K. Prasad
  Journal of Instrumentation 15 (2020) C10020

National conference proceedings & Internal notes

- **Charging-up effect in single mask triple GEM chamber**
  S. Chatterjee, A. Sen, S. Das, S. K. Ghosh, S. Biswas
  CBM Progress Report 2021, 99; DOI:10.15120/GSI-2022-00599

- **Reconstruction of low mass dimuon cocktail at top SIS100 energy**
  S. Chatterjee, P. P. Bhaduri, S. Chattopadhyay
  CBM Progress Report 2021, 215; DOI:10.15120/GSI-2022-00599

- **Reconstruction of di-muons with the low energy setup of MuCh**
  S. Chatterjee, P. P. Bhaduri, S. Chattopadhyay
  CBM Progress Report 2021, 216; DOI:10.15120/GSI-2022-00599

- **Di-muon combinatorial background estimation using different techniques**
  S. Chatterjee, P. P. Bhaduri, S. Chattopadhyay
  CBM Progress Report 2021, 218; DOI:10.15120/GSI-2022-00599

- **Estimation of J/ψ production cross-section in 30 GeV p+A collision at CBM SIS100**
  S. Chatterjee, P. P. Bhaduri, S. Chattopadhyay
  CBM Progress Report 2020, 190; DOI:10.15120/GSI-2021-00421

- **Generation of input signals for dilepton simulation using Pluto event generator**
  S. Chatterjee, T. Galatyuk, P. P. Bhaduri
  CBM Progress Report 2020, 193; DOI:10.15120/GSI-2021-00421

- **Reconstruction of di-muon cocktail using GEANT3 & GEANT4**
  S. Chatterjee, A. Senger, P. P. Bhaduri, S. Chattopadhyay
  CBM Progress Report 2020, 197; DOI:10.15120/GSI-2021-00421

- **Non-monolithic design of the 5^{th} MuCh absorber parameters and tolerances**
  S. Chatterjee, P. P. Bhaduri, O. Singh, V. Nikulin, S. Chattopadhyay
  CBM-TN-20006

- **Effect of absorbers surface tolerance on the Muon Chamber (MuCh) performance for the CBM experiment at FAIR**
  S. Chatterjee, O. Singh, P. P. Bhaduri, S. Chattopadhyay, A. Senger and V. Nikulin
  CBM Progress Report 2019, 97; DOI: 10.15120/GSI-2020-00904

- **Effect of gaps on the fifth absorber of Muon Chamber (MuCh) for the CBM experiment at FAIR**
  S. Chatterjee, O. Singh, P. P. Bhaduri, S. Chattopadhyay, and V. Nikulin
  CBM Progress Report 2019, 99; DOI: 10.15120/GSI-2020-00904

- **Reconstruction of J/ψ mesons at SIS100 energies with realistic MuCh set up**
  S. Chatterjee, O. Singh, A. Senger, P. P. Bhaduri, and S. Chattopadhyay
  CBM Progress Report 2019, 181; DOI: 10.15120/GSI-2020-00904

- **Study of charging up effect in GEM detector**
  K. Nivedita G, A. Paul, **S. Chatterjee**, S. Roy, A. Sen, S. Biswas, S. Das
  Proceedings of the DAE-BRNS Symposium on Nucl. Phys. Vol. 64, (2019) 976

- **Stability and uniformity study of triple GEM detector**
  S. Chatterjee, S. Roy, S. Chakraborty, S. Rudra, S. Shaw, R.P. Adak, S. Biswas, S. Das, S.K. Ghosh, S.K. Prasad & S. Raha
  CBM Progress Report 2018, 65; DOI:10.15120/GSI-2019-01018

Preprints

- **Effect of relative humidity on the long-term operation of a single mask triple GEM chamber**
  S. Chatterjee, A. Sen, S. Das, S. Biswas; **arXiv:2206.04051**
- **Visual investigation of possible degradation in GEM foil under test**
  S. Chatterjee, A. Sen, S. Das, S. Biswas; **arXiv:2206.04052**
- **Effect of charging-up on the uniformity of a single mask triple GEM detector**
  S. Chatterjee, A. Sen, S. Das, S. Biswas; **arXiv:2206.10876**

Other publications

Journals

- **Development and implementation of a time-based signal generation scheme for the Muon Chamber simulation of the CBM experiment at FAIR**
  V. Singhal, **S. Chatterjee**, V. Frise, S. Chattopadhyay
  Journal of Instrumentation 16 (2021) P08043 [**arXiv:2104.12012**]
- **Stability study and time resolution measurement of Straw Tube detectors**
  S. Roy, S. Jaiswal, **S. Chatterjee**, A. Sen, S. Das, S. K. Ghosh, S. Raha, V. M. Lysan, G. D. Kekelidze, V. V. Myalkovsky, S. Biswas
  Pramana – J. Phys. 95, (2021) 50 [**arXiv:2007.12547**]
- **Cosmic ray flux and lockdown due to COVID19 in Kolkata – any correlation?**

A. Sen, **S. Chatterjee**, S. Roy, R. Biswas, S. Das, S. K. Ghosh, S. Biswas
Pramana – J. Phys. 95, (2021) 64 [arXiv:2010.06648]

- **Interplay between eclipses and soft cosmic rays**
  S. Roy, **S. Chatterjee**, S. Chakraborty, S. Biswas, S. Das, S. K. Ghosh, S. K. Gupta, A. Jain, I. Mazumdar, P. K. Nayak and S. Raha
  Proceedings of Science (ICRC2021) 131

- **Characterisation of an RPC prototype with moderate resistivity plates using tetrafluoroethane ($C_2H_2F_4$)**
  A. Sen, **S. Chatterjee**, S. Roy, S. Biswas, S. Das
  Journal of Instrumentation 15 (2020) C06055 [arXiv:2004.05469]

- **A new type of RPC with very low resistive material**
  S. Chakraborty, **S. Chatterjee**, S. Roy, A. Roy, S. Biswas, S. Das, S. K. Ghosh, S. K. Prasad, S. Raha
  Nuclear Inst. and Methods in Physics Research, A 936 (2019) 424
  [arXiv:1807.04961]

- **Plastic scintillator detector array for detection of cosmic ray air shower**
  S. Roy, S. Chakraborty, **S. Chatterjee**, S. Biswas, S. Das, S. K. Ghosh, A. Maulik, S. Raha
  Nuclear Inst. and Methods in Physics Research, A 936 (2019) 249
  [arXiv:1807.04951]

- **Stability study of gain and energy resolution for GEM detector**
  S. Roy, S. Rudra, S. Shaw, **S. Chatterjee**, S. Chakraborty, R. P. Adak, S. Biswas, S. Das, S. K. Ghosh, S. K. Prasad, S. Raha
  Nuclear Inst. and Methods in Physics Research, A 936 (2019) 485

National conference proceedings & Internal notes

- **R&D of Straw Tube detector for High Energy Physics experiments**
  S. Roy, S. Jaiswal, **S. Chatterjee**, A. Sen, S. Biswas, S. Das, S. K. Ghosh, S. Raha, V. M. Lysan, G. D. Kekelidze, V. V. Myalkovsky
  Proceedings of the DAE-BRNS Symposium on Nucl. Phys. Vol. 64, (2019) 990

- **Development and issues of bakelite RPC**
  A. Sen, R. Banerjee, A. Roy, **S. Chatterjee**, S. Roy, S. Biswas, S. Das
  Proceedings of the DAE-BRNS Symposium on Nucl. Phys. Vol. 64, (2019) 996

- **Study of cosmic ray with plastic scintillator detector**
  S. Shaw, N. Nandi, **S. Chatterjee**, P. Chawla, S. Roy, R. P. Adak, S. Biswas, S. Das, S. K. Ghosh, S. Raha
  Proceeding of the DAE symposium on Nuclear Physics. Volume 62, (2017), 1030

Preprints

- **Characterisation of a new RPC prototype using conventional gas mixture**
  A. Sen, **S. Chatterjee**, S. Das, S. Biswas; **arXiv:2206.04259**

Contents

List of Figures

List of Tables

Glossary of acronyms used in this thesis

$\sqrt{s_{NN}}$ Centre of mass energy.

AGS Alternating Gradient Synchrotron.

APPA Atomic, Plasma Physics and Applications.

BM@N Baryonic Matter at Nuclotron.

BNL Brookhaven National Laboratory.

CBM Compressed Baryonic Matter.

CEE Cooler storage ring External-target Experiment.

CERN European Organisation for Nuclear Research.

CF Calibration Factor.

CMS Compact Muon Solenoid.

CNM Cold Nuclear Matter.

COMPASS Common Muon and Proton Apparatus for Structure and Spectroscopy.

CP Critical Point.

DHS Dipole Hadron Spectrometer.

DM Double Mask.

$\mathbf{E}_{beam}$ Beam total energy.

$\mathbf{E}_{kinetic}$ Beam kinetic energy.

ECAL Electro Magnetic Calorimeter.

EOS Equation Of State.

FAIR Facility for Antiproton and Ion Research.

FEB Front End Boards.

FIFO Fan In Fan Out.

FLUKA FLUktuierende KAskade.

GEANT GEometry ANd Tracking.

GEM Gas Electron Multiplier.

GSI GSI Helmholtzzentrum für Schwerionenforschung.

HADES High Acceptance DiElectron Spectrometer.

HEP High Energy Physics.

HERA Hadron Electron Ring Accelerator.

HI Heavy-Ion.

HIAF High Intensity heavy ion Accelerator Facility.

HV High Voltage.

J-PARC Japan Proton Accelerator Research Complex.

LED Leading Edge Discriminator.

LHC Large Hadron Collider.

LHCb Large Hadron Collider beauty.

LMVM Low Mass Vector Meson.

LQCD Lattice QCD.

MC Monte Carlo.

MCA Multi Channel Analyser.

mCBM mini CBM.

MIP Minimum Ionizing Particle.

mMUCH mini MUon CHamber.

MPD Multi Purpose Detector.

MPGD Micro Pattern Gas Detector.

MPV Most Probable Value.

mRICH mini Ring Imaging CHerenkov.

MSGC Micro Strip Gas Counter.

mSTS mini Silicon Tracking Station.

mTOF mini Time Of Flight.

mTRD mini Transition Radiation Detector.

MTS Muon Tomography Station.

MuCh Muon Chamber.

MVD Micro Vertex Detector.

MWPC Multi Wire Proportional Counter.

NICA Nuclotron based Ion Collider fAcility.

NIM Nuclear Instrumentation Module.

NS2 No Stretch No Spacer.

NuSTAR Nuclear Structure, Astrophysics and Reactions.

$\mathbf{P}_{beam}$ Beam momentum.

PANDA antiProton ANnihilation at DArmstadt.

PRR Proton Range Radiography.

PSD Projectile Spectator Detector.

PU tubes Polyurethane tubes.

QCD Quantum Chromo Dynamics.

QGP Quark Gluon Plasma.

RH Relative Humidity.

RHIC Relativistic Heavy Ion Collider.

RHIC-BES Relativistic Heavy Ion Collider-Beam Energy Scan.

RICH Ring Imaging CHerenkov.

RPC Resistive Plate Chamber.

SCA Single Channel Analyser.

SE Super Event.

SIS Schwer Ionen Synchrotron.

SM Standard Model.

SM Single Mask.

SPS Super Proton Synchrotron.

STP Standard Temperature and Pressure.

STS Silicon Tracking System.

TAC Time to Amplitude Converter.

Thermal-FIST Thermal-Fast and Interactive Statistical Toolkit.

TOF Time Of Flight.

TOTEM TOTal Elastic and diffractive cross section Measurement.

TPC Time Projection Chamber.

TRD Transition Radiation Detector.

TSCA Timing Single Channel Analyser.

TTL Transistor Transistor Logic.

UrQMD Ultra relativistic Quantum Molecular Dynamics.

Chapter 1

Introduction

1.1 Introduction

Rutherford's famous gold foil experiment in the early 1900's revealed the atomic structure of Gold (Au) and established the fact that the entire mass of the atom is concentrated in a very small volume and the rest of the space is empty [1]. The concentrated region of the atom is known as the nucleus, which consists of positively charged protons and neutral neutrons. The negatively charged electrons are revolving in different orbits around the nucleus making the atom electrically neutral. Further scattering experiments have revealed that the protons and neutrons are not the elementary constituents [2]. They are made up of quarks and gluons which are considered as the elementary particles according to the Standard Model (SM) [3] of Particle Physics. All the matter around us, made up of atoms, can be characterized by its properties. The matter can be broadly classified into three states, namely solid, liquid and gas. For example, at the Standard Temperature and Pressure (STP), water is liquid, Nitrogen (N) is gaseous and Iron (Fe) is solid. In thermal equilibrium, the properties of matter can be characterized by certain macroscopic observables like temperature, pressure, etc. known as control parameters. The variation of the control parameters can change the state of matter. The different states of a particular type of matter are usually represented in terms of a diagram known as the phase diagram. The most common and well-known example is the phase diagram of

water. It consists of mainly three phases: solid (ice), liquid (water) and gas (steam). The variation of these as a function of control parameters is well known and can be found in any standard textbook of thermodynamics [4]. Similarly, the properties of nuclear matter, governed by the strong nuclear force, can have different phases. The different phases of nuclear matter can be accessed by either heating the nucleons to extremely high temperatures or by compressing them to high densities. The strong nuclear force is explained using a relativistic quantum field theory, known as Quantum Chromo Dynamics (QCD) [5]. The phase diagram of strongly interacting matter is known as the QCD phase diagram [6, 7]. The conjectured phases of strongly interacting matter as functions of temperature (T in MeV) and baryon chemical potential (μ_B in MeV) are shown in Fig. 1.1 [8].

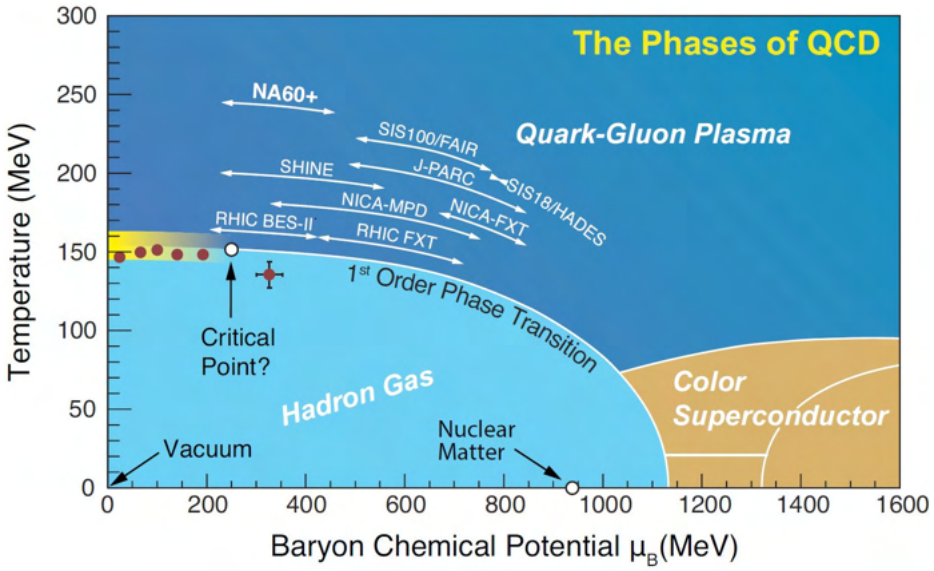

Figure 1.1: The conjectured phase diagram of strongly interacting matter, known as the QCD phase diagram. The region of operations for different heavy-ion experiments is shown in the figure by curved white lines with arrows at both ends. The figure is taken from Ref. [8].

The only possible way to study such extreme states of strongly interacting matter in the laboratory is by colliding heavy-ions at relativistic speeds. The advancement of the accelerator facility provides us with the opportunity to probe the smallest distances in nature. It also helps us to understand the behaviour of the elementary particles and their interactions. Experimental High Energy

Nuclear Physics allows us to find the answers to a few most important unsolved questions of physics, for example how the universe was created, what are the building blocks of the universe and how they interact, interaction properties of the elementary particles and also the evolution of the early universe. There are several accelerator facilities devoted to study the different regions of the QCD phase diagram. In Fig. 1.1, the anticipated region of operation of a few past, ongoing and upcoming heavy-ion experiments is illustrated. Experiments at the LHC (Large Hadron Collider) and the top RHIC (Relativistic Heavy Ion Collider) energies explore the high temperature and vanishing baryon density regime of the QCD phase diagram [9, 10, 11]. The vanishing net baryon density regime exists for a few microseconds after the BigBang [12]. While expanding from this situation, the system hadronizes and finally freezes out chemically at a temperature around 160 MeV [13, 14]. A smooth crossover transition from the Quark Gluon Plasma (QGP) [1] phase to the hadronic phase is observed in vanishing baryon chemical potentials [15]. This temperature and the transition from the partonic phase (QGP) to the hadronic phase matches well with the prediction from the Lattice QCD (LQCD) calculations [2] [16, 17]. However, the LQCD calculations can be applied only for a vanishing baryon chemical potential. At a non-vanishing value of the baryon chemical potential, the LQCD calculations suffer from the so called sign problem [18]. For large baryon chemical potential and low temperature regimes, LQCD inspired field theory calculations suggest a rich structure of the QCD phase diagram, such as a first order phase transition from hadronic matter to partonic matter which terminates at a second order Critical Point (CP) [19, 20, 21]. The experimental evidence of such a structure is currently one of the major goals of the ongoing and upcoming heavy-ion experiments. The existing data from the last few decades of huge experimental works, such as Relativistic Heavy Ion Collider-Beam Energy Scan (RHIC-BES) at BNL, New York, Super Proton Synchrotron (SPS) at CERN, Geneva, Alternating Gradient Synchrotron (AGS) at BNL, New York, etc. shed light on the

[1] QGP is a new state of matter created after the collision of heavy-ions at relativistic speeds. It is a thermalised soup of deconfined quarks and gluons.

[2] Lattice QCD is the only known theoretical formulation which can describe the thermodynamics of quarks and gluons.

thermal properties of the QGP by studying the bulk properties of the matter created in heavy-ion collisions. However, the location of the CP, the order of phase transition from partonic matter to hadronic matter at a finite baryon chemical potential, and the Equation Of State (EOS) at high baryon chemical potential regimes remain open questions to the High Energy Physics (HEP) community. Therefore, the systematic measurement of rare diagnostic probes in the finite to high baryon chemical potential region with unprecedented precision should have a large discovery potential. However, the prerequisite to achieve success in the exploration of the yet uncharted territory of the QCD phase diagram is the combination of high intensity beams and detectors with high efficiency and high rate handling capabilities. New accelerator facilities are coming up to serve the requirement of high luminosity beams and substantial progress is made in detector technologies to handle the expected high particle rates.

A summary of the upcoming experimental facilities planning to scan the QCD phase diagram at moderate to high baryon density and the low temperature regime, are given below and the foreseen interaction rates are shown as functions of the centre of mass energy in Fig. 1.2 [22, 23].

The Nuclotron-based Ion Collider fAcility (NICA) [24] is under construction at JINR, Dubna, Russia. The Baryonic Matter at Nuclotron (BM@N) [25] is a fixed target experiment planning to cover the energy range of $\sqrt{s_{NN}}$ = 2.3 - 3.5 GeV for the heavy-ions. It aims to study the electromagnetic probes (γ, e^+, e^-), strange mesons and multi-strange hyperons. The Multi-Purpose Detector (MPD) [26] at NICA is for a collider experiment. The energy range covered by this experiment will be $\sqrt{s_{NN}}$ = 4 - 11 GeV for the heavy-ions. The MPD is designed to detect charged hadrons, light nuclei, photons and electrons.

The High Intensity heavy-ion Accelerator Facility (HIAF) [27] in China aims to provide intense primary and radioactive ion beams for atomic physics, nuclear physics and related research fields. The Cooler storage ring External-target

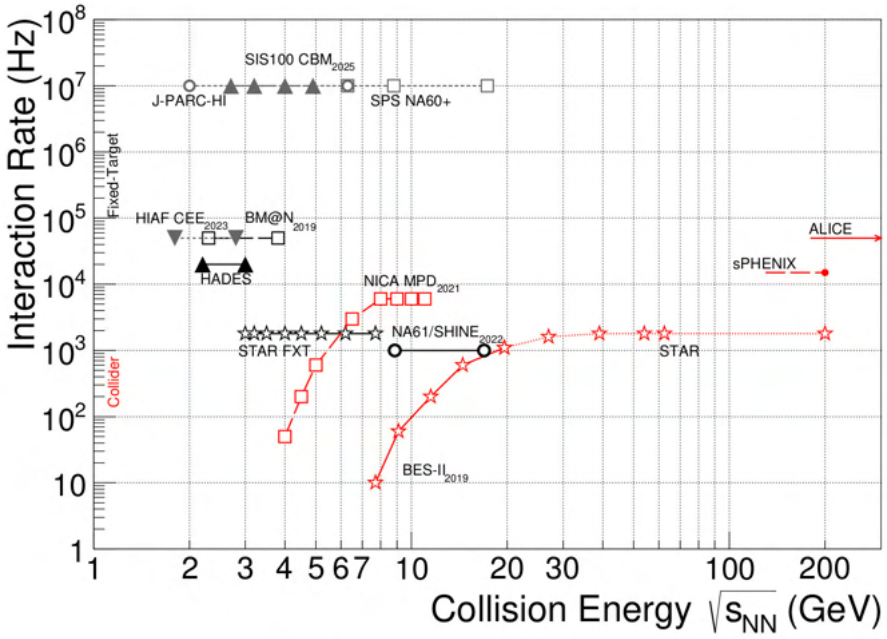

Figure 1.2: Interaction rates achieved by existing and planned experimental facilities as a function of the centre of mass energy. The figure is taken from Ref. [23].

Experiment (CEE) [28] is a fixed target hadron detector. It will span the energy range of $\sqrt{s_{NN}}$ = 1.2 - 2.7 GeV for the heavy-ions.

A heavy-ion accelerator scheme is proposed for the Japan Proton Accelerator Research Complex (J-PARC-HI) [29]. The Dipole Hadron Spectrometer (DHS) there is being designed to measure both the hadrons and leptons simultaneously at an energy range of $\sqrt{s_{NN}}$ = 2 - 6.2 GeV for the heavy-ions.

The Super Proton Synchrotron (SPS) is a running heavy-ion facility at the European Organisation for Nuclear Research (CERN). The NA61/SHINE [30] is a proposed detector setup at the SPS to study the production of open charm and multi-strange hadrons using heavy-ion beams in the energy range of SPS [30]. The high statistics open charm measurements in Pb+Pb collisions at 150 A GeV and 40 A GeV will be conducted in 2022-2024. Another proposed detector setup at SPS is NA60+ [31]: the successor to the NA60 experiment [32]. It aims to measure the thermal di-muons, charmonium states and open charm production in a beam energy range of $\sqrt{s_{NN}}$ = 4.5 - 17.3 GeV with heavy-ions.

The Facility for Antiproton and Ion Research (FAIR) [33, 34, 35] at Darmstadt, Germany is currently under construction and is designed to deliver high intensity primary beams starting from the proton up to uranium. The Compressed Baryonic Matter (CBM) [36, 37, 38, 39] experiment at the FAIR accelerator complex is a fixed target experiment designed to detect hadrons, electrons and muons in the heavy-ion collisions over the energy range of $\sqrt{s_{NN}}$ = 2.7 - 5.0 GeV [40, 41]. The uniqueness of the CBM experiment is its foreseen high interaction rates which can reach up to 10 MHz, orders of magnitude higher compared to the existing or planned experimental facilities [22, 23]. Such high interaction rates will help to achieve an unprecedented precision in the measurement of rare diagnostic probes such as multi strange (anti-) hyperons and charmed particles.

This thesis is aimed at studying the feasibility of di-muon detection in the CBM experiment and to investigate the performance of the Gas Electron Multiplier (GEM) detector, proposed to be used as the tracking detector for the detection of muon pairs coming from the decay of Low Mass Vector Mesons (LMVM) and J/ψ. In the following sections, a detailed overview of the FAIR accelerator facility, the CBM detector setup, the physics goals of the CBM experiment and the aim of the thesis are discussed respectively.

1.2 Facility for Antiproton and Ion Research (FAIR)

The FAIR accelerator facility is currently under construction using the existing SIS18 (Schwer Ionen Synchrotron 18) accelerator facility at GSI, Darmstadt, Germany [33, 34, 35]. The schematic of the FAIR accelerator facility is shown in Fig. 1.3 [40]. The FAIR accelerator facility consists of a synchrotron having a magnetic rigidity [3] of 100 Tm and hence it is known as the SIS100 accelerator ring. The existing SIS18 synchrotron ring acts as the injector of the

[3]Magnetic rigidity is a measure of the angular deflection when a charged particle travels through a given magnetic field. It is defined as $\frac{p}{e} = B \times \rho$, where p is the magnitude of the particle momentum, e is the charge of the particle, B is the magnetic field and ρ is the bending radius of the particle in the magnetic field B.

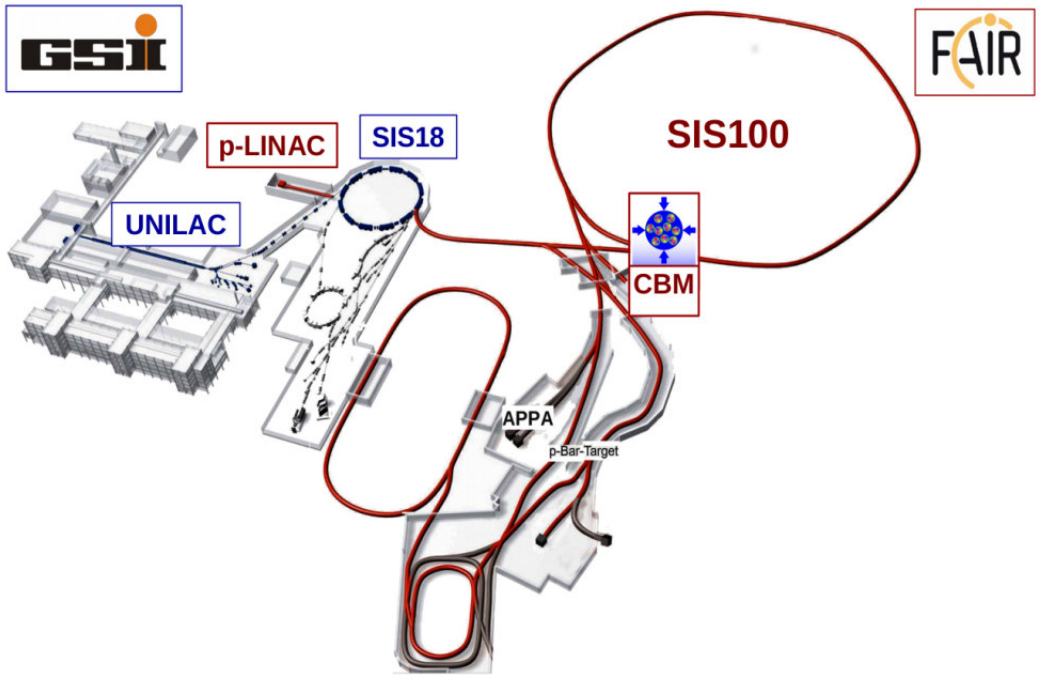

Figure 1.3: Schematic of the FAIR accelerator facility under construction at GSI, Germany [33, 34, 35]. The red marker indicates the facility under construction and the blue marker indicates the existing SIS18 facility at GSI, Germany. The figure is taken from Ref. [40].

primary beams to the SIS100 accelerator ring. Some of the unique features of the SIS100 ring over the existing SIS18 ring include the 100 - 1000 increase in the intensity of the beam and $\sim$ 10 times increase in the energy of the beam [34]. While the construction of the SIS100 accelerator ring is ongoing, the respective collaborations are preparing to take the first beam on target by the end of 2025.

At FAIR, there are four experimental pillars, namely Atomic, Plasma Physics and Applications (APPA) [42], antiProton ANnihilation at DArmstadt (PANDA) [43], Compressed Baryonic Matter (CBM) [39] and Nuclear Structure, Astrophysics and Reactions (NuSTAR) [44]. The APPA collaboration aims to explore different branches of Atomic Physics, Plasma Physics and Material Science and also applications in the field of Biophysics. The PANDA collaboration aims to explore the structure of hadrons to understand the mechanism behind the mass generation of hadrons and also the confinement of quarks and gluons. The NuSTAR collaboration aims to combine nuclear physics with precision astronomy to understand different astrophysical scenarios. The CBM

collaboration aims to explore the state of strongly interacting matter under a moderate to high baryon density environment. The science goal of the FAIR facility spans a broad range which includes the understanding and investigation of all aspects of matter, starting from the quark gluon structure of the hadrons to the macroscopic objects in the universe like stars and supernovae.

1.2.1 Compressed Baryonic Matter (CBM) experiment

The CBM, a fixed target experiment, at the FAIR accelerator facility is aimed to study the QCD phase diagram at low temperature and moderate to high baryon density regime by colliding heavy-ions (Au+Au) at relativistic speeds [45]. The high baryon density regime of the QCD phase diagram is still an uncharted territory where different theoretical models predict the existence of a first order phase transition from hadronic matter to partonic matter that ends at a second order CP [46, 47]. The CBM experiment aims to scan the QCD phase diagram with an Au beam on an Au target over an energy range of $\sqrt{s_{NN}} = 2.7$ - 5.0 GeV. The CBM experiment aims to investigate the following points at moderate to high baryon chemical potentials [45] involved in the process of nucleus-nucleus collision;

- The equation of state of QCD matter and the relevant degrees of freedom
- Phase transition from hadronic matter to partonic matter or existence of phase coexistence
- Modification of hadrons in the dense baryonic matter
- Location of the critical point
- Creation and propagation of charm quarks close to and below the production threshold

The above mentioned physics cases will be investigated at the CBM experiment by studying the following observables:

The equation of state can be investigated by studying the collective flow of identified particles generated due to the density gradient of the early fireball and also by multi-strange hyperons, preferentially produced in the dense phase of the fireball via sequential collisions. The phase transition from the hadronic to the partonic medium can produce the following effects: a) multi-strange hyperons driven into equilibrium at the phase boundary and b) the excitation function of the fireball temperature reflecting a caloric curve. The event-by-event fluctuation of conserved quantities such as charge, baryon number and strangeness number should indicate the location of the critical point. The invariant mass spectra of di-leptons are sensitive to the in-medium modification of the hadrons in the dense baryonic matter. The production and propagation of charm quarks can shed light on the early stage of collision and can offer the possibility of probing the degrees of freedom over the entire collision history.

To achieve the above mentioned goals of the CBM experiment, a multi-purpose detector setup is needed which can detect all the particles produced in the collision. In Fig. 1.4, a simulated picture of the CBM detector setup is shown. A brief description of the individual detector sub-systems is given below.

Beam Pipe: The task of the beam pipe is to guide the incoming beam to the beam dump. Therefore a proper design of the beam pipe is very crucial since it may affect the performance of individual detector sub-systems. The design of the beam pipe is not yet finalized for the CBM setup. However, the latest beam pipe design used in the performance simulation consists of several sections. Inside the Silicon Tracking System (STS) and Muon Chamber (MuCh) (/Ring Imaging CHerenkov (RICH)) sub-system the shape of the beam pipe is conical and beyond MuCh, it is cylindrical in shape. The beam pipe is made of carbon fiber of 0.5 mm thickness. Several simulation studies are ongoing to finalize the design of the beam pipe and details of them can be found in Ref. [49, 50, 51].

Dipole magnet: The dipole magnet of CBM will be a superconducting magnet with an aperture of $\pm$ 25°. The magnet will provide a magnetic field with a total bending power of 1 Tm. The magnet will be used to identify charged

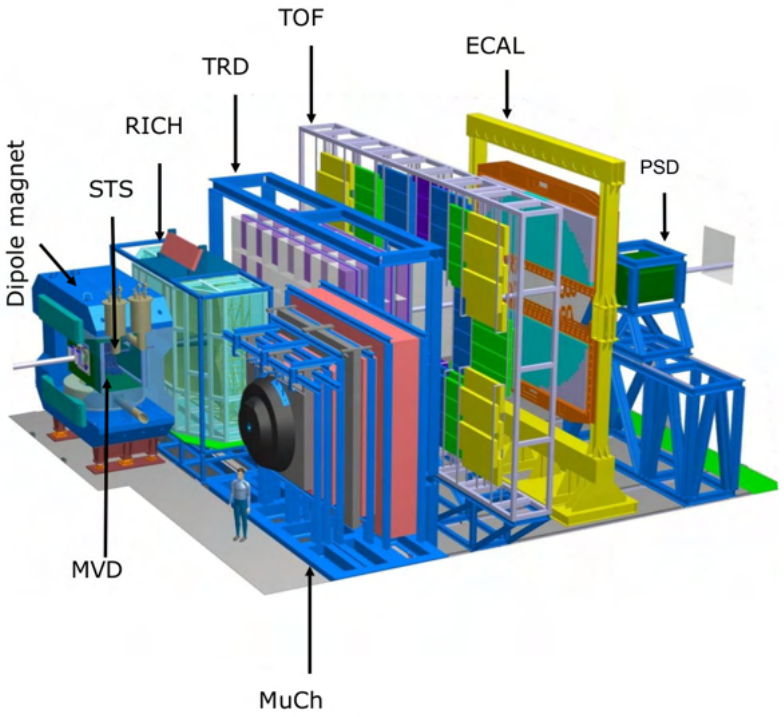

Figure 1.4: Simulated image of the CBM detector setup. It consists of a dipole magnet, Micro Vertex Detector (MVD), Silicon Tracking System (STS), Ring Imaging CHerenkov detector (RICH), Muon Chamber (MuCh), Transition Radiation Detector (TRD), Time Of Flight (TOF) wall, Electromagnetic CALorimeter (ECAL) and Projectile Spectator Detector (PSD). The figure is taken from Ref. [48].

particles by bending their trajectories. More details about the dipole magnet can be found in Ref. [52].

Micro Vertex Detector (MVD): The MVD detector will be placed inside the dipole magnet for measuring the secondary vertices of the produced short lived particles like D mesons. The measurement of the decay vertices of the short lived particles requires detectors with good position resolution and low material budgets. To match the requirement, Monolithic Active Pixel Sensors (MAPS) will be placed in a vacuum box at 5 cm, 10 cm and 15 cm downstream of the target. The typical material budget of the sensors is kept between 300 μm to 500 μm of silicon equivalent. The typical hit position resolution varies from 3.5 μm to 6 μm with pixel sizes 18 μm $\times$ 18 μm and 20 μm $\times$ 40 μm. More details about the MVD can be found in Ref. [53, 54].

Silicon Tracking System (STS): The STS detector will be placed downstream of the MVD detector and inside the dipole magnet. It will be used for track reconstruction and momentum determination of the charged particles. STS will be built of eight tracking layers populated with both sided micro-strip silicon sensors. It will be placed roughly at a distance of 30 cm to 100 cm from the target position. This system will allow track reconstruction over a very broad momentum range (typically $\sim$ 100 MeV/c to $\sim$ 10 GeV/c). The required momentum resolution of the system is $\sim$ 1 %. To reduce the material budget of the system, the front-end electronics will be placed outside the active area of the system and will be connected to the sensors via low mass cables. The typical material budget of the STS system including the support structures will be around 800 μm silicon equivalent. More details on the STS can be found in Ref. [55].

Ring Imaging CHerenkov Detector (RICH): The RICH detector will be used to identify the di-electrons coming from the decay of Low Mass Vector Mesons (LMVM) and J/ψ. It will also be used for pion suppression in the momentum range below 10 GeV/c. It will consist of a gas radiator ($\sim$ 1.7 m in length) filled with Carbon dioxide (CO_2). The Cherenkov radiation will be reflected by mirrors and will be detected using Multi Anode Photo Multiplier Tubes. More details regarding the RICH detector can be found in Ref. [56].

Muon Chamber (MuCh): The MuCh detector system will be placed in place of the RICH detector when the di-muons will be measured. MuCh detector system is made up of several hadron absorbers and detector layers are placed in between the absorbers. It will be placed at a distance of $\sim$ 1.3 m from the target position. One of the important challenges of the MuCh detector system is the identification of low momentum muons in the high particle density environment. That is why the hadron absorbers of MuCh are made of different thicknesses. The MuCh system consists of five hadron absorbers and four detector stations. Each of the detector stations has three detector layers. The Gas Electron Multiplier (GEM) detector will be used as a tracking detector in the first two stations of MuCh due to the foreseen high particle flux.

Resistive Plate Chambers (RPC) are proposed as tracking devices for the third and fourth detector stations of MuCh where particle density is relatively lower. More details about MuCh can be found in Ref. [57].

Transition Radiation Detector (TRD): The TRD will be placed behind the MuCh or RICH detector sub-system. The TRD will be used for the identification of electrons and pions with momenta greater than 1.5 GeV/c. It will consist of three detector layers and will be placed at a distance of $\sim$ 5 m from the target position. The first TRD layer will also be used as the trigger detector for the detection of the J/ψ meson. More details about the TRD can be found in Ref. [58].

Time Of Flight (TOF): The TOF detector system will be placed at the end of the TRD detector sub-system and will be used for the hadron identifications via time of flight measurements. Glass multigap Resistive Plate Chambers will be used for the TOF wall. The active area of the chamber will be $\sim$ 120 m^2. The detector will be located at a distance of $\sim$ 10 m from the target position. The required time resolution of the detector sub-system is $\sim$ 80 ps. More details about the TOF can be found in Ref. [59].

Electromagnetic CALorimeter (ECAL): The ECAL detector system will be used to measure direct photons and the photons coming from the decay of neutral mesons (e.g. π^0, η). The ECAL sub-system will be made up of 140 layers of 1 mm lead and 1 mm scintillators. The details about the ECAL sub-system can be found in Ref. [53, 54].

Projectile Spectator Detector (PSD): The PSD will be used to measure the spectators in the nucleus-nucleus collisions. It will provide information about the reaction plane and collision centrality. It will consist of 60 lead and scintillator layers with a typical surface area of 10 cm $\times$ 10 cm. The details about the PSD can be found in Ref. [60].

1.2.2 Measurement of di-leptons at CBM

Leptons being electromagnetic in nature, are considered as one of the most promising and efficient tools to characterize different stages of heavy-ion collision. Di-leptons are produced over all stages of the evolution of the fireball starting from the pre-equilibrium stage to the freezeout. Since leptons interact only via electromagnetic interactions, they remain unaffected due to their relatively larger mean free path [61] and thus carry the unaltered information about the interior of the fireball where they have been produced. Di-leptons are thus known as penetrating probes of the hot and dense matter produced in the heavy-ion collision. The di-lepton invariant mass (M) and the transverse momentum (p_T) can be used to identify the characteristics of the different phases of the expanding fireball. Di-leptons with larger invariant mass and high p_T are usually emitted at the early stage of the collision; similarly, lower invariant mass and p_T indicate the emission from a relatively cooler system [62, 63]. Depending on the lepton pair invariant mass, the entire di-lepton spectra can be divided into three parts: a) low mass region (M $\leq$ 1.02 GeV), b) intermediate mass region (1.02 $<$ M $<$ 3.1 GeV) and c) high mass region (M $\geq$3.1 GeV). In the low mass region, the dominating source of di-lepton production is vector meson decay. The decay of LMVM (ρ, ω, ϕ) in the di-lepton channel is considered as one of the most useful probes to study the in-medium modification of the hadrons [64]. In the intermediate mass region, the radiation from the QGP medium dominates the di-lepton spectra and thus this region is very important for getting any possible QGP signature [65]. The excitation function of the fireball temperature could indicate the order of the phase transition from partonic matter to hadronic matter. The high mass region is populated by the heavy quarkonia like J/ψ, $\psi^{'}$ decaying to di-leptons and their suppression can indicate the existence of QGP [66]. The experimentally measured di-lepton spectra also contain the background continuum having a major contribution from the weak decays of mesons. However, the background continuum can be subtracted from the raw spectra by using the invariant mass analysis technique.

The MuCh detector sub-system at CBM is dedicatedly designed to track the di-muons coming from the decay of LMVM and J/ψ and the RICH detector sub-system will be used to detect the di-electrons so that the entire di-lepton spectra can be measured at CBM SIS100 energies.

1.3 Aim of the thesis

The motivation behind this thesis includes the optimisation study of the MuCh absorber and detector sub-systems for the detection of muons coming from the decay of LMVM and J/ψ. The feasibility of di-muon reconstruction with the optimised MuCh detector sub-system is investigated at CBM SIS100 energies. The foreseen high interaction rate imposes a great challenge on the detector sub-systems. As GEM will be used as the tracking device in the first two stations of MuCh, an R&D on the GEM detector is carried out to understand the behaviour of the chamber under prolonged irradiation. Four important aspects of GEM detectors such as uniformity in characteristics, stability under the long-term irradiation, charging-up effect and spark probability are addressed in this thesis.

1.4 Structure of the thesis

The work done for this thesis can be broadly divided into the following parts: Monte Carlo (MC) based simulations and R&D on GEM prototypes:

Chapter 2 discusses the MC based simulation studies including the optimisation of the MuCh sub-system geometry configuration and the reconstruction of the muon pairs with the optimised MuCh sub-system for CBM SIS100 energies. The details of the simulated MuCh geometry, simulation framework and generation of the input signals are also discussed in this chapter.

After discussing the feasibility of di-muon detection using the MuCh subsystem, Chapter 3 gives a brief introduction to the first era of gas-filled detectors including the introduction and description of the GEM detector. The applications of the GEM detector, not only in the field of experimental HEP but also in the field of medical applications are also discussed at the end of this chapter.

In Chapter 4, the performance study of the triple GEM chamber prototypes is discussed. Details of the assembling process, basic characterisation studies, effect of environmental parameters on the performance, uniformity in response over the active area, radiation induced effects on the performance and long-term stability study of the triple GEM chambers are discussed. The chapter ends with the discussion of spark probability measurement of a triple GEM chamber at the CERN-SPS beam line facility with a pion beam of momentum 150 GeV/c.

In Chapter 5, the performance of the real size GEM modules tested at the mini-CBM beam time campaign at the existing SIS18 facility of GSI, Germany is discussed.

Finally, a summary of the works and outlook are drawn in Chapter 6 based on the various investigations reported in earlier chapters.

References

[1] E. Rutherford, Philosophical Magazine, Series 6, vol. 21, May, 669 (1911)

[2] M. Riordan, The Discovery of Quarks, SLAC-PUB-5274, (1992)

[3] https://en.wikipedia.org/wiki/Standard_Model

[4] L. Glasser, J. Chem. Educ. 81, 3, 414 (2004)

[5] G. Ecker, Quantum Chromodynamics, arXiv:hep-ph/0604165

[6] J. N. Guenther, Overview of the QCD phase diagram - Recent progress from the lattice, arXiv:2010.15503v2

[7] M. Stephanov, QCD Phase Diagram and the Critical Point, Progress of Theoretical Physics Supplement No. 153, (2004)

[8] Alessandro D. Falco, CPOD-2021
https://indico.cern.ch/event/985460/contributions/4264615/attachments/2211234/3742919/adf_cpod.pdf

[9] B. Jacak, B. MÜller, Science 337, 310, (2012)

[10] K. Fukushima, T. Hatsuda, Rept. Prog. Phys. 74:014001, (2011)

[11] P. Foka, M. A. Janik, Reviews in Physics 1, 154 (2016)

[12] U. Heinz, Concepts of Heavy-Ion Physics,
https://cds.cern.ch/record/735568/files/p127.pdf

[13] F. Becattini *et al.,* Phys. Rev. Lett. 111, 082302 (2013)

[14] J. Stachel *et al.,* J. Phys. Conf. Ser. 509, 012019 (2014)

[15] Y. Aoki *et al.,* Nature 443, 675 (2006)

[16] S. Borsanyi *et al.,* JHEP 1009, 073 (2010)

[17] A. Bazavov *et al.,* Phys. Rev. D 85, 054503 (2012)

[18] V. A. Goy *et al.,* Prog. Theor. Exp. Phys. 2017, 031 https://doi.org/10.1093/ptep/ptx018

[19] K. Kashiwa *et al.,* Phys. Lett. B 662, 26 (2008)

[20] C. S. Fischer, J. Luecker and C. A. Welzbacher, Phys. Rev. D 90, 034022 (2014)

[21] A. N. Tawfik and A. M. Diab, Phys. Rev. C 91, 015204 (2015)

[22] CBM Collaboration, EPJA 53, 3, 60 (2017)

[23] T. Galatyuk, NPA 982 (2019), update (2021)

[24] I. N. Meshkov, Phys. Atom. Nucl. 75, 594 (2012)

[25] V. Kekelidze, NPA 982 (2019)

[26] V. Toneev, PoSCPOD07:057, 2007, arXiv:0709.1459v2

[27] S. Ruan *et al.,* Nucl. Instrum. Meth. A 892, 53 (2018)

[28] http://www-rnc.lbl.gov/ nxu/group/talk2017/nxu_CBM_CEE_Sept2017.pdf

[29] H. Sako et al., JPS Conf. Ser. 8 022010, (2015) http://silver.j-parc.jp/sako/white-paper-v1.21.pdf

[30] A. Aduszkiewicz *et al.,* [NA61/SHINE Collab.], CERN-SPSC-2018-008, SPSC-P-330-ADD-10.

[31] G. Usai, PBC, Nov 2017, https://indico.cern.ch/event/644287/contributions/2724482/

[32] R. Arnaldi *et al.,* [NA60 Collab.], Phys. Rev. Lett. 96 162302, (2006)

[33] https://fair-center.eu/

[34] W. F. Henning, Proceedings of EPAC (2004)

[35] I Selyuzhenkov, J. Phys.: Conf. Ser. 1685, 012020 (2020)

[36] D. Almaalol *et al.,* arXiv:2209.05009

[37] P. Senger, Nucl. Phys. A 862, 139 (2011)

[38] B. Friman et al., The CBM Physics Book, Lecture Notes in Physics, Vol. 814, 2011
https://www.cbm.gsi.de/physics/book

[39] https://fair-center.eu/for-users/experiments/cbm

[40] I. Augustin et al., Fission and Properties of Neutron-Rich Nuclei, 128 (2008), arXiv:0804.0177

[41] P. Senger, Particles 3, 320 (2020)

[42] https://fair-center.eu/public/experiment-program/appa-physics

[43] https://panda.gsi.de/

[44] https://fair-center.eu/for-users/experiments/nustar

[45] T. Ablyazimov *et al.,* (CBM Collaboration) European Physical Journal A, 53 3, (2017)

[46] C. S. Fischer, l. Fister, J. Luecker and J. M. Pawlowski, Phys. Lett. b 732, 273 (2014)

[47] R. Critelli *et al.,* Phys. Rev. D 96, 096026 (2017)

[48] https://cbm-wiki.gsi.de/foswiki/bin/view/PWG/Figures

[49] Design simulations of beam pipe and radiation studies for the CBM experiment, CBM Internal Note, Anna Senger
https://cbm-wiki.gsi.de/foswiki/pub/PWG/C2F/BeamPipe/20180530_Internal_Note_beam_pipe-AS.pdf

[50] E. Clerkin, CBM Progress Report 2021, p155, DOI: 10.15120/GSI-2022-00599

[51] A. Senger, CBM Progress Report 2021, p159, DOI: 10.15120/GSI-2022-00599

[52] A. Malakhov and A. Shabunov, editors. Technical Design Report for the CBM Superconducting Dipole Magnet. GSI, Darmstadt, 2013

[53] P. Senger and V. Friese. CBM Progress Report 2020. Technical Report 2021-00421, 2021

[54] CBM Progress Report 2019. Technical Report CBM-PR-2019, 2020

[55] J. Heuser *et al.,* editors. [GSI Report 2013-4] Technical Design Report for the CBM Silicon Tracking System (STS). GSI, Darmstadt, 2013

[56] Technical Design Report for the CBM Ring Imaging Cherenkov Detector. Technical report, 2013

[57] S. Chattopadhyay *et al.,* editors. The Muon Chamber of the CBM Experiment at FAIR : Technical Design Report for the CBM Muon Chamber (MuCh).
https://repository.gsi.de/record/161297

[58] The Transition Radiation Detector of the CBM Experiment at FAIR : Technical Design Report for the CBM Transition Radiation Detector (TRD). Technical report, Darmstadt, 2018

[59] Norbert Herrmann, editor. Technical Design Report for the CBM Time-of-Flight System (TOF). GSI, Darmstadt, 2014

[60] Fedor Guber and Ilya Selyuzhenkov, editors. Technical Design Report for the CBM Projectile Spectator Detector (PSD). GSI, Darmstadt, 2015

[61] J. Kapusta, P. Lichard, and D. Seibert. Phys. Rev. D 44, 2774 (1991) , Erratum-ibid 47, 4171 (1993)

[62] C. Y. Wong, Introduction to high energy heavy ion collisions, World Scientific, Singapore (1994)

[63] Ramona Vogt, Ultrarelativistic Heavy-Ion Collisions, Elsevier, The Netherlands, (2007)

[64] P.Roy, S. Sarkar, J. Alam, B. Dutta-Roy, and B. Sinha, Phys. Rev. C 59, 2778 (1999)

[65] J. K. Nayak, J. Alam, S. Sarkar and B. Sinha, Phys. Rev. C 78, 034903 (2008)

[66] T. Matsui and H. Satz, Phys. Lett. B 178, 416 (1986)

Chapter 2

Feasibility studies of di-muon detection at the CBM experiment

2.1 Introduction

The Muon Chamber (MuCh) at the CBM experiment is dedicatedly designed to track the di-muons coming from the decay of Low Mass Vector Mesons (LMVM) and charmonium [1]. The schematic of the di-muon measurement setup at CBM (SIS100) is shown in Fig. 2.1 [2]. One of the major challenges with the MuCh sub-system is the measurement of low momenta muons coming from the decay of LMVM due to the large combinatorial background. To measure such soft muons, the MuCh sub-system features a variable number of hadron absorbers and detector stations with triplets of detector layers placed in between the absorbers. The hadron absorbers will reduce the hadronic backgrounds. The Gas Electron Multiplier (GEM) [3] detectors will be used in the first two stations of MuCh to cope up with the expected large particle densities. The Resistive Plate Chamber (RPC) [4] is proposed as the tracking device for the third and fourth stations of MuCh. Each detector station contains three detector layers arranged on an aluminium support structure which also acts as the cooling plate for the electronics. The expected point densities at the different MuCh stations for central (0-10%) Au+Au collision at beam momentum of 12 A GeV/c are shown in Fig. 2.2. Taking the interaction rate of 10 MHz and

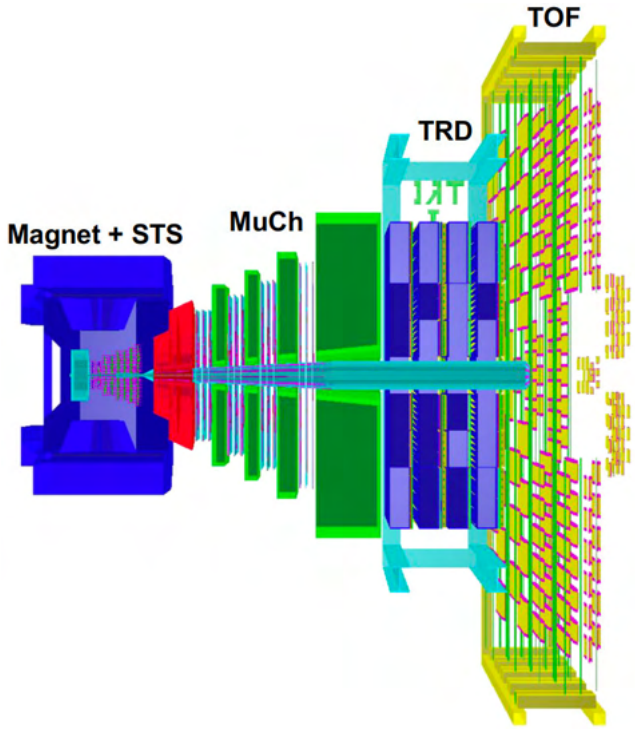

Figure 2.1: Schematic of the di-muon detection setup at CBM SIS100 energies.

using the approximate scaling factor (1/4) for going from central events to minimum bias [1] events, the maximum particle flux (near the beam pipe) at the four MuCh stations for a minimum bias Au+Au collision at 12 A GeV/c is expected to be $\sim$ 0.5 MHz/cm^2, $\sim$ 0.4 MHz/cm^2, $\sim$ 35 kHz/cm^2 and $\sim$ 15 kHz/cm^2 respectively. The density at the respective stations will increase by a factor of $\sim$4 in case of central collisions. Therefore, to establish the fact that GEM can be used in the harsh radiation environment, an R&D program for the studies of the radiation-induced effects on triple GEM chamber is undertaken at Bose Institute. This study aims to understand the possible effects on the performance of the chamber under continuous high irradiation.

This work is initiated by investigating the feasibility of di-muon detection with the MuCh setup at CBM (SIS100 energies) followed by a detailed R&D on the

[1]Minimum bias events are those events where the collisions can take place at all possible impact parameters. The impact parameter is defined as the perpendicular distance between the centre of the target and projectile nucleons.

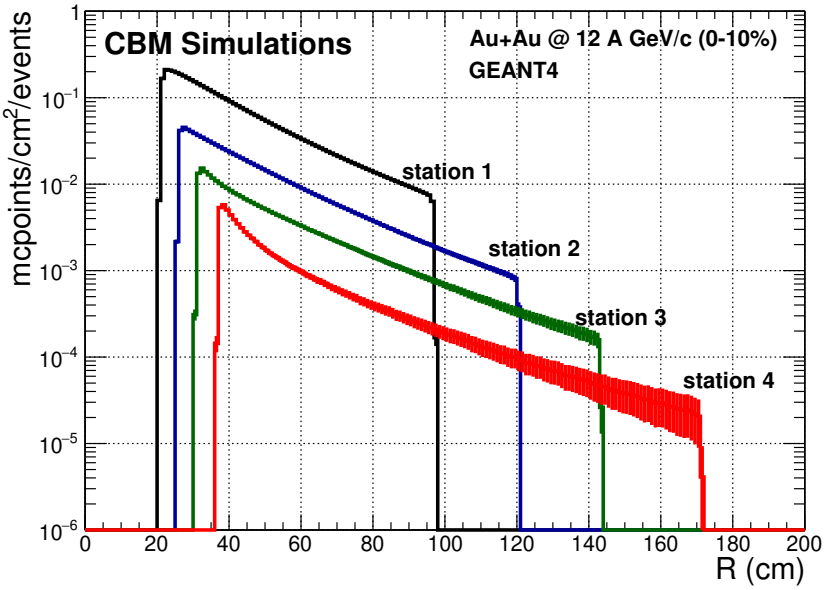

Figure 2.2: Monte Carlo (MC) point density at different stations of MuCh for central (0-10%) Au+Au collision with beam momentum of 12 A GeV/c.

performance of GEM detector prototypes under high irradiations. The details of the GEM detector R&D are discussed in Chapter 4.

The feasibility study of di-muon detection includes the optimisation of the MuCh hadron absorber design and simulation studies on the reconstruction performance of the LMVM ($\rightarrow \mu^+\mu^-$) and J/ψ ($\rightarrow \mu^+\mu^-$) with MuCh subsystem at SIS100 energies using the CBMROOT software. CBMROOT is the software package dedicatedly designed for the CBM experiment to perform the simulation, reconstruction, and data analysis [5]. Details of the CBMROOT software are discussed in section 2.3.

2.2 MuCh: layout and configurations

The general philosophy of muon detection in any HEP experiment is to use absorbers which are capable of absorbing hadrons but not the muons and a set of detectors for the identification of muons from their tracks. The basic idea is that

all other particles produced in the high energy nuclear collisions get absorbed inside the absorber and the muons being highly penetrating, pass through the absorbers and reach the detector. In CBM, the muon measurements are enabled by the MuCh sub-system located downstream of the dipole magnet. The dipole magnet houses the Silicon Tracking System (STS) with an angular acceptance of 2.5° to 25°, required for the momentum determination of the charged particles. The MuCh sub-system spans from 5.7° to 25°. The experimental challenge for the muon measurements in heavy-ion collisions at CBM energies is to identify low-momentum muons in an environment of high particle densities.

Table 2.1: Foreseen energies for nucleus-nucleus collisions at SIS100 [6]. P_{beam} represents the momentum of the beam, E_{beam} represents the beam total energy, $E_{kinetic}$ represents the beam kinetic energy and $\sqrt{s_{NN}}$ represents the centre of mass energy.

P_{beam} (A GeV/c)	E_{beam} (A GeV)	$E_{kinetic}$ (A GeV)	$\sqrt{s_{NN}}$ (GeV)
3.3	3.43	2.49	2.9
4.4	4.5	3.56	3.2
7.95	8.0	7.06	4.1
12.0	12.04	11.1	4.9

The strategy for muon detection in the CBM experiment is to track the particles through a segmented hadron absorber system and to perform a momentum-dependent muon identification. This concept is realized by a segmented hadron absorber equipped with three detector layers placed in between two consecutive absorber layers, known as stations [1]. Within the FAIR modularised start version, the SIS100 ring will provide beams with kinetic energies up to 11 A GeV for heavy-ions, and up to 29 GeV for proton beams [5]. In Table 2.1, the foreseen energies for Nucleus-Nucleus (heavy-ion) collision at CBM are summarised [6]. Thus the modularised design of the MuCh detector sub-system offers additional flexibility for hassle-free up-gradation as per requirement. Based on the beam energy and physics interest, three different geometry variants of the MuCh sub-system are currently investigated. The low energy version of MuCh will consist of 3 absorbers and 2 detector stations for beam momentum $P_{beam} < 4$ A GeV/c. The simulated image of the CBM detector setup with the MuCh low energy ver-

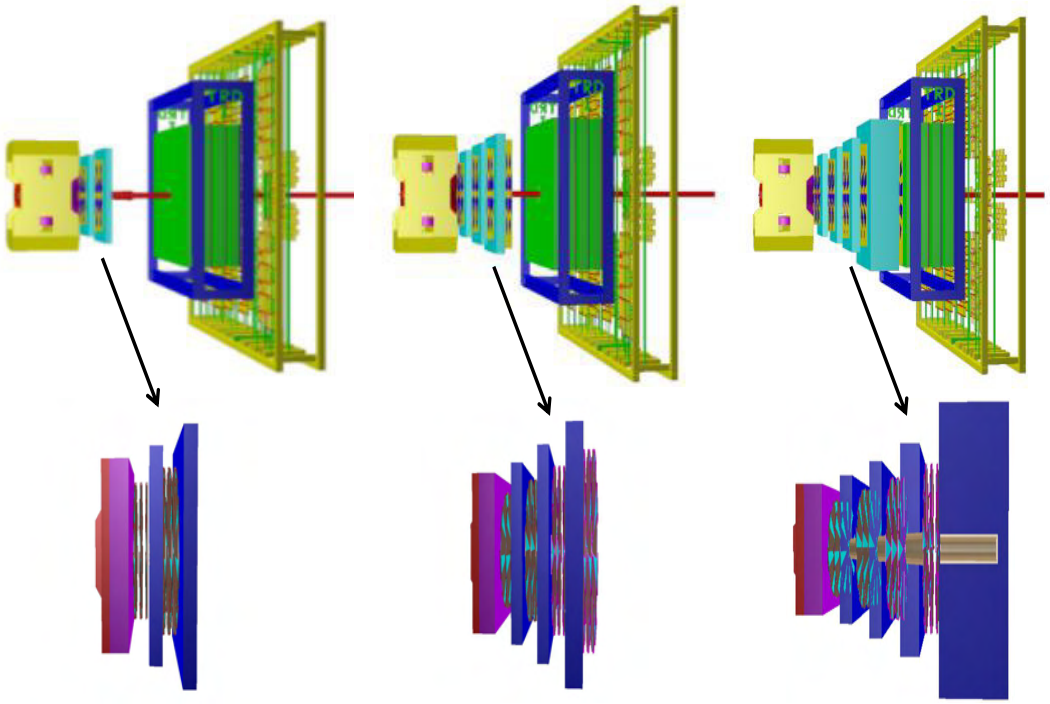

Figure 2.3: Detector setups of the CBM experiment with MuCh geometry for the low energy setup (left) (P_{beam} < 4 A GeV/c), for the P_{beam} > 4 A GeV/c LMVM setup (middle) and for the J/ψ detection setup (right). The details of absorber specifications are mentioned in Table 2.2.

sion is shown in Fig. 2.3 (left). For the beam momentum P_{beam} > 4 A GeV/c, the MuCh sub-system will comprise of 4 absorbers and 4 detector stations, as shown in Fig. 2.3 (middle). The J/ψ measurement setup will be equipped with an additional iron block of 100 cm thickness at the end of the fourth detector station. The simulated geometry is shown in Fig. 2.3 (right). The additional 100 cm thick iron absorber is used to reduce the background at the Transition Radiation Detector (TRD) stations, which will be used as a trigger detector for the J/ψ measurement. The first absorber block is 58 cm thick, composite in nature, and made of graphite (28 cm) and concrete (30 cm) [2]. The 2^{nd}, 3^{rd}

[2]The earlier design of the MuCh 1^{st} absorber consist of 60 cm thick graphite. However, from the realistic design simulations it is observed that the optimised configuration would be graphite (28 cm) and concrete (30 cm) for the 1^{st} absorber. The details of the study can be found in Ref. [7].

Table 2.2: Specification of different MuCh absorbers. The 1^{st} absorber is made of three parts and with two different materials. The portion of the 1^{st} absorber which is inside the magnet is of trapezium shape and the rest of the absorbers are parallelopiped in shape. The 5^{th} absorber is used for the J/ψ detection.

Absorber No.	Composition	Density (g/cm^3)	Thickness (cm)	Shape	Dimension (cm^3)
I (a)	Graphite	1.78	16	Trapezium	-
I (b)	Graphite	1.78	12	Parallelopiped	260×250×12
I (c)	Concrete	2.3	30	Parallelopiped	260×250×30
II	Iron	7.87	20	Parallelopiped	279×279×20
III	Iron	7.87	20	Parallelopiped	326×326×20
IV	Iron	7.87	30	Parallelopiped	382×382×30
V	Iron	7.87 (7.2)	100	Parallelopiped	500×500×100

and 4^{th} absorbers are made of iron of density 7.87 g/cm^3 having thicknesses of 20 cm, 20 cm and 30 cm respectively. In the J/ψ measurement setup, the 100 cm thick iron block will be used with a density of 7.2 g/cc. The optimisation of the 5^{th} absorber is discussed in section 2.5.2. The details of the MuCh absorbers is tabulated in Table 2.2[3]. To avoid the effect of the fringing magnetic field, stainless steel will be used instead of soft iron. Each detector station has three layers made of gas-filled ionization chambers. The detectors are placed at equal spacing in the air gap between two consecutive absorbers. The gap between two successive absorber is 30 cm except for the first one. The gap between the first and the second absorber is 32 cm. The GEM detectors are used in the first two stations for their high rate handling capabilities. For the third and fourth stations, the RPC detectors are used in the simulation geometry. In Fig. 2.4, the simulated detector stations are shown. To reduce the activation of the MuCh absorber materials, additional shielding (only in the absorber region) is used around the beam pipe and below the MuCh absorbers. To simplify the geometry, the shapes of these inserts were chosen as cylindrical tubes. The length of each tube is equal to the thickness of the corresponding absorbers. The simulated image of the shielding around the beam pipe and below the MuCh absorbers is shown in Fig. 2.5. The opening angle of the hole

[3]Realistic studies by the MuCh mechanical colleagues revealed the non-availability of the large size iron blocks of density 7.87 g/cm^3. The highest feasible option available in the market is 7.2 g/cm^3. Therefore, both values are written in Table 2.2. The observed effects of reduced iron density are discussed in section 2.5.2.

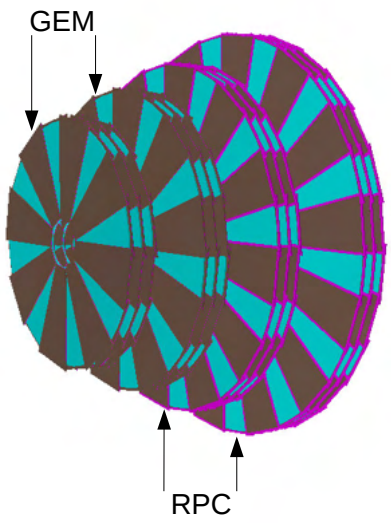

Figure 2.4: Simulated detector arrangement for MuCh detector sub-system.

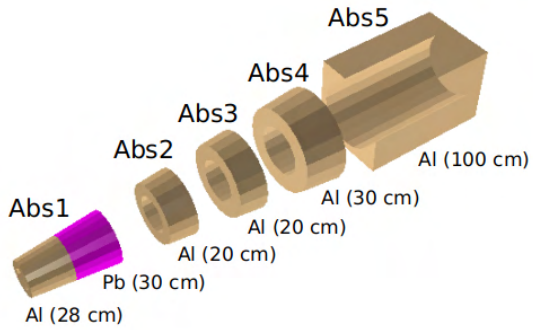

Figure 2.5: Simulated arrangement for the shielding below the MuCh absorbers.

in the shielding is 2.9° for all absorbers. The simulation study for the optimisation of the opening of the beam-pipe has been performed earlier and reported in [8]. In the latest configurations, in order to accommodate the latest design of beam pipe shielding, 28 cm Aluminium (Al) and 30 cm Lead (Pb) are used for shielding below the first absorber. Al is used for the rest and the opening angle of the hole in the shielding is reduced to 2.5° for the first absorber. Al is preferred in a high radiation environment due to its low activity. The shape of the beam-pipe is evolving and has not been fixed yet. Therefore, the study on the influence of beam pipe shielding on the performance of di-muon detection is also ongoing.

2.3 Simulation framework

HEP experiments are very expensive due to their complex structures. The aim of such experiments may not be fulfilled if there are some errors or problems in the design of the different detector sub-systems. It is, therefore, very important to perform detailed simulations in terms of the performance of the individual detector sub-systems with realistic simulation tools. In this thesis, the optimisation of the MuCh sub-system, as carried out with the CBMROOT simulation framework, is discussed. The simulation studies are broadly classified into two parts. One includes the optimisation of the geometry of the MuCh sub-system and the other includes the physics performance simulation using the optimised MuCh sub-system at SIS100 energies.

The CBMROOT simulation package is dedicatedly designed for the CBM experiment. This framework is developed using the ROOT analysis package. Using the framework, both the simulation and data analysis can be performed. This framework also provides the base classes for the construction of different detector geometries, visualization of tracks and also other general functions. The details of the framework is reported in Ref. [5].

The muon simulation with the CBMROOT framework includes the following steps:

- Event generation
- Implementation of detector sub-systems
- Transportation of the generated particles through the detector sub-systems
- Segmentation of detector readout
- Digitization
- Clustering and hit finding
- Track reconstruction

- Identification of muon track candidates

The goal of the MuCh sub-system is to detect the muon pairs coming from the decay of LMVM and J/ψ in a high density charged particle environment. To mimic the situation, the UrQMD (Ultra relativistic Quantum Molecular Dynamics) [9] event generator is used to generate the hadronic background and the PLUTO [10] event generator is used to generate the signal muons. The generation of input signals using the PLUTO event generator is discussed in section 2.4. The detector sub-systems are selected to transport the generated particles through them. The transportation is done with the help of GEANT (GEometry ANd Tracking) [11] transport engine. After the transportation, GEANT gives information about the position of the energy deposition in the detector modules. In the next step, the segmentation of the readout modules of respective detectors is performed. This segmentation is needed to get the spatial information of a particle falling on the respective detectors. After segmenting the detector readout planes, in the digitization process, the detector responses are taken into consideration. The digis (fired pads) produced after digitization are clubbed to form a cluster and finally, the clusters are deconvoluted to produce hits. Then the hits at the different detector stations are used to reconstruct the tracks. From the reconstructed global tracks, the muon track candidates are selected using some topological cuts on the reconstructed global tracks. The selection of muon track candidates is discussed in the following sections.

2.4 Generation of input signals using PLUTO

The PLUTO event generator was originally developed for HADES experiment but it is successfully used by other collaborations in the hadronic physics field as well. Its design enhanced its flexibility and provided new features which allow one to meet new challenges coming with the simulation studies for the new FAIR experiments; PANDA and CBM. The Thermal Fireball model, which

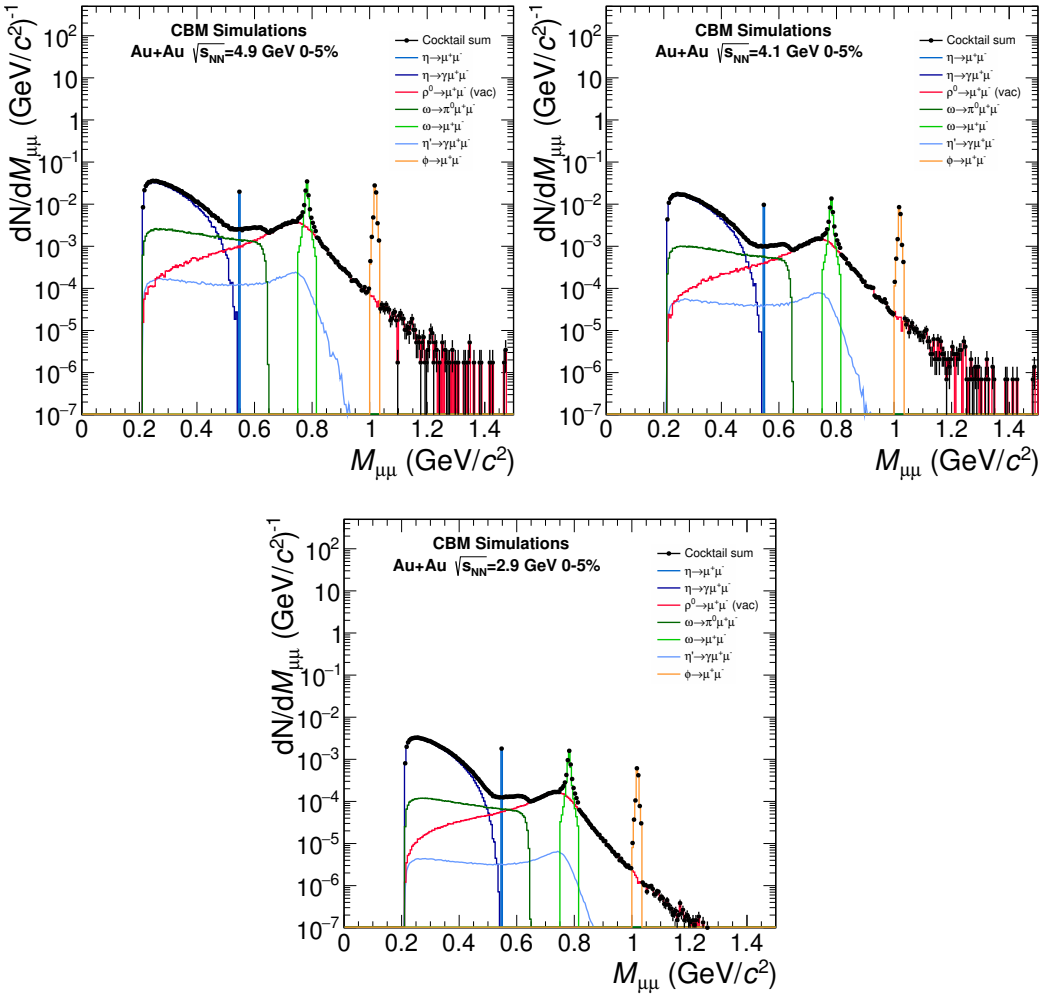

Figure 2.6: Di-lepton cocktail in di-muon channel for $\sqrt{S_{NN}}$ = 4.9 GeV (top left), 4.1 GeV (top right) and 2.9 GeV (bottom) for central (0-5%) Au+Au collision.

is used in the PLUTO event generator, generates vector mesons with thermal transverse mass (m_T) as well as Gaussian rapidity spectra and decays them isotropically into di-leptons. A more detailed description of the PLUTO event generator is reported in Ref. [10].

The di-lepton cocktail for Au+Au 0-5% central collision at the centre of mass energies ($\sqrt{s_{NN}}$) of 4.9, 4.1 and 2.9 GeV is shown here as an illustration in Fig. 2.6. The respective meson multiplicities are used from the Thermal-FIST (Thermal-Fast and Interactive Statistical Toolkit) model and can be found at Ref. [12]. To generate the input signals, only two input parameters, namely beam en-

ergy and temperature of the system, are provided [13]. The list of the input parameters is tabulated in Table 2.3.

Table 2.3: Input parameters of PLUTO for different beam energies.

System ($\sqrt{s_{NN}}$)	Beam energy	Temperature
Au+Au (2.9 GeV)	3.42 A GeV	0.09 GeV
Au+Au (4.1 GeV)	8 A GeV	0.12 GeV
Au+Au (4.9 GeV)	12 A GeV	0.13 GeV

In Fig. 2.7 and Fig. 2.8, a typical rapidity (y) and the transverse momentum (p_T) distribution of the signal particles for three different energies are shown. The

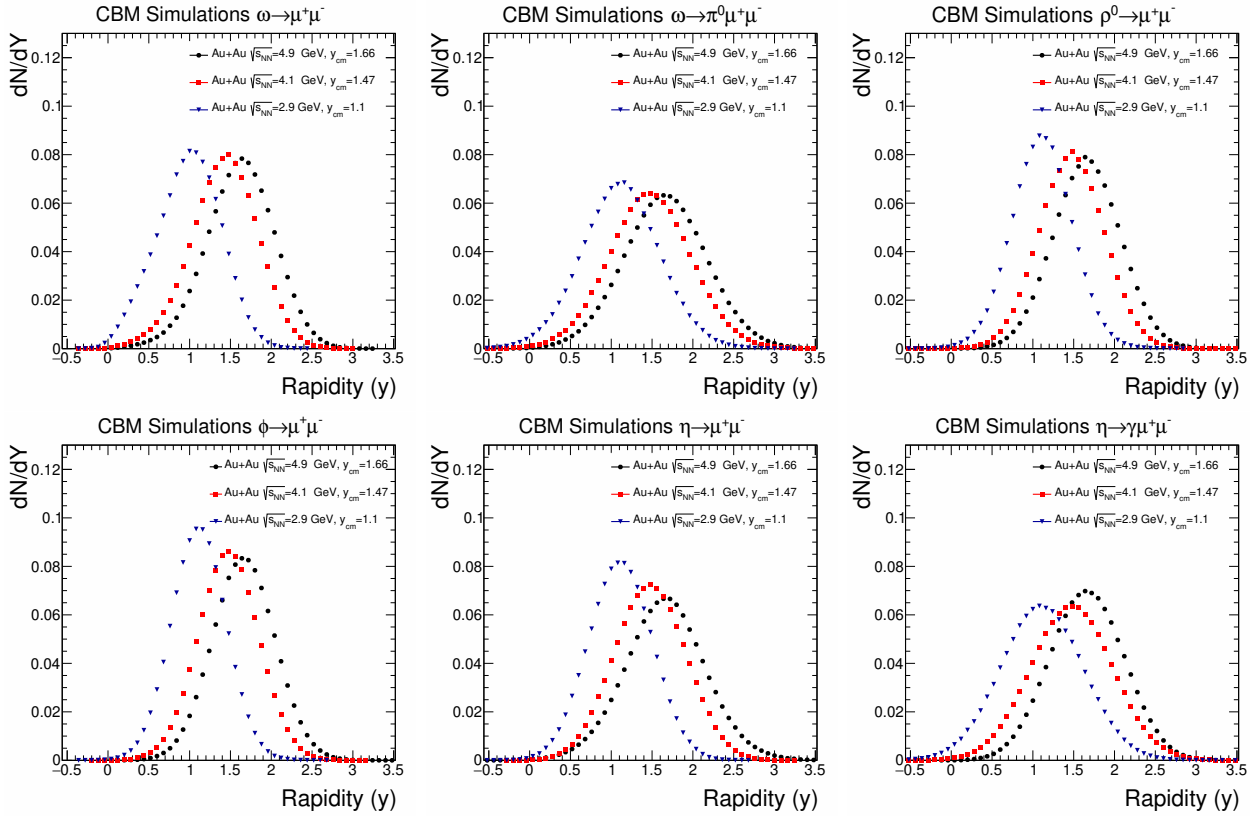

Figure 2.7: Rapidity distribution of signal particles for three different beam energies. The respective mid rapidity values are quoted in the legend. The error bars are smaller than the marker size.

p_T spectra are fitted with a functional form as shown in Eqn. 2.1,

$$dN/dp_T \propto p_T m_T K_1(m_T/T) \tag{2.1}$$

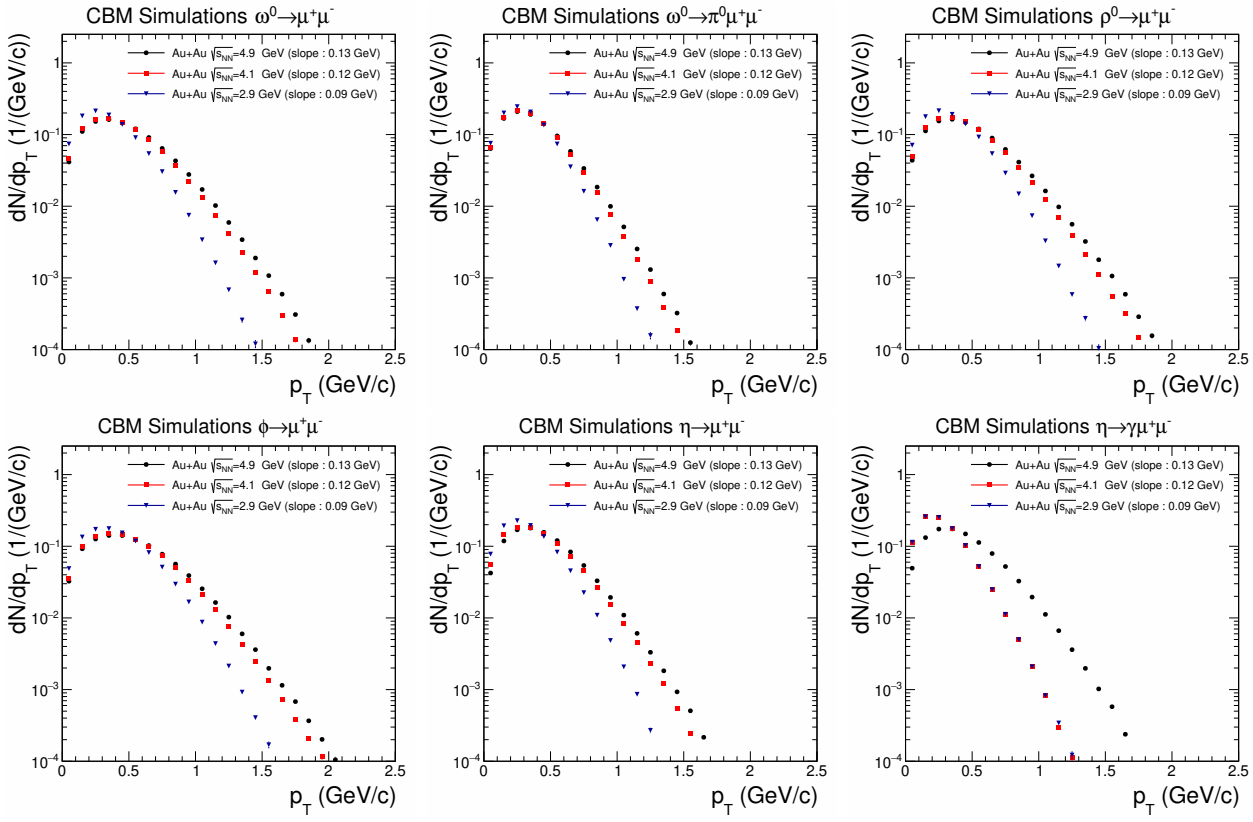

Figure 2.8: p_T spectra of signal particles for three different beam energies. Legends indicate the different slope values extracted after the fitting. The error bars are smaller than the marker size.

where K_1 denotes the Bessel function of the second kind, m_T is the transverse mass and T is the temperature. The inverse slope of the p_T spectra after fitting gives the temperature. The extracted temperature matches well with the input temperature.

2.5 Optimisation of MuCh geometry configuration

The optimisation of MuCh absorber configurations and the feasibility studies of di-muon detection at SIS100 energies with the MuCh detector sub-system are discussed here.

Detailed investigations on the MuCh mechanics revealed that it is difficult to attain uniform surface smoothness over the entire volume of the iron absorbers,

which might affect the detector performance. Hence it is necessary to investigate the effect of surface tolerance of the absorber blocks on the overall di-muon reconstruction performance of the muon system. The phase space distribution of the decay $\omega \rightarrow \mu^+\mu^-$ from PLUTO is used as the signal probe to optimize the MuCh sub-system geometry configuration. Since it is not feasible to investigate the effects of MuCh sub-system geometry modifications on the di-muon reconstruction performance with the entire LMVM cocktail, only the decay ω ($\rightarrow \mu^+\mu^-$) is taken as the reference signal.

2.5.1 Surface tolerance study of intermediate MuCh absorbers

As the first step, four different LMVM geometry configurations have been considered where the thicknesses of the 2^{nd}, 3^{rd} and 4^{th} absorber are varied keeping the thickness of the 1^{st} absorber fixed. The thickness of the absorbers used in the simulation are the following: 60 cm - 20 cm - 20 cm - 30 cm (reference configuration), 60 cm - 19 cm - 19 cm - 29 cm, 60 cm - 18 cm - 18 cm - 28 cm and 60 cm - 17 cm - 17 cm - 27 cm. The overall thickness of the iron absorbers is reduced by 3 cm in each step. The reconstruction of the ω ($\rightarrow \mu^+\mu^-$) mesons, in central Au+Au collision at $\sqrt{s_{NN}}$ = 4.1 GeV, is used for the comparison of different absorber configurations. The phase space decay of ω ($\rightarrow \mu^+\mu^-$) is simulated using the PLUTO event generator. The signal muon pairs embedded into the background, generated using the UrQMD event generator. One ω ($\rightarrow \mu^+\mu^-$) candidate from PLUTO is embedded per event into the background. All the particles are transported through the entire CBM detector setup using the GEANT3 transport engine.

The ratio of the radial distribution of the MuCh point density (number of Monte Carlo points per unit area per event) for all four MuCh stations is shown in Fig. 2.9 where the ratio is taken with respect to that of the 60 cm -20 cm - 20 cm - 30 cm configuration. As expected, no change is seen for station 1, as the thickness of the first absorber is kept fixed. For the rest of the stations, the particle density monotonically increases with decreasing absorber thickness due

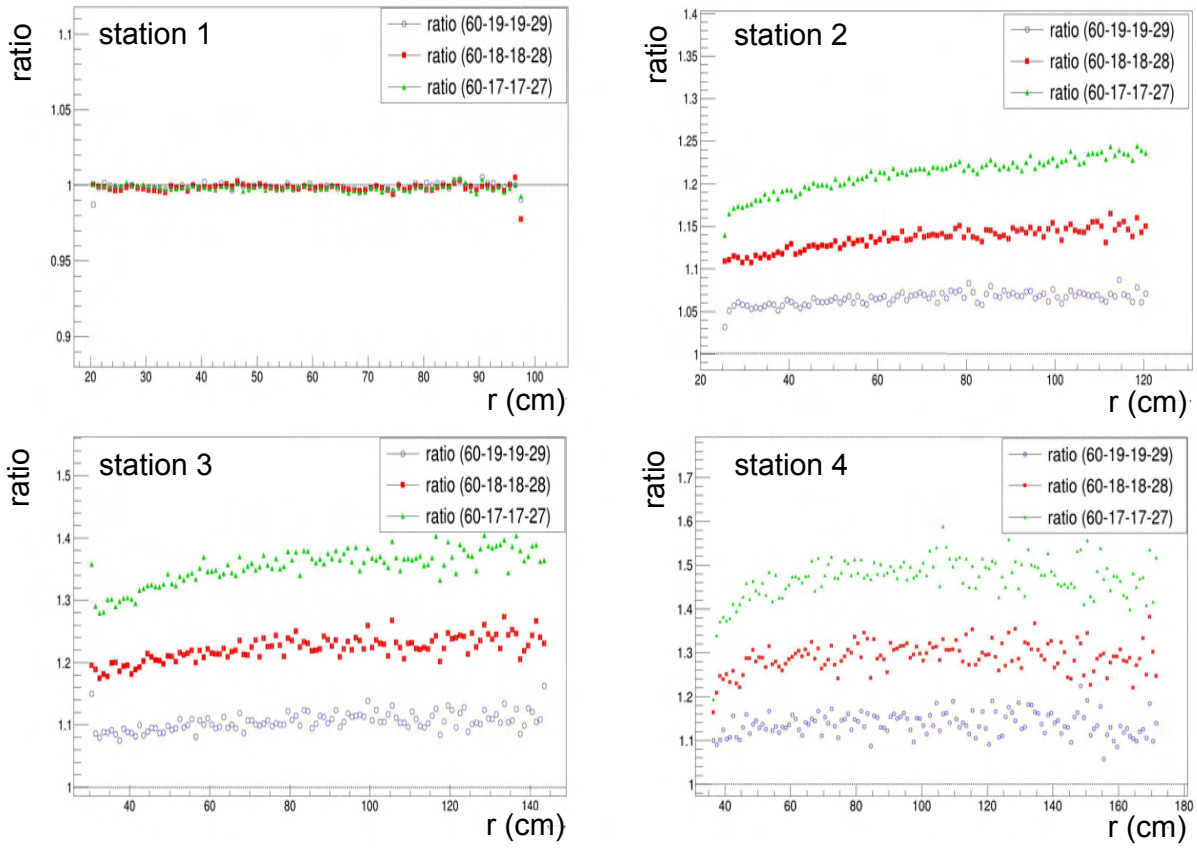

Figure 2.9: Ratio of the radial distribution of MuCh point density for all four MuCh stations and for all the different absorber configurations. The ratio is taken with respect to that of the 60 cm - 20 cm - 20 cm - 30 cm configuration. The error bars are smaller than the marker size.

to reduced absorption. Around 50% increase in the point density is observed when the absorber thicknesses are changed from 60 cm - 20 cm - 20 cm - 30 cm to 60 cm - 17 cm - 17 cm - 27 cm. A similar increasing trend is seen for the radial distribution of occupancy [4] of the stations 2, 3 and 4 while reducing the thickness of the absorbers and is shown in Fig. 2.10.

Finally, in order to test the effect of surface tolerance on the signal reconstruction, invariant mass is calculated for all the four different geometry configurations, after full simulation and reconstruction. The muon software, as available within the CBMROOT framework (CBMROOT TRUNK, Revision no. 15516), is used for the analysis. A set of single track quality cuts are applied to the re-

[4]Occupancy is defined as the fraction of the fired pads per event.

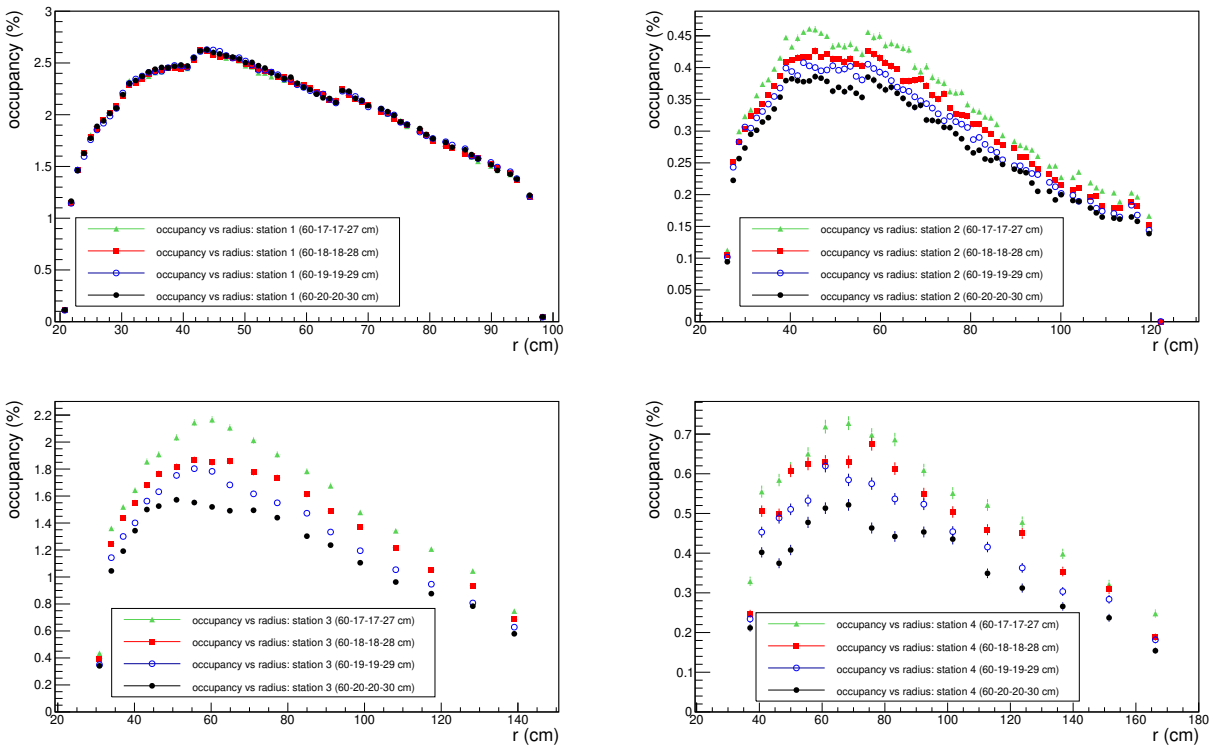

Figure 2.10: Occupancy distribution as a function of radii for different absorber configurations of MuCh detector stations. Occupancy as a function of radius for station 1 (top left), station 2 (top right), station 3 (bottom left) and station 4 (bottom right).

constructed global tracks to identify the muon track candidates. Reconstructed global tracks with associated STS hits ≥ 7, MuCh hits ≥ 10, TRD hits ≥ 1, $\chi^2_{Vertex} \leq 2.5$, $\chi^2_{STS} \leq 2.0$ and $\chi^2_{MuCh} \leq 2.8$, are selected as valid muon track candidates. The contribution of non-muonic tracks is further reduced by applying a 2σ cut on the reconstructed TOF mass. The signal is extracted from the embedded set of events by selecting oppositely charged muon candidate tracks on an event by event basis. The background is calculated using the Super Event (SE) technique, where one muon candidate track is combined with all the other oppositely charged muon candidate tracks to calculate the combinatorial background. The invariant mass distribution of the reconstructed ω mesons along with the combinatorial background, for the nominal absorber configuration (60 cm-20 cm-20 cm-30 cm), is shown in Fig. 2.11. The pair reconstruction efficiency (ϵ_ω), signal to background ratio (S/B) and significance

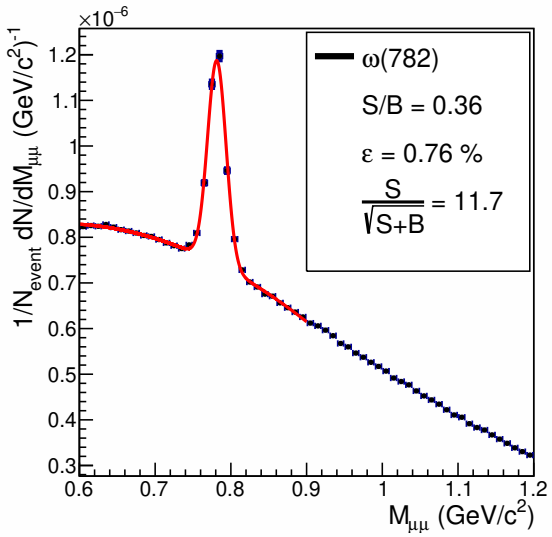

Figure 2.11: Invariant mass distribution with a 60 cm-20 cm-20 cm-30 cm absorber configuration. One ω has been embedded per event. The error bars are smaller than the marker size.

$(S/\sqrt{S+B})$ [5], for all four different absorber configurations, are given in Table 2.4. As evident from the table, with decreasing absorber thickness, the

Table 2.4: Reconstruction efficiency and Signal to background ratio for ω in central Au+Au collision at $\sqrt{s_{NN}}$ = 4.1 GeV for different geometry configurations.

MuCh geometry Configuration	ϵ_ω (%)	**S/B**	**Significance** $(S/\sqrt{(S+B)})$
60-20-20-30 cm	0.76	0.36	11.7
60-19-19-29 cm	0.78	0.33	11.5
60-18-18-28 cm	0.80	0.29	11.1
60-17-17-27 cm	0.81	0.26	10.6

pair reconstruction efficiency increases because of less absorption of the signal muons but S/B decreases due to an increase in the background. In Fig. 2.12, the variation of omega reconstruction efficiency and signal to background ratio is shown for different absorber thickness configurations.

Finally, to study the effect of reduced absorber thickness over the full di-muon spectrum, in Fig. 2.13, the ratio of the combinatorial background over the entire di-muon mass range, for all the geometries to the reference geometry, is

[5]The significance value tells us the visibility of the signal peak over the background in the invariant mass spectra.

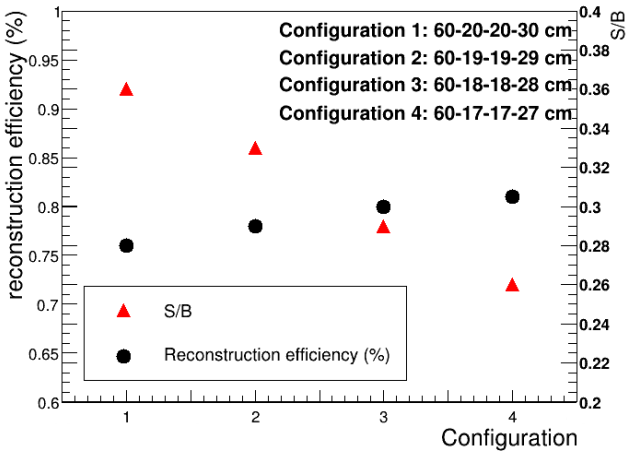

Figure 2.12: The ratio of reconstruction efficiencies and the signal to background (S/B) ratio for different absorber configurations. The error bars are smaller than the marker size.

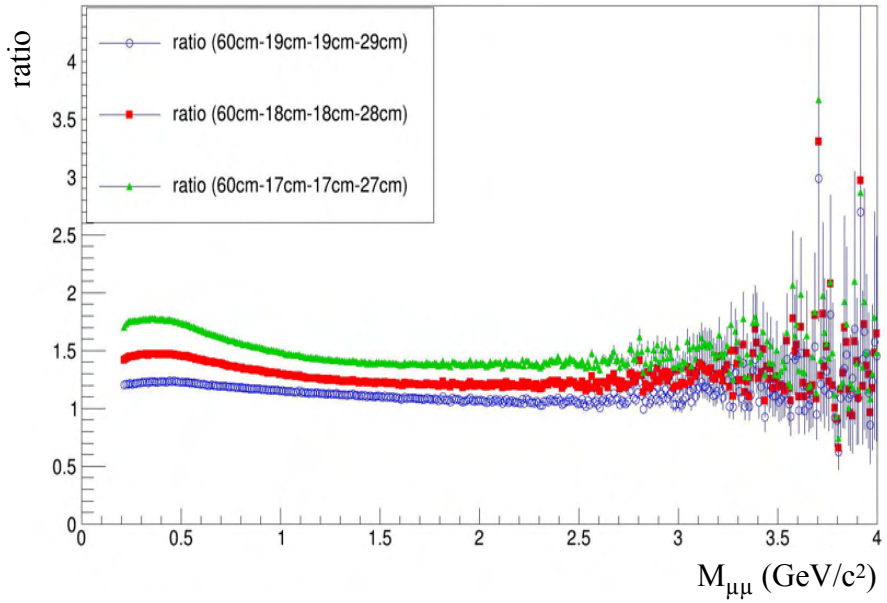

Figure 2.13: Ratios of combinatorial background with respect to 60 cm-20 cm-20 cm-30 cm absorber configuration as functions of the di-muon invariant mass.

displayed. In the low mass region (m_{inv} $\leq$0.5 GeV/c^2), a sizeable enhancement is observed in the ratio and that may be due to the decay of pions since the air gap increases with the decreasing absorber thickness.

These studies reveal that any reduction of the thickness of the iron absorbers, of the order of a few centimetres, would degrade the performance of di-muon

measurements at SIS100 energies. It is anticipated that a surface tolerance of the order of a few millimetres might preserve the feasibility of di-muon detection [14].

2.5.2 Optimisation of the MuCh 5^{th} absorber

As mentioned earlier, the MuCh detector sub-system is made of five absorber blocks and four tracking stations for the J/ψ detection setup. The 5^{th} absorber will be used as a muon filter, to reduce the background hit load in the following TRD gas chambers. In the transverse plane, the surface area of the proposed 5^{th} absorber is 500×500 cm^2 with a thickness of 100 cm along the beam direction. The wall area reflects the effective di-muon acceptance, while its thicknesses are sufficient for a nearly complete absorption of the background particles within the detector acceptance. The 5^{th} absorber was implemented as a monolithic block of iron with a density of 7.87 g/cm^3 in the simulations. Investigations related to MuCh mechanics revealed that due to the large volume of the 5^{th} absorber, it is very difficult to produce a monolithic iron block of this dimension (500×500×100 cm^3). As an alternative, it is proposed to break the entire block into smaller pieces. Such a modular design would also make the assembly and disassembly process easier. In this configuration, the entire absorber is divided into ten iron plates. Among these ten blocks, eight blocks are of dimension 500×55×100 cm^3 and the remaining two opening blocks are of dimension 220×60×100 cm^3. An Aluminium box of dimension 60×60×100 cm^3 along with a 50 cm diameter hole along the length is used to reduce the activation of the iron absorber. As the absorber will be built of not fine-machined plates, there could be cracks in between successive plates. The maximum crack width should be defined by the plate machining tolerance. In principle, the introduction of cracks will lead to a reduction in the effective thickness of the wall. This in turn should cause a rise in the background hit load in the trigger station. Hence the influence of the crack width is studied, as discussed in detail in Ref. [15].

Moreover, further studies on MuCh mechanics have also revealed the non-availability of large size iron blocks of density 7.87 g/cm^3, suitable for building the 5$^{\text{th}}$ absorber. The highest feasible density appears to be 7.2 g/cm^3. To keep the effective hadronic interaction length constant, the reduction in density must be compensated by the physical thickness of the absorber from 100 cm to nearly 110 cm. However, this would imply a 10 cm downstream shift of all subsequent sub-detectors including TRD and TOF, which would affect their acceptance. Thus the thickness of the absorber is kept unaltered but the density is reduced to 7.2 g/cm^3. That meant less absorption of the incoming particles incident on the TRD. The design of the rest of the iron absorbers is kept unchanged.

In the simulation, the cracks are represented by vertical gaps of predefined widths. The absorber wall is composed of floating iron slabs. The slabs are positioned symmetrically with respect to the beam axis. Three different gap widths namely, 0 mm, 3 mm and 6 mm, each with two different iron densities, namely 7.87 g/cm^3 and 7.2 g/cm^3, are simulated to see the effect on the J/ψ reconstruction. The schematic configuration of the MuCh 5$^{\text{th}}$ absorber, according to the engineering design, is shown in Fig. 2.14 for three different gap configurations. Configuration 1 stands for an ideal case with zero separation between the absorber plates and thus closely resembles the monolithic design. Configuration 2 stands for a realistic modular design with a 3 mm vertical separation between the absorber plates. The absorber geometry with a 6 mm gap between the iron slabs is labelled as configuration 3. For all configurations, a 3 mm gap is maintained between the aluminium shielding, used to reduce the activation of the iron over the beam pipe, and the iron blocks to make the simulation more realistic.

Simulations are carried out with the APR20 release version of CBMROOT. The reconstruction of the J/ψ mesons, in central Au+Au collision at $\sqrt{s_{NN}} = 4.54$ GeV, is used for the comparison of different absorber configurations. The phase space decay of J/ψ ($\rightarrow \mu^+\mu^-$) is simulated using the PLUTO event generator. The signal muon pairs are embedded into the background, generated using the UrQMD event generator. One J/ψ ($\rightarrow \mu^+\mu^-$) from PLUTO

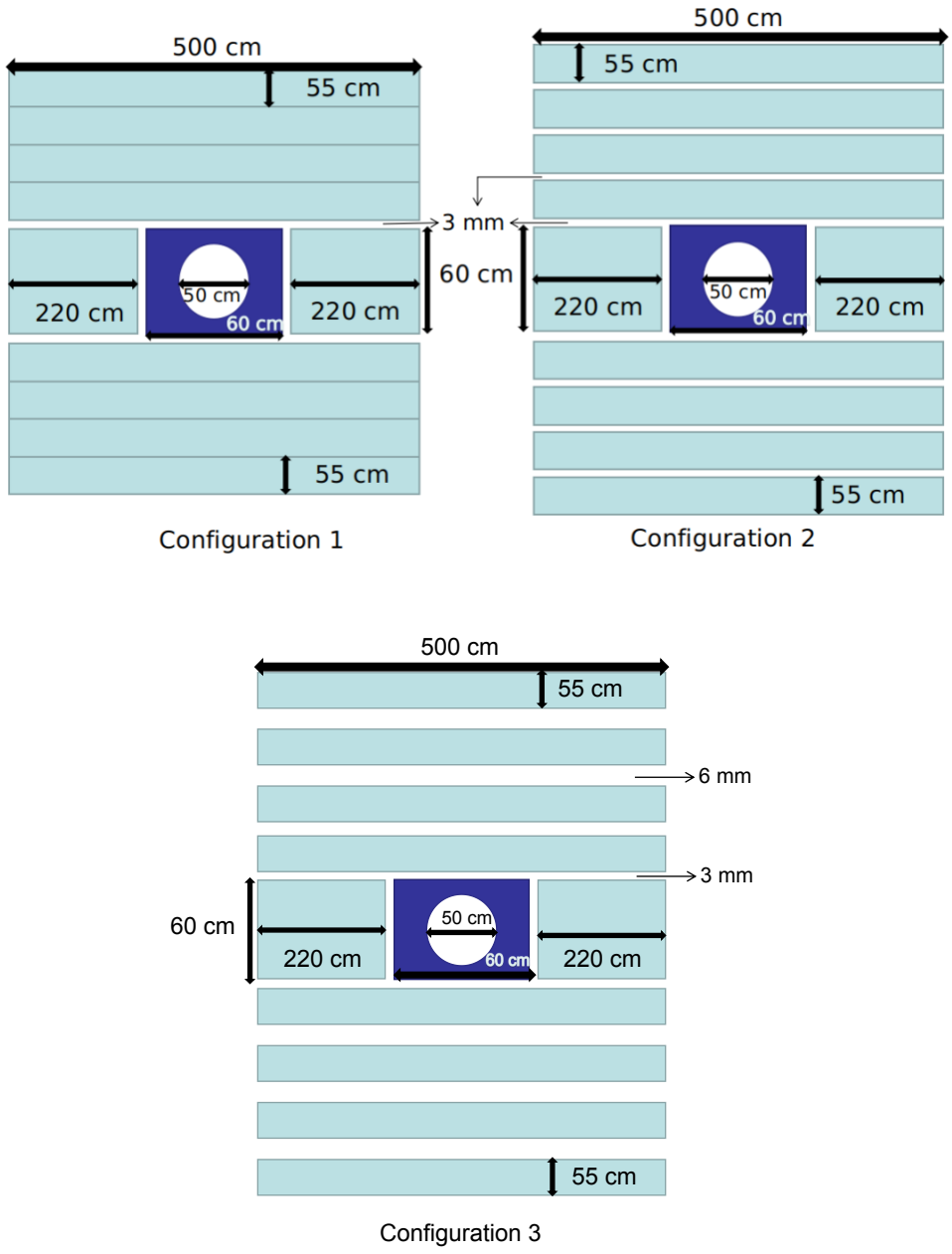

Figure 2.14: Schematic design of the MuCh 5th absorber. Cyan colour indicates the iron blocks and blue indicates the aluminium block. In configurations 1 & 2, the gap between the iron blocks are 0 mm and 3 mm respectively. The thickness and length for both the configurations are 100 cm and 500 cm respectively. An Aluminium box of dimension 60×60×100 cm^3 along with a 50 cm diameter hole is used to reduce the activation of the absorber iron. A 3 mm gap is maintained between the aluminium shielding and iron blocks. In configuration 3, the gap between the iron blocks is 6 mm. The gaps shown in the picture are not scaled.

is embedded per event into the background. All the particles are transported through the entire CBM detector setup using the GEANT3 transport engine. The total number of events simulated to perform this study is 2.5×10^6.

Investigations are initiated with the study of the effect for the reduced density of the MuCh 5^{th} absorber. For this purpose, the load of the Monte Carlo (MC) points and reconstructed hits on TRD layers, placed at a distance of $\sim$ 46 cm from the 5^{th} MuCh absorber are studied. In Fig. 2.15, the ratio of different densities, namely 7.87 g/cm^3 (d_2) and 7.2 g/cm^3 (d_1), for MC TRD points (left) and reconstructed TRD hits (right) are shown for configuration 1 for the 5^{th} absorber plate. Note that the density of the absorbers 2, 3, and 4 are fixed to be 7.87 g/cm^3. It is evident that the MC TRD points and reconstructed TRD hits are increased due to the decrease in iron density and the resulting reduction in effective interaction length. However, the increase is less than 3%. The MC MuCh points, registered in the three detector layers of the 4^{th}

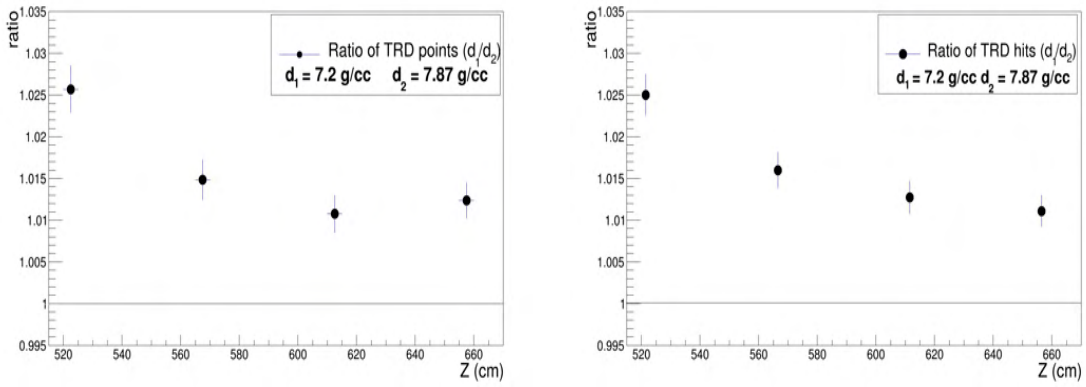

Figure 2.15: Ratios of different densities (d_1=7.2 g/cm^3 & d_2=7.87 g/cm^3) for MC TRD points (left plot) and reconstructed TRD hits (right plot) for configuration 1. Iron of density 7.87 g/cm^3 is used as the reference density.

MuCh station, are also investigated to see the effect of backscattering due to the reduced density (7.2 g/cm^3) of the iron and no visible effect is seen. Next, the effect of the vertical gaps in the 5^{th} absorber is investigated. In Fig. 2.16, the ratios of Monte Carlo (MC) points at different layers of MuCh and TRD is shown. Configuration 1 is taken as the reference configuration. No significant increase in Monte Carlo (MC) points at the different TRD chambers is seen due

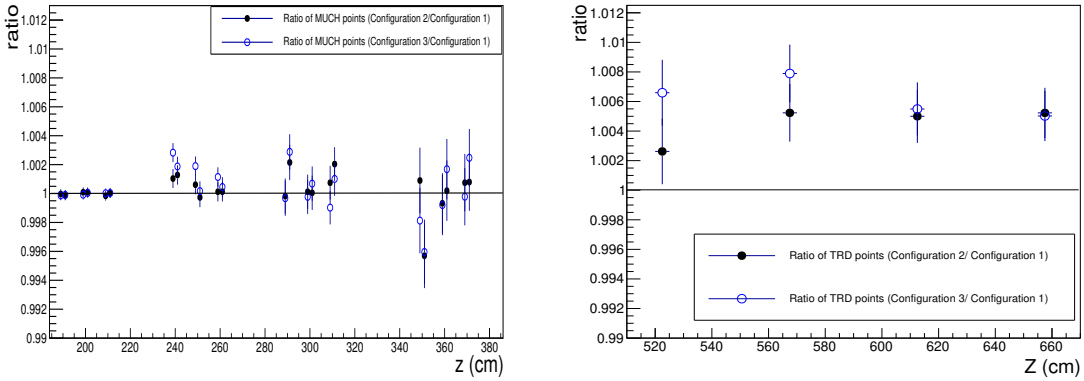

Figure 2.16: Ratios of MC MuCh points (left plot) and MC TRD points (right plot) for the configurations 2 and 3 with respect to configuration 1.

to the increasing gaps between the absorber blocks. From Fig. 2.16, it is shown that the change in the MC TRD points due to the different configurations of 5^{th} absorber is less than 1%.

Finally, the effect of reduced iron density and the implementation of vertical gaps on the performance of J/ψ detection in Au+Au collisions is studied. To identify the muon track candidates, a set of track quality cuts are applied to the reconstructed global tracks. Reconstructed global tracks having STS hits ≥ 7, MuCh hits ≥ 11, TRD hits ≥ 3, TOF hits ≥ 1, $\chi^2_{VERTEX} \leq 3.5$, $\chi^2_{STS} \leq 3.0$, $\chi^2_{MuCh} \leq 4.0$, and $\chi^2_{TRD} \leq 5.5$ are considered as the muon track candidates. Such a choice on the number of reconstructed hits associated with a global track, at different sub-detectors, indirectly accommodates detector inefficiency. In the absence of double hits, the maximum possible number of hits associated with a global track at STS, MuCh and TRD are 8, 12 and 4 respectively. An additional 2σ cut on the reconstructed TOF mass is used to reduce the background further. For all three different configurations, the same set of analysis cuts is used to ensure uniformity.

In Fig. 2.17, the invariant mass distributions with two different iron densities are plotted for configuration 1 (i.e. the gap between the successive iron plates is set to 0 mm). From the figure, it is visible that, with changing the density of the iron from 7.87 g/cm^3 to 7.2 g/cm^3, both the signal and the di-muon

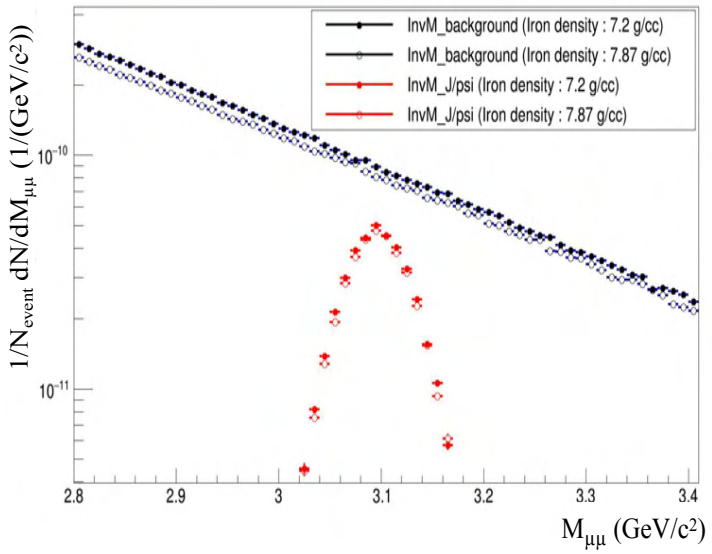

Figure 2.17: Invariant mass distributions for two different iron densities with configuration 1. The solid and hollow black markers indicate the background distribution with the iron of density 7.2 g/cm^3 and 7.87 g/cm^3 respectively. The solid and hollow red markers indicate the signal distribution with the iron of density 7.2 g/cm^3 and 7.87 g/cm^3 respectively.

combinatorial background slightly increase due to their less absorption. The multiplicity (5×10^{-6}) [16] of the J/ψ is taken from UrQMD [6]. The signal is extracted from the embedded set of events using the MC information (mcpdg = $\pm$ 13 & GeantProcessId = KPPrimary). The different methods of signal extraction are discussed in Ref. [17]. The values of J/ψ reconstruction efficiency ($\epsilon_{J/\psi}$), signal to background ratio (S/B) and the significance are listed in Table 2.5 for all the different configurations and the variation is displayed in Fig. 2.18. It is evident from Table 2.5 and Fig. 2.18 that the $\epsilon_{J/\psi}$ and S/B values do not change significantly with the gaps between the absorber blocks. They are well consistent within statistical errors. This can be attributed to the fact that the solid angle subtended by the gaps is rather small compared to the background angular distribution and thus does not admit a significant number of additional background tracks to reach the TRD planes in presence of cracks. From this study, it is concluded that the physics performance is rather

[6]In the current simulation scheme, one J/ψ going to $\mu^+\mu^-$ is embedded per event to the background to reduce the statistical uncertainties on the simulated results. To make the invariant mass spectra realistic, the reconstructed spectra is scaled with multiplicity $\times$ branching ratio values for the signal. The value used for the branching ratio of the decay channel J/$\psi \rightarrow \mu^+\mu^-$ is $\sim 6\%$.

Table 2.5: List of J/ψ reconstruction efficiency ($\epsilon_{J/\psi}$) and signal to background (S/B) ratios for central Au+Au collision at $\sqrt{s_{NN}} = 4.54$ GeV with different geometry configurations of the 5^{th} absorber. The statistical errors associated with the obtained values are also quoted.

Gaps b/w the iron blocks (mm)	**Iron density (g/cm^3)**	$\epsilon_{J/\psi}$ (%)	**S/B**	**Significance**
0.0	7.87	1.22 ($\pm$ 0.02)	0.31 ($\pm$ 0.04)	20.2
3.0	7.87	1.21 ($\pm$ 0.02)	0.28 ($\pm$ 0.04)	19.8
6.0	7.87	1.22 ($\pm$ 0.01)	0.30 ($\pm$ 0.02)	20.1
0.0	7.2	1.28 ($\pm$ 0.01)	0.29 ($\pm$ 0.03)	20.5
3.0	7.2	1.29 ($\pm$ 0.02)	0.27 ($\pm$ 0.02)	20.3
6.0	7.2	1.27 ($\pm$ 0.01)	0.26 ($\pm$ 0.04)	19.9

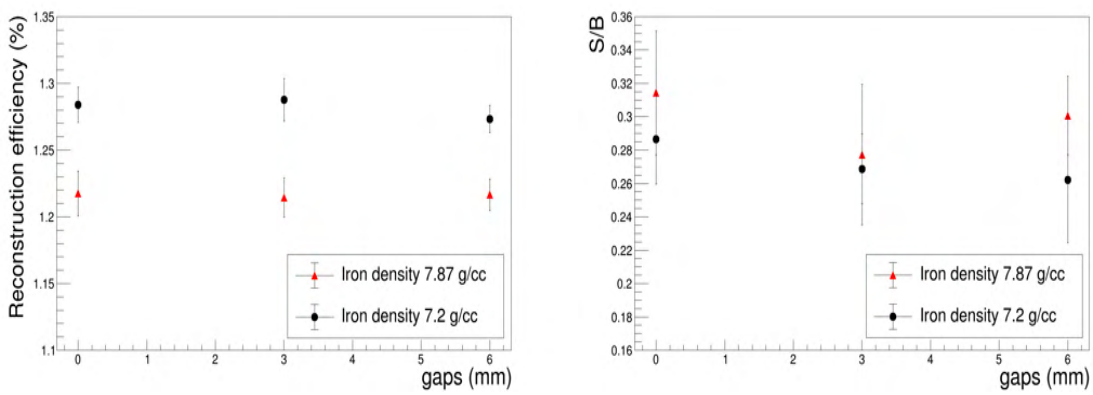

Figure 2.18: Reconstruction efficiency (left) and signal to background ratio (right) as a function of gaps between the absorber blocks for two different iron densities. The black solid circle is for iron of density 7.2 g/cm^3 and the red triangle is for iron of density 7.87 g/cm^3.

insensitive to the foreseen vertical gaps of realistic size (as investigated in this study), between the absorber plates. The reduced density of MuCh 5$^{\text{th}}$ absorber will not affect TRD stations significantly and hence its thickness can be kept unchanged.

2.6 Reconstruction performance in the di-muon channel

In the following section, the reconstruction performance of muon pairs coming from the decays of LMVM and J/ψ is discussed with the realistic MuCh subsystem configurations at the foreseen SIS100 energies with heavy-ions.

2.6.1 Simulation details

The hadronic background is calculated with the UrQMD [9] event generator, and the phase-space distribution and the decays of LMVM ($\rightarrow \mu^+\mu^-$) and J/ψ ($\rightarrow \mu^+\mu^-$) are simulated using the PLUTO [10] event generator, as discussed in section 2.4. One signal from PLUTO is embedded per event into the background. All the particles are transported through the entire CBM detector setup using the GEANT3 transport engine. The hits registered in the STS, MuCh, TRD and TOF detectors are used for track reconstruction based on a Cellular Automaton algorithm, which is a part of the CBM reconstruction software package. The momentum is extracted from the bending of the track segments inside the STS only which is placed inside the magnet. This helps to get better momentum and hence pair mass resolution due to the low material budget of STS. The reconstructed global tracks are used for the selection of muon track candidates. For the feasibility study of LMVM detection, Au+Au collision at three different energies, namely $\sqrt{s_{NN}}$ = 4.9, 4.1 & 2.9 GeV are simulated. For the feasibility study of the J/ψ detection, two different collision systems, namely Au+Au and Ni+Ni are studied for central collisions with $\sqrt{s_{NN}}$ = 4.54 & 5.47 GeV respectively. The multiplicity values of the LMVM cocktails are taken from the Thermal-FIST model [12]. The J/ψ multiplicities for Au+Au and Ni+Ni are estimated from model calculations. For the Au+Au collision system, the sub-threshold multiplicity value is adopted from the UrQMD calculation [16]. The HSD (Hadron-String Dynamics) transport model prediction [18] is used to extract the multiplicity value for the Ni+Ni collision system. Since the multiplicity value for the Ni+Ni system is not directly available in the literature, the multiplicity value of the Au+Au system (from HSD) is scaled down by the average number of binary collisions to get the multiplicity value for the Ni+Ni system with the underlying assumptions that, for both collision systems, the J/ψ's are produced by the initial nucleon-nucleon (NN) hard scattering and the contribution from the thermal sources can be neglected.

2.6.2 Reconstruction of LMVM's

The detection of LMVM through the di-muon decay channel at the SIS100 having the CM energy ($\sqrt{s_{NN}}$) in the range of 2.7 - 5.5 GeV is one of the unique opportunities at CBM to measure the caloric curve which will validate the theoretical prediction of a 1^{st} order phase transition from the hadronic phase to the Quark-Gluon-Plasma (QGP) phase at the high baryon density regime [19]. At invariant masses up to about 1 GeV/c^2, the spectrum is dominated by decays of η, ω, ρ and ϕ mesons. The measurement of their decay leptons, in particular from the short-lived ρ mesons, provides information on their in-medium mass modifications due to chiral symmetry restoration [20]. Above 1 GeV/c^2, the di-lepton invariant mass spectra reflect the average temperature of the emitting source integrated over the entire collision history since the contributions from vector meson decay is strongly reduced in this mass range. As the slope of the di-lepton mass spectra is not affected by the radial flow, the source temperature can be directly extracted from it.

In this section, the reconstruction performance of the LMVM for central (0-5%) Au+Au collisions at $\sqrt{s_{NN}}$ = 4.9, 4.1 & 2.9 GeV corresponding to P_{beam} of 12, 7.95 & 3.3 A GeV/c are discussed with a realistic MuCh setup, as implemented in GEANT3 and within the CBMROOT (Version: APR21) framework. The input distribution from the PLUTO event generator is shown in Fig. 2.6 in section 2.4 [10]. The muon track candidates are selected using the following cuts for $\sqrt{s_{NN}}$ = 2.9 GeV: STS hits $\geq$ 7, MuCh hits $\geq$ 5, TOF hits $\geq$ 1, $\chi^2_{VERTEX} \leq 2.0$, $\chi^2_{STS} \leq 2.0$, $\chi^2_{MuCh} \leq 4.5$. Again for $\sqrt{s_{NN}}$ = 4.9 & 4.1 GeV: STS hits $\geq$ 7, MuCh hits $\geq$ 11, TOF hits $\geq$ 1, $\chi^2_{VERTEX} \leq 2.0$, $\chi^2_{STS} \leq 2.0$, $\chi^2_{MuCh} \leq 4.5$. An additional 2σ mass cut is applied on the reconstructed TOF mass to reduce the combinatorial background further.

The reconstruction performance of the di-muons, selected using the MC particle ID (MCPID) tag, is shown in Fig. 2.19. The signal to background ratio of the reconstructed LMVM cocktail is shown in Fig. 2.20. The background is calculated using the super event (SE) technique (explained in detail in sec-

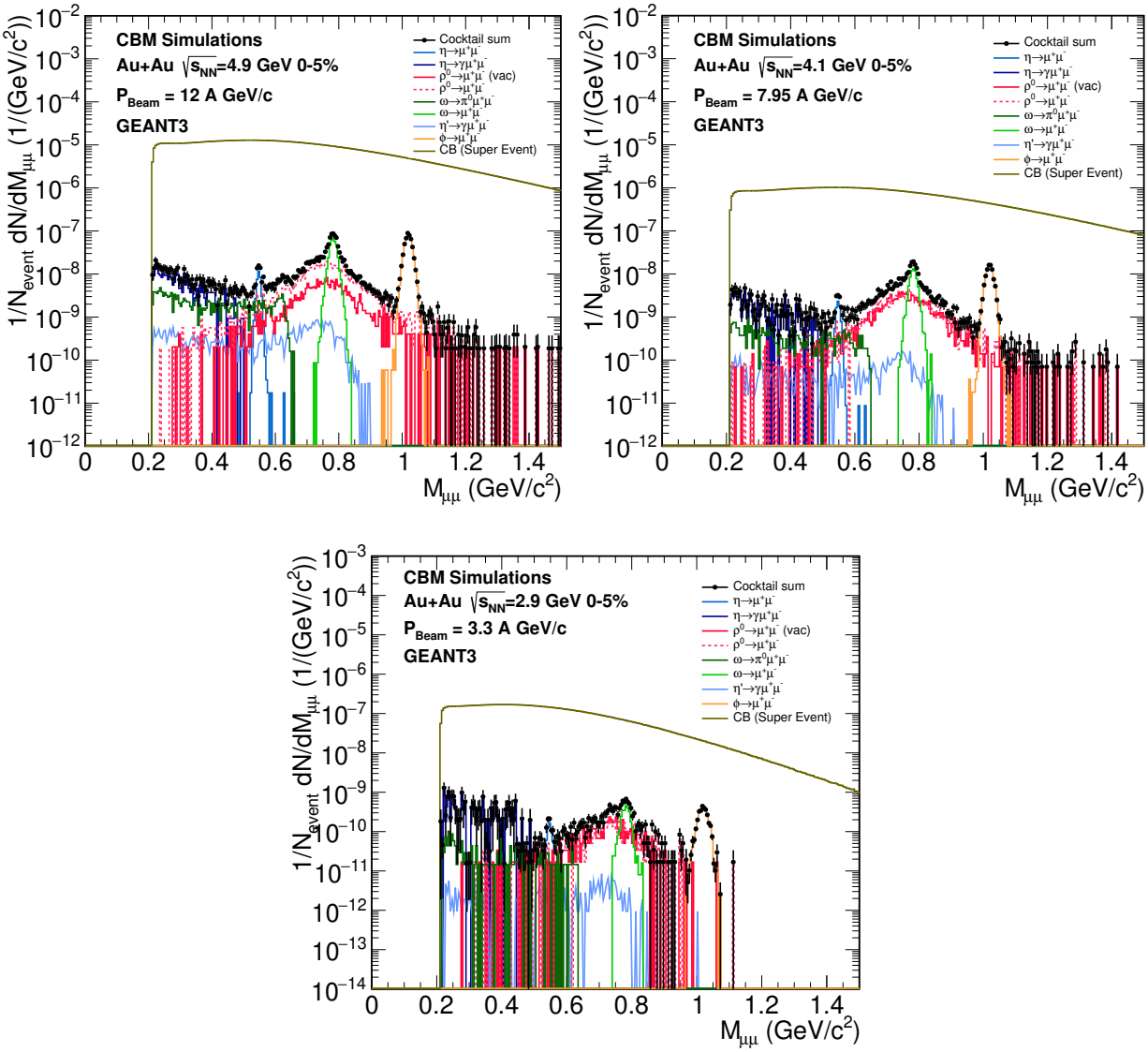

Figure 2.19: Invariant mass distribution of LMVM cocktail for central (0-5%) Au+Au collision at $\sqrt{s_{NN}}$ =4.9 GeV (top left), 4.1 GeV (top right) and 2.9 GeV (bottom). The background is calculated using the Super Event (SE) technique.

tion 2.6.3). In this process, the combinatorial background is estimated where one muon candidate track, from a reconstructed sample of pure UrQMD events is combined with all the other oppositely charged muon candidate tracks. The SE technique can be used for the cases where comparable track multiplicities are expected for all the events. The reconstruction performance and S/B value show that to extract the signal information, the background needs to be esti-

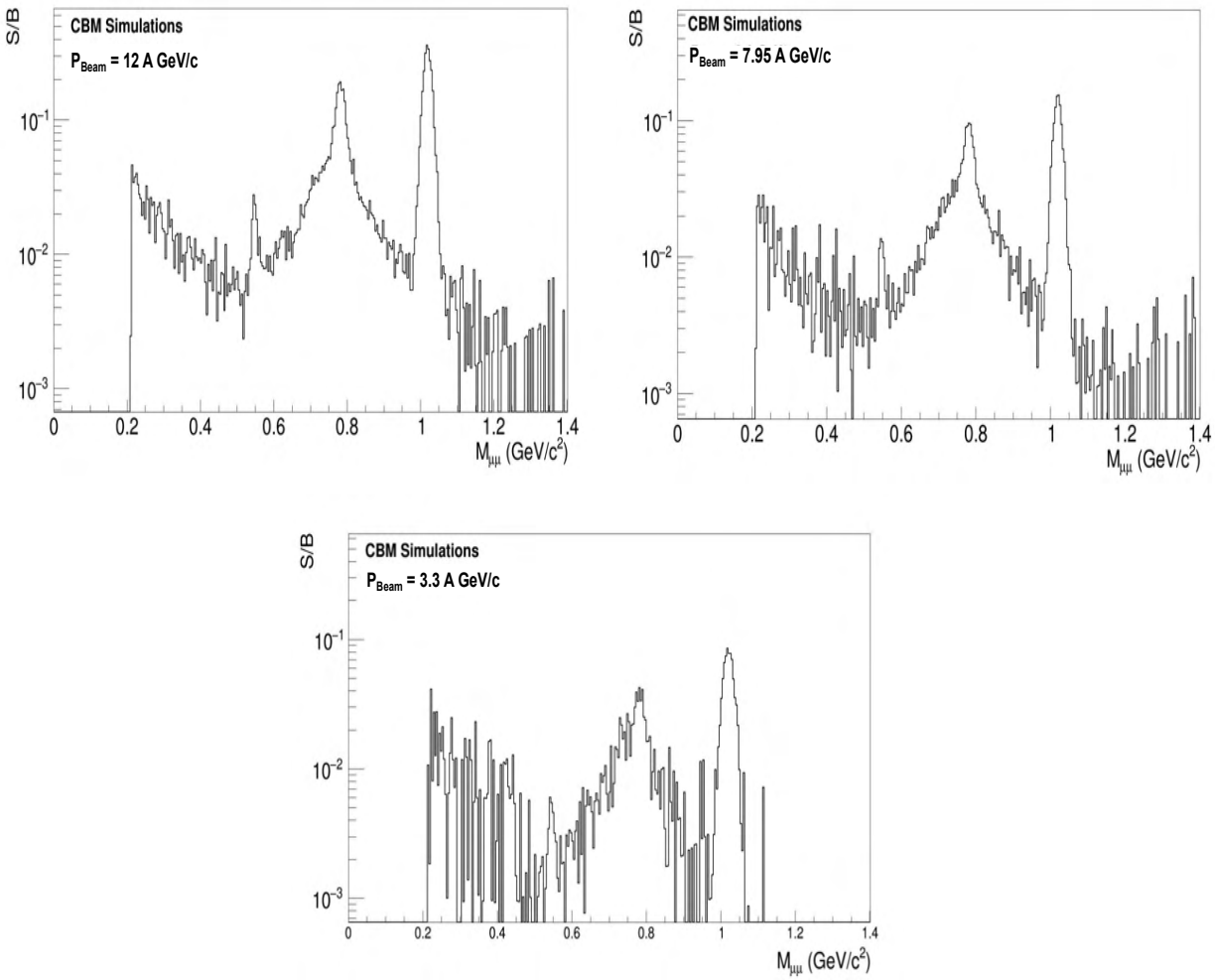

Figure 2.20: Signal to background (S/B) ratio for central (0-5%) Au+Au collision at $\sqrt{s_{NN}}$ = 4.9 GeV (top left), 4.1 GeV (top right) and 2.9 GeV (bottom).

mated very carefully because the signal peaks are well below the background distribution as shown in Fig. 2.20.

2.6.3 Di-muon combinatorial background estimation using different techniques

In this section, different techniques for the di-muon combinatorial background estimation are discussed. Four different methods, as available in the literature, are employed for this purpose: namely, the super event method, the mixed event method, the like-sign method and the event by event method. The goal

of this exercise is to precisely model the shape of the combinatorial background for di-muon measurements in SIS100 heavy-ion collisions and estimate the related systematics. Due to the very small branching ratio×multiplicity values of the different physical sources at CBM, the signal peaks are well below the di-muon combinatorial background. Therefore, a precise understanding of the background distribution is very crucial to extract the signal yields from the measured raw $\mu^+\mu^-$ spectra. The weak decays of pions and kaons are two of the major sources of the combinatorial background. For our present investigation, the combinatorial background is calculated for 0-10% central Au+Au collisions at $\sqrt{s_{NN}}$ = 4.9 GeV. The Super Event (SE) method is the default

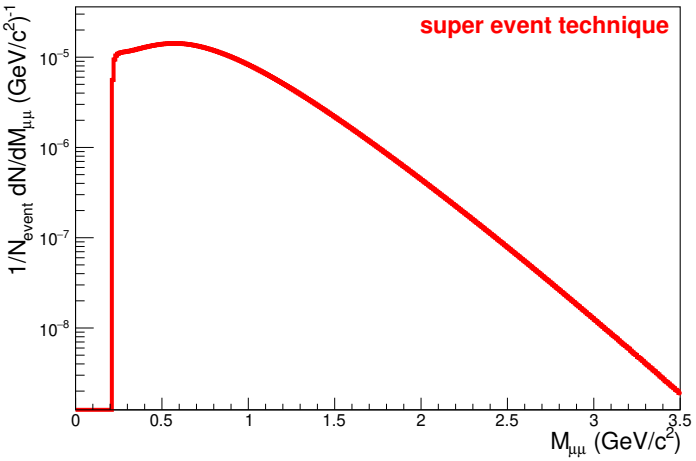

Figure 2.21: Invariant mass distribution using super event technique. The error bars are smaller than the marker size.

technique available within CBMROOT software to estimate the combinatorial background for di-lepton simulation. In this method, one muon track candidate is combined with all the other oppositely charged muon track candidates of all the events to calculate the uncorrelated invariant mass distribution as shown in Fig. 2.21. The advantage of using the super event technique is that due to the large combination of the muon pairs, the statistical uncertainties associated with the large mass bins are rather small. However, this method is not realistic because the event information is restored at the time of combining the muon

track candidates. Also, the method is only suitable for purely central collisions, where all the events have nearly the same track multiplicities.

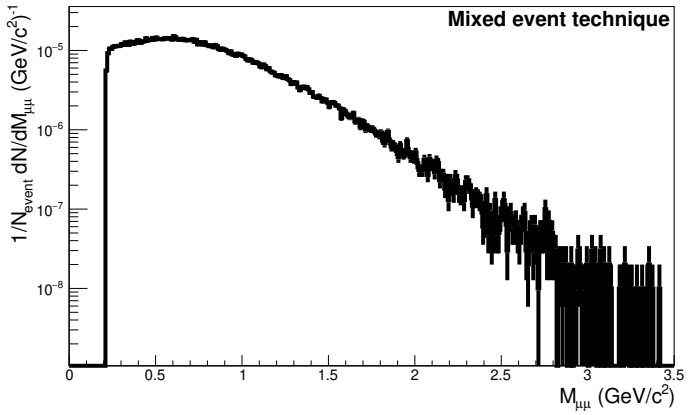

Figure 2.22: Invariant mass distribution using mixed event technique.

In the mixed event technique, an artificial pool of events is created with similar multiplicities or, in other words, the events having similar impact parameters. Since, in this current investigation, all events are of 0-10% central Au+Au collisions, an event pool is created by using some randomly chosen mutually exclusive events. Within the pool, oppositely charged muon track candidates are combined to calculate the combinatorial background. The mixed event technique is more realistic compared to the SE technique. The combinatorial pair mass spectrum, calculated using the mixed event technique is shown in Fig. 2.22.

In the event by event analysis, oppositely charged muon track candidates are combined within the same event. This is the most general and realistic way to calculate the combinatorial background in any raw data analysis. However, the main disadvantage of this method is that it requires larger statistics as compared to the above-mentioned methods with comparable statistical uncertainties at the respective mass bins. The invariant mass distribution using the event by event analysis is shown in Fig. 2.23.

The like-sign method had been extensively used in di-muon analyses by the NA50, NA60 experiments [21, 22] at the CERN-SPS. In this method, the com-

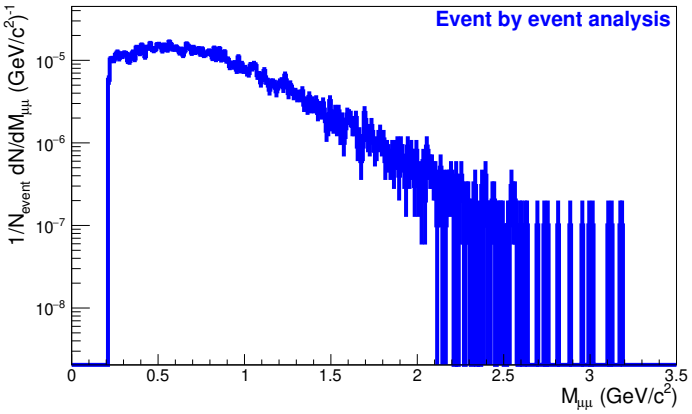

Figure 2.23: Invariant mass distribution using event by event technique.

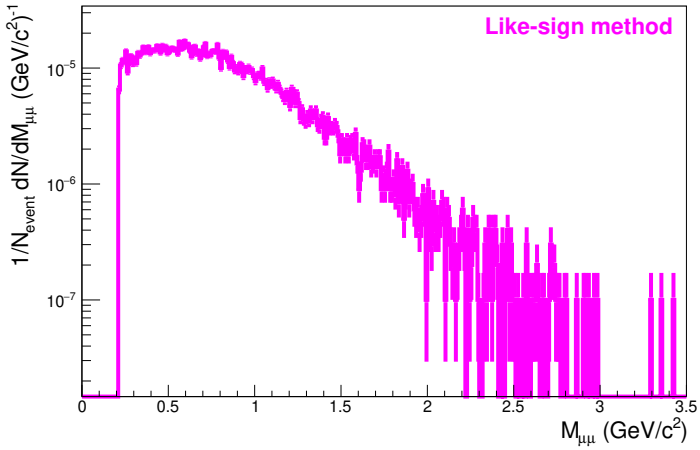

Figure 2.24: Invariant mass distribution using like-sign method.

binatorial background is calculated by taking the combination of like-sign pairs within the same events. After combining the like-sign pairs, the unlike sign combinatorial background is expressed as $N^{\mu^+\mu^-}\ (BG) = 2\sqrt{N^{\mu^+\mu^+}N^{\mu^-\mu^-}}$. The distribution of the combinatorial background, calculated using the like-sign method, is shown in Fig. 2.24. For a comparison, the distribution of the combinatorial background, calculated using different techniques as discussed above, is shown in Fig. 2.25. The SE technique requires fewer statistics and is relatively fast, as compared to the other techniques discussed above. Therefore, for the course of this thesis, the SE technique is used to calculate the di-muon combinatorial background.

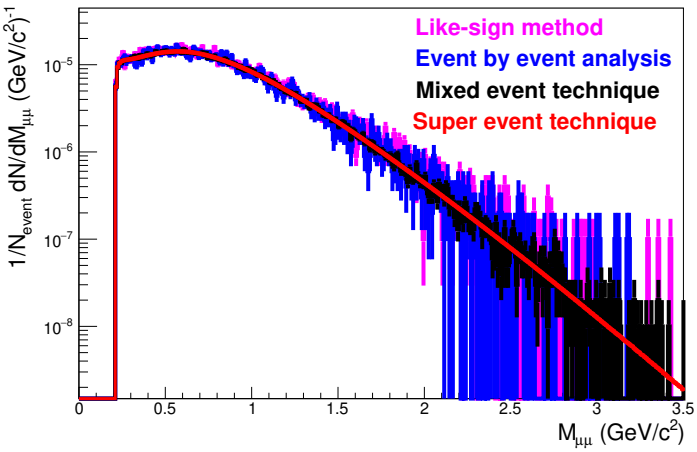

Figure 2.25: Invariant mass distribution using different techniques. The legends have been explained earlier in the text.

2.7 Reconstruction of J/ψ

The observation of J/ψ suppression in relativistic heavy-ion collisions is considered as an important signature for the formation of Quark Gluon Plasma (QGP) [23]. If QGP is created at the collision zone, the c$\bar{c}$ binding potential gets shielded due to the Debye screening of the colour charges leading to the reduction of the J/ψ yield. However, to identify J/ψ suppression as a signature of deconfined matter, it is very important to understand its production in vacuum and also how the production is affected due to the presence of the hadronic medium. In proton-nucleus (p+A) collisions, a considerable amount of J/ψ suppression has been observed because of the dissociation of the resonant (or pre-resonant) state of the evolving c$\bar{c}$ pairs due to their interaction with the spectator nucleons in the target nucleus. This effect is known as Cold Nuclear Matter (CNM) effect. Hence p+A collisions are studied extensively to get a measure of the effect induced by confined nuclear matter on the J/ψ production. In a p+A collision, it is generally expected that there is no formation of any hot secondary medium, thus such types of collisions provide a baseline for the J/ψ absorption in confined matter. The CNM effect

involves both the modification of the initial state parton distribution functions inside the bound nucleons leading to the reduction (enhancement) of the $c\bar{c}$ production (w.r.t p+p collisions) known as shadowing (anti-shadowing) effect and dissociation of the resonance (pre-resonance) $c\bar{c}$ pairs due to the successive interaction with the target nucleus. All these modifications are expected to occur before any deconfined medium is formed. They would also contribute in the case of nucleus-nucleus (A+A) collisions over a time span before any secondary medium is formed. A precise understanding of this so-called "normal" suppression is thus crucial to establish a baseline, with reference to which the "anomalous" suppression pattern, due to the presence of deconfined media, can be distinguished. The J/ψ production in p+A and A+A collisions is studied extensively for several fixed target experiments at SPS in the beam energy range of E_b = 158 - 450 A GeV and with variety of nuclear targets [24, 25, 26, 27, 28]. The NA50 collaboration first reported the anomalous suppression of J/ψ at E_b = 158 A GeV ($\sqrt{s_{NN}}$ = 17.3 GeV) for the Pb+Pb collision system [29]. Subsequently, the NA60 collaboration at SPS measured J/ψ suppression in 158 A GeV In+In collisions and the observed suppression pattern was in line with normal suppression. The J/ψ suppression pattern obtained from RHIC at $\sqrt{s_{NN}}$ = 200 GeV Au+Au collision revealed an almost similar pattern as observed from SPS data [30, 31]. Such an observation is consistent with the concept of regeneration of J/ψ mesons by the recombination of the uncorrelated charm quarks at higher energies. A good amount of J/ψ data are also available from the LHC for p+A and A+A collision systems [32]. However, the J/ψ production at the lower collision energies is less explored mainly due to the extremely small charm production cross-section. No data on J/ψ production in A+A collisions is available below top SPS energy. One of the major goals of the CBM experiment at FAIR [33] is to perform pioneering measurements on the production of J/ψ in relativistic nuclear collisions at moderate beam energies with unprecedented interaction rates [34], thanks to the foreseen heavy-ion beams of high-intensity and the detectors having state-of-the-art technology with high rate handling capability. The estimated interaction

rate at CBM is ∼10 MHz which is much higher than all the existing and most of the upcoming experiments. Note that the production of J/ψ mesons at $\sqrt{s_{NN}} = 4.54$ GeV is kinematically forbidden for elementary p+p collision. However, model calculations, based on sub-threshold production of resonances via multiple collisions in a dense baryonic medium, predict non-zero J/ψ cross-sections at $\sqrt{s_{NN}} = 4.54$ GeV [16]. Hence the physics potentials of these foreseen measurements include the opportunity to understand charm production and propagation in cold matter close to the kinematic production threshold and to make pioneering measurements to test the mechanism of sub-threshold charm production predicted for heavy-ion (Au) beams.

2.7.1 A+A systems

The J/ψ's are reconstructed using the invariant mass technique by combining oppositely charged muon track candidates. Muon track candidates are identified by applying a set of single track quality cuts on the reconstructed global tracks. The tracks reconstructed in STS are extrapolated through MuCh and TRD up to TOF taking into account the reconstructed momentum of the tracks. The resulting tracks when extrapolated to the interaction vertex, are known as the global tracks. The details of the track selection cuts are listed in Table 2.6. The contribution of non-muonic tracks is further reduced by applying a 2σ cut on the reconstructed TOF mass. The track selection cuts are optimised to ensure the optimum significance value of the J/ψ signal. The significance value is an indicator of how well the signal peak can be visible over the background.

Different approaches are employed to calculate the pair reconstruction efficiency and the signal to background (S/B) ratio. The first approach is rather idealistic and is based on the MC information. After reconstruction, the signal tracks are extracted using the GEANT3 information based on particle type and identity, and the background is calculated using the Super Event (SE) technique. The entries within the 2σ mass range of the signal, fitted with a symmetric Gaussian distribution function, give the signal yield. Further, dividing the number by the

Table 2.6: Selection cuts on the reconstructed global tracks to select the muon track candidates. The hit cuts on the detector sub-systems indicate the acceptance criteria of the muon pairs.

Collision System	**Cut on detector hits associated with the track segment of a reconstructed global track**	**Cut on χ^2/Ndf of the reconstructed track segment**
Au+Au (b = 0 fm)	-	VERTEX $\chi^2/Ndf \leq 2.2$
	STS hits ≥ 7	STS $\chi^2/Ndf \leq 3.4$
	MuCh hits ≥ 11	MuCh $\chi^2/Ndf \leq 2.6$
	TRD hits ≥ 3	TRD $\chi^2/Ndf \leq 6.0$
	TOF hits ≥ 1	-
Ni+Ni (b = 0 fm)	-	VERTEX $\chi^2/Ndf \leq 2.3$
	STS hits ≥ 7	STS $\chi^2/Ndf \leq 2.8$
	MuCh hits ≥ 11	MuCh $\chi^2/Ndf \leq 2.4$
	TRD hits ≥ 3	TRD $\chi^2/Ndf \leq 5.5$
	TOF hits ≥ 1	-

input yield one obtains the efficiency: the effect of the detector geometrical acceptance is thus included. In the same mass range, the background is calculated in order to get the S/B ratio. However, such an approach is not useful in real data due to its direct dependence on MC information. Hence a more realistic alternate approach is adopted which can also be applied to the raw data when available. The unlike sign invariant mass spectra from embedded events are fitted with a combined Gaussian (signal) + polynomial (background) function and then the background is subtracted to calculate the signal yield from the 2σ mass range of the fitted signal distribution by a symmetric Gaussian function. In Fig. 2.26, after normalising with multiplicity times branching ratio the fitted spectra using the second approach is shown and the results of the fitting are summarised in Table 2.7.

As evident, the results from two different fit procedures show a good agreement and validate the realistic method of signal extraction. The obtained mass resolution ($\sim$ 30 MeV) is small enough to distinguish between J/ψ and $\psi^{'}$ [7] signals, thanks to the low material budget of STS. The laboratory rapidity (y) and transverse momentum (p_T) distribution of the signal muon pairs, at the

[7] $\psi\prime$ is the higher order state (2S) of c$\bar{c}$ quarks. J/ψ is the lowest energy state (1S) of c$\bar{c}$ quarks. The mass of J/ψ is around 3.1 GeV whereas $\psi\prime$ mass is around 3.7 GeV.

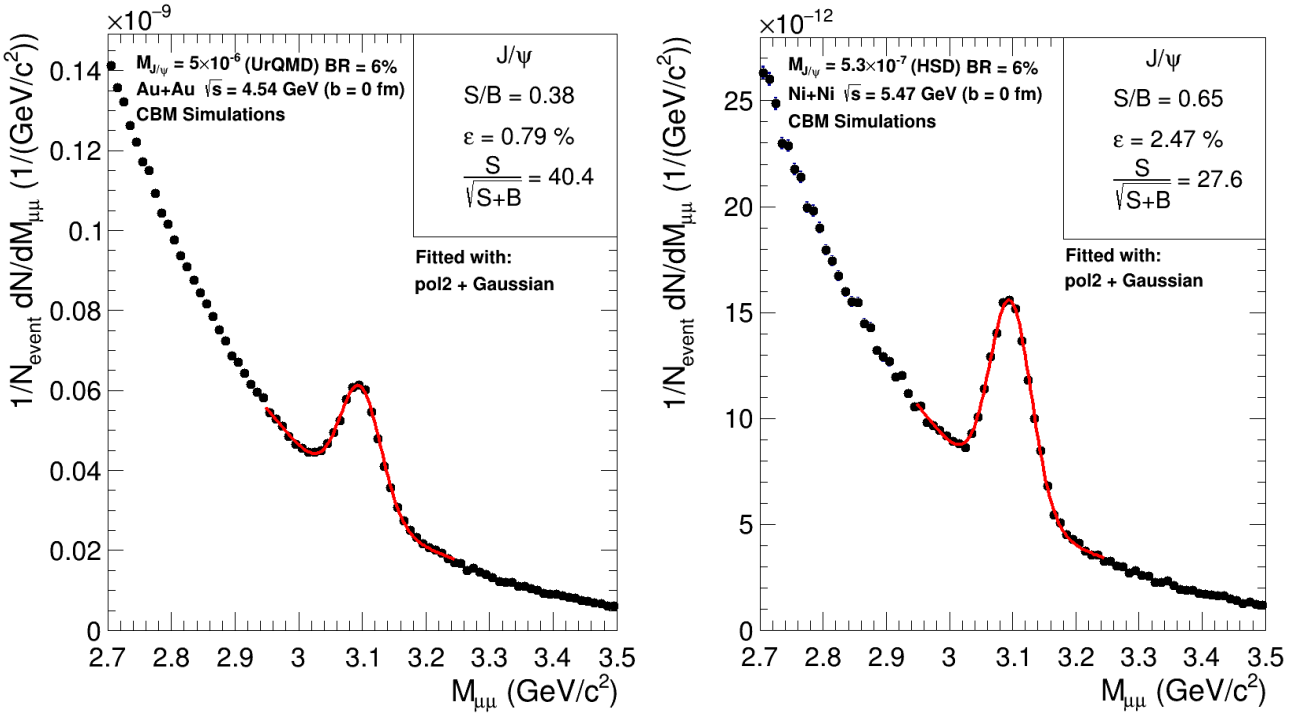

Figure 2.26: Invariant mass distribution of the reconstructed J/ψ mesons for 10 A GeV/c Au+Au (left) and 15 A GeV/c Ni+Ni (right) collisions fitted by Gaussian (signal) and 2^{nd} order polynomial (background) and scaled with the multiplicity times branching ratio. The error bars are smaller than the marker size.

Table 2.7: Reconstruction efficiency ($\epsilon_{J/\psi}$) and S/B ratio for J/ψ mesons in central Au+Au and Ni+Ni collision at $\sqrt{s_{NN}}$ = 4.54 GeV and $\sqrt{s_{NN}}$ = 5.47 GeV respectively from different fitting methods. Method 1 & 2 are based on the MC information and full fit respectively.

Method (System)	$\epsilon_{J/\psi}$ (%)	**S/B**	**Peak Mass resolution (MeV)**	**Significance** $S/\sqrt{S+B}$
method 1 (Au+Au)	0.81 ($\pm$0.01)	0.36 ($\pm$0.01)	33 ($\pm$1)	39.4
method 2 (Au+Au)	0.79 ($\pm$0.01)	0.38 ($\pm$0.01)	32 ($\pm$1)	40.4
method 1 (Ni+Ni)	2.53 ($\pm$0.01)	0.62 ($\pm$0.01)	34 ($\pm$1)	27.6
method 2 (Ni+Ni)	2.47 ($\pm$0.01)	0.65 ($\pm$0.01)	33 ($\pm$1)	27.6

reconstructed level (selected using MC information), are shown in Fig. 2.27 for Au+Au (left) and Ni+Ni (right) collision systems at $\sqrt{s_{NN}}$= 4.54 & 5.47 GeV respectively; good mid-rapidity coverage is observed. The variation of the J/ψ reconstruction efficiency and of the S/B ratio in different p_T ranges (y-inclusive) and in different y ranges (p_T-inclusive) are also investigated. In Fig. 2.28, the variation of the J/ψ reconstruction efficiency and the signal to background ratio

are shown as functions of the mean value of different p_T bins (y-inclusive) and as functions of the mean value of different y bins (p_T-inclusive). The decrease in the reconstruction efficiency at the higher p_T region is due to the nature of the input distribution of the muons coming from the decay of J/ψ's and also due to the effect of detector acceptance. The y and p_T distributions of the input (PLUTO), accepted and reconstructed spectra are shown in Fig. 2.29.

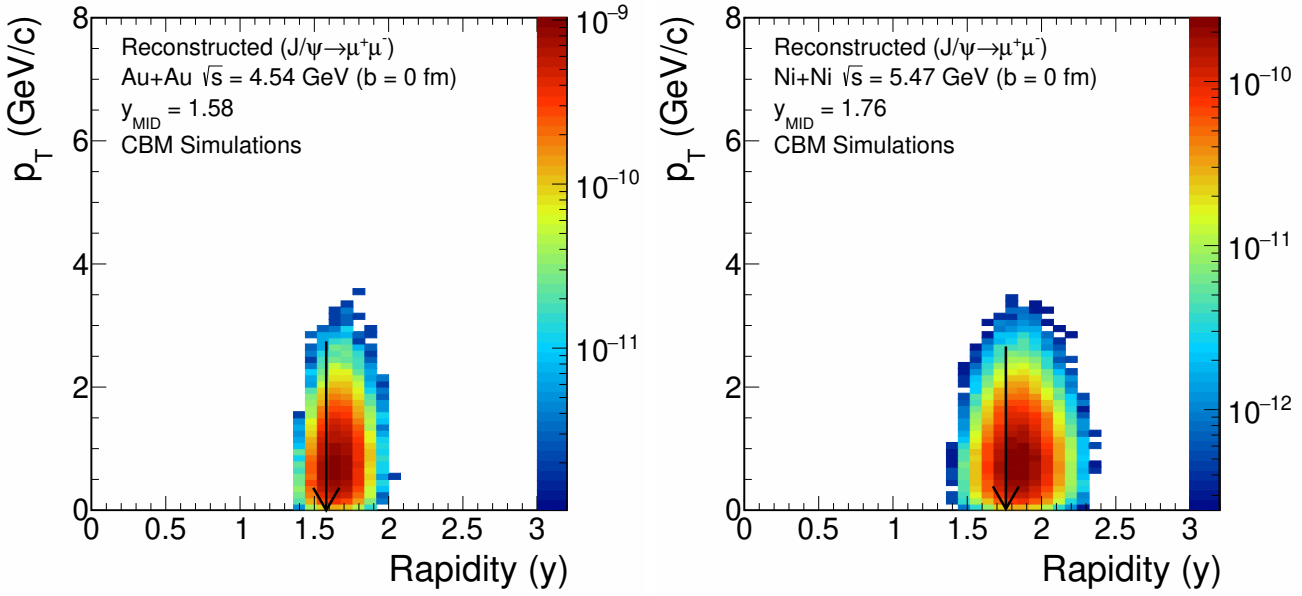

Figure 2.27: Laboratory rapidity (y) and transverse momentum (p_T) distribution of reconstructed muon pairs for 10 A GeV/c central Au+Au (left) and 15 A GeV/c central Ni+Ni (right) collision respectively. The arrow indicates the mid-rapidity region.

Our ultimate goal is to perform the efficiency×acceptance correction to the reconstructed spectra in a way that it becomes comparable with the input spectra. To perform this correction, a three-dimensional histogram is first constructed by filling the reconstructed invariant mass distributions for different $y - p_T$ bins. Then the projection of the histogram of the J/ψ mass region is taken for different $y - p_T$ bins and the J/ψ yield is extracted for every $y - p_T$ bin using the full fit method. The information of the number of pairs, accepted in different $y - p_T$ bins are extracted, using the MC information from the full phase space input signal distribution, depending on the acceptance criteria as listed in Table 2.6. The ratio of the reconstructed to the accepted muon pairs

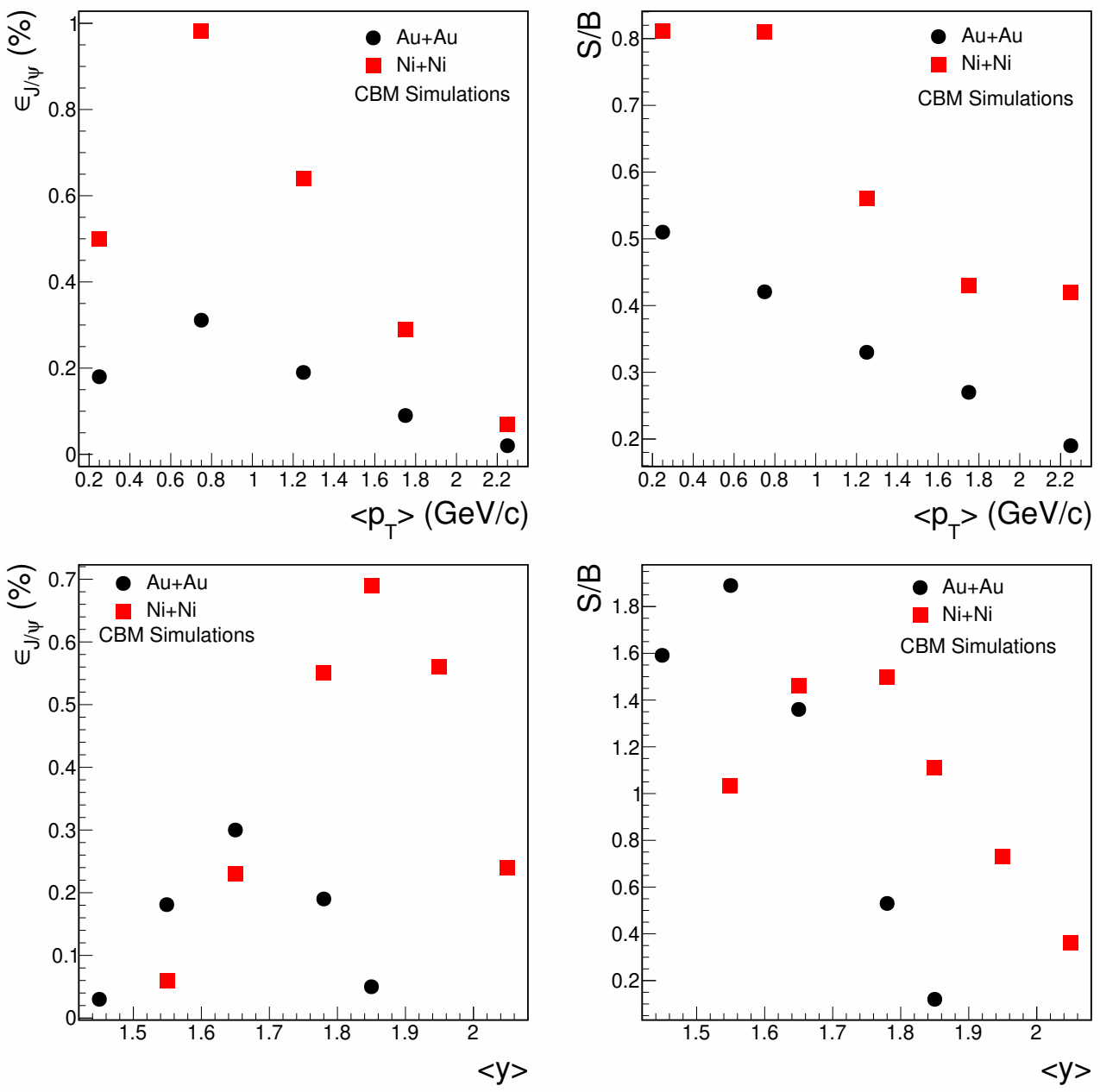

Figure 2.28: Variation of J/ψ reconstruction efficiency and signal to background ratio as function of mean value of p_T (y inclusive) (top) and mean value of y (p_T inclusive) (bottom) for 10 A GeV Au+Au & 15 A GeV Ni+Ni collision. The error bars are smaller than the marker size.

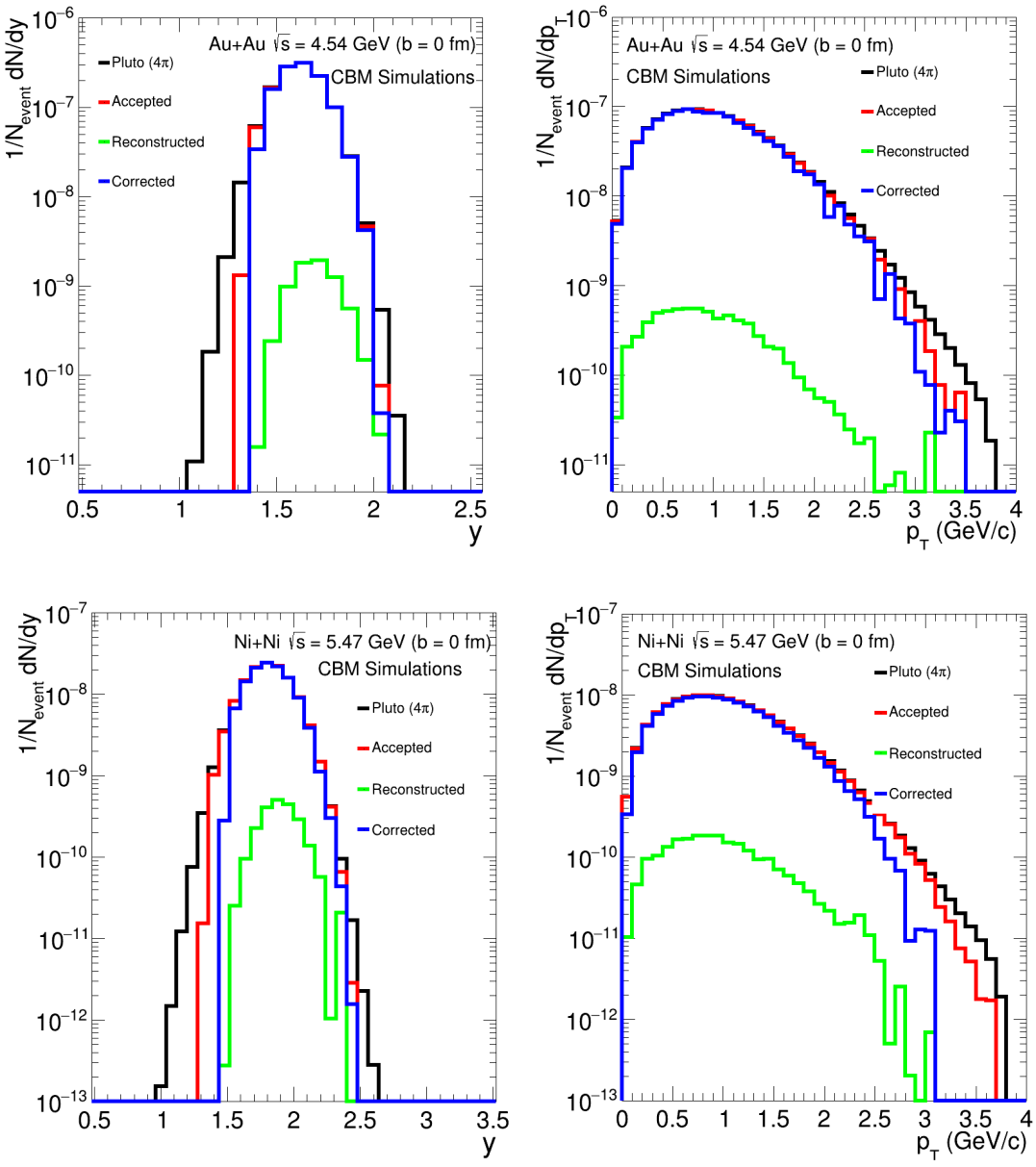

Figure 2.29: Input, Accepted, reconstructed and corrected y and p_T spectra for central Au+Au collision at $\sqrt{s_{NN}}$ = 4.54 GeV (top) and Ni+Ni (bottom) collision at $\sqrt{s_{NN}}$ = 5.47 GeV. The error bars are smaller than the marker size.

gives us the efficiency matrix and then the ratio of the reconstructed matrix to the efficiency matrix gives us the corrected spectra. In Fig. 2.29, the corrected y and p_T spectra along with the input, accepted and reconstructed spectra are shown for the central Au+Au and Ni+Ni collision systems. After the efficiency correction, the reconstructed spectra matches well with the accepted spectra.

2.8 Summary

A comparative study of the effect of MuCh hadron absorbers on the ω ($\rightarrow\mu^+\mu^-$) and J/ψ ($\rightarrow\mu^+\mu^-$) reconstructions is performed using the CBMROOT framework at $\sqrt{s_{NN}}$ = 4.1 and 4.54 GeV respectively for central Au+Au collisions. The effect for the surface tolerance of the intermediate MuCh absorbers on the reconstruction of ω ($\rightarrow\mu^+\mu^-$) is studied by varying the thicknesses of the absorbers in the step of few centimeters. It is observed that the reduction of a few centimeters in the thickness of the iron absorbers would degrade the performance of di-muon measurement at SIS100 energies. It is anticipated that a surface tolerance of the order of a few millimeters might preserve the feasibility of di-muon detection at SIS100 energies using MuCh detector sub-system. For the detection of J/ψ ($\rightarrow\mu^+\mu^-$), an additional 100 cm thick iron absorber (MuCh 5^{th} absorber) is used at the end of the last detector station of MuCh. The realistic design of the MuCh 5^{th} absorber is implemented in the simulation and its effect on the J/ψ reconstruction is studied. Three different geometry configurations of MuCh 5^{th} absorber are considered. A similar reconstruction performance is obtained with each of the investigated geometries.

After optimizing the absorber configurations, the MC-based feasibility study of the di-muon detection coming from the decay of LMVMs and J/ψ is investigated with the MuCh setup. The reconstruction of LMVM is performed for 0-5% central Au+Au collisions at $\sqrt{s_{NN}}$ of 4.9, 4.1 & 2.9 GeV. It is observed that the signal peaks are well below the combinatorial background distribution and that is why the careful estimation of the combinatorial background is very crucial

for the measurement of the di-muons coming from the decay of LMVM. The reconstruction performance of J/ψ is investigated for central (b=0 fm) Au+Au and Ni+Ni collisions at $\sqrt{s_{NN}}$ = 4.54 & 5.47 GeV respectively. It is concluded that, with the predicted multiplicities from different model calculations at the mentioned energies, the J/ψ detection is feasible with the MuCh setup at SIS100 energies.

References

[1] S. Chattopadhyay *et al.,* Technical Design Report for the CBM: Muon Chambers (MuCh), GSI, 2015; https://repository.gsi.de/record/161297

[2] T. Balog, Journal of Physics: Conference Series 503, 012019 (2014)

[3] F. Sauli, Nucl. Instr. Meth. Phys. Res. A 386, 531 (1997)

[4] R. Santonico and R. Cardarelli, Nucl. Instr. Meth. Phys. Res. A 187, 377 (1981)

[5] https://redmine.cbm.gsi.de/projects/cbmroot/wiki

[6] https://cbmwiki.gsi.de/foswiki/bin/view/PWG/

[7] O. Singh *et al.,* "Evolution of First Absorber in Muon Chamber", CBM Progress Report 2019, Darmstadt 2020, p. 95

[8] S. Ahmad *et al.,* "Simulation of the beam pipe for MUCH", CBM Progress Report 2015, Darmstadt 2016, p.69

[9] M. Bleicher et al., J. Phys. G 25, 1859 (1999)

[10] I Fröhlich et al 2010 J. Phys.: Conf. Ser. 219 032039, arXiv:0905.2568v1

[11] https://web.archive.org/web/20050324092214/http://wwwasd.web.cern.ch/wwwasd

[12] CBM Collaboration wiki page (https://cbm-wiki.gsi.de/cgi-bin/view)

[13] S. Chatterjee *et al.,* "Generation of input signals for dilepton simulation using Pluto event generator", CBM Progress Report 2020, Darmstadt 2021, p. 193

[14] S. Chatterjee *et al.,* "Effect of absorbers surface tolerance on the Muon Chamber (MuCh) performance for the CBM experiment at FAIR", CBM Progress Report 2019, Darmstadt 2020, p. 97

[15] S. Chatterjee *et al.,* "Effect of gaps on the fifth absorber of Muon Chamber (MuCh) for the CBM experiment at FAIR", CBM Progress Report 2019, Darmstadt 2020, p. 99

[16] J. Steinheimer *et al.,* "Sub-threshold charm production in nuclear collisions", Phys. Rev. C95 (2017) 014911

[17] S. Chatterjee *et al.,* "Reconstruction of J/ψ mesons at SIS100 energies with realistic MuCh set up", CBM Progress Report 2019, Darmstadt 2020, p. 181

[18] W. Cassing et al., Nucl. Phys. A 691, 753 (2001)

[19] R. A. Tripolt, Nucl. Phys. A 1005, 121755 (2021)

[20] P. M. Hohler *et al.,* EPJ Web of Conf. 36, 00012 (2012)

[21] R. Shahoyan, NA60 Note 2004-3

[22] P. Crochet *et al.,* Nucl.Instrum.Meth. A484, 564-572, (2002)

[23] T. Matsui and H. Satz, Phys. Lett. B 178, 416 (1986)

[24] The NA38 Collaboration, C. Baglin *et al.,* Phys. Lett. B220, 471 (1989); B221, 465 (1990); B221, 472 (1990); B225, 459 (1991).

[25] M.C. Abreu *et al.,* NA50 Collaboration, Phys. Lett. B410, 337 (1997).

[26] B. Alessandro *et al.,* NA50 Collaboration, Euro. J.Phys 48 329 (2006).

[27] B. Alessandro *et al.,*. NA50 Collaboration, Euro. J.Phys 33 31 (2004).

[28] Roberta Arnaldi, for the NA60 Collaboration, Nucl. Phys. A830 345c-352c, (2009); R. Arnaldi et. al., NA60 Collaboration, Phys. Lett. B 706 263 (2012).

[29] B. Alessandro et al. NA50 Collaboration, Eur. Phys. J. C39, 335 (2005).

[30] A. Adare *et al.,* PHENIX Collaboration, Phys. Rev. C 84, 054912 (2011)

[31] Z. Tang, STAR Collaboration, J. Phys. G 38, 124107 (2011)

[32] I. Das (for the ALICE collaboration), PoS (ICPAQGP2015) 021

[33] P. Senger, Nucl. Phys. A 862, 139 (2011)

[34] T. Galatyuk, Nucl. Phys. A 982, 163 (2019)

Chapter 3

Gas Electron Multiplier

3.1 Introduction

The main aim of the detector used in High Energy Physics (HEP) experiments is to identify the charge particles produced after the collision of the ions or nuclei and to find their trajectories so that we can reconstruct the event and try to understand the underlying physics at the time of collision and afterwards.

The evolution of radiation detectors started with J. J. Thomson's detector, just a few months after the discovery of the unknown X-rays. During that time, the design was relatively simple: just an ion chamber with one positive and one negative flat electrode separated by air. The readings from the chamber were obtained by measuring the current across the two electrodes, which provided major discoveries that led to the understanding of the fundamentals of radiation interactions with matter [1]. The observation of John Townsend that a significant increase in an ion chambers current is produced at reduced gas pressures when the high voltage is increased well beyond that at which the saturation current is reached, led to the invention of the first counting tubes (today known as proportional counters) by Rutherford and Hans Geiger in 1908 [2]. Shortly after the invention of the proportional counter, the voltage across the electrodes was increased even further which laid the basis for the creation of Geiger Mueller tubes in 1928 [3, 4].

The possibility of light output from a barium platinocyanide screen, when exposed to X-rays, leads to the development of a new kind of detector, the scintillator detector in 1944 [5].

Around the same time, Bell Laboratories invented the semiconductor detector that used the reverse-biased p-n junction to detect alpha particles [6]. From that time, independent of the size, shape, or purpose of any radiation detector, all detectors can be divided into three main categories, which are: the gaseous detector, scintillator detector, and semiconductor detector.

3.2 Chronological development of advanced gaseous detectors

In 1968, the invention of the Multi Wire Proportional Counter (MWPC) [7] at CERN stood out in gas detector development. The MWPC provided a breakthrough in particle detection since it was capable of both particle tracking and energy reading. For this reason, the inventor Georges Charpak was awarded the Nobel Prize in Physics in 1992. The typical dimensions of the anode wire radius spans from $\sim$ 20-25 μm [7, 8]. The typical time resolution, obtained with an MWPC is $\sim$ 30-50 ns and the spatial resolution of $\sim$ 250-500 μm [7, 8]. However, the gain of MWPC reduces with increasing particle rate because of positive ion space charges which dynamically modify the electric fields. The rate handling capability of MWPCs is limited to $\sim 10^4$ Hz/mm^2 due to this space charge issue. Another drawback of MWPC is their poor spatial resolution and that is mainly due to the limitation of two anode wires placed very close to each other due to electrostatic repulsions.

In 1988 at the Institute Laue-Langevin (ILL) in Grenoble, Anton Oed developed a detector with a new concept named Micro Strip Gas Counter (MSGC) [10], which promised to improve the rate capability and also made the detector more

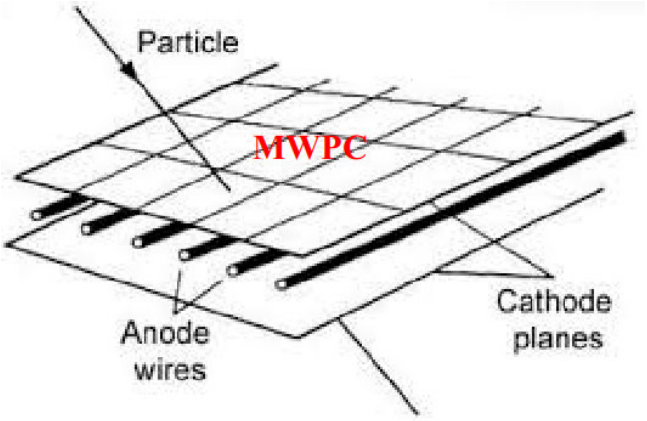

Figure 3.1: Schematic of Multi Wire Proportional Counter (MWPC). The figure is taken from Ref. [9].

reliable for long runs. The typical anode width and pitch (separation between the centres of two anodes) of the detector were kept at $\sim$ 9 μm and $\sim$ 200 μm respectively. The drift gap of the chamber was kept at $\sim$ 2-6 mm and the typical cathode width was $\sim$ 70 μm [11]. The typical spatial resolution obtained

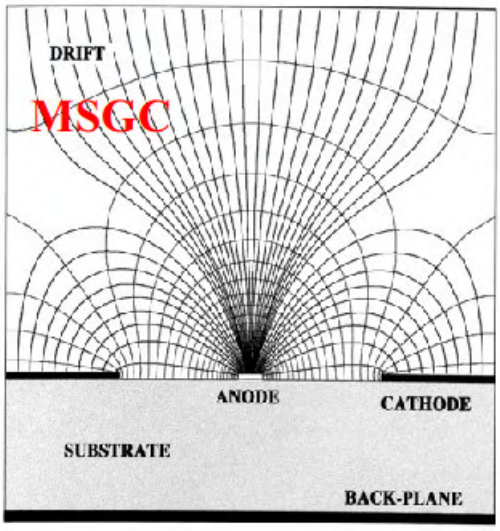

Figure 3.2: Schematic of Micro Strip Gas Counter (MSGC). The figure is taken from Ref. [12].

with MSGC was $\sim$ 50-100 μm and the rate handling capability was found to be $\sim$ 10^6 Hz/mm^2, which was better as compared with that of MWPC. Unfortunately, this development did not help much because various operating instabilities like time-dependent gain shifts, polarisation, charging up of the

substrate as well as permanent deterioration during sustained irradiation had also been observed [13].

Parallel investigations led to the inventions of Micro Groove [14] and Micro Gap [15] chambers which were better in performance as compared to the MSGC in terms of radiation-induced gain shifts. In the Micro Groove detector, a groove

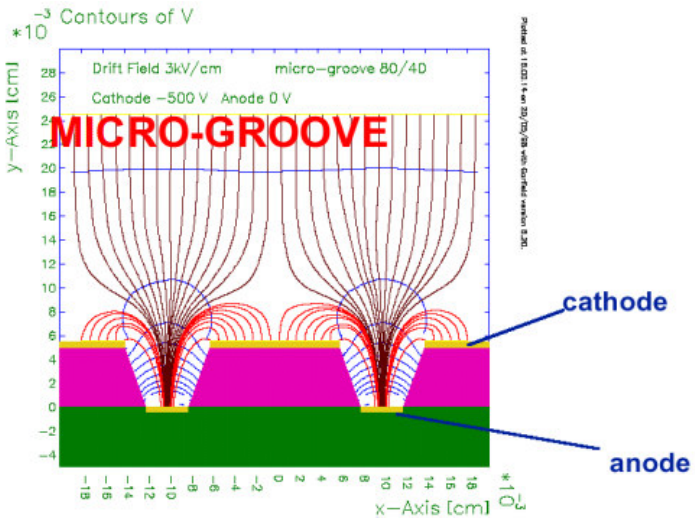

Figure 3.3: Schematic of a Micro Groove chamber. The figure is taken from Ref. [14].

kind of structure was implemented to reduce the exposure of the dielectric to external irradiation. The typical anode pitch was kept at $\sim$ 200 μm. The rate handling capability was limited to $\sim 10^6$ Hz/mm^2 and a two-dimensional readout was possible [14]. Though the issues regarding the radiation-induced gain shifts and the charging-up of the substrate had improved as compared to the earlier detectors, still they were not completely resolved by this detector technology.

In the case of the Micro Gap detector [15], the dielectric exposure to the external irradiation was completely minimized by using a metal layer on top of the dielectric surface; and that surface also acted as the cathode for the chamber. The anodes were implemented at the top of the cathode surface by using a polyimide layer. The typical anode pitch was $\sim$ 50-100 μm with a drift gap of $\sim$ 2-5 mm. The rate handling capability of the chamber was found to be limited to $\sim 8 \times 10^6$ Hz/mm^2 and no charging-up effect was seen [16].

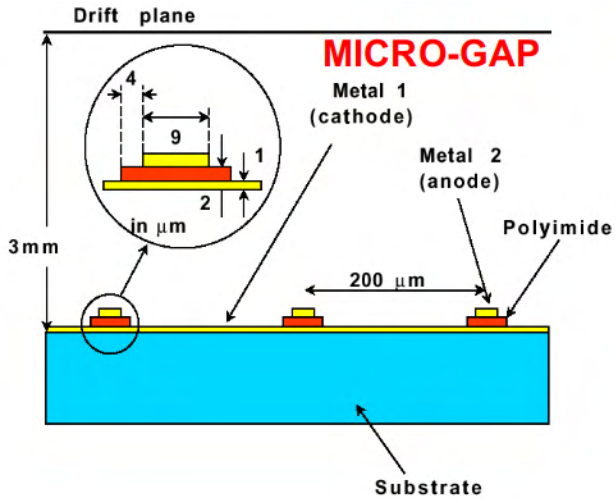

Figure 3.4: Schematic of Micro Gap chamber. The figure is taken from Ref. [17].

However, due to the presence of the dielectric medium, the material budget of those detectors was found to be significantly high. To reduce the material budget without affecting the performance of the detector, several other detectors like Micro Wire and Micro Pin Array came up in the field of gaseous detectors.

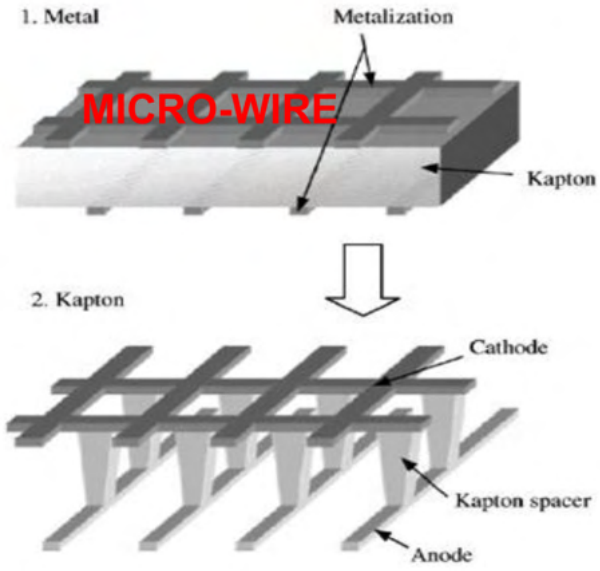

Figure 3.5: Schematic of Micro Wire chamber. The figure is taken from Ref. [18].

A Micro Wire detector consists typically of a Kapton foil of thickness 50 μm with a 5 μm copper layer on both sides [18]. On one side of the chamber,

square holes of typical dimensions 70 μm $\times$ 70 μm had been created after etching using lithographic techniques. On the opposite side, wide strips of a typical width 25 μm were created after etching. The strips were produced after etching in such a way that they passed through the middle of the square holes. The strips and the square holes were treated as the anode and the cathode respectively for this chamber. The typical anode pitch of the chamber was kept at $\sim$ 100 μm. Several R&D's had been performed with different Kapton thicknesses, and cathode apertures, as reported in Ref. [18] and in the references therein. Since no additional substrate was required to support the anode strips, the typical material budget of this kind of chamber was very small ($\sim$ 0.037% of radiation length). The granularity of the chamber was also better as compared to that of the MSGC or the Micro Groove chamber. The rate handling capability ($\sim 10^6$ Hz/mm^2) was comparable to that of an MSGC and was better than those of MWPC and Micro Groove chambers.

The Micro Pin Array [19] consisted of an array of pins, which acted as an anode, immersed into the cathode of hexagonal shape. It was very similar to that of the MWPC but micro-pattern technologies were used to build the chamber. The typical anode pin diameter was $\sim$ 50 μm with a height of $\sim$ 200 μm. The

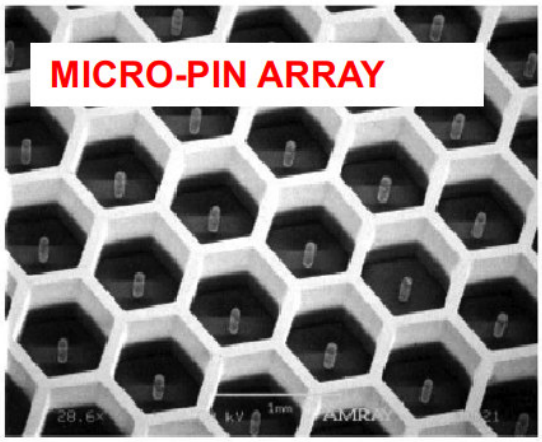

Figure 3.6: Schematic of Micro Pin Array chamber. The figure is taken from Ref. [19].

cathode planes were designed in the shape of a hexagon to minimize the dead space of the chamber. The typical diameter of the cathode was $\sim$ 600 μm and the wall thickness was $\sim$ 50 μm [19]. The electron multiplication was only

limited to close proximity of the anode pins and then fell off with 1/r (r being the distance from the anode pin). The advantage of this geometry was that the amplification region was located far away from any dielectric surface, therefore, the gain of the chamber was insensitive to the charge state of the surface. The rate handling of the chamber was found to be limited to $\sim 10^6$ Hz/mm^2 and the discharge probability was found to be low [19].

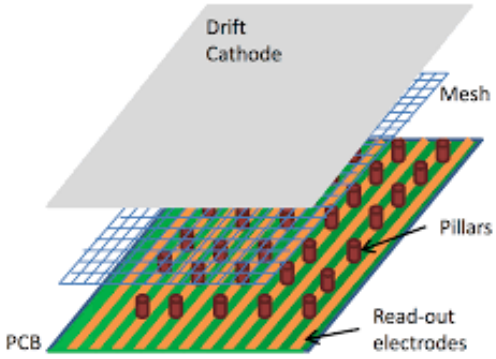

Figure 3.7: Schematic of Micromegas chamber. The figure is taken from Ref. [20].

The concept of Micromegas [21] came up from the expectation of achieving higher gain by applying higher electric fields inside thin sub-millimetre gaps and also of minimizing the sensitivity of gain variation with the gas gap. The micromegas detector consisted of a thin metal grid (act as the cathode) stretched to a very small distance (~ 100 μm) above the readout plane. A very high electric field ($>$ 30 kV/cm) was applied across the grid and the electrons coming from the drift region were multiplied inside the gaps of the metal grid. The typical drift gap was kept at ~ 5 mm and the amplification gap was ~ 100 μm. Due to the small amplification gaps and high electric fields, the positive ions moved very fast and were collected at the cathode mesh. As a result, space charge accumulation was prevented and fast signals were achieved ($\sim$ 50-100 ns) [22, 23].

A summary of the characteristics of the first era of gaseous detectors is given in Table 3.1.

Table 3.1: Overview on the characteristics of the first era of gas-filled detectors.

Detector	Characteristics	Remarks
Multi Wire Proportional Counter (MWPC) [7, 8]	Time resolution ∼30-50 ns Position resolution ∼250-500 μm Length ∼5-10 mm Anode wire radius ∼20-25 μm	Rate is limited to ∼10^4 Hz/mm^2 Difficult to build thin wires Spatial resolution is not good
Multi Strip Gas Counter (MSGC) [10, 11, 13]	Anode pitch ∼200 μm Anode width ∼9 μm Drift gap ∼2-6 mm Cathode width ∼70 μm Spatial resolution ∼50-100 μm Time resolution ∼ few ns	Rate is limited to ∼10^6 Hz/mm^2 Charging-up effect due to the insulating substrate Discharge prone
Micro Groove [14]	Anode pitch ∼200 μm 50 μm Kapton as the dielectric substrate with 5 μm metal cladding	Rate is limited to ∼10^6 Hz/mm^2 2D readout is possible Energy resolution is better compared to MWPC & MSGC
Micro Gap [15, 16]	Anode pitch ∼50-100 μm Anode width ∼9 μm Drift gap ∼2-5 mm Insulating material thickness ∼2 μm Metal layer thickness ∼1 μm	Rate is limited to ∼8×10^6 Hz/mm^2 Ion collection is very fast No charging-up effect
Micro Wire [18]	Anode pitch ∼100 μm Anode width ∼20-25 μm Drift gap ∼3 mm Square holes ∼70 μm×70 μm	Rate is limited to ∼10^6 Hz/mm^2 High granularity Material budget is low
Micro Pin Array [19]	Anode pin diameter ∼50 μm Height ∼200 μm Hexagon radius ∼300 μm Wall thickness ∼50 μm	Rate is limited to ∼10^6 Hz/mm^2 Discharge probability is small Material budget is low
Micromegas [22, 23]	Drift gap ∼5 mm Position resolution ∼10-30 μm Time resolution ∼1-5 ns	Rate is limited to ∼10^6 Hz/mm^2 Good spatial and energy resolution Fast ion collection

In 1997 Fabio Sauli invented the Gas Electron Multiplier (GEM) detector, which is one of the advanced members of the Micro Pattern Gas Detectors (MPGD) group [24, 25].

The GEM detector consists of one or multiple GEM foils. A GEM foil is made of a thin ($\sim$ 50 μm) polyimide (Kapton), copper cladded ($\sim$ 5 μm) on both sides and pierced with a high density of holes, typically $\sim$ 50 - 100 mm^{-2}. Typically, the diameter of each hole is 70 μm and pitch is 140 μm. The holes are pierced in the Copper cladded Kapton foil using photo-lithographic techniques. Depending on the technique used, the GEM foils can be classified as Double Mask (DM) and Single Mask (SM) foils [26]. The schematic of the photo-lithographic technique is shown in Fig. 3.8. For the DM GEM foils, the masking

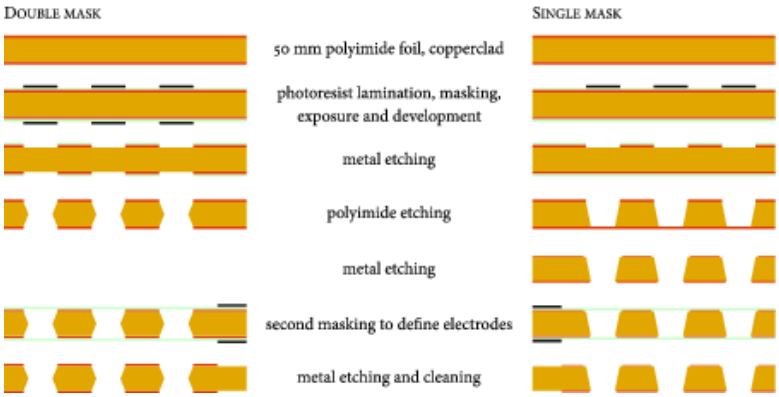

Figure 3.8: Different techniques of photo-lithography.Left: Double Mask (DM); Right: Single Mask (SM) technique. The figure is taken from Ref. [25].

is done on both sides of the copper cladded Kapton foil to engrave the desired hole patterns. After the masking process, the etching of the foil is done. The etching is done isotropically from both directions and results in a symmetrical bi-conical hole. In the case of the DM technique, the alignment of the hole patterns (i.e. of the top and bottom masks) is an essential criterion to avoid creating slanted holes. In the case of large area GEM foils, the alignment of the holes is not practically possible and that is what triggered the invention of the SM technique. In the case of the SM technique, the masking is done only in one direction and the etching is done from that side only. As a result, asymmetric holes are created and the performance of the detector depends on the orientation of the GEM foil. The effects of GEM hole geometry on the performance of the chamber are discussed in Refs. [27, 28, 29].

In the GEM detector, an electrode is placed on the top, called the drift electrode and a charge collection electrode is placed as a read-out. The electrons produced in the drift region (the region between the drift electrode and the top of the GEM foil) are directed towards the holes by an electric field ($\sim$ 2-3 kV/cm), known as the drift field. The typical potential difference $\sim$ 400 V is applied between the two sides of the GEM foil to create a high electric field ($\sim$ 80 kV/cm) inside the holes. Because of a very high electric field, an avalanche of electrons is created inside the holes. A sizeable fraction of the electrons, produced in the avalanche, leave the multiplication region and transfer into the lower section

of the structure, where they can be collected by an electrode or injected into a second multiplying region (in case of more than one GEM foil). In a triple GEM detector, usually, the applied high voltage is distributed among the three GEM foils and the different gaps (drift gap, transfer gaps, induction gap) using a resistive chain. In case of a triple GEM chamber, the gap between the drift electrode and the top of the 1^{st} GEM foil is called the drift region. The gap between the bottom of the 1^{st} GEM foil and the top of the 2^{nd} GEM foil and that between the bottom of 2^{nd} GEM foil and the top of 3^{rd} GEM foil are called transfer gap 1 and transfer gap 2 respectively. The gap between the bottom of the 3^{rd} GEM foil and the detector readout plane is called the induction gap. When any radiation or charged particle enters the drift region, it first interacts with the gas molecules and produces electron-ion pairs. Those electrons are known as the primary electrons. Due to the presence of the electric field in the drift gap, the primary electrons are accelerated towards the first GEM foil. Due to the geometry of the GEM foils, the strength of the electric field becomes very high within the holes, and as a result, the primary electrons gain enough kinetic energy to produce avalanche multiplication by ionizing the gas molecules there. Thus, after the first GEM foil, we get a large number of electrons. Those elec-

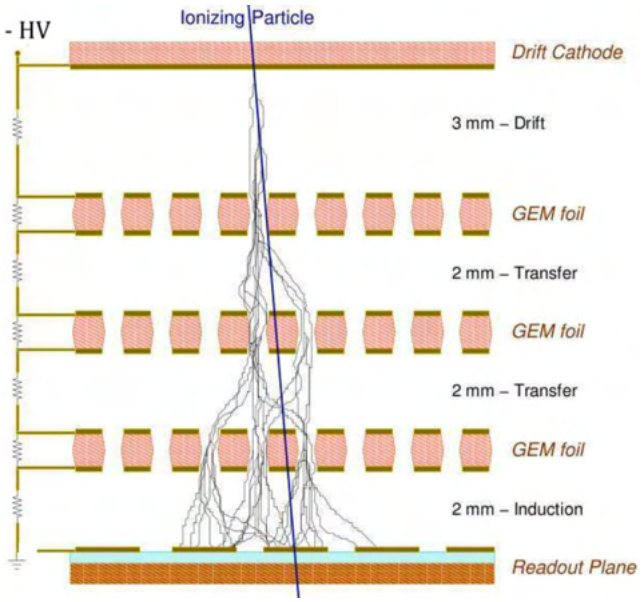

Figure 3.9: Schematic of a triple GEM chamber in 3-2-2-2 configuration. The figure is taken from Ref. [30].

trons are again guided by the field in the transfer gap 1 to the 2^{nd} GEM foil and the same multiplication phenomena occur for both the 2^{nd} and the 3^{rd} GEM foils and finally the electrons after the 3^{rd} GEM foil are guided to the readout plane by the electric field in the induction gap. In Fig. 3.9, the schematic of the operation of a triple GEM chamber is shown. One of the advantages of the GEM detector is that it can be operated in the cascaded mode. This means that we can reach our required gain just by increasing the number of GEM foils instead of increasing the applied voltage to a single GEM foil. It also reduces the spark probability. The electrode (GEM foil) is metal-coated on both sides, therefore, it reduces the ion back flow. The high efficiency, high rate handling capacity of the GEM detector and its good position resolution makes it suitable as a tracking detector in HEP experiments where the particle flux is expected to be very high. As an example, after upgradation in the CMS muon detection system, triple GEM detectors are used whereas after the upgradation in ALICE TPC, quadrupole GEM detectors are used to handle high particle rates and also to minimize the ion-back flow.

3.3 Choice of gas mixture

The choice of the gas mixture used in a gaseous detector is something quite complicated and depends on the requirement of the experiment and the expected performance of the chamber. The important parameters to be taken into account in the choice of the gas mixture are: low working voltage, high gain operation, good proportionality, long lifetime, high rate capability, etc. The avalanche multiplication occurs at relatively lower fields in noble gases as compared to the polyatomic gases. The main reason for that is the complex structure of the polyatomic gases and their different non-ionizing energy dissipation modes. The choice of Argon (Ar) is quite conventional, because the primary ionization for Minimum Ionizing Particles (MIP)[1] is high enough. Fur-

[1]The particles whose mean energy loss through a media is minimum, referred as Minimum Ionizing Particle. Any particle is said to be minimum ionizing if its energy is much much greater than its rest mass energy.

ther, as compared to other noble gases (like Xenon and Krypton), Argon is inexpensive. It happens frequently that the detectors need to be operated at a high gain, i.e. with a high electric field, which increases the risk of discharges. To increase the electric field while avoiding any discharge, a polyatomic gas is usually added. The polyatomic gases have the property of having other atomic degrees of freedom such as rotation, vibration etc. They can, therefore, absorb ultraviolet photons produced in the avalanche, and thus avoid spurious signals. This type of gas is called a quencher. Gases generally used as quenchers are CO_2, CH_4 etc. In the course of this thesis, the performance of triple GEM chambers is investigated with premixed Ar/CO_2 gas mixtures in different volume ratios. A detailed study on the properties of the gas mixture used in the tracking detectors can be found in Ref. [31].

3.4 Applications of the GEM detector

New generation nuclear and particle physics experiments require charged particle tracking devices with a low material budget, good efficiency, high rate handling capability and excellent position resolution. For the last several decades, various types of MPGD [12] have been developed for their use in experiments at major accelerator facilities as well as for applications in imaging technologies. The GEM detector is one of the most used new generation MPGDs, which fulfil the stringent conditions of existing and proposed large-scale experiments. Several HEP experiments are already making use of this technology. A brief description of the experiments is given below where GEM chambers have been used and proposed to be used.

The first example of the application of a GEM foil in a tracking detector subsystem was in the HERA-B [32] experiment at the HERA (Hadron Electron Ring Accelerator) [33] storage ring (at DESY, Germany). The HERA-B Inner Tracker system consists of an MSGC with the GEM foil as the pre-amplifying

device in the gas volume. The GEM foil was introduced as a first amplifying stage to reduce the discharge probability of the MSGC chamber [34]. A typical distance between the drift electrode and GEM foil was $\sim$ 3 mm and the gap between the GEM foil and MSGC chamber was $\sim$ 2.8 mm. Typical dimensions of the chambers were 25 cm $\times$ 25 cm. Argon based gas mixtures were used in the detector. The hybrid GEM-MSGC detectors have helped to overcome many major problems in the tracking system and allowed stable operations with a high reliability and a good efficiency [35, 36].

The triple GEM chambers were first used as a tracking device in the COMPASS (Common Muon and Proton Apparatus for Structure and Spectroscopy) [37] experiment, the first high luminosity particle physics experiment at CERN SPS (Super Proton Synchrotron). The requirements for the performance of the tracking chambers included the rate handling ($\sim$ 25 kHz/mm^2) capability by maintaining good spatial ($\sim$ few tens of μm) and time resolution ($\sim$ few tens of ns). The dimension of the triple GEM chambers used as a tracker near the beam area was 31 cm $\times$ 31 cm. The drift gap, transfer gaps and induction gap were kept at 3 mm, 2 mm and 2 mm respectively. The chambers were operated with an Ar/CO_2 gas mixture in a 70/30 volume ratio. A typical gas gain of $\sim$ 8000 was used for the operation of the chamber. The spatial and temporal resolution of the chambers were found to be $\sim$ 70 μm and $\sim$ 12 ns respectively. The details of the chamber fabrications and their operations are reported in Refs. [38, 39, 40] and in the references therein.

Triple GEM chambers were used as a triggering device in the inner region of the first muon station of the LHCb (Large Hadron Collider beauty) [41] experiment. The idea for the application of triple GEM chambers as a triggering device was unique at that time and several R&D's were performed to demonstrate the same. The performance requirement of the GEM chambers includes the long-term stability in performance with a rate handling capability up to $\sim$ 500 kHz/cm^2 with an efficiency higher than 90% (within 20 ns time window). The drift, transfer and induction gaps of the chambers were kept at 3 mm, 1 mm, 2 mm and 1 mm respectively. The dimensions of the chambers were optimised to be

20 cm × 24 cm in each case. To improve the timing performance, the chambers were operated with different Argon based gas mixtures. A time resolution better than 5 ns (RMS) was obtained with an $Ar/CO_2/CF_4$ gas mixture in the volume ratio of 45/15/40. Using the same gas mixture, the aging study was performed using a 5.9 keV X-ray source and the detector did not show any degradation in terms of its performance even after the accumulation of 4.2 C/cm^2 of charge (equivalent to 10 LHCb years). The details of the R&D and performance studies of the detector are reported in Refs. [42, 43] and in the references therein.

The successful operation of the triple GEM chambers in the COMPASS [37] experiment perturbed the decision of using triple GEM chambers in the T2 telescope of the TOTEM (TOTal Elastic and diffractive cross section Measurement) [44] experiment at LHC for tracking and triggering. The GEM chambers were semi-cylindrical in geometry and placed at the forward rapidity region ($5.3 < |\eta| < 6.5$). The typical radial extension of the chambers was from 4.25 cm to 14.45 cm. The triple GEM chambers were used to achieve a nominal gain of $\sim$ 8000 with Ar/CO_2 gas mixture in a 70/30 volume ratio. The details about the experimental setup and performance studies are reported in Refs. [45, 46] and in the references therein.

Several experiments are planning to upgrade their detector systems with GEM detectors due to increasing particle flux that is foreseen; for example, the CMS (Compact Muon Solenoid) [47] detector system at LHC (Large Hadron Collider), CERN, is planning to upgrade the muon spectrometer with triple GEM chambers. The upgradation is needed to cope with the foreseen upgradation of LHC to High Luminosity (HL)-LHC. The drift, transfer and induction gaps of the chamber are proposed to be 3 mm, 1 mm, 2 mm and 1 mm respectively. An Ar/CO_2 gas in 70/30 volume ratio will be used in the chambers. The typical dimensions of the trapezoidal-shaped chambers will be $\sim$ 99 cm (height) × 45.5 cm (width at the wider side) and $\sim$ 190 cm (height)× 120 cm (width at the wider side). Much R&D on the large area GEM foils has been done and reported in Refs. [48, 49] and in the references therein.

The upgradation of the TPC (Time Projection Chamber) at the ALICE (A Large Ion Collider Experiment) [50] detector system at LHC involves the replacement of wire chamber based TPC readout system by quadruple GEM chambers. The quadrupole GEM configuration is chosen over the triple GEM configuration mainly to reduce the ion back flow to <2% at a gain of $\sim$ 2000 and also to achieve an energy resolution of $\sim$ 14% with an Fe^{55} X-ray source. The pitch of the GEM holes was also modified to ensure that the ion back flow was minimized. The typical trapezoidal-shaped chambers are of height $\sim$ 49.7 cm and width of 46.7 cm of the long parallel side of the module. The chambers will be operated with a $Ne/CO_2/N_2$ (90/10/5) gas mixture. The primary reason behind choosing a Ne based gas mixture is to reduce the size of the space charge distortions. A detailed discussion of the optimisation of the gas mixture is reported in Ref. [51]. Several R&D studies on the quadrupole GEM chambers have been performed to optimize the configuration of the GEM foils and are reported in Ref. [52] and references therein. The applications of the GEM chamber in the HEP experiments are summarised in Table 3.2.

Apart from the HEP experiments, the GEM chambers are also being used in many other medical and societal applications. A triple GEM chamber based Muon Tomography Station (MTS), reported in Ref. [53], has been used for the imaging of the high-Z material using cosmic ray muons. The dimension of the chambers used was 30 cm $\times$ 30 cm and operated with Ar/CO_2 gas mixture in a 70/30 volume ratio. The drift gap, transfer gaps and induction gap are kept at 3 mm, 2 mm and 2 mm respectively. Ref. [53] gives the proof of principle that the GEM based muon tomography is possible. GEM based readout systems are used in medium to high energy (MeV-GeV) gamma-ray polarimetry. The details of the instrumentation and their R&D are nicely summarised in Refs. [54, 55]. GEM based detectors are also used in neutron detection. The performance of the GEM based neutron detector is investigated with different neutron converters. A brief review of neutron detection using GEM chambers is available in Ref. [56]. A set of triple GEM (similar to the GEMs built for the COMPASS experiment) trackers has been used to design a medical diagnostic

Table 3.2: Summary of the application of the GEM detector in HEP experiments.

Experiment	Purpose (& requirement)	Dimension	Gas gap configuration	Gas mixture
HERA-B [34, 35, 36]	Pre-amplifying stage of MSGC (Reduce the discharge probability of MSGC)	25 cm × 25 cm	Drift gap: 3 mm Gap between GEM and MSGC: 2.8 mm	Ar based gas mixtures
COMPASS [38, 39, 40]	Tracking [Rate ($\sim$ 25 kHz/mm^2) handling with good resolution]	31 cm × 31 cm	Drift gap: 3 mm Transfer gaps: 2 mm Induction gap: 2 mm	Ar/CO_2 (70/30)
LHCb [42, 43]	Trigger [Rate ($\sim$ 500 kHz/cm^2) handling with high efficiency]	20 cm × 24 cm	Drift gap: 3 mm Transfer gap 1: 1 mm Transfer gap 2 : 2 mm Induction gap: 1 mm	$Ar/CO_2/CF_4$ (45/15/40)
TOTEM [45, 46]	Trigger & tracking (-)	Semi-cylindrical with radial extension from 4.25 cm to 14.45 cm	Drift gap: 3 mm Transfer gaps: 2 mm Transfer gap 2 : 2 mm Induction gap: 1 mm	Ar/CO_2 (70/30)
CMS [48, 49]	Tracking (Cope up with the upgradation of LHC to HL-LHC)	Trapezoidal modules 99 cm (height) × 45.5 cm (width at the wider side) 190 cm (height) × 120 cm (width at the wider side)	Drift gap: 3 mm Transfer gap 1: 1 mm Transfer gap 2 : 2 mm Induction gap: 1 mm	Ar/CO_2 (70/30)
ALICE [51, 52]	Readout of TPC (Reduce the ion back flow below)	Trapezoidal modules 49.7 cm (height) × 46.7 cm (width)	Quadrupole GEM Drift, transfer and induction gaps: 2 mm	$Ne/CO_2/N_2$ (90/10/5)

tool for hadron therapy, known as Proton Range Radiography (PRR) [57]. The concept used in the device is to get the correlation between the measured position and energy loss profile, which will yield the density distribution in the target. Performance studies of GEM based detectors for medical applications are discussed in detail in the Refs. [58, 59, 60].

Future HEP experiments like CBM (Compressed Baryonic Matter) at FAIR, NA60+ at CERN SPS (Super Proton Synchrotron) have planned to use triple GEM chambers as the tracking device in the muon chambers [61, 62]. In Chapter 4, the details of the performance studies of triple GEM chambers will be discussed for the CBM Muon Chamber.

References

[1] F. N. Flakus, Detecting and measuring ionizing radiation - a short history; https://www.iaea.org/sites/default/files/publications/magazines/bulletin/bull23-4/23405043136.pdf

[2] E. Rutherford and H. Geiger, Proceedings of the Royal Society (London), Series A, vol. 81, no. 546, pp. 141–161 (1908)

[3] The Geiger Counter; http://large.stanford.edu/courses/2017/ph241/russo2/

[4] U.S. Patent 1,995,018, H. J. Spanner, "Gas Filled Tube"

[5] A. T. Krebs, SCIENCE Vol 122, Issue 3157, pp. 17-18 (1955)

[6] https://www.sciencedirect.com/topics/engineering/bell-laboratories

[7] G. Charpak *et al.*, Nucl. Instr. Meth. Phys. Res. A, 62, 262 (1968)

[8] G. Charpak *et al.*, Nucl. Instr. Meth. Phys. Res. A, 80, 13 (1970)

[9] https://physicsmasterclasses.org/exercises/hands-on-cern/hoc_v21en/main_frame/de_track2.html

[10] A. Oed, Nucl. Instr. Meth. Phys. Res. A, 263, 351 (1988)

[11] F. Angelini *et al.*, Nuclear Physics B (Proc. Suppl.) 23A, 254 (1991)

[12] F. Sauli and A. Sharma, Annu. Rev. Nucl. Part. Sci. 49, 341 (1999)

[13] R. Bouclier *et al.*, IEEE TRANSACTIONS ON NUCLEAR SCIENCE, VOL 43, NO 3, JUNE 1996

[14] R. Bellazzini *et al.*, Nucl. Instr. Meth. Phys. Res. A, 424, 444 (1999)

[15] E. Christophel and M. Dracos, Nucl. Instr. Meth. Phys. Res. A, 398, 195 (1997)

[16] J. F. Clergeau *et al.*, Nucl. Instr. Meth. Phys. Res. A, 392, 140 (1997)

[17] F.Angelini *et al.*, Nucl. Instr. Meth. Phys. Res. A, 335, 69 (1993)

[18] B. Adeva *et al.*, Nucl. Instr. Meth. Phys. Res. A, 435, 402 (1999)

[19] P. Rehak *et al.*, Proceedings of International Workshop on Micro-Pattern Gas Detectors, pp. 119-123 (1999); pres. at Micro-Pattern Gas Detectors Workshop, Orsay, Frame, 28-30 June (1999)

[20] T. Vafeiadis (on behalf of the ATLAS muon collaboration), ATL-MUON-PROC-2020-021, ICHEP2020

[21] I. Giomataris *et al.*, Nucl. Instr. Meth. Phys. Res. A, 376, 29 (1996)

[22] Y. Giomataris, Nucl. Instr. Meth. Phys. Res. A, 419, 239 (1998)

[23] G. Barouch *et al.*, Nucl. Instr. Meth. Phys. Res. A, 423, 32 (1999)

[24] F. Sauli, Nucl. Instr. Meth. Phys. Res. A, 386, 531 (1997)

[25] F. Sauli Nucl. Instr. Meth. Phys. Res. A, 805, 2 (2016)

[26] Oliveira *et al.*, United States Patent, Patent No.: US 8,597,490 B2

[27] H. Keller *et al.*, JINST 15, C06004 (2020)

[28] P. Roy *et al.*, JINST 17, P03016 (2022)

[29] E. Brücken *et al.*, Nucl. Instr. Meth. Phys. Res. A, 1002, 165271 (2021)

[30] V. D. Smet, Master thesis, Study of a GEM tracker of charged particles for the Hall A high luminosity spectrometers at Jefferson Lab; DOI: 10.13140/RG.2.2.15950.46402

[31] A. Sharma, Properties of some gas mixtures used in tracking detectors, https://www.slac.stanford.edu/pubs/icfa/summer98/paper3/paper3.pdf

[32] HERA-B; http://www-hera-b.desy.de/

[33] HERA; https://www.desy.de/research/facilities__projects/hera/index_eng.html

[34] T. Zeuner for the HERA-B Inner Tracker Collaboration, Nucl. Instr. Meth. Phys. Res. A, 446, 324 (2000)

[35] W. Gradl for the HERA-B Inner Tracker Collaboration, Nucl. Instr. Meth. Phys. Res. A, 461, 80 (2001)

[36] T. Hott for the HERA-B Inner Tracker Collaboration, Nucl. Instr. Meth. Phys. Res. A, 515, 242 (2003)

[37] COMPASS; https://home.cern/science/experiments/compass

[38] B. Ketzer *et al.*, Nucl. Instr. Meth. Phys. Res. A, 535, 314 (2004)

[39] C. Altunbas et al., Nucl. Instr. Meth. Phys. Res. A, 490, 177 (2002)

[40] F. Simon, Commissioning of the GEM detectors in the COMPASS experiment, 2001 thesis, Technische Universität München

[41] LHCb; https://home.cern/science/experiments/lhcb

[42] M. Alfonsi *et al.*, Nucl. Instr. Meth. Phys. Res. A, 518, 106 (2004)

[43] M.P. Lener, Triple-GEM detectors for the innermost region of the muon apparatus at the LHCb experiment, PhD thesis (2006), Università degli Studi di Roma "Tor Vergata"

[44] TOTEM, https://totem-experiment.web.cern.ch/

[45] S. Lami *et al.*, Nuclear Physics B (Proc. Suppl.) 172, 231 (2007)

[46] O. Eraldo, The forward inelastic telescope T2 for the TOTEM experiment at the LHC, PhD thesis, University of Siena

[47] CMS; https://home.cern/science/experiments/cms

[48] G. Mocellin, on behalf of the CMS Muon Group, J. Phys.: Conf. Ser. 1390, 012116 (2019)

[49] C. Calabria, on behalf of the CMS GEM Collaboration, Nuclear and Particle Physics Proceedings 273, 1042 (2016)

[50] ALICE; https://home.cern/science/experiments/alice

[51] ALICE TPC collaboration *et al.*, JINST 16 P03022 (2021)

[52] B. Ketzer, For the GEM-TPC and ALICE TPC Collaborations, Nucl. Instr. Meth. Phys. Res. A, 732, 237 (2013)

[53] K. Gnanvo *et al.*, Nucl. Instr. Meth. Phys. Res. A, 652, 16 (2011)

[54] P. Gros *et al.*,, POS(TIPP2014)133

[55] S. D. Hunter *et al.*, Astroparticle Physics 59, 18 (2014)

[56] S. D. Pinto, Modern Physics Letters A Vol. 28, No. 13, 1340025 (2013)

[57] M. Bucciantonio, and F. Sauli, Modern Phys. Lett. A, 30(17), 1540024 (2015)

[58] F. Anulli *et al.*, Nucl. Instr. Meth. Phys. Res. A, 572, 266 (2007)

[59] E. Tsyganov *et al.*, Nucl. Instr. Meth. Phys. Res. A, 597, 257 (2008)

[60] R. M. Gutierrez *et al.*, JINST, 7, C07007 (2012)

[61] S. Chattopadhyay *et al.*, Technical Design Report for the CBM : Muon Chambers (MuCh); GSI, 2015; https://repository.gsi.de/record/161297

[62] A. D. Falco for the NA60+ Collaboration, EPJ Web of Conferences 259, 09003 (2022)

Chapter 4

Performance studies of GEM for CBM Muon Chamber

4.1 Introduction

Future high-rate experiments, like the CBM experiment, require large area detectors capable of precise tracking of charged particles with very high detection efficiency and good spatial resolution. The GEM detector is a potential candidate as tracker for any high-rate experiment and the requirement of large area is taken care of by the newly developed Single Mask (SM) technology. In the CBM experiment, a dedicated detector sub-system will be used for muon tracking, known as the Muon Chamber (MuCh) [1]. The GEM detectors will be placed in the first two stations of MuCh because of their high-rate handling capacity as discussed in section 2.1. Since GEM detector will be used in places where the particle flux is very high, it is necessary to perform the stability test of the GEM detector in terms of its gain, energy resolution, and count rate under very high and continuous radiation. If in a long-term operation under continuous radiation, the detector shows any significant degradation then it cannot be used in the real experiment. Degradation of the performance of gas detectors under irradiation has been observed since the start of their application in particle physics experiments. In general, the observed damage depends on the amount of radiation seen by the detector. In addition, many other parameters like gas

composition, gas quality, particle rate and particle type play extremely important roles. It has been shown in several studies that GEMs, and in particular staged triple GEMs show very good performance against prolonged irradiation or in other words they are radiation hard. However, in the long-term, intense irradiation with slow, heavily ionizing particles, as foreseen in the CBM experiment, might provoke yet unknown aging characteristics. The expected accumulated charge per unit area at CBM is 0.76 mC/mm^2 in 10 years[1]. Thus the investigation of long-term stability is one of the most important aspects of the R&D work carried out at Bose Institute. Also, the uniformity over the active area of the detector is investigated in terms of gain, energy resolution, and count rate.

One of the major issues with micro pattern gaseous detectors is discharges. The high electric fields used for the amplification can provoke discharges or sparks in high-rate operations. These sparks can be devastating for the detectors. So these discharges need to be avoided as much as possible and the detector should be operated in a safe region since they (being a statistical phenomenon) can never be entirely excluded. The first method in trying to avoid discharges in GEM detectors is the cascaded operation of the GEM foils. This is of particular relevance for the proposed CBM GEM tracker since we expect a high track density of slow, highly ionizing particles after the hadron absorbers. The spark probability of a SM triple GEM chamber prototype is tested at the CERN SPS beam-line and the results are discussed in the following sections.

The questions to be addressed to validate the applicability of GEM detectors for any high-rate experiment are the following:

- Effect of ambient parameters such as temperature [T (in K) = t + 273, t in °C], pressure (p in mbar) and Relative Humidity (RH) on the gain and energy resolution of the chamber

[1]The accumulated charge per unit area is calculated using the following information;
Average interaction rate: 1 MHz, Primary electrons/track for MIP: $\sim$ 30, Gain: 10^3,
Tracks/cm^2/event: $\sim$ 0.05 (Fig. 2.2: Scaled by 1/4 to get the number for minimum bias Au+Au collision)
Accumulated charge/area/sec = $0.05\times10^6\times30\times10^3\times1.6\times10^{-19}$ C Hz/cm^2 = 2.4×10^{-10} C Hz/cm^2
Accumulated charge/area/year = accumulated charge$\times365\times24\times60\times60 \approx$ 7.6 mC/cm^2/year

- Uniformity in performance
- Gain variation of the chamber due to the external radiation
- Long-term stability of operation
- Discharge probability
- Variation of efficiency with different irradiation rates

The efficiency variation of the GEM chamber as a function of irradiation rates has already been studied and reported in Ref. [2]. In this thesis, the detailed results of the investigations on the effect of ambient parameters on the performance of the GEM chamber, uniformity in performance, long-term operation, rate induced gain variation and discharge probability of triple GEM chamber prototypes are included.

4.2 R&D on triple GEM chambers

To establish the fact that GEM detectors can be used in the harsh radiation environment, an R&D program for the study of the radiation-induced effects on triple GEM chambers has been undertaken in the detector laboratory at Bose Institute. This study aims to understand the possible effects on the performance of the chamber under continuous high irradiation. The detector characterisation study after assembling the chamber is started by investigating the uniformity in terms of its gain, energy resolution and count rate over the active area of GEM chamber prototypes of dimension 10 cm $\times$ 10 cm. The long-term stability is also studied with different Argon based gas mixtures. The effect of dielectric charging-up due to the external irradiation is also investigated for triple GEM chambers. To test whether the GEM chambers can withstand the high particle densities at high-rate experiments, the spark probability of a SM triple GEM chamber is tested at the CERN SPS/H4 beam-line facility with pion beam of momentum 150 GeV/c and also for the shower environment.

The R&D program is initiated with the characterisation of a 10 cm × 10 cm Double Mask (DM) triple GEM detector. For that chamber, the research includes the measurement of gain, energy resolution, the study of their variation with temperature and pressure as well as the long-term stability, uniformity of performance and study of charging-up effects.

As in the CBM experiment, large size GEM chambers will be used and for that, since the only option is SM GEM detectors, all the above mentioned studies are also performed on SM GEM detectors. In addition, the spark probability is also measured for the SM GEM chamber in a test beam at CERN SPS.

4.2.1 Fabrication steps of a triple GEM chamber

The GEM foils obtained from CERN are first stretched using the thermal stretching method. The uniform stretching of the GEM foils is one of the important points to be kept in mind while fabricating the detectors. Non-uniform stretching will alter the electric fields between the GEM layers and that will affect the performance of the chamber. Therefore, a uniform stretching of the GEM foils is an essential criterion for obtaining a uniform performance of the chamber. In the thermal stretching method, the GEM foil is placed between two acrylic jigs and the jigs are placed inside an oven. The acrylic jigs and Kapton of the GEM foils then expand according to their respective thermal expansion coefficients and as a result, the GEM foils get stretched. Once the GEM foils are thermally expanded the G-10 frames, also obtained from CERN are glued from top and bottom sides of the foil. The width of the G-10 frame is 1 cm and the thickness is 0.5 mm. The limitation of the stretching technique, using the thermal method, is that it can only be used for small area GEM foils. For large area GEM foils, it is difficult to have an oven to accommodate the foils. Another technique called the NS2 involves the stretching of the foils mechanically by using inner frames and screws passing through the frames. The screws

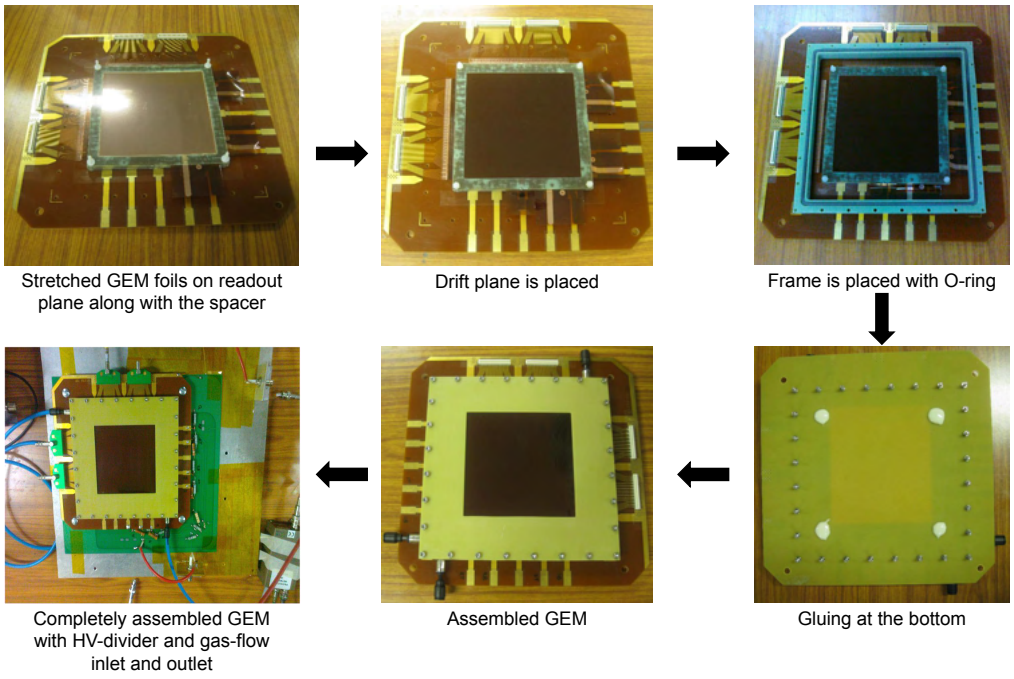

Figure 4.1: Fabrication steps of triple GEM chambers.

are tightened to provide the required stretching of the GEM foils. Compared to the thermal technique, the NS2 technique is faster, easier and can be done in a controlled way [3]. The GEM foils used for the fabrication of the GEM chambers discussed in this thesis, are stretched using the thermal stretching technique at CERN.

On the readout plane firstly four plastic screws are placed as the pillars to make the GEM stack. The stretched GEM foils are arranged with the help of the circular spacer each of thickness 0.5 mm to maintain the required gaps between the respective GEM foils. The drift gap is kept fixed at 3 mm, the transfer and induction gaps are kept fixed at 2 mm. At first the third GEM foil is placed on the readout plane. To keep a 2 mm induction gap, i.e. the gap between the readout and the third GEM foil, three circular spacers are placed in each pillar as a 0.5 mm G-10 frame is already attached with the foil. On top of that, second and first GEM foils are placed using proper number of circular spacers. After placing all the GEM foils along with the spacers on the readout board,

the drift plane is inserted on top of the 1^{st} GEM foil. The drift plane is made with copper cladded on one side of the Kapton foil. The copper side faces the first GEM layer. After that, two 1 cm thick G-10 frame of width 1 cm are placed along with the O-ring for the gas tightness. The outer cover plane is placed on top of the G-10 frame and tightened using the screw and nut system, as shown the in Fig. 4.1. After that, the gas pipes (PU tubes) are connected at the inlet and the outlet of the chamber for gas circulation. Finally, the resistor chain, used for biasing the GEM chamber, is shouldered on the readout PCB board. The steps of GEM fabrication are shown in Fig. 4.1.

4.3 Characterisation of triple GEM chambers

The basic characteristics study of a triple GEM detector is carried out using a Fe^{55} X-ray source of energy 5.9 keV and activity $\sim$ 20 mCi with Ar/CO_2 gas mixtures in different volume ratios and operated just above the atmospheric pressure. The image of the GEM chamber under testing at the laboratory is shown in Fig. 4.2.

The schematic of the powering scheme of the SM triple GEM chamber using a voltage divider chain is shown in Fig. 4.3. In the case of the DM triple GEM chamber, the additional High Voltage (HV) filter is not used between the HV line and resistive chain. The drift, transfer and induction gaps of the chambers are kept at 3 mm, 2 mm and 2 mm respectively. 10 MΩ protection resistors are connected to the top of each of the GEM foils and also to the drift plane. The readout of the DM triple GEM chamber is made up of nine pads of dimension 9 mm $\times$ 9 mm each. The signals from all the pads of the chamber are summed up using a sum-up board and then taken for further signal processing.

In the case of the SM GEM chamber, the readout is an XY printed board (256 X & 256 Y tracks). Each XY track is connected to two 128 pin connectors. However, for the work presented in this thesis, an individual track readout is not used. Instead, a sum-up board (provided by CERN) is used for each 128

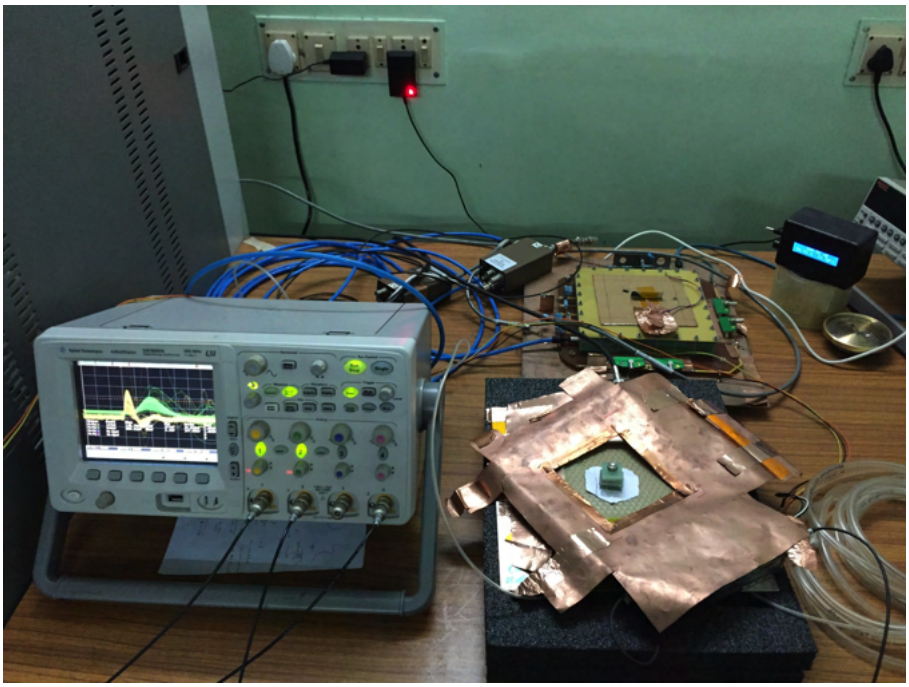

Figure 4.2: Triple GEM chamber under testing with Fe^{55} X-ray source.

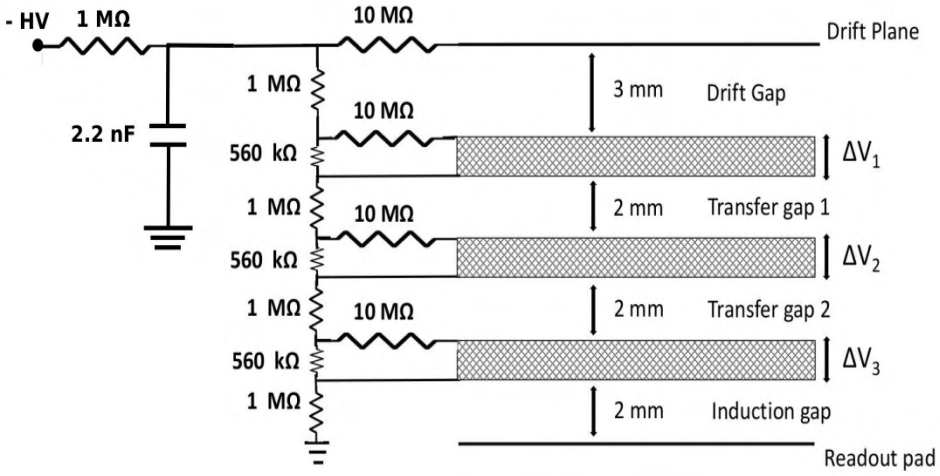

Figure 4.3: Schematic of the voltage divider network in the SM triple GEM prototype.

pin connector. A total of 4 sum-up boards are used in the SM GEM prototype. The signal from one of the sum-up boards is used for further signal processing. The schematic of the electronic setup for signal counting and storing the X-ray spectra are shown in Fig. 4.4. Negative HV is applied to the drift using the filter. The output from the GEM chamber is fed to a charge sensitive preamplifier

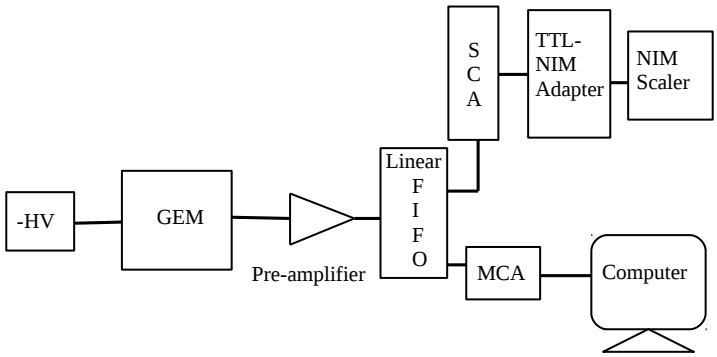

Figure 4.4: Schematic of the electronic setup.

(VV50-2) having a gain of 2 mV/fC and shaping time of 300 ns [4]. The output signal from the preamplifier is fed to a linear Fan-in-Fan-out module (linear FIFO). This module creates identical copies of the input analog signal. One analog signal from the output of linear FIFO is put to a Single Channel Analyser (SCA) which is operated in the integral mode. The lower level in the SCA is used as the threshold for the signal. The discriminated signal from the SCA, which is TTL [2] in nature, is put into a TTL-NIM adapter and the NIM scaler is used to count the output NIM signal [3]. The Fe^{55} energy spectra are stored in computer by feeding another output of the linear FIFO to a Multi-Channel Analyser (MCA).

The MCA is calibrated initially with known pulses and the pulse height and the MCA channel number are related by the following relation:

$$Pulse\ height\ (in\ V) = MCA\ channel\ no \times 0.0014\ + 0.1428 \tag{4.1}$$

In Fig. 4.5, the typical Fe^{55} spectrum is shown for $\Delta V \sim 410$ V across each of the SM GEM foils. The corresponding drift field, transfer fields and induction field are ~ 2.4 kV/cm, ~ 3.7 kV/cm and ~ 3.7 kV/cm respectively. The large peak, known as the main peak, is due to the full energy deposition of the 5.9 keV

[2]TTL is an acronym for Transistor Transistor Logic. A TTL signal has the following definition of a digital "1" and a digital "0": When a signal voltage is between 1.5 V and 5 V, it's a digital "1". When a signal voltage is between 0 V and 0.7 V, it's a digital "0".

[3]NIM is an acronym for Nuclear Instrument Modules. A NIM signal has the following definition of a digital "1" and a digital "0": When a signal voltage is between -0.8 V and -1 V, it's a digital "1". When a signal voltage is exactly 0 V, it's a digital "0".

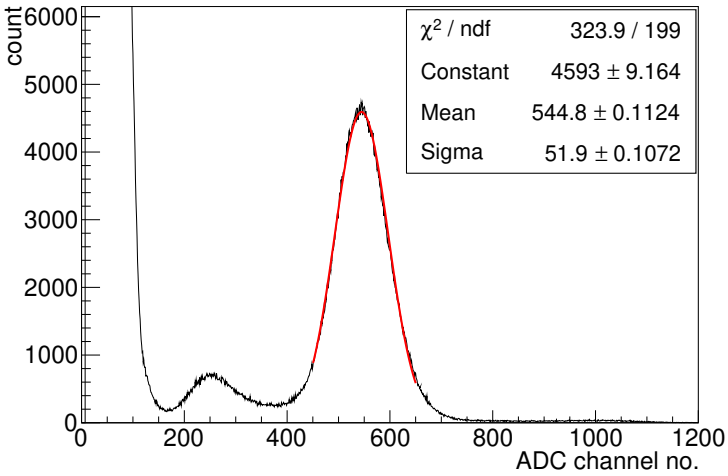

Figure 4.5: Typical Fe^{55} spectra obtained for $\Delta V \sim 410$ V across each of the SM GEM foils. The corresponding drift field, transfer fields and induction field are ~ 2.4 kV/cm, ~ 3.7 kV/cm and ~ 3.7 kV/cm respectively.

X-ray in the 3 mm drift volume of the chamber. There is a finite probability that the 5.9 keV X-ray knocks an electron from the K-shell of the Argon atom via the photoelectric effect. The vacancy of the K-shell is filled by an electron coming from the higher shell and $\sim$ 3 keV X-ray is emitted as a result of the rearrangement of the electrons. If this X-ray emits the detector volume then a peak at $\sim$ (5.9-3.0) keV = 2.9 keV is visible. The smaller peak, as shown in Fig. 4.5, is known as the escape peak. The larger peak behind the escape peak is the noise peak and it is visible near to 0 channel and well separated from the escape peak.

The gain of the detector is calculated in the following way [5]. The 5.9 keV peak of the Fe^{55} X-ray spectrum is fitted with a Gaussian distribution. The mean value of the fit is then used to calculate the total output charge, using the gain of the preamplifier and the calibration factor (CF) (Eqn. 4.1) of the MCA. The gain of the chamber is defined as,

$$gain = \frac{Output\ charge}{Input\ charge} = \frac{((mean \times CF)\ /\ 2\ mV\ )fC}{No.\ of\ primary\ electrons\ \times\ e\ C} \tag{4.2}$$

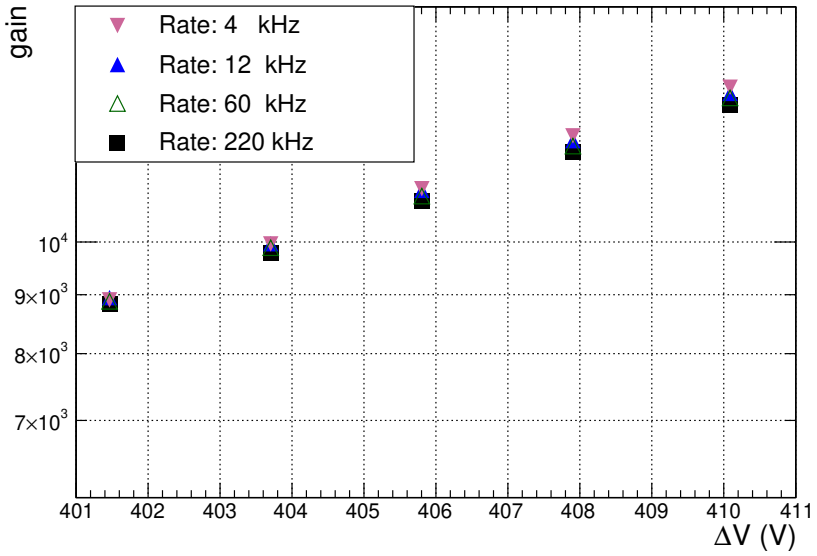

Figure 4.6: Gain of the SM triple GEM detector prototype as a function of the ΔV across each of the GEM foils and for different irradiation rates. Error bars are smaller than the marker size.

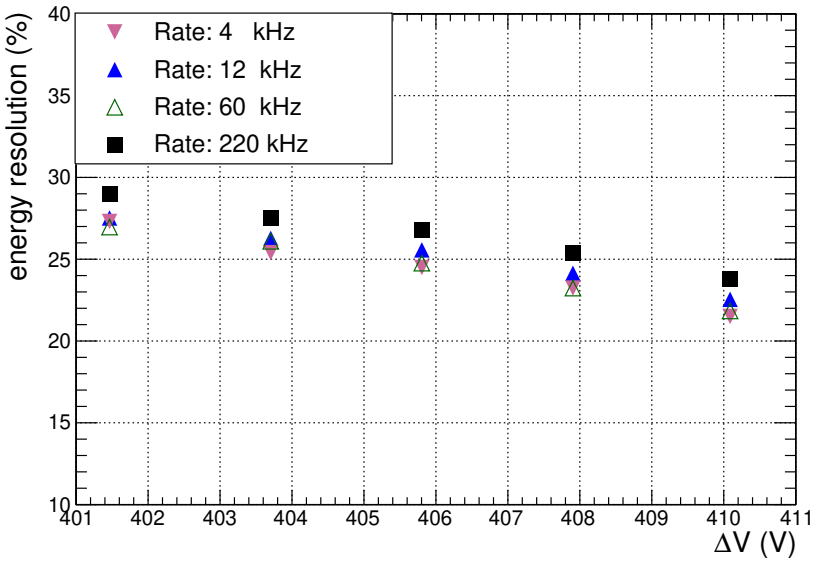

Figure 4.7: Energy resolution of the SM triple GEM detector prototype as a function of the ΔV across each of the GEM foils and for different irradiation rates. Error bars are smaller than the marker size.

where the mean is obtained from the Gaussian fitting of the 5.9 keV main peak, e being the electronic charge. The average number of primary electrons

produced in the 3 mm drift gap is 212 in case of full energy deposition of the 5.9 keV X-ray for an Ar/CO_2 gas mixture in 70/30 volume ratio [4]. The energy resolution of the chamber is defined as,

$$energy\ resolution = \frac{sigma\ \times\ 2.355}{mean}\ \times\ 100\ \% \tag{4.3}$$

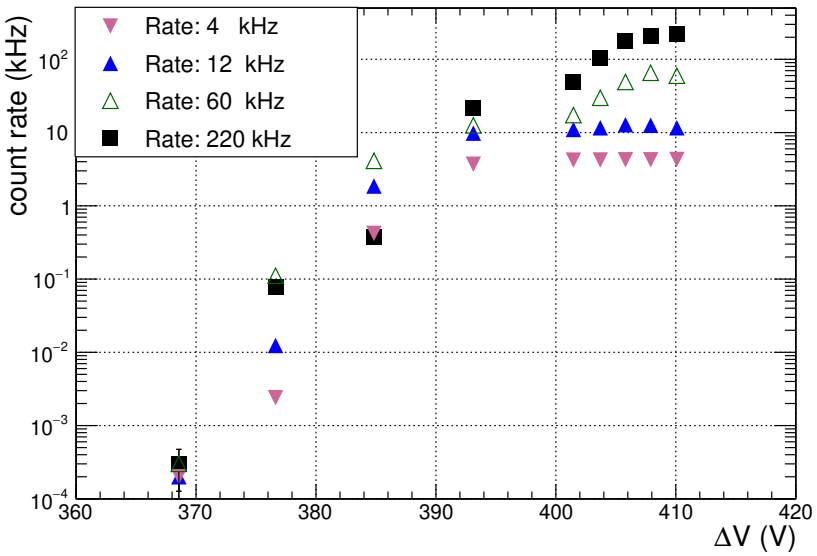

Figure 4.8: Count rate of the SM triple GEM detector prototype as a function of the ΔV across each of the GEM foils and for different irradiation rates.

where *sigma* is obtained from a Gaussian fitting of the 5.9 keV main peak. In Fig. 4.6, the variation of the gain of the SM triple GEM chamber for different irradiation rates is shown as a function of the voltage (ΔV) applied across each of the GEM foils. The different irradiation rates are set using collimators. It is observed that due to the increasing potential drop across the protection resistances with increasing irradiation rates, the gain of the chamber is a bit lower

[4]The number of primary electrons in gas mixture is calculated in the following way;
Number of primary electrons $N_0 = E_\gamma(\frac{\%Ar}{W_{Ar}} + \frac{\%CO_2}{W_{CO_2}})$,
where E_γ is the energy of the photon (5.9 keV X-ray for Fe^{55} source), W_{Ar} ($\approx$ 26 eV) and W_{CO_2} ($\approx$ 33 eV) are the mean energy required for the creation of electron-ion pair in Ar and CO_2 respectively.
Therefore, in Ar/CO_2: 70/30, $N_0 \approx 212$.
Ar/CO_2: 80/20 $N_0 \approx 217$.
Ar/CO_2: 90/10 $N_0 \approx 222$.

at the highest rate as compared with the lowest rate. The energy resolution as a function of ΔV is shown in Fig. 4.7. As expected, with increasing the biasing voltage, the gain of the chamber increases as a result, the energy resolution of the chamber improves. The count rate from the scaler as a function of ΔV for different irradiation rates is shown in Fig. 4.8. A plateau in the counting rate is observed from a ΔV of 405 V onwards. The plateau region in the count rate plot gives an idea of the operating ΔV at which the detector gives the optimum efficiency because a radioactive source is used for this measurement which gives a constant rate.

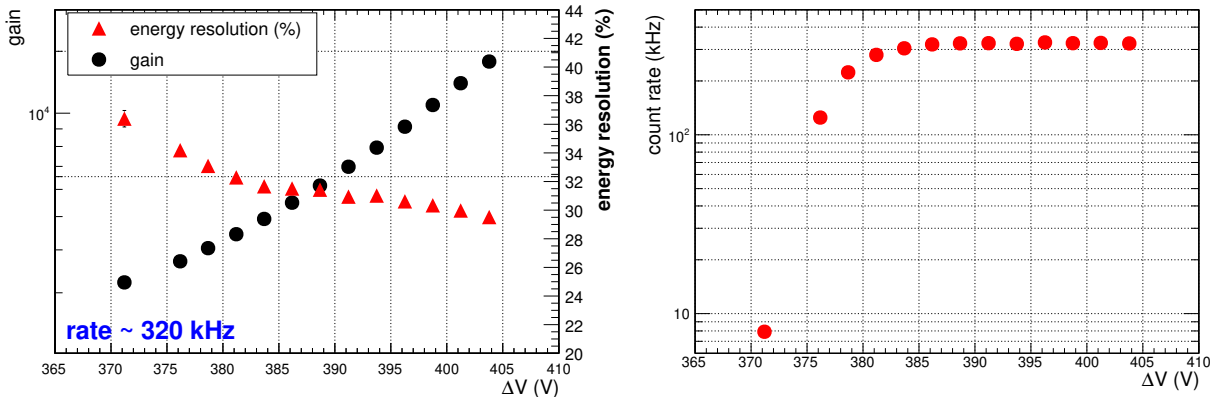

Figure 4.9: Variation of gain, energy resolution (left) and count rate (right) as a function of the ΔV across each of the GEM foils of a DM triple GEM chamber. Error bars are smaller than the marker size.

Similar studies are also performed for the DM triple GEM chamber with Ar/CO_2 gas mixture in 70/30 volume ratio. The variation of gain, energy resolution and counting rate is shown as a function of the potential difference applied across each of the GEM foils in Fig. 4.9. The gain of the chamber increases exponentially with the applied voltage and the energy resolution of the chamber improves with increasing gain. A plateau in the count rate plot is also observed for the DM GEM chamber for ΔV of 385 V onwards and the saturated count rate is found to be $\sim$ 320 kHz.

4.4 Efficiency and time resolution measurement of the triple GEM chamber

The efficiency of the SM triple GEM chamber is measured as a function of the applied voltage using cosmic ray muons and with an Ar/CO_2 gas mixture in the 70/30 volume ratio. Three scintillation detectors, having dimensions 20 cm $\times$ 20 cm (SC1), 2 cm $\times$ 10 cm (SC2) and 10 cm $\times$ 10 cm (SC3) are used to generate the cosmic muon trigger. SC2 and SC3 are placed on top of the detector and SC1 is placed at the bottom. The coincidence signal from the three scintillators is referred as the three-fold signal (3F). The signal from the GEM chamber is taken in coincidence with the 3F signal and this is referred as the four-fold signal (4F). The ratio of the 4F signal to the 3F signal is defined as the efficiency of the GEM chamber. The detector setup in the laboratory (top) and the schematic of the electronics setup (bottom) for the efficiency measurement of SM triple GEM chamber is shown respectively in Fig. 4.10. The scintillators are operated at a biasing voltage of +1550 V. The threshold to the Leading Edge Discriminator (LED) are set to - 10 mV for the scintillators. The output of the LED is fed to an AND gate for producing the 3F trigger logic. The coincidence signal from all the three scintillators are fed to a dual timer module. The dual timer module helps to stretch the 3F signal so that the GEM signal comes in coincidence with the 3F signal. The width of the 3F signal is kept at ~ 4 μs. The output signal from the GEM is first fed to a preamplifier. The output of the preamplifier is fed to the Timing Single Channel Amplifier (TSCA) to set the lower level threshold to the signal. The output of the TSCA is fed to a NIM-TTL adapter to convert the TTL signal into a NIM signal. After that, the logical AND operation is performed with the 3F signal and the GEM signal to get the 4F signal. The 3F and 4F signals are counted using a NIM scaler. The threshold to the TSCA is set at 0.15 V. The signal from the GEM chamber is found to be delayed, as compared to the scintillator signal and that is mainly due to the finite shaping time of the preamplifier and TSCA. That is why the

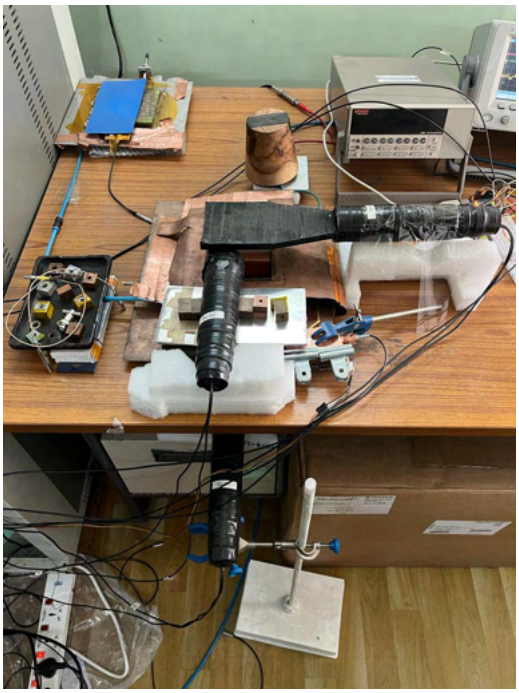

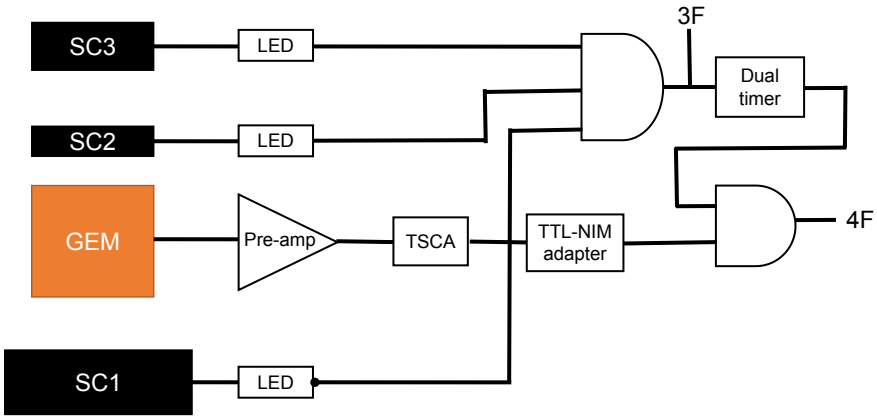

Figure 4.10: Top: Setup for the efficiency measurement of SM triple GEM chamber. Bottom: schematic of the electronic setup for the efficiency measurement of SM triple GEM chamber.

3F signal from the scintillators is stretched before performing the logical AND operation with the GEM signal. The typical 3F signal and the discriminated GEM signal (after TTL-NIM adapter), as observed in the oscilloscope, are shown in Fig. 4.11. The energy spectra for cosmic ray are also stored using MCA. In this case the MCA is operated in gated mode. The gate is generated

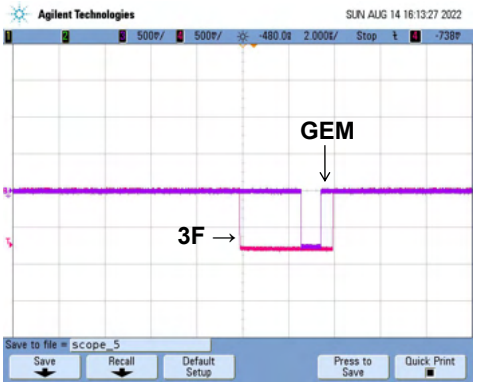

Figure 4.11: 3F signal (pink) and discriminated GEM signal after TTL-NIM adapter (magenta) as observed in the oscilloscope. The time scale is set at 2 μs/div, the voltage scale is set at 500 mV/div and the load is 50 Ω.

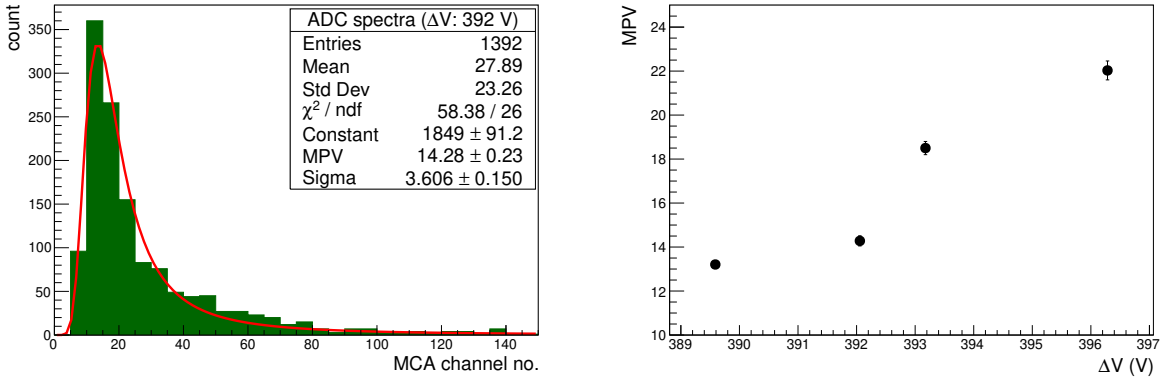

Figure 4.12: Left: A typical cosmic muon spectrum from the GEM chamber at a ΔV of 392 V across each of the GEM foils. The spectrum is fitted with a Landau distribution. Right: The variation of the MPV as a function of the applied voltage (ΔV) across the GEM foil.

with the 3F scintillator signal having a width of 4 μs. Fig. 4.12 (left) shows a typical spectrum of cosmic ray muons from the GEM chamber. The spectrum of the cosmic ray muons is fitted with Landau distribution and the variation of the Most probable value (MPV) of the fitted distribution is plotted as functions of ΔV across each GEM foil and shown in Fig. 4.12 (right). The variation of the efficiency, defined as the ratio of 4F and 3F of the chamber, is studied as a function of the ΔV across each of the GEM foils. In Fig. 4.13 shows the

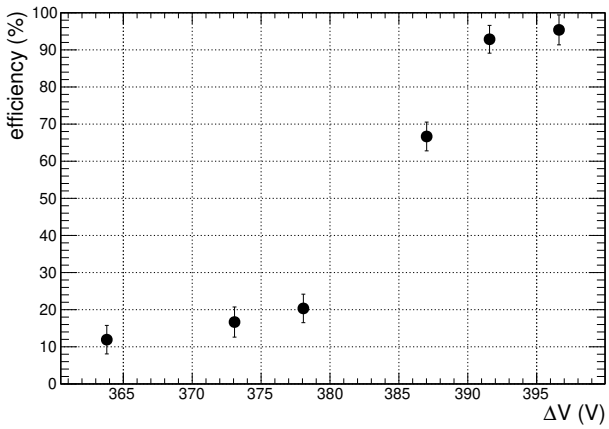

Figure 4.13: Variation of the efficiency (4F/3F) of the chamber as functions of ΔV across each GEM foil.

variation of efficiency as a function of ΔV. An efficiency value greater than 90% is obtained for ΔV of 390 V onwards.

In order to measure the time resolution of the chamber, the Time to Amplitude Converter (TAC) module is used. To accumulate sufficient statistics at relatively smaller time duration, a gamma source (^{137}Cs) of energy 661 keV is used to study the time resolution of the chamber. The detector arrangement (left) and the schematic of the electronics setup (right) to measure the time resolution of the SM triple GEM chamber are shown in Fig. 4.14. The two-fold (2F)

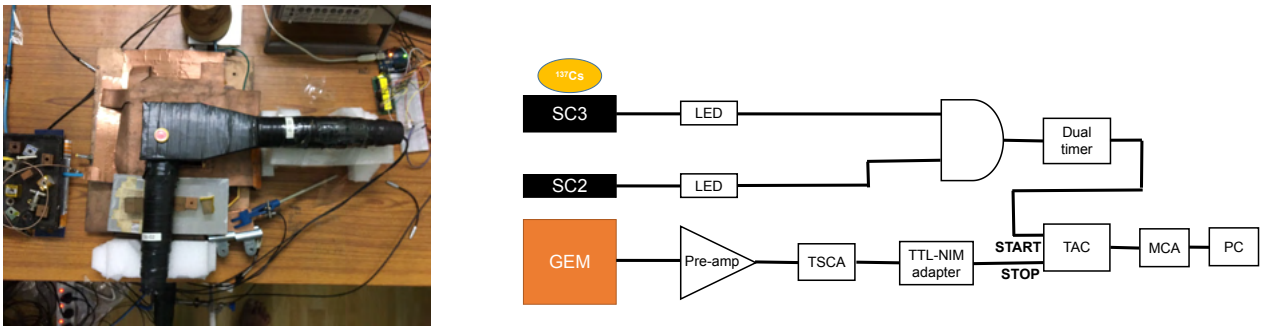

Figure 4.14: Left: Detector arrangement for the time resolution measurement of SM triple GEM chamber. Right: Schematic of the electronics setup for the time resolution measurement of SM triple GEM chamber. The ^{137}Cs source is placed on top of scintillator SC3.

signal from SC3 and SC2 is used as the start signal and the GEM signal is

taken as the stop signal for the TAC module. The output of the TAC module is stored in the desktop using an MCA. The typical start signal, stop signal and output of the TAC module are shown in Fig. 4.15. The threshold to the LED

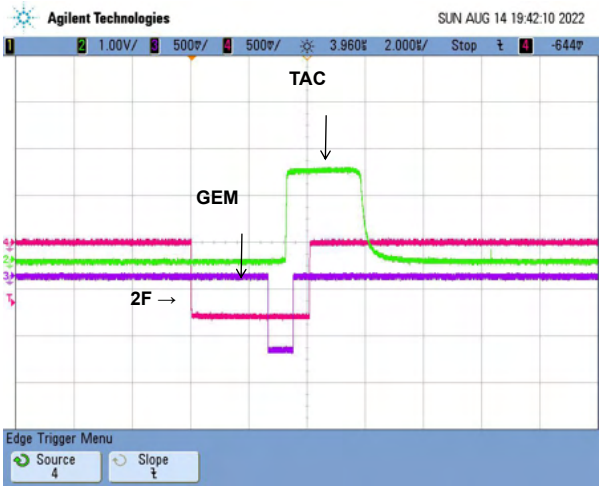

Figure 4.15: 2F signal (pink), discriminated GEM signal after TTL-NIM adapter (magenta) and TAC output (green) as observed in the oscilloscope. The time scale is set at 2 μs/div and the voltage scale is set at 500 mV/div for 2F and GEM signal, 1.0 V/div for the TAC output and the load is 50 Ω.

for the scintillators is kept at -10 mV while the threshold to the TSCA for GEM chamber is kept at 0.25 V. A typical timing spectrum at a ΔV of 390 V across each of the GEM foils is shown in Fig. 4.16. The timing spectrum is fitted with a Gaussian distribution. The mean of the fitted spectrum gives the time difference between the start and stop signal and from the sigma (σ) the time resolution of the chamber (σ_{GEM}) is extracted subtracting the combination of scintillators [5] using the formula;

$$\begin{aligned} \sigma^2 &= \sigma^2_{GEM} + \sigma^2_{SC2} + \sigma^2_{SC3} \\ \sigma_{GEM} &= \sqrt{\sigma^2 - \sigma^2_{SC2} - \sigma^2_{SC3}} \end{aligned} \tag{4.4}$$

The variation of the mean and the sigma of the fitted spectra is investigated by varying the voltage across the GEM foils. In Fig. 4.17, the variation of the

[5]The time resolution of the scintillators SC2 (σ_{SC2}) and SC3 (σ_{SC3}) are 0.38$\pm$0.04 ns and 0.56$\pm$0.04 ns respectively.

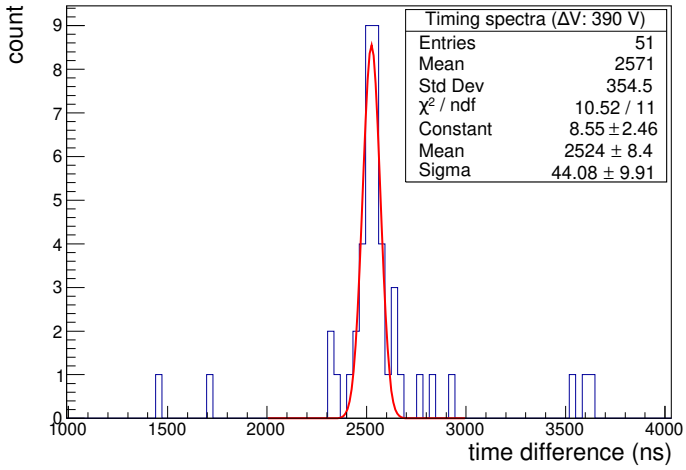

Figure 4.16: Typical timing spectrum with 2F scintillator signal as the start signal and GEM signal as the stop signal. The timing spectrum is fitted with a Gaussian distribution.

time difference between the start and stop signal (left) and of the respective σ_{GEM} values (right) are plotted as a function of ΔV across each GEM foil. It is

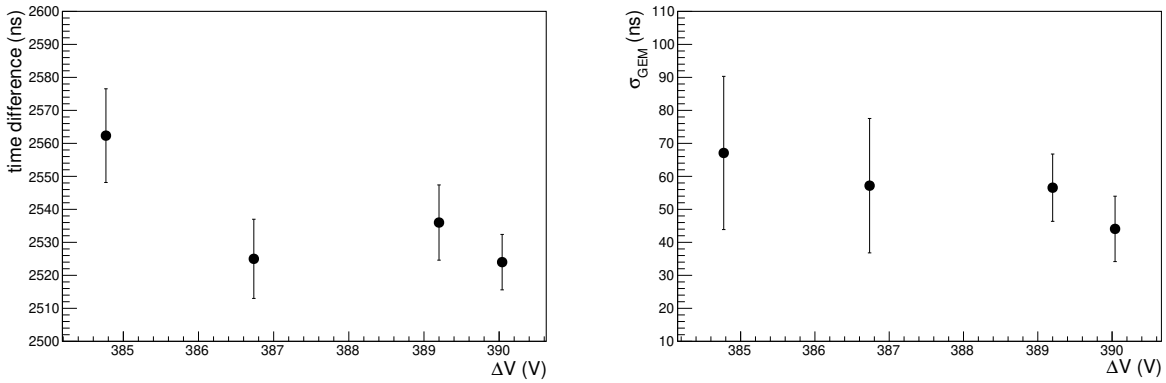

Figure 4.17: Variation of the time difference between the start and stop signal (left) and of the respective σ_{GEM} values (right) as a function of ΔV across each GEM foil.

observed that with increasing voltage across the GEM foil, the time difference between the start and stop signal decreases. That is mainly due to the increase of voltage of the GEM chamber which results in a faster signal formation. The best time resolution value obtained from this study is 44.08 $\pm$ 9.91 ns at a ΔV of 390 V across each GEM foil. The time resolution of the real size GEM

chambers during the beam test is found to be $\sim$ 19 ($\pm$ 5) ns [6] in a nucleus-nucleus collision system. The probable reason behind observing such relatively larger time resolution values from the timing spectra is due to the time-walk effect. As TSCA is used in integral mode to discriminate the signals, therefore, depending on the pulse height, the signal will cross the threshold at different instances and thus contribute to the σ of the timing spectrum.

4.5 Effect of temperature, pressure and humidity on gain and energy resolution

The gain of any gas-filled detector depends on the temperature [T (in K) = t + 273, t in °C] and pressure (p in atm) [6]. It is well known that the gain of any gaseous detector increases with increasing temperature and decreases with increasing pressure, or in other words, the gain of the chamber is found to be positively correlated with the T/p variation [7]. As it is expected that with increasing gain, the energy resolution of the chamber improves, therefore, the energy resolution is also expected to be anti-correlated with T/p variations. In Fig. 4.18, the typical variation of the gain, energy resolution, ambient temperature, pressure and relative humidity are shown as a function of time for the SM triple GEM chamber, operated with an Ar/CO_2 gas mixture in a 70/30 volume ratio. The voltage across each of the GEM foils is kept at $\sim$ 405 V and the chamber is irradiated continuously with Fe^{55} X-rays at a rate of $\sim$ 2 kHz/mm^2. The dependence of the gain and energy resolution with T/p can be expressed as,

$$gain(T/p) \;=\; A\ exp(BT/p) \tag{4.5}$$

$$energy\ resolution(T/p) \;=\; A^{'}\ exp(B'T/p) \tag{4.6}$$

[6]The gain (G) of gaseous detectors can be expressed as G = $e^{\alpha x}$, where α is known as the first Townsend coefficient and x is the path length. Here α represents the inverse of the mean free path for ionization. Now the mean free path for ionization changes with changing temperature and pressure. With increasing temperature or decreasing pressure, the mean free path decreases and as a result, the Townsend coefficient increases and thus the gain of the chamber increases. Therefore, it is expected that the gain of the chamber should be related to T and p as G $\propto$ $e^{T/p}$.

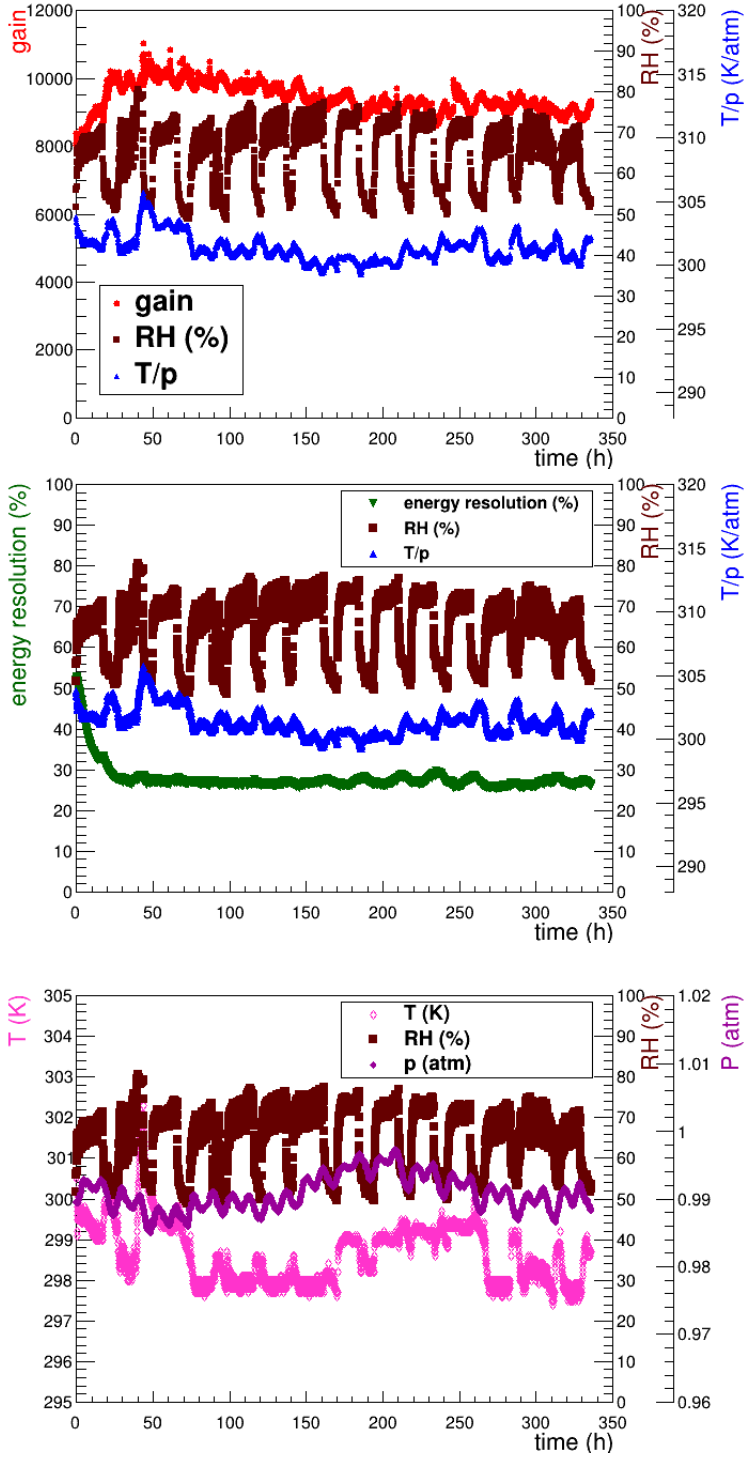

Figure 4.18: Variation of gain (top), energy resolution (middle), T, p and RH (bottom) as a function of time. Error bars are smaller than the marker size.

where A, B, A$'$ and B$'$ are the parameters to be determined from the correlation plot. The correlation of gain and energy resolution with the temperature by pressure (T/p) ratio are shown in Fig. 4.19. The fit parameters from the gain correlation plot are found to be A=0.22 $\pm$ 0.01 and B=0.0356 $\pm$ 0.0001 atm/K. The parameters obtained from the correlation of energy resolution with T/p are A$'$=42.82$\pm$0.24 and B$'$=-0.0016$\pm$0.0001 atm/K.

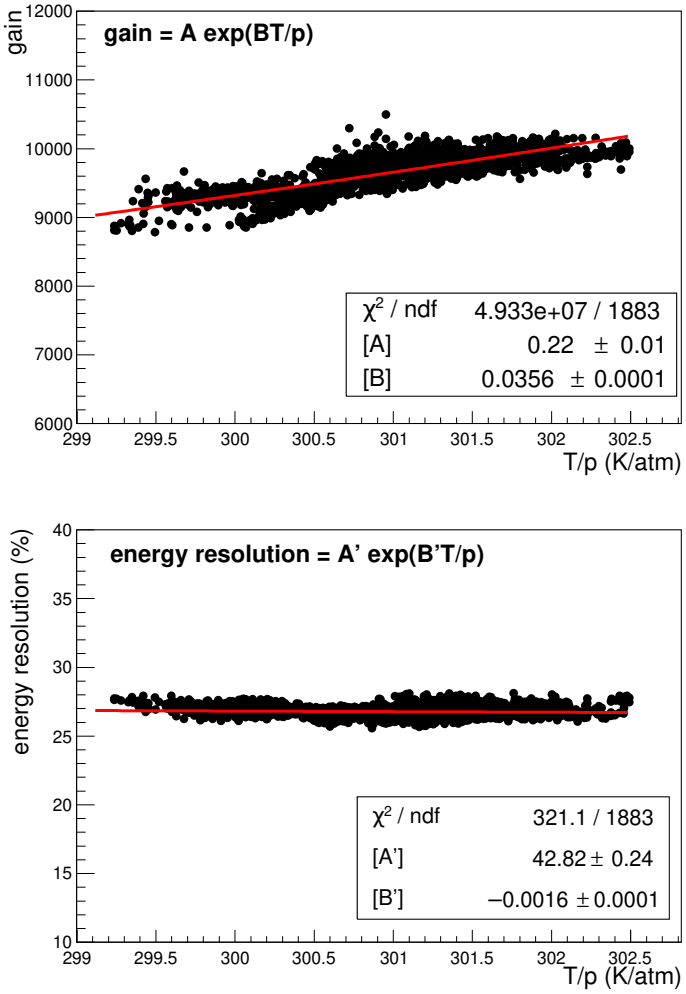

Figure 4.19: Correlation of gain (top) and energy resolution (bottom) with T/p. Error bars are smaller than the marker size.

The gain and energy resolution of the chamber are normalised using the parameters obtained from the correlation curves to eliminate the effects of T/p

variations using the following formula:

$$gain_{normalised} = gain_{measured}/A\ exp(BT/p) \quad (4.7)$$

$$energy\,resolution_{normalised} = energy\,resolution_{measured}/A^{'}\ exp(B^{'}T/p) \quad (4.8)$$

The variation of normalised gain and energy resolution is shown in Fig. 4.20 as a function of the accumulated charge per unit area. The accumulated charge per unit area is calculated using the formula

$$\frac{dq}{dA} = \frac{r \times n \times e \times G \times dt}{dA} \quad (4.9)$$

where r is the rate (in Hz) of the incident radiation falling on an area dA, n is the number of primary electrons produced by full absorption of a single X-ray photon in the drift region, e is the electronic charge (in Coulomb), G is the gain of the chamber and dt is the irradiation time (in second).

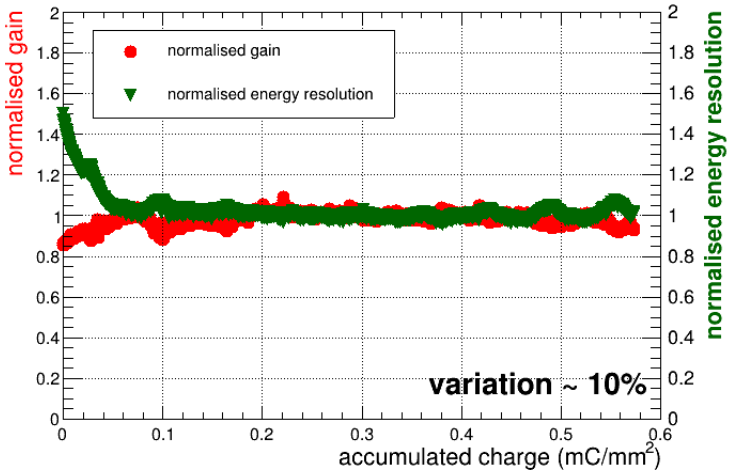

Figure 4.20: Variation of the normalised gain and normalised energy resolution as a function of accumulated charge. The error bars are smaller than the marker size.

The initial decrease in the normalised gain and increase in the normalised energy resolution is due to the charging-up effect of the chamber [8, 9] and will be discussed in more detail in the following sections.

To study the effect of RH on the performance of the chamber, the gain and energy resolution of the chamber, normalised with T/p are plotted as functions

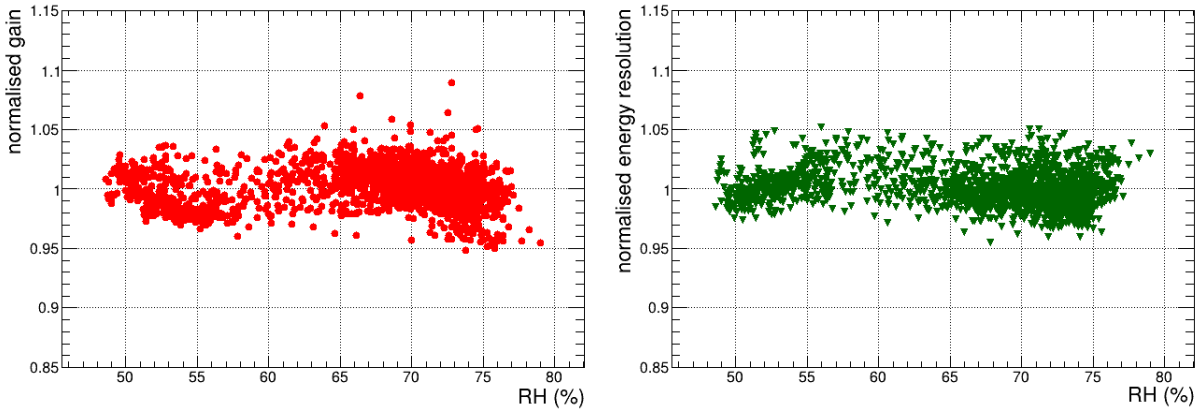

Figure 4.21: Variation of normalised gain (left) and energy resolution (right) as a function of RH.

of RH and shown in Fig. 4.21. No significant correlation is observed between the T/p normalised gain and energy resolution with RH [10, 11].

4.6 Uniformity study of DM triple GEM chambers

A systematic study of the uniformity in gain, energy resolution and count rate over the active area of a 10 cm × 10 cm DM triple GEM detector prototype is carried out using an Fe^{55} X-ray source and with an Ar/CO_2 gas mixture in 70/30 volume ratio and at a constant gas flow rate.

The summed-up signal from all the nine pads (as described in section 4.3) is taken and then fed to a charge sensitive preamplifier having a gain of 2 mV/fC and a shaping time of 300 ns [4]. The electronic setup is the same as discussed in section 4.3. All the measurements are performed within a grid of 5×4 positions in the central part of the chamber. The uniformity study for the DM chamber is carried out at ΔV of 385.9 V across each of the GEM foils. The variation observed in gain, energy resolution and count rate are shown in Fig. 4.22, Fig. 4.23 and Fig. 4.24 respectively. Over the scanned area, a 10 % fluctuation in gain and a 20 % fluctuation in energy resolution and count rate are observed [12]. For some zones, the count rate is found to be as low as 100 kHz. So, for the

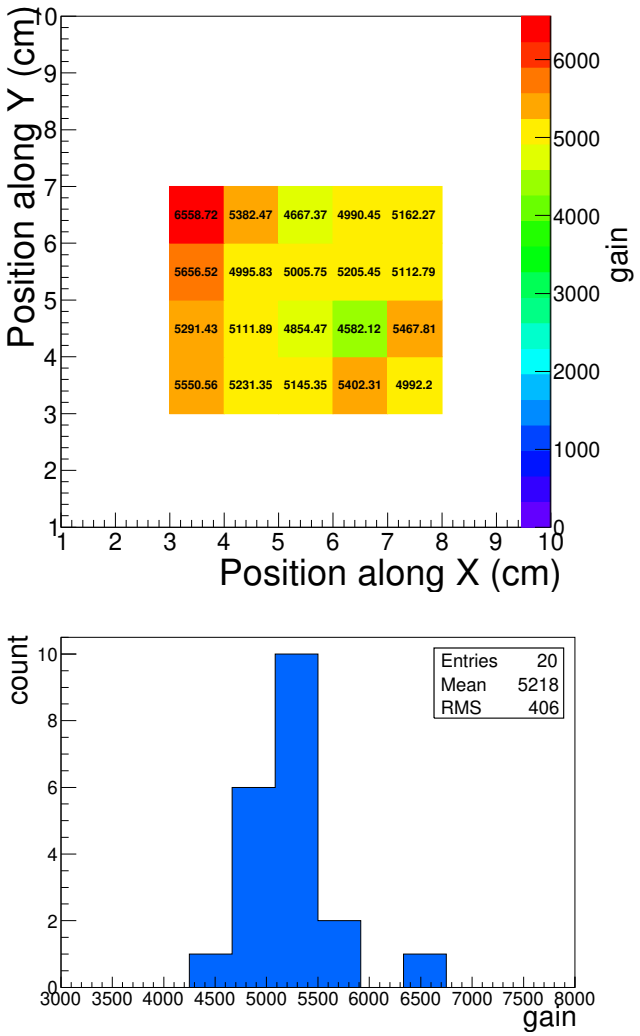

Figure 4.22: Top: Variation in gain over the central part of the DM triple GEM chamber. Bottom: Distribution of the measured gain.

count rate distribution, a lower cut of 150 kHz is used during the analysis. A variation of 20% in gain is also reported for a DM triple GEM chamber of dimension 10 cm $\times$ 10 cm in Ref. [13].

The observed variation in gain and energy resolution could be attributed to the intrinsic inhomogeneity of the GEM geometry and the gap between the respective GEM foils [14].

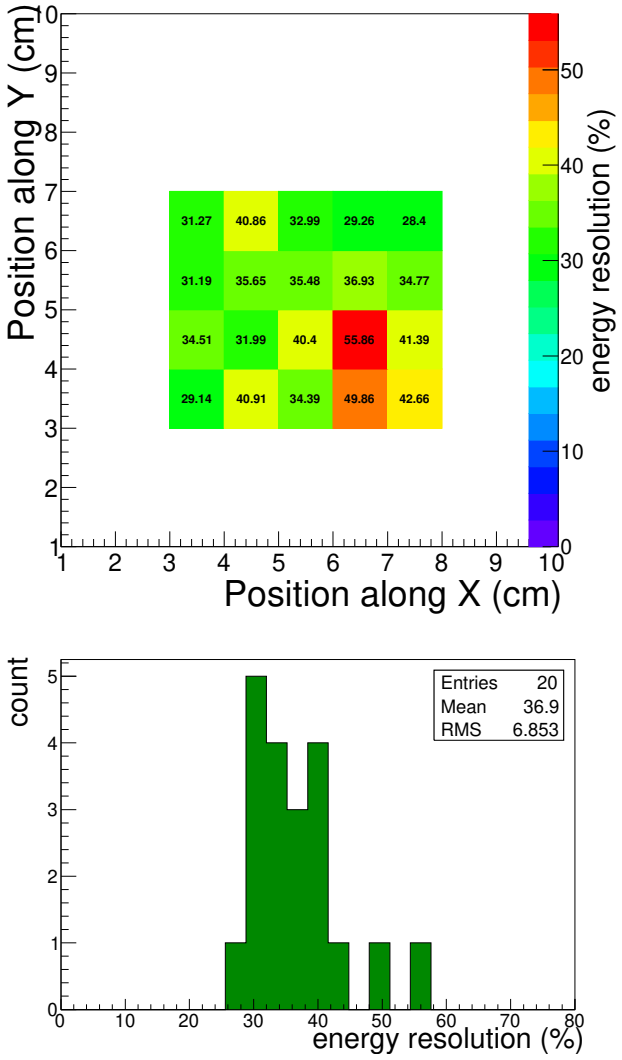

Figure 4.23: Top: Variation in energy resolution over the central part of the DM triple GEM chamber. Bottom: Distribution of the energy resolution.

4.6.1 Charging-up effect in triple GEM chambers

The presence of the Kapton foil inside the active part of the detector changes its behaviour when exposed to external radiation. Due to the high electric field ($\sim$ 80 kV/cm) inside the GEM holes, the incoming electrons get sufficient kinetic energy to start an avalanche of further ionization. Due to the dielectric properties of the polyimide (Kapton), they get polarised by the external electric field. During the multiplication process of the primary charges inside the GEM

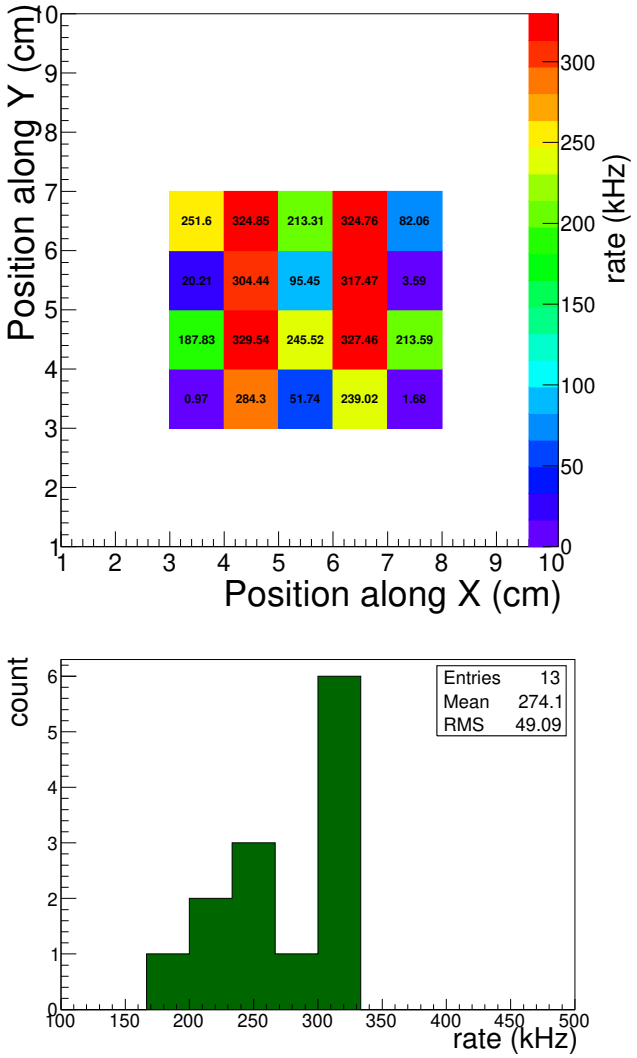

Figure 4.24: Top: Variation in count rate over the central part of the DM triple GEM chamber. Bottom: Distribution of the measured count rate.

hole, the electrons and ions may diffuse to the polyimide surface and due to the polarisation of the polyimide by the external HV, the ions or electrons can be adsorbed on the wall of the Kapton foil. This phenomenon is illustrated in Fig. 4.25. Due to the high resistivity of the Kapton, the charges remain there for a rather long time. As a result of sufficient accumulation of charge on the wall, the electric field configuration inside the GEM hole changes dynamically and this phenomenon is known as the charging up effect. The accumulated charges on the surface of the Kapton foil increase the field inside the GEM holes and

as a result, the gain of the chamber increases with time. Many studies have reported that the charging up effect is responsible for a time-dependent change in gain, which asymptotically reaches a constant value [15, 16, 17, 18].

In this section, a systematic investigation of the charging up process with different irradiation rates in triple GEM detector prototypes built using the DM and SM GEM foils and operated with Ar/CO_2 gas mixture in the 70/30 volume ratio is reported. A strong Fe^{55} source is used to irradiate the chamber as well as to record the 5.9 keV X-ray spectra from the chamber.

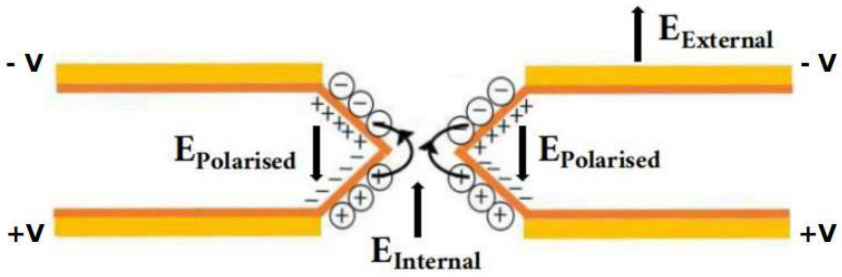

Figure 4.25: Schematic representation of the Charging up effect inside a GEM hole. $E_{Polarised}$ indicates the electric field generated due to the dielectric polarisation. $E_{External}$ indicates the electric field generated due to the external high voltage and $E_{Internal}$ indicates the electric field generated due to the accumulation of the charges on the Kapton wall.

4.6.2 Charging-up study for DM triple GEM chamber

The variation of the gain as a function of time for three different rates of the X-rays, 1 kHz, 10 kHz and 90 kHz respectively along with the ratio of ambient temperature (T) to pressure (p) are shown in the top (a), middle (b) and bottom (c) plot of Fig. 4.26. Using collimators, X-rays of rates 1 kHz, 10 kHz and

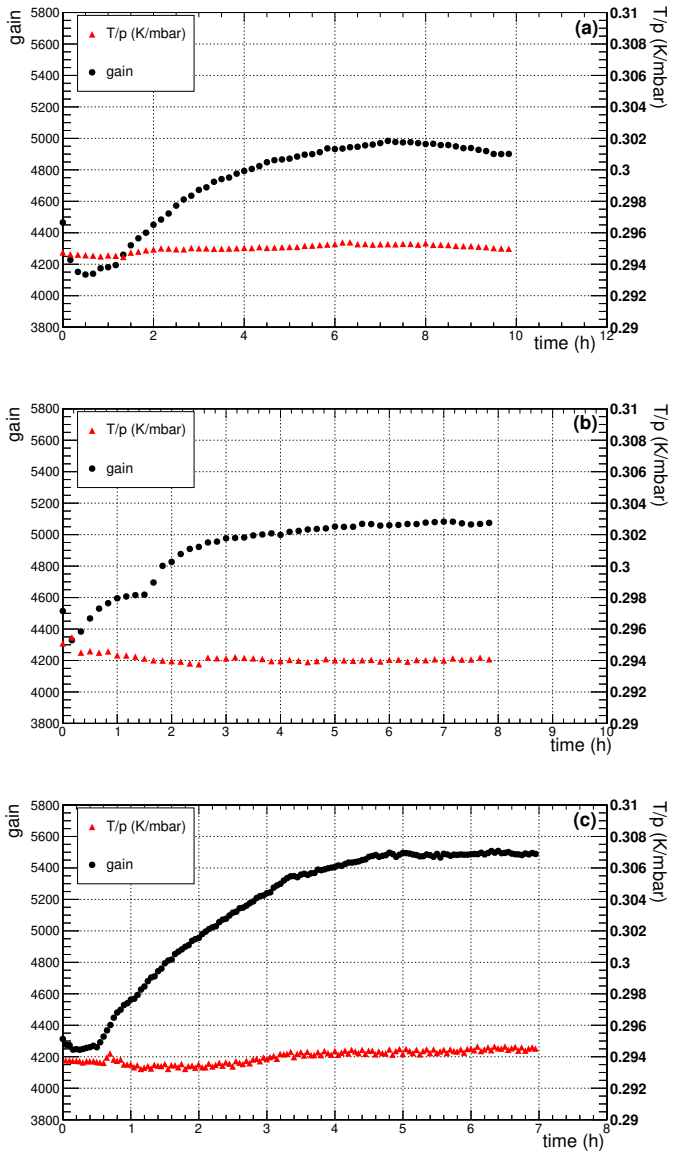

Figure 4.26: Variation of gain and T/p as a function of time. The top (a), middle (b) and bottom (c) plots are for 1 kHz, 10 kHz and 90 kHz X-rays irradiation rates falling on 13 mm^2 (flux: 0.08 kHz/mm^2), 50 mm^2 (flux: 0.2 kHz/mm^2) and 28 mm^2 (flux: 3.2 kHz/mm^2) area of the GEM chamber respectively. All the measurements are carried out at an HV of - 4.2 kV (corresponding to ΔV $\sim$ 390 V across each of the GEM foils) and at three different positions on the active area of the chamber. The corresponding drift, transfer and induction fields are 2.3 kV/cm, 3.5 kV/cm and 3.5 kV/cm respectively. The error bars are smaller than the marker size.

90 kHz are made to incident on 13 mm^2, 50 mm^2 and 28 mm^2 areas of the chamber implying particle fluxes of 0.08 kHz/mm^2, 0.2 kHz/mm^2 and 3.2 kHz/mm^2

respectively. All the measurements are carried out at an HV of - 4.2 kV which corresponds to ΔV $\sim$ 390 V across each of the GEM foils. The corresponding drift, transfer and induction fields are 2.3 kV/cm, 3.5 kV/cm and 3.5 kV/cm respectively.

In all three cases, the data taking starts immediately after the HV is switched ON and the source is placed on the active area of the detector. The energy spectra are stored at an interval of 10 minutes for 1 kHz and 10 kHz rates and 3 minutes for 90 kHz X-ray rates respectively. The same Fe^{55} source is used to irradiate the chamber as well as to obtain the spectra. From Fig. 4.26, it is evident that the gain decreases for the first few minutes and then increases for a few hours of operation and reaches a saturation asymptotically. The decrease in the initial gain is due to the loss of the primary electrons which are stuck on the polarised dielectric (Kapton) surface. Since the polarisation of the dielectric medium itself takes some finite time, whenever the HV and irradiation started simultaneously, an initial decrease in gain is observed. Afterwards, the gain increases sharply for the first few hours due to the lensing effect created by the accumulated charges on the wall of the Kapton foil because this effect increases the electric field strength inside the GEM hole. The absolute gain values after saturation are not the same for all three cases as these measurements are done at different positions of the detector, i.e. the source is placed at different positions of the chamber. The variation in gain over the active area of the particular chamber is discussed in section 4.6 and a variation of 10% (RMS) is reported. For all the measurements, the gain shows a saturation after an initial increase for the first few hours. The gain is normalised further to eliminate the T/p dependence on the gain as discussed in section 4.5. For the T/p normalisation, the saturated gain value obtained after $\sim$6 hours of operation is used where only the T/p effect is dominant on the gain variation. The normalised gain is fitted with an exponential function of the form [19]

$$G = p0(1 - p1e^{(-t/p2)}) \tag{4.10}$$

where G is the normalised gain, p0 & p1 are the constants, t is the measurement time in hours, and p2 is the time constant of the charging-up effect, in analogy with that in the charging up mechanism of any RC network [20].

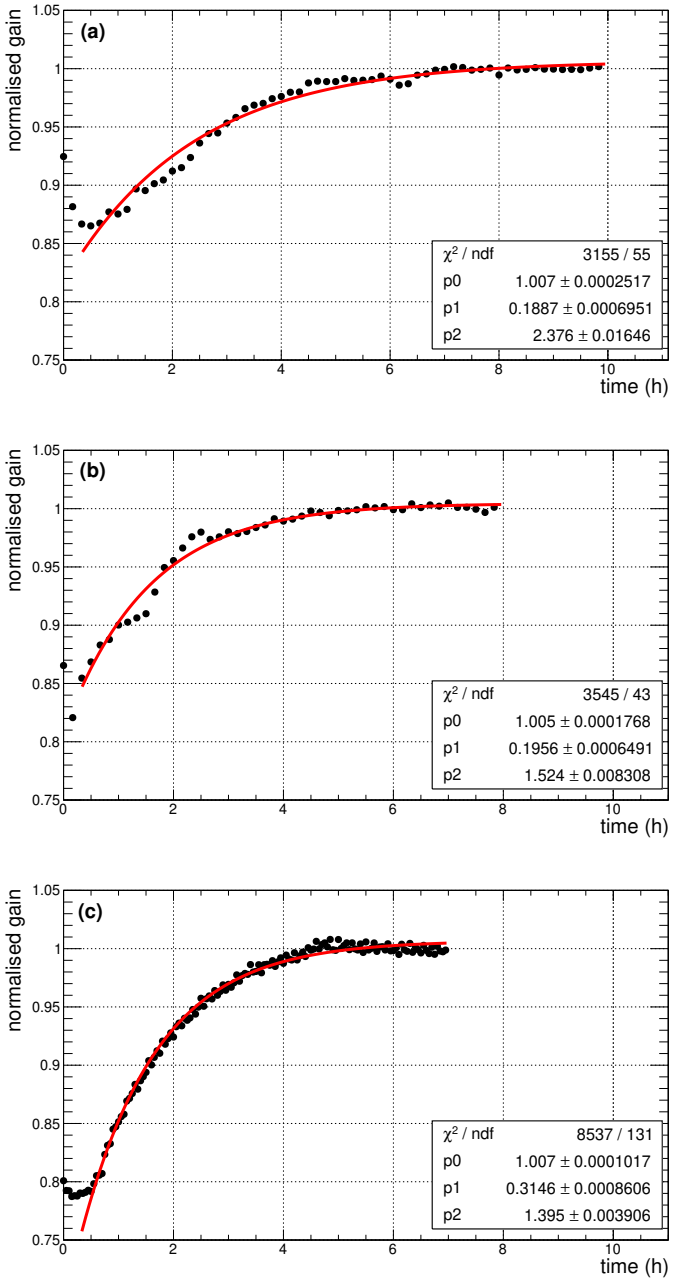

Figure 4.27: Variation of the normalised gain as a function of time. The top (a), middle (b) and bottom (c) plots are for 1 kHz, 10 kHz and 90 kHz X-ray irradiation rates falling on 13 mm^2 (flux: 0.08 kHz/mm^2), 50 mm^2 (flux: 0.2 kHz/mm^2), 28 mm^2 (flux: 3.2 kHz/mm^2) area of the GEM chamber respectively. The error bars are smaller than the marker size.

The fitted normalised gain is shown in Fig. 4.27 for the 1 kHz (top), 10 kHz (middle) and 90 kHz (bottom) X-ray irradiation rates, corresponding to flux of 0.08 kHz/mm^2, 0.2 kHz/mm^2 and 3.2 kHz/mm^2 respectively. For the fit, the first ∼20 minutes are excluded because that includes both the effect of dielectric polarisation and charging up. After that, the charging up effect is dominant and is fitted with Eqn. 4.10 to get an idea about the time constant of the charging up effect. In Fig. 4.26 (b), a small change is visible in the trend of increasing gain from 1-2 hours along the time axis; that is due to the two opposite effects: namely charging-up and T/p variation. The charging-up process will

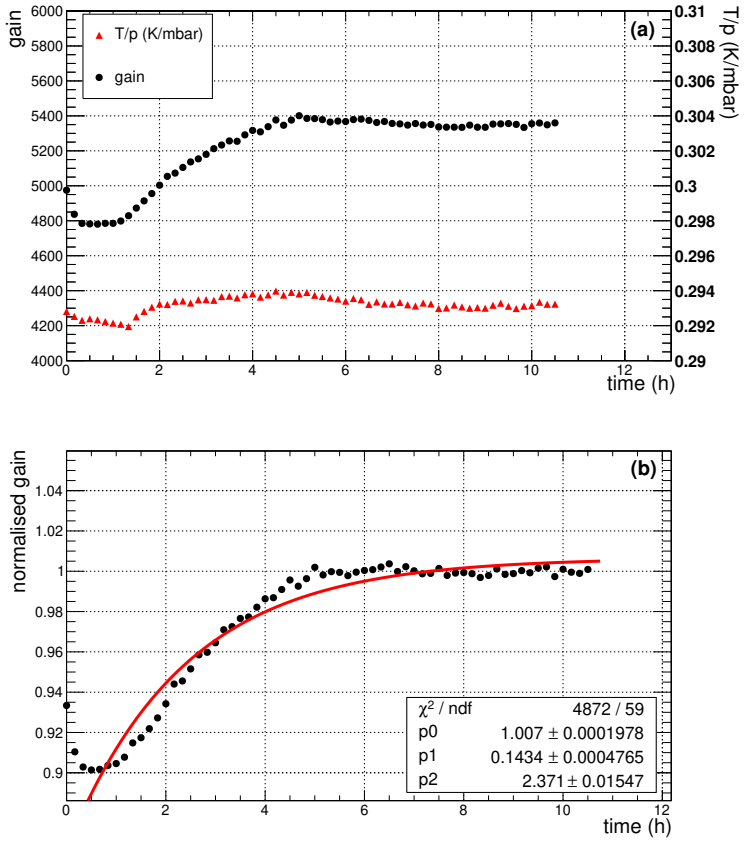

Figure 4.28: Variation of gain, (a) T/p and (b) normalised gain as a function of time for 1 kHz X-rays irradiating a 13 mm^2 (flux: 0.08 kHz/mm^2) area of the GEM chamber. The measurement has been carried out at a HV of - 4.2 kV. The HV was kept OFF for ∼ 60 minutes before taking the first measurement with the Fe^{55} X-ray source. The error bars are smaller than the marker size.

tend to increase the gain while a decrease in T/p will tend to reduce the gain.

As a result of these two competing processes, the slope of the curve changes, and that is also reflected in Fig. 4.27 (b). This competing effect between the charging-up and T/p variation is distinct in Fig. 4.28 where 1 kHz X-rays irradiated the 13 mm^2 area of the GEM chamber. For this measurement, the HV is switched ON, the source is placed on the detector, and data-taking is started. Before that, the HV is kept OFF for $\sim$ 60 minutes. The first three points in Fig. 4.28 (a) show a decreasing trend in the gain which is a combined effect of T/p and dielectric polarisation. After that, though the T/p value shows a decreasing trend, there is no visible decrease in the gain. That is due to two competing processes: the effect of the decreasing T/p and the charging-up on the gain which are anti-correlated. Then, after $\sim$1.5 hour, the gain increases because of both the charging-up and the T/p variation. The corresponding normalised gain variation is shown in Fig. 4.28 (b).

In order to identify whether the decrease in the gain in the first few minutes is due to the dielectric polarisation or not, a different measurement is performed by keeping the HV ON for $\sim$24 hours before the first measurement. The HV is kept at -4.1 kV which corresponds to $\Delta V \sim 382$ V across each GEM foil and the drift field, the transfer field, and the induction field of 2.3 kV/cm, 3.4 kV/cm and 3.4 kV/cm respectively. The chamber is irradiated with a 1 kHz X-ray falling on 13 mm^2 area of the chamber. Once the source is placed, the measurement is started immediately. The variation of gain, T/p, and normalised gain is shown as a function of time in Fig. 4.29 (a) and (b) respectively. The data is stored at an interval of 10 minutes. It is evident from the plot that there is no decrease in gain observed at the beginning.

Since the charging-up process is due to the accumulation of the charges on the GEM holes, therefore, the charging-up process depends on the flux of incident radiation. The more the flux of the incident particle, the faster will be the charging-up process and the same behaviour also appears in this study. From Fig. 4.27, for 1 kHz, 10 kHz, and 90 kHz operations, the time constants of the charging-up effect are found to be 2.376 $\pm$ 0.020 hours, 1.524 $\pm$ 0.008 and 1.395 $\pm$ 0.004 hours respectively. The time constant of the charging-

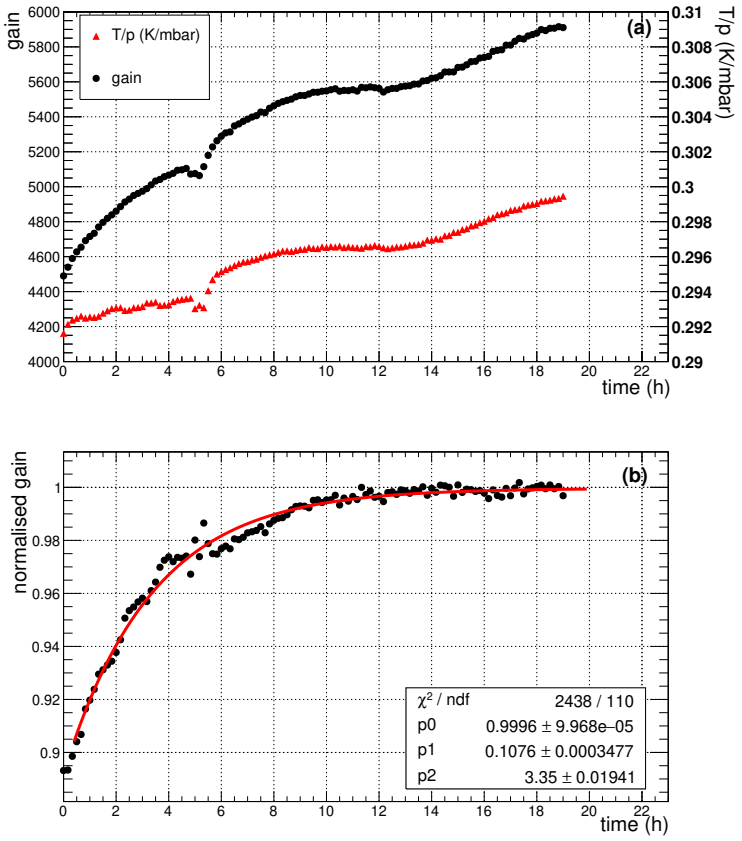

Figure 4.29: Variation of gain, (a) T/p and (b) normalised gain as a function of time for 1 kHz X-rays irradiating a 13 mm^2 (flux: 0.08 kHz/mm^2) area of the GEM chamber. The measurement is carried out at an HV of - 4.1 kV which corresponds to a $\Delta V \sim 382$ V across each GEM foil and drift field, transfer field, and induction field of 2.3 kV/cm, 3.4 kV/cm and 3.4 kV/cm respectively. The HV is kept ON for 24 hours before taking the first measurement with the Fe^{55} X-ray source. The error bars are smaller than the marker size.

up effect, obtained from Fig. 4.28 (b), agrees well with that from 4.27 (a). From Fig. 4.29 (b), the time constant of the charging-up effect is found to be 3.294 $\pm$ 0.018 for 1 kHz X-rays. The time constant of the charging-up effect, obtained from 4.29 (b), cannot be compared with those from Fig. 4.27 (a) and Fig. 4.28 (b) because the HV is different in each case. The residual voltage dependence on the charging-up effect has also been seen in Ref. [19]. The details of the charging-up time, X-ray flux and the voltage across the GEM foil are tabulated in Table 4.1.

Table 4.1: Summary of charging-up time for different radiation flux and gain of the DM triple GEM chamber.

ΔV (V)	Electric fields (kV/cm)	Flux (kHz/mm^2)	Saturated gain	Charging-up time (h)
390	Drift field: 2.3	$\sim$ 0.08	$\sim$ 4900	2.376 ($\pm$ 0.020)
	Transfer fields: 3.5	$\sim$ 0.20	$\sim$ 5100	1.524 ($\pm$ 0.008)
	Induction field: 3.5	$\sim$ 3.20	$\sim$ 5500	1.395 ($\pm$ 0.004)

4.6.3 Charging-up study for SM triple GEM chamber

The effect of charging-up on a single mask triple GEM chamber of dimension 10 cm $\times$ 10 cm, operated with a Ar/CO_2 gas mixture in 70/30 volume ratio is also investigated with an Fe^{55} X-ray source and discussed in this section. The effect of initial polarisation of the dielectric is also investigated for different gains of the chamber and with different irradiation rates. The details of the GEM prototype and experimental setup are discussed in section 4.3.

The Fe^{55} energy spectra obtained from the MCA are analysed and the gain is calculated in the same way as mentioned earlier in section 4.3. To measure the initial polarisation effect of the dielectric, the recording of the spectra is started as soon as the HV reaches its specific set value and the source is placed at a particular position on the chamber. It is already mentioned that the same Fe^{55} source is used to irradiate the chamber as well as to record the X-ray spectra. To see the effect of HV and irradiation rates on the initial polarisation of the dielectric, X-ray spectra with different HV and collimator settings are recorded for 20 seconds each, without any interval between two consecutive measurements. The details of the HV settings, used for the study of the initial polarisation effect, their corresponding ΔV across each GEM foil, average gain (after saturation) and the electric field strengths in the drift, transfer and induction gaps are listed in Table 4.2.

Due to the initial polarisation effect, the decrease in gain for the first few minutes, as observed in the DM triple GEM chamber, is also observed in this

Table 4.2: ΔV across each GEM foil, average gain and fields on the various gaps of the SM triple GEM chamber for different HV settings. The gain values are measured with X-ray flux of ~ 0.14 kHz/mm^2.

HV (V)	ΔV (V)	Average gain	Drift field (kV/cm)	Transfer field (kV/cm)	Induction field (kV/cm)
- 5085	409	$\sim$ 12950	$\sim$ 2.4	$\sim$ 3.6	$\sim$ 3.6
- 5100	410	$\sim$ 13600	$\sim$ 2.4	$\sim$ 3.7	$\sim$ 3.7
- 5115	411	$\sim$ 14300	$\sim$ 2.4	$\sim$ 3.7	$\sim$ 3.7

study. In Fig. 4.30, the variation of the gain as a function of time is shown for a X-ray flux of ~ 0.14 kHz/mm^2 at a HV of - 5100 V. The variation in the ambient

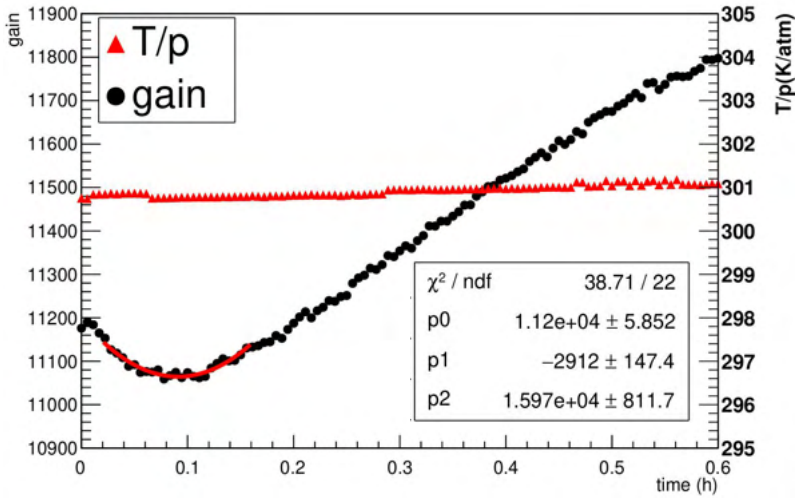

Figure 4.30: Variation of the gain and T/p (K/atm) as a function of time at a HV of - 5100 V. The initial decrease in gain due to the polarisation effect is fitted with a 2^{nd} degree polynomial. The error bars are smaller than the marker size.

temperature (T) to pressure (p) ratio for the first 20 minutes is below 1% for all the measurements. Though the variation of gain in any gaseous detector with temperature and pressure is a well-known phenomenon [21], but since the variation in the temperature to pressure ratio is small, no T/p normalisation is performed for this initial period. To identify the time up to which the gain decreases initially, the gain is fitted with a 2^{nd} degree polynomial using the chi-square minimisation technique, as available in ROOT [22]. From the fitting

parameters, the ratio p1/2p2 [7] gives the minima. The fitted curve with the respective chi-square value is shown in Fig. 4.30. The same technique is repeated for different gain and rate configurations to find out the time up to which the gain reduces due to the initial polarisation of the dielectric and then again starts to increase due to the charging-up effect.

Table 4.3: Variation of time in hour up to which the initial gain decreases with different ΔV and radiation flux.

ΔV (V)	time (h)			
	rate $\sim$ 0.04 (kHz/mm^2)	flux $\sim$ 0.14 (kHz/mm^2)	flux $\sim$ 0.42 (kHz/mm^2)	flux $\sim$ 7.78 (kHz/mm^2)
409	0.133 ($\pm$ 0.018)	0.110 ($\pm$ 0.013)	0.115 ($\pm$ 0.005)	0.126 ($\pm$ 0.004)
410	0.115 ($\pm$ 0.018)	0.098 ($\pm$ 0.006)	0.103 ($\pm$ 0.003)	0.097 ($\pm$ 0.004)
411	0.128 ($\pm$ 0.019)	0.091 ($\pm$ 0.010)	0.075 ($\pm$ 0.004)	0.076 ($\pm$ 0.003)

In table 4.3, the time in hour up to which the initial gain decreases due to the initial polarisation effect, is listed for different ΔV and irradiation rates.

In Fig. 4.31, the variation in the time of the initial decrease of the gain for different irradiation rates is shown. The data points are fitted with a linear function. It is observed that the time up to which the gain decreases initially due to the polarisation effect is anti-correlated (as observed from the slope p1 of the fitted data points) with the voltage across the GEM foil. An effect of the irradiation rates on the polarisation effect is also observed. As shown in Fig. 4.32, p1 i.e. the rate of decrease of time with ΔV, increases with the increasing rate of irradiation.

To observe the effect of the charging-up phenomenon, the HV is switched on for around $\sim$ 60 minutes before starting the measurement to ensure that the polarisation of the dielectric in the GEM foil is over. After that, the measurement is started as soon as the Fe^{55} X-ray source is placed on the chamber. The

[7] Fitted with a 2^{nd} degree polynomial of the form, y = p0 + p1 x + p2 x^2. To calculate the minima, $\frac{dy}{dx}|_x$=0 is evaluated for which $\frac{d^2x}{dy^2}|_x$ >0.

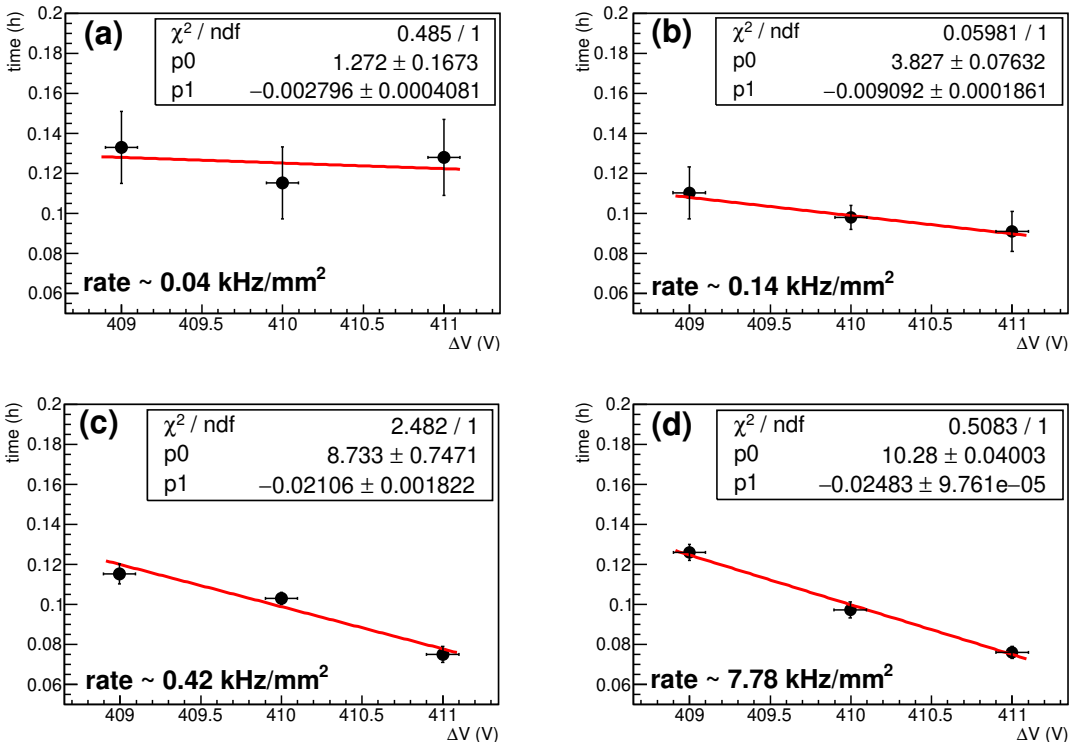

Figure 4.31: Variation of the initial gain decrease time as a function of voltage across the GEM foil (ΔV) for different irradiation rates.

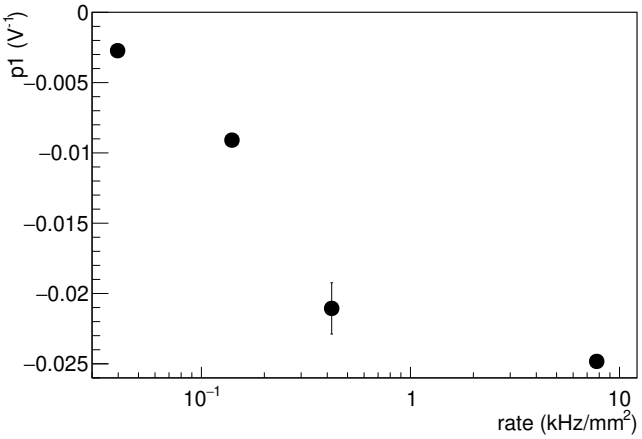

Figure 4.32: Variation of the slope (p1) as a function of irradiation rates.

spectra are stored for 60 seconds at an interval of 120 seconds and analysed to obtain the gain of the chamber. Ambient temperature, pressure and relative

humidity are also monitored continuously. To nullify the effect of temperature and pressure on the gain of the chamber, the measured gain is normalised for the T/p effect and then fitted with the exponential function (Eqn. 4.10), as done in the case of the DM triple GEM chamber.

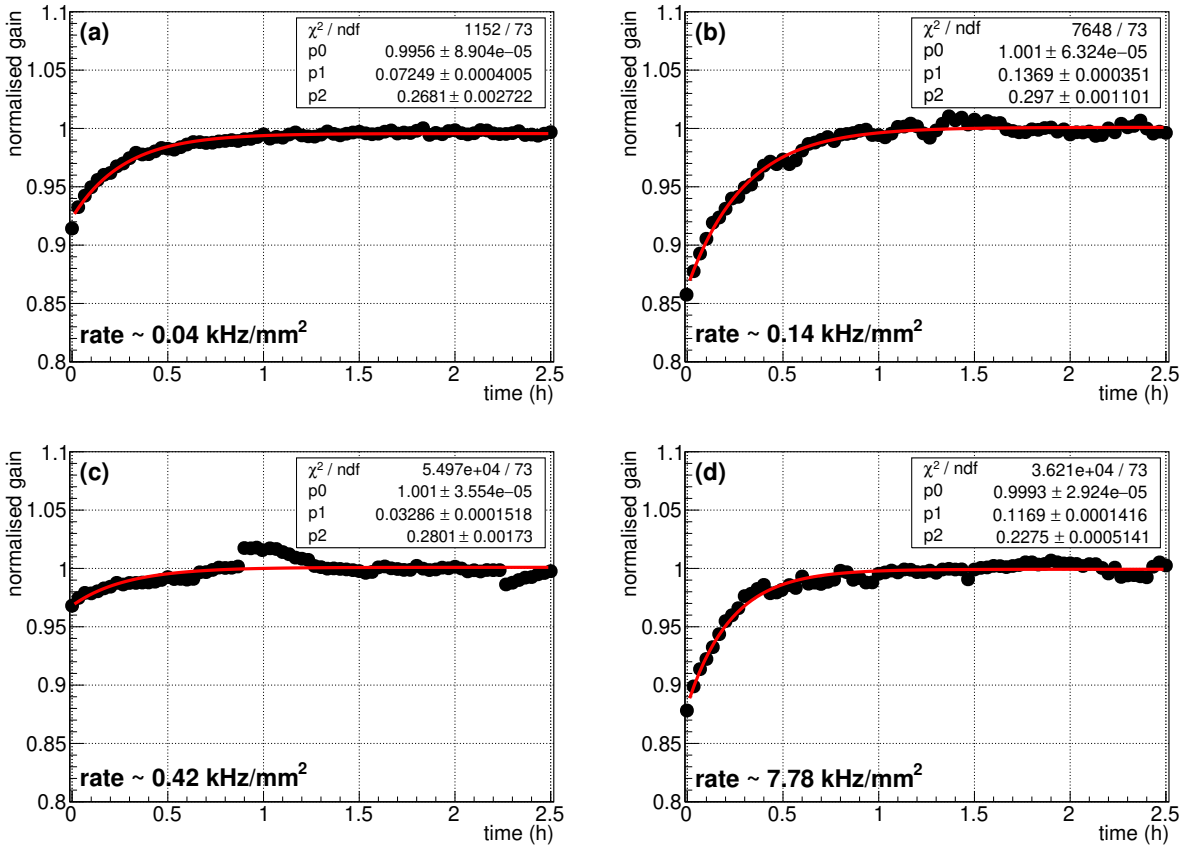

Figure 4.33: Variation of normalised gain as a function of time (hour) for different irradiation rates. All the measurements are carried out at a HV of - 5085 V (ΔV = 409 V). The error bars are smaller than the marker size.

In Fig. 4.33, the variation of normalised gain as a function of time (hour) at an HV of - 5085 V is shown for different irradiation rates as listed in table 4.4. In the case of Fig. 4.33 (c), the small jumps in the normalised gain around 0.9 hour and 2.2 hour are due to some sudden changes in the ambient T/p value, as recorded by the data logger. The details of the charging-up time, irradiation rates and saturated gain are listed in table 4.4.

Table 4.4: Saturated gain and charging-up time for different radiation flux.

ΔV (V)	Flux (kHz/mm^2)	Saturated gain	Charging-up time (h)
409	$\sim$ 0.04	$\sim$ 13000	0.268 ($\pm$0.003)
	$\sim$ 0.14	$\sim$ 11800	0.297 ($\pm$0.001)
	$\sim$ 0.42	$\sim$ 12600	0.280 ($\pm$0.002)
	$\sim$ 7.78	$\sim$ 12200	0.228 ($\pm$0.001)
410	$\sim$ 0.04	$\sim$ 13800	0.285 ($\pm$0.005)
	$\sim$ 0.14	$\sim$ 13700	0.351 ($\pm$0.003)
	$\sim$ 0.42	$\sim$ 13500	0.407 ($\pm$0.002)
	$\sim$ 7.78	$\sim$ 13400	0.335 ($\pm$0.002)
411	$\sim$ 0.14	$\sim$ 14500	0.190 ($\pm$0.002)
	$\sim$ 0.42	$\sim$ 14700	0.436 ($\pm$0.002)
	$\sim$ 7.78	$\sim$ 14000	0.186 ($\pm$0.001)

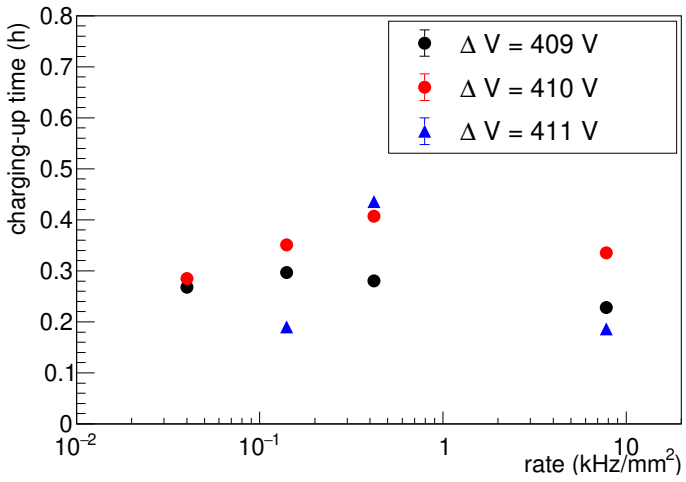

Figure 4.34: Charging-up time as a function of rate for different voltage settings. The error bars are smaller than the marker size.

The charging-up time for different X-ray fluxes is shown in Fig. 4.34. The charging up time varies between 0.2 - 0.4 hours depending on the rate of irradiation as shown in Fig. 4.34. In Fig. 4.35, the variation of normalised gain as a function of time (hour) is shown to illustrate both the effects of polarisation and of the charging-up of the dielectric medium on the gain of the chamber. It is visible in Fig. 4.35 that initially the normalised gain decreases due to the initial polarisation effect of the dielectric for around 0.1 hour. After that, due

to the charging-up effect, the normalised gain starts to increase and saturates after around 1.0 hours.

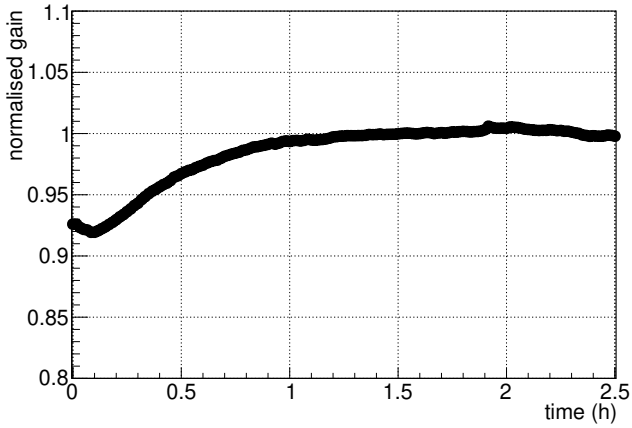

Figure 4.35: Variation of normalised gain as a function of time (in hour) at a ΔV of 409 V across each GEM foil (HV of -5085 V) and particle flux $\sim$ 7.78 kHz/mm^2. The measurement is started as soon as the HV reached to its specific value and the source placed on the chamber.

4.6.4 Uniformity study of a SM triple GEM chamber with and without the charged-up GEM foils

As discussed in section 4.6.3, the charging-up effect changes the gain of the chamber with time. Therefore, it will be interesting to study the uniformity in the performance over the active area of the chamber taking into account the charging-up effect and without considering the charging-up effect.

The 10 cm$\times$ 10 cm active area of the SM triple GEM chamber is divided into 4 $\times$ 4 regions. A collimator having a diameter of 8 mm is used to irradiate the chamber by the Fe^{55} X-ray source. To measure the uniformity in the characteristics of the chamber, the source is placed on top of the collimator and the collimator is placed at the respective positions on the active area of the chamber.

The data taking is done using two different methods. In the first case, the HV is kept ON for $\sim$ 60 minutes before starting the measurement and the data

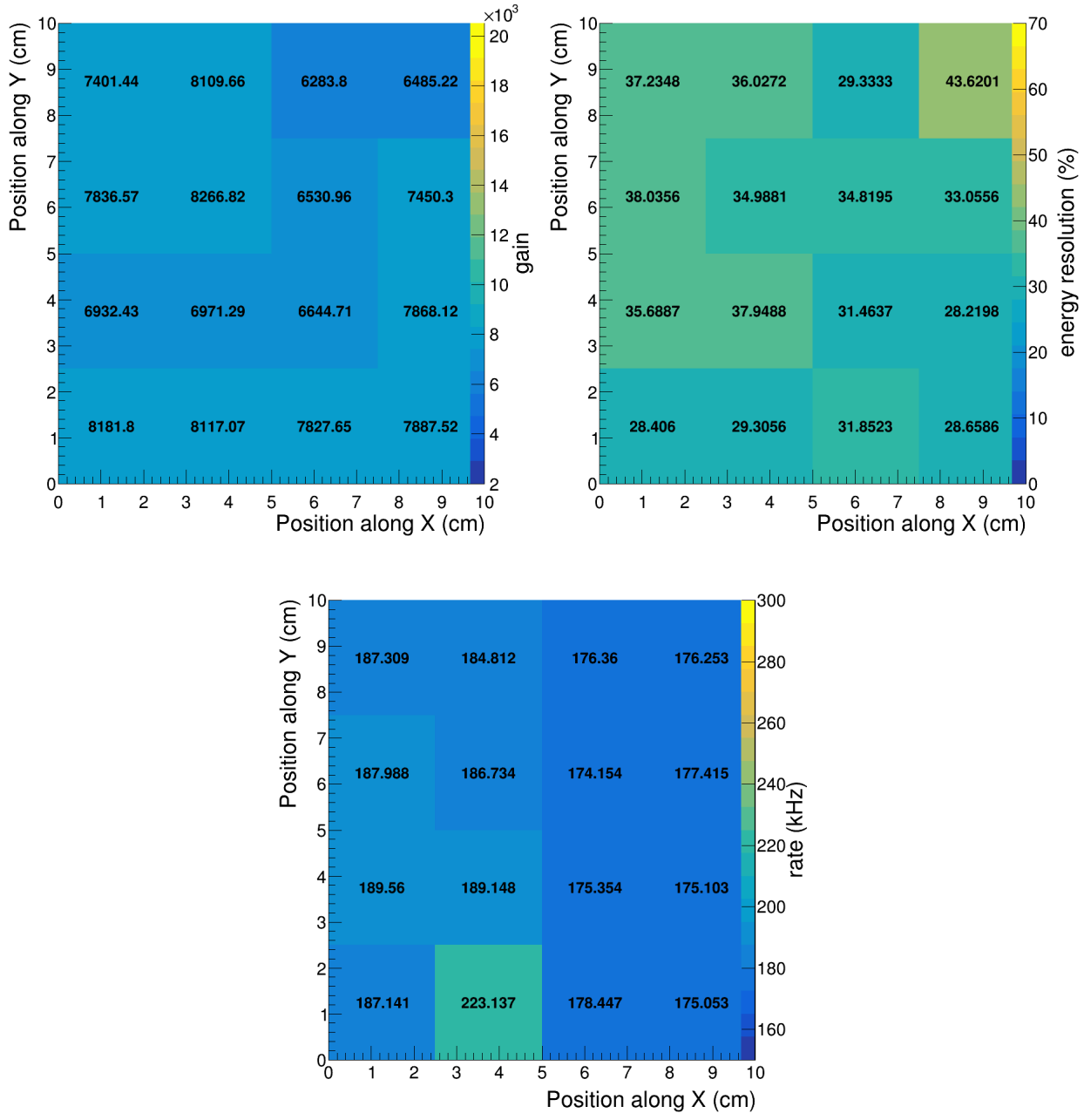

Figure 4.36: Variations of gain (top left), energy resolution (top right) and count rate (bottom) over the scanned 10 cm × 10 cm area of the SM triple GEM chamber at a HV of -5075 V. The ΔV across each of the GEM foils is $\sim$ 402.7 V.

taking is started as soon as the source is placed on the chamber. The X-ray energy spectra are recorded for 1 minute and then the source along with the collimator is moved to the next position manually. As a result, the foil does

not get sufficient time to get charged up. Therefore, the results obtained are essentially with the uncharged GEM foils. In Fig. 4.36, the variation in gain, energy resolution and count rate over the scanned area is shown at a ΔV of $\sim$ 402.7 V across each of the GEM foils. In Fig. 4.37, the distribution of gain, energy resolution and count rate is shown. The variation in gain and count rate

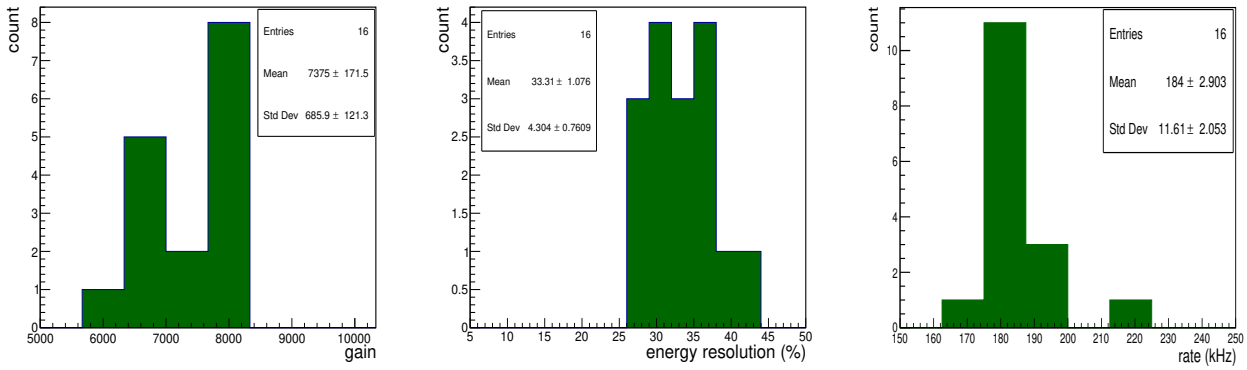

Figure 4.37: Distribution of gain (left), energy resolution (middle) and count rate (right) over the scanned 10 cm $\times$ 10 cm area of the SM triple GEM chamber at a HV of -5075 V. The ΔV across each of the GEM foils is $\sim$ 402.7 V.

is found to be $\sim$ 10% and the variation in energy resolution is $\sim$ 15%.

In the second case, the HV is switched ON and the source is placed on the detector as soon as the HV reaches its specific set value. The data taking is started as soon as the source is placed on the chamber. The spectra are recorded every 30 seconds without any interval. The data is collected and then normalised to eliminate the effect of temperature and pressure variations on the gain and energy resolution of the chamber. The details of the T/p normalisation are discussed in section 4.5. The variation of the normalised gain and energy resolution as a function of time is shown in Fig. 4.38. The energy resolution improves with an increased gain of the chamber due to the charging-up effect. The normalised gain is fitted using an exponential parameterisation (Eqn. 4.10) to extract the charging-up time. The fitted normalised gain is shown in Fig. 4.38 (top). The variation of the charging-up time over the scanned 10 cm $\times$ 10 cm area of the SM triple GEM chamber with HV of

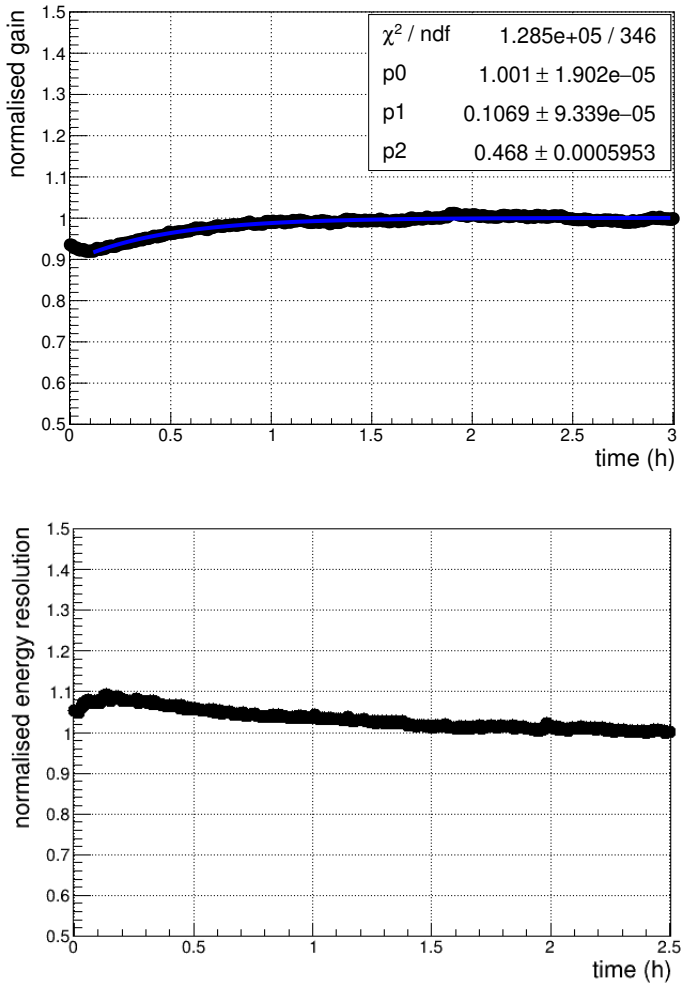

Figure 4.38: Variation of normalised gain (top) and energy resolution (bottom) as a function of time with HV of -5075 V. The ΔV across each of the GEM foils is $\sim$ 402.7 V. The normalised gain is fitted with an exponential function ($p0(1 - p1e^{-t/p2})$) to extract the charging-up time (p2).

-5075 V is shown in Fig. 4.39 (Top) and the distribution of the charging up time is shown in Fig. 4.39 (Bottom). The mean charging-up time is found to be 0.76 ($\pm$ 0.08) hour with a standard deviation of 0.33 ($\pm$ 0.06) hour. Except one region similar charging-up time is obtained over the scanned area of the chamber. The normalised gain decreases initially due to the polarisation of the dielectric medium [23] and after that, the charging-up phenomena take over and the gain increases and asymptotically reaches a constant value. To find out

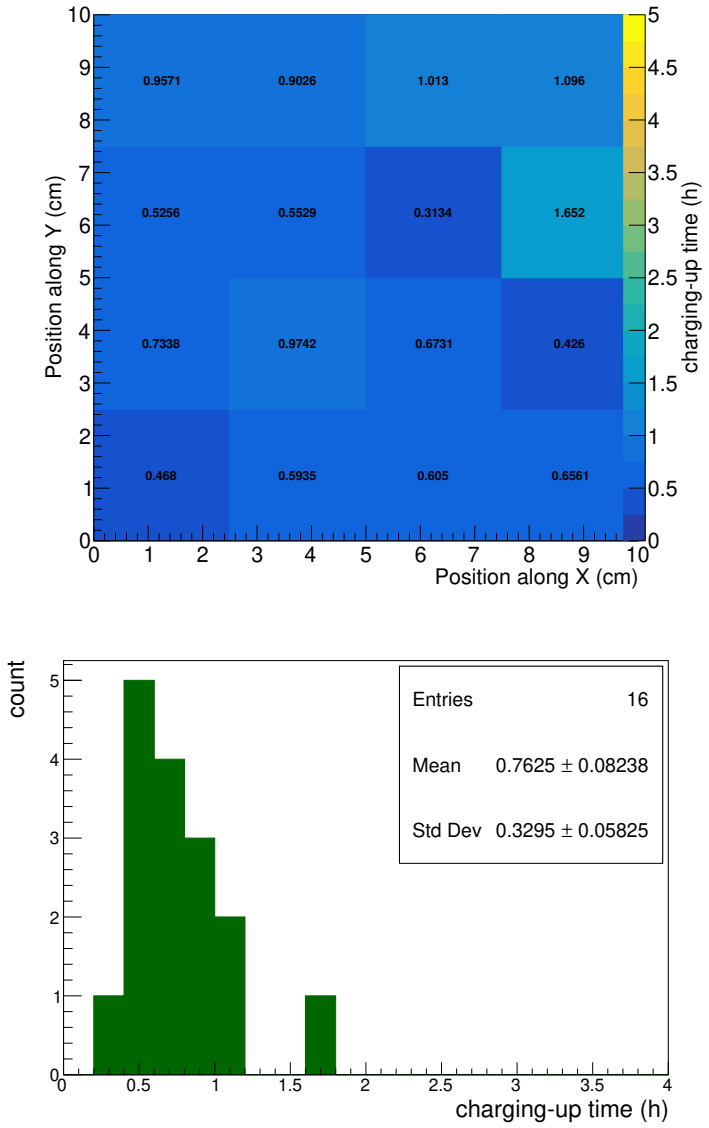

Figure 4.39: (Top) Variation of the charging-up time over the scanned 10 cm × 10 cm area of the SM triple GEM chamber with HV of -5075 V. The ΔV across each of the GEM foils is $\sim$ 402.7 V. (Bottom) Distribution of the charging-up time.

the variation in gain, energy resolution and count rate after the charging-up phenomena is completed, the gain and energy resolution are measured after $\sim$ 150 minutes of exposure of the chamber with an X-ray from Fe^{55} source and the count rate is recorded simultaneously from the NIM scaler. The variation of the gain, energy resolution and count rate over the surface with the

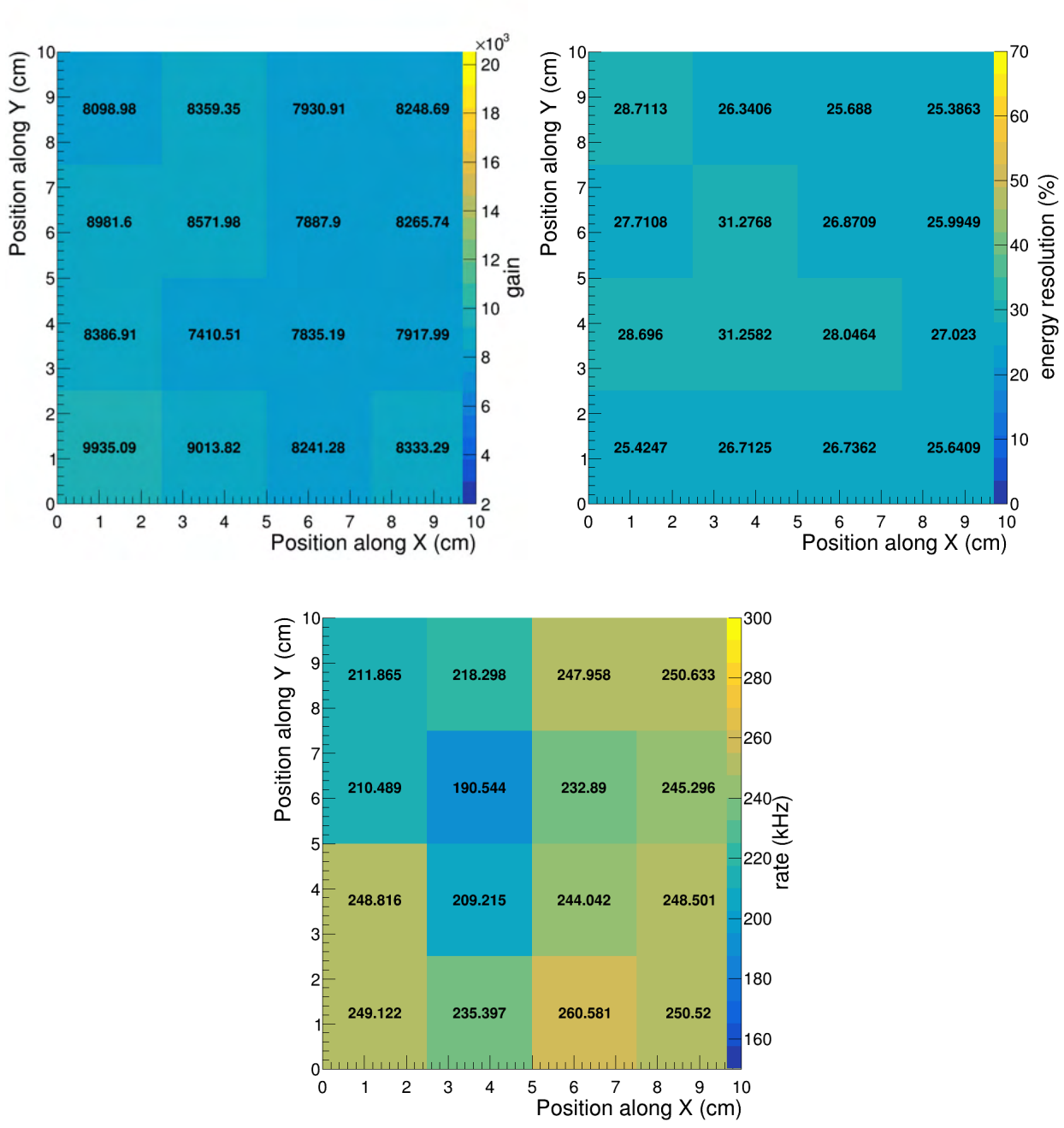

Figure 4.40: Variations of gain (top left), energy resolution (top right) and count rate (bottom) over the scanned 10 cm × 10 cm area of the SM triple GEM chamber with HV of -5075 V. The ΔV across each of the GEM foils is $\sim$ 402.7 V.

charged-up GEM foils are shown in Fig. 4.40 and their distributions are shown in Fig. 4.41 respectively. Over the scanned area, the gain, energy resolution and count rate are found to be varied $\sim$ 10%. No significant change is observed

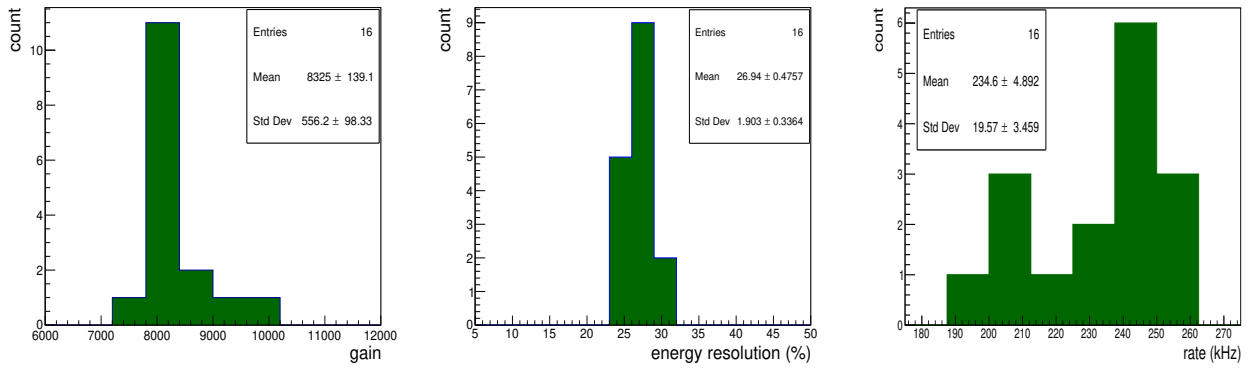

Figure 4.41: Distribution of gain (left), energy resolution (middle) and count rate (right) over the scanned 10 cm × 10 cm area of the SM triple GEM chamber at a HV of -5075 V. The ΔV across each of the GEM foils is $\sim$ 402.7 V.

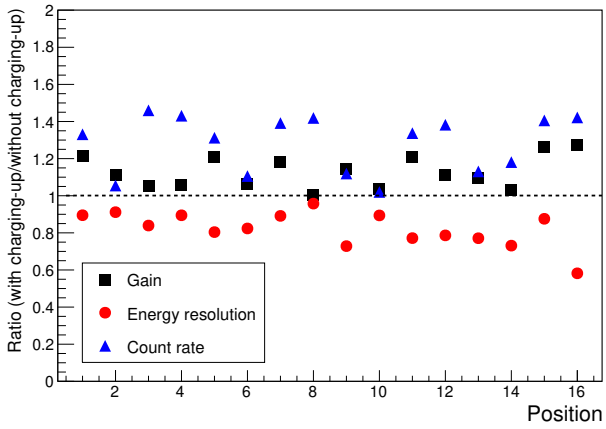

Figure 4.42: The ratios of gain, energy resolution and count rate with and without considering the charging-up effect of the SM triple GEM chamber at the sixteen different positions of the chamber. The error bars are smaller than the marker size.

in the uniformity of the chamber over the scanned area in terms of gain, energy resolution and count rate. Only the absolute value of the gain is found to be more in the second case because of the charging-up effect of the GEM foils. Due to the increased gain, the energy resolution improves in the second case. The mean values of the gain and energy resolution without charged up GEM foils are found to be 7375 ($\pm$171.5), 33.31 ($\pm$1.08) % and that with the charged-up GEM foil are found to be 8325 ($\pm$139.1) and 26.94 ($\pm$0.48) % respectively. The

count rate from the chamber is also found to be increased after the charging-up effect. The average count rate is found to be 184.0 ($\pm$2.9) kHz without considering the charging-up effect and 234.6 ($\pm$4.9) kHz after the charging-up effect. The ratio of the gain, energy resolution and count rate considering the charging-up phenomena with respect to that of the uncharged GEM foils is shown Fig. 4.42. The position along the x-axis indicates the sixteen different regions of the chamber. It is observed that the gain and count rate of the chamber with the charged-up GEM foils are always greater than that of the uncharged GEM foils. Moreover, the energy resolution of the chamber improves with the charging-up effect. Since an Fe^{55} radioactive source is used to irradiate the chamber and it emits X-rays at a fixed rate, we can say that due to the charging-up of the GEM foils the efficiency of the chamber also improves because of the increased gain. The probable reason behind the observation of less variation with the charged-up GEM foil in energy resolution could be the stabilization of the chamber.

4.6.5 Long-term stability study of triple GEM chambers

The long-term stability in terms of gain and energy resolution is an essential criterion for any detector used as a tracking device in high-rate experiments. In this study, the stability of DM and SM triple GEM chambers are investigated under the high irradiation of Fe^{55} X-ray. The uniqueness of this work is that the same Fe^{55} source is used to irradiate the chamber as well as to record the spectra. The investigation is carried out with the DM triple GEM chamber using Ar/CO_2 gas mixtures in different volume ratios namely 70/30, 80/20 and 90/10. The chamber is operated with a ΔV of 383.7 V, 359 V and 331 V across each GEM foil for the 70/30, 80/20 and 90/10 gas mixture and with the particle fluxes of 7 kHz/mm^2, 20 kHz/mm^2 and 20 kHz/mm^2 respectively. The variation of the gain and energy resolution as a function of time and the normalised gain and normalised energy resolution of the DM GEM chamber

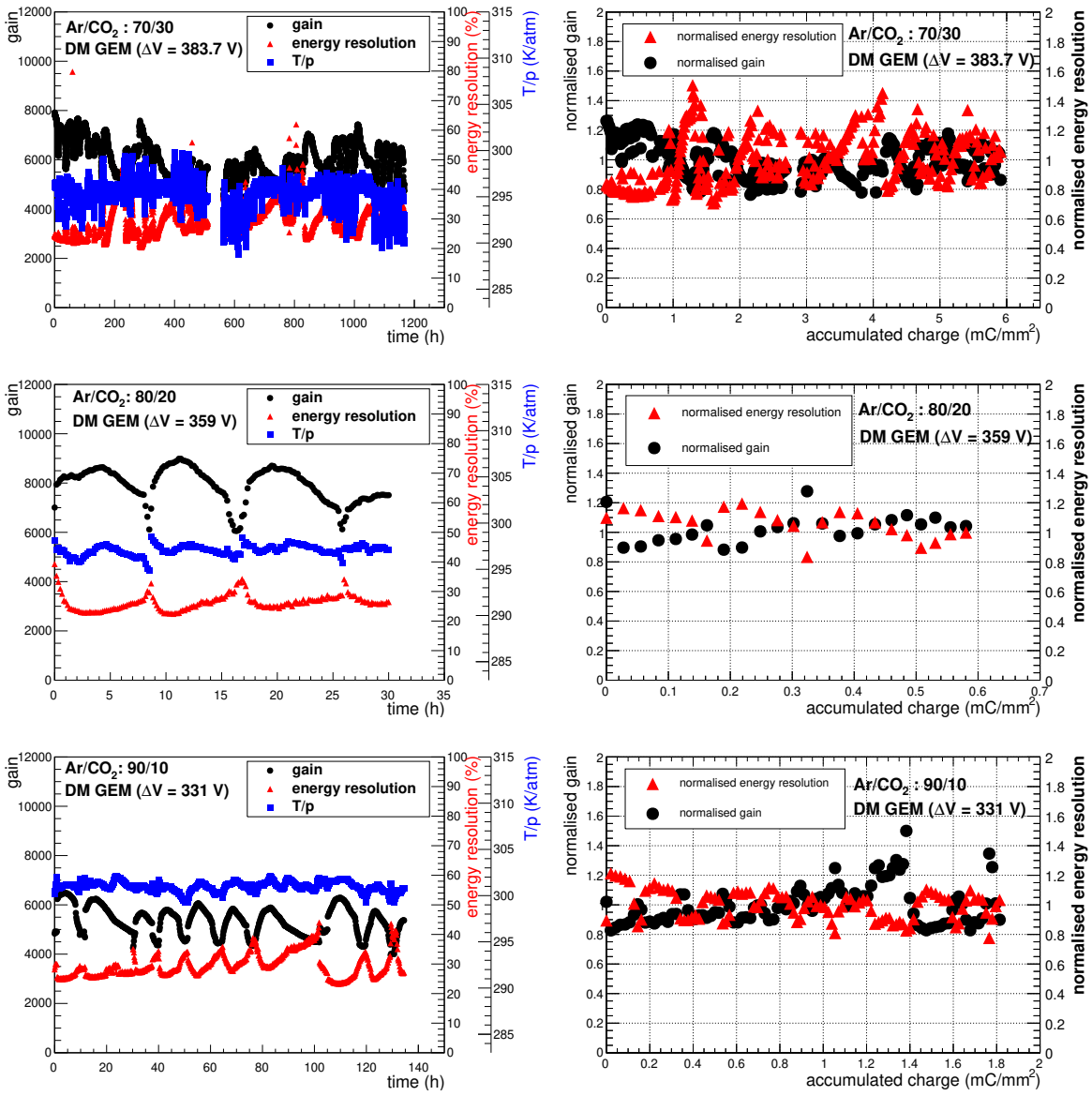

Figure 4.43: Left: Variation in gain, energy resolution and T/p as a function of time. Right: Variation of normalised gain and normalised energy resolution as a function of the total accumulated charge for Ar/CO_2 gas mixture in 70/30 volume ratio (top), 80/20 volume ratio (middle) and 90/10 volume ratio (bottom) of the DM triple GEM chamber. The error bars are smaller than the marker size.

is shown in Fig. 4.43 as a function of the accumulated charge per unit area and the distributions of normalised gain and normalised energy resolution are shown in Fig. 4.44. The accumulated charge per unit area is calculated using Eqn. 4.9 as discussed in section 4.5.

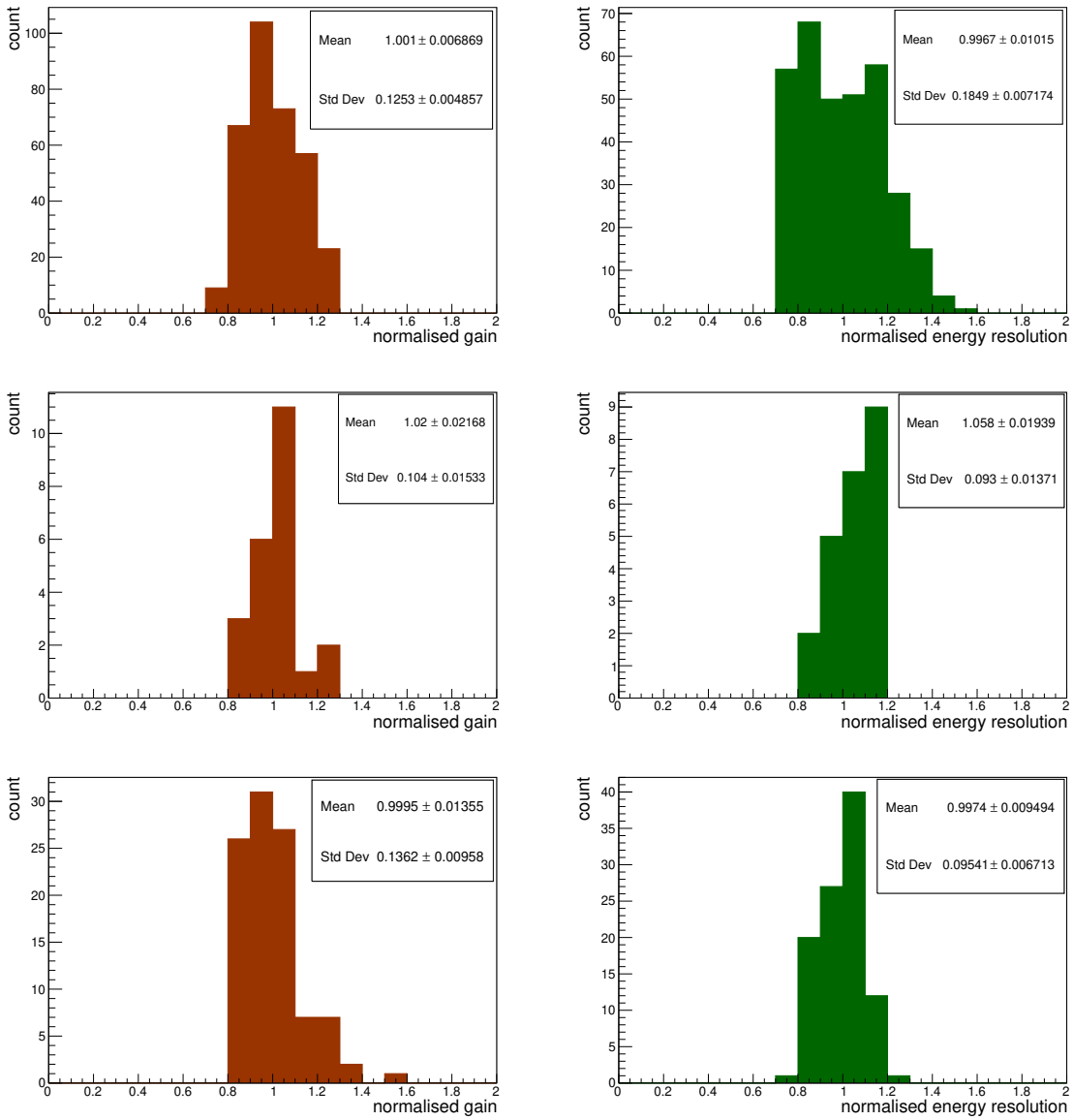

Figure 4.44: Distributions of normalised gain and normalised energy resolution for Ar/CO_2 gas mixture in 70/30 volume ratio (top), 80/20 volume ratio (middle) and 90/10 volume ratio (bottom) of the DM triple GEM chamber.

No degradation is observed in gain and energy resolution after accumulating a total charge of 6 mC/mm^2, 0.6 mC/mm^2 and 1.8 mC/mm^2 for Ar/CO_2 gas mixtures in the 70/30, 80/20 and 90/10 volume ratios respectively [24]. It is observed that for an Ar/CO_2 gas mixture in the 70/30 volume ratio, the variations in the normalised gain and normalised energy resolution are $\sim$15% and $\sim$20%

respectively. For 80/20 and 90/10 volume ratios, the variations in normalised gain and energy resolution is found to be ∼15% and ∼10% respectively.

The reason behind the observation of a larger variation in the normalised gain and normalised energy resolution in some cases might be due to the effect of environment parameters which cannot be entirely excluded by performing the T/p normalisation as discussed in section 4.5. The detector is irradiated continuously with 5.9 keV X-rays from the Fe^{55} source for long durations with Ar/CO_2 gas mixtures. Over such long periods, some sudden changes in the environmental parameter affect the normalisation of the data. To nullify such effects, a better idea might be to use two chambers in the same gas line and use one chamber as the reference chamber and the other as the irradiating chamber; the normalisation can be performed with respect to the reference chamber. In this way, any other environmental effects could be eliminated from the data obtained from the chamber.

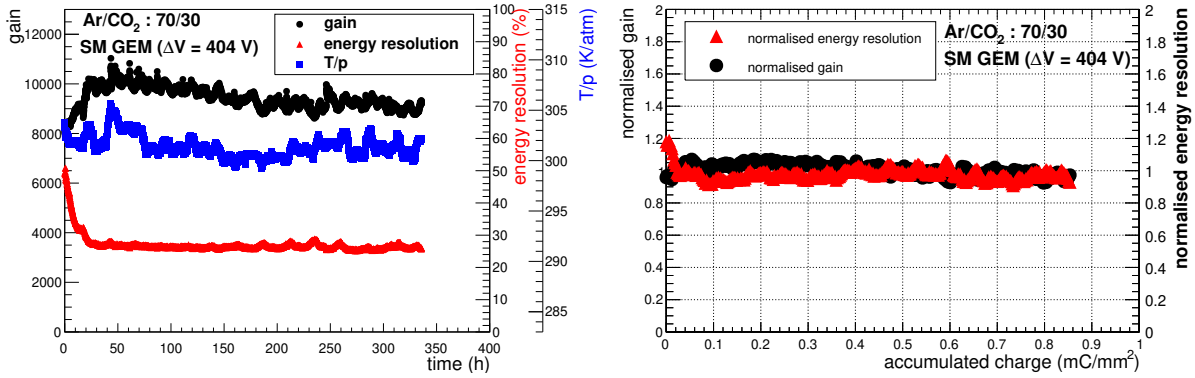

Figure 4.45: Left: Variations in gain, energy resolution and T/p as functions of time. Right: Variation in normalised gain and normalised energy resolution as a function of total accumulated charge per unit area with Ar/CO_2 gas mixture in 70/30 volume ratio for the SM triple GEM chamber. The error bars are smaller than the marker size.

The long-term stability study of the SM triple GEM chamber is also carried out with the Ar/CO_2 gas mixture in a 70/30 volume ratio with a particle rate of $\sim$ 2.3 kHz/mm^2 at ΔV of 404 V across each of the GEM foils. The variation of the normalised gain and normalised energy resolution is shown in Fig. 4.45 (right) as a function of the total accumulated charge. The distri-

bution of the normalised gain and normalised energy resolution are shown in Fig. 4.46. No degradation is observed in gain and energy resolution other than a fluctuation of $\sim$ 5% after accumulating a total charge of 0.85 mC/mm^2.

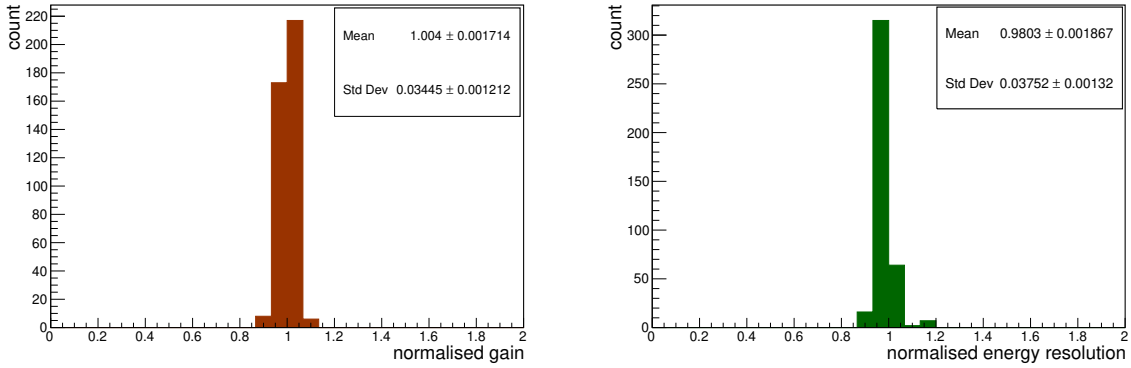

Figure 4.46: Distribution of normalised gain (left) and normalised energy resolution (right) with an Ar/CO_2 gas mixture in the 70/30 volume ratio for the SM triple GEM chamber.

It is to be mentioned here that taking a typical number of hits for the MIPs in the first GEM station of MuCh to be $\sim$ 0.05 hits cm^{-2} event^{-1} (Au+Au minimum bias collision at beam momentum of 12 A GeV/c) and with the foreseen average interaction rate of 1 MHz, the approximated charge accumulation over 10 years will be $\sim$ 0.76 mC/mm^2 for a typical gas gain of 10^3. Thus, with the investigated limit of accumulated charge using the Fe^{55} X-ray source at the laboratory, it can be concluded that the detector can be used safely for around 10 CBM years.

4.7 Cleaning of the GEM foil

During the long-term test with a SM triple GEM chamber, it is observed that the detector suddenly stopped producing the signal. To understand the problem, the triple GEM chamber prototype is disassembled and the individual foil resistances are measured. It is found that the resistance of the 3^{rd} GEM foil is $\sim$ 40 kΩ which indicates that there are some short paths created between

the top and bottom electrodes of the foil. The short-circuited path might be created due to the accumulation of impurities inside the GEM holes or due to the degradation of the foil itself.

4.7.1 Visual investigation of GEM foils

The stretched GEM foils are scanned using an optical microscope (Nikon eclipse Ni) with different magnifications before assembling the detector. The micro-

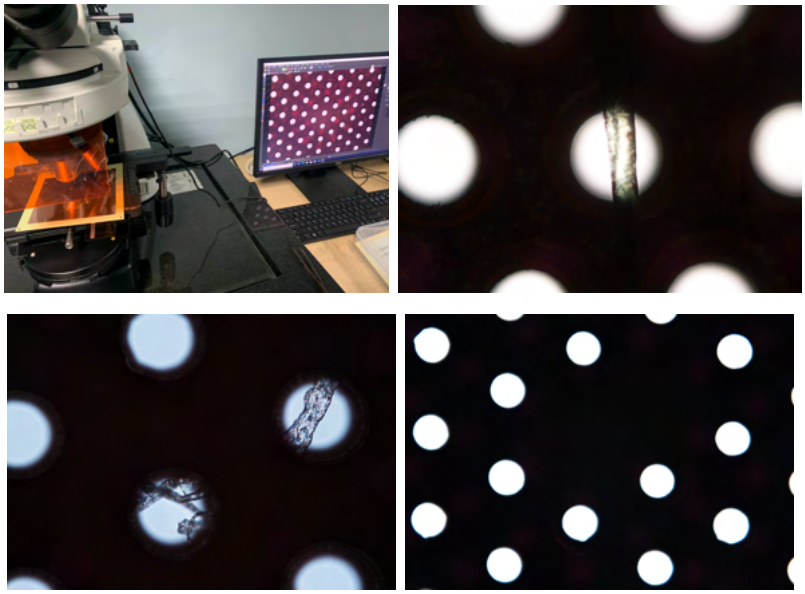

Figure 4.47: Microscope setup for scanning the GEM foil (top left). Imperfections in the GEM foil at different magnifications (top right, bottom left image with the 40X magnification and bottom right image with 20X magnification.)

scope setup is shown in Fig. 4.47 (top left). The microscope is connected to a PC for taking and storing the image of the object under scanning. The visual inspection revealed several imperfections in the foil and they are shown in Fig. 4.47. The pitch [8] and diameter of the GEM holes are also measured using the microscope and their distributions are shown in Fig. 4.48. The average hole diameter is found to be 69.58 $\pm$ 0.09 μm and the average pitch is found to

[8]Pitch is defined as the centre to centre distance of the holes in the GEM foil.

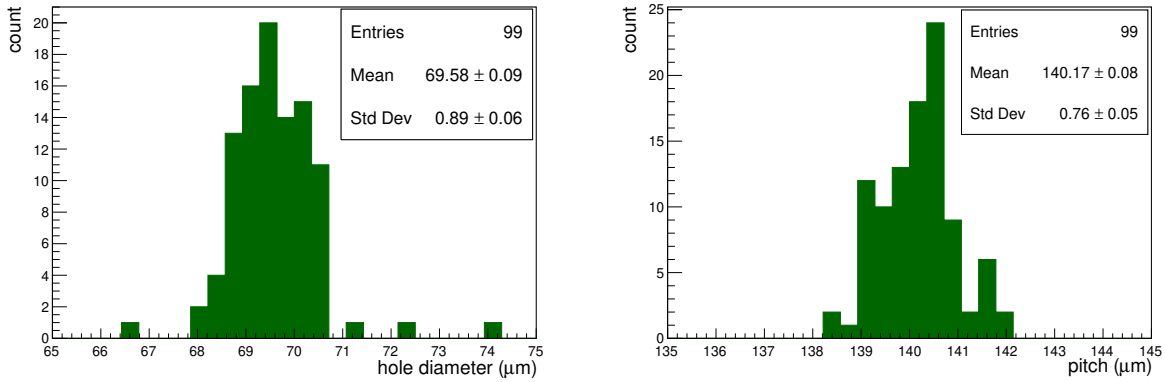

Figure 4.48: Distribution of GEM hole diameter (left) and pitch (right).

be 140.17 $\pm$ 0.80 μm which match with the conventional GEM hole diameter (70 μm) and pitch (140 μm) values.

The foil is cleaned using Millipore water which is nothing but de-ionized water and with an ultrasonic ($\sim$ 20 kHz) bath [25]. After cleaning, the foil resistance and the leakage current of the foil are measured. The cleaning methodologies, the setup and results of the leakage current measurement of the foil are discussed below.

4.7.2 Methodology for cleaning the GEM foil

First, the GEM foil is immersed in the Millipore water which is nothing but de-ionized water, bath for $\sim$ 60 minutes and then the foil is removed and kept for drying under continuous hot air flow for $\sim$ 30 minutes. After that, the foil resistance is measured and still, it is found that the resistance of the foil is low ($\sim$ 1 MΩ). The foil is kept for another 24 hours in a closed box and then again the foil resistance is measured, but still the resistance is found to be $\sim$ 1 MΩ. Fig. 4.49 shows the GEM foil in the Millipore water bath.

After the water bath, the foil is put in the ultrasonic ($\sim$ 20 kHz) bath with Millipore water as the medium. The foil is kept in the ultrasonic bath for

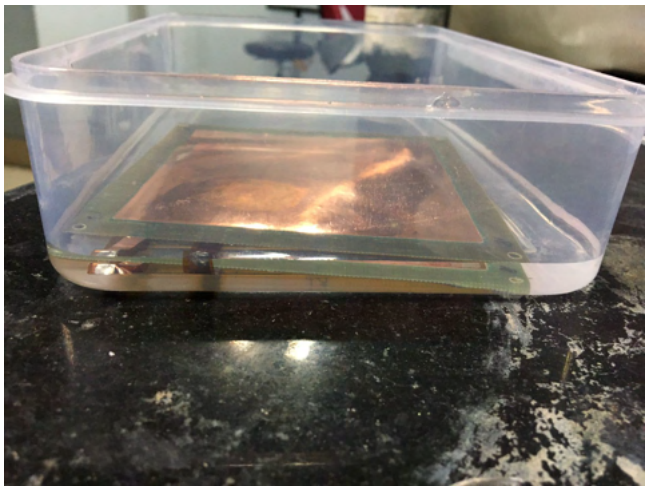

Figure 4.49: Millipore water bath of the GEM foil.

$\sim$ 5 minutes. After removing the foil from the ultrasonic bath, the foil is dried for $\sim$ 30 minutes under continuous hot air flow.

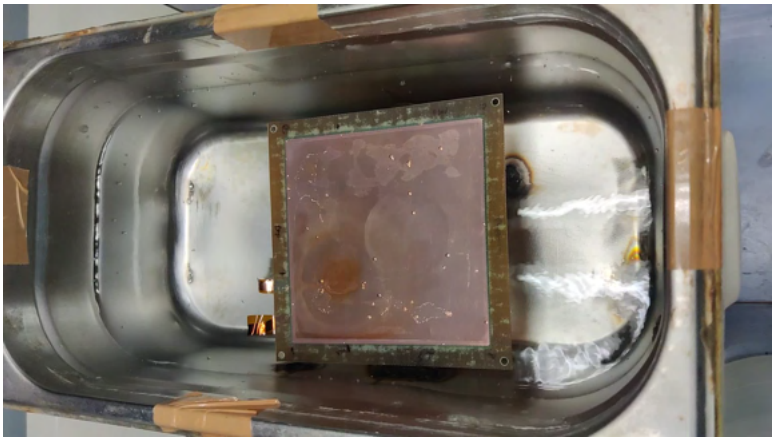

Figure 4.50: Ultrasonic bath of the GEM foil with Millipore water as the medium.

4.7.3 Leakage current measurement of the foil

After cleaning with the ultrasonic bath, the leakage current of the foil is measured under a continuous flow of Ar/CO_2 gas mixture. The voltage is applied across the GEM foil by connecting the two leads of the foil to the external High Voltage module. The current is measured using a Keithley pico-

ammeter (Mod No.: 6485). The setup of the leakage current measurement is shown in Fig. 4.51 (top). The voltage across the GEM foil is kept at $\Delta V \sim 300$ V

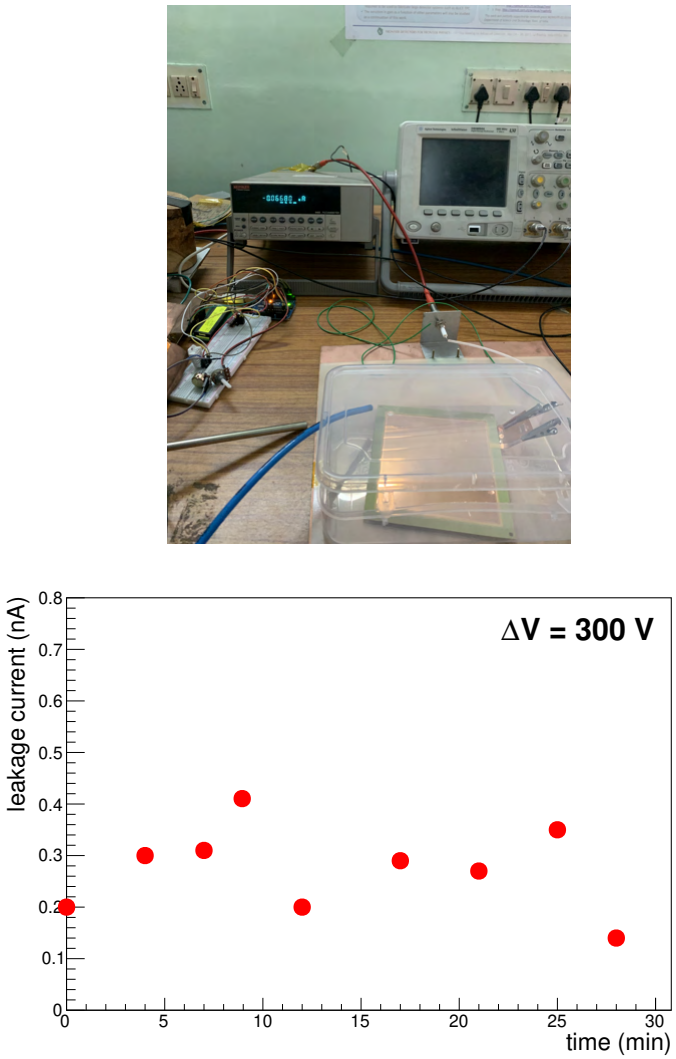

Figure 4.51: Setup for leakage current measurement of the GEM foil (top). Leakage current as a function of time (bottom). The error bars are smaller than the marker size.

and the leakage current of the foil is measured for 30 minutes. The leakage current is found to be $\sim$ 0.3 nA at a RH of $\sim$ 50 %. From the value of the applied voltage across the foil and the leakage current, the resistance of the foil is quantified to be $\sim 10^6$ MΩ which is comparable with that of Kapton [26]. This implies that the short paths are removed after the ultrasonic cleaning. The measured leakage current as a function of time is shown in Fig. 4.51 (bottom).

The ultrasonic bath technique [25] is found to be useful to clean the foil showing a low resistance, which might be due to the accumulation of impurities in the foil.

4.8 Spark probability measurement at CERN SPS beam-line facility

Since the CBM GEM detectors will be of the single mask type because of their large size, it is thus very important to measure the spark probability of a SM GEM detector. The main goal of this study is to measure the spark probability of a SM triple GEM detector with a high momentum pion beam and also for a shower environment. A SM triple GEM detector prototype is tested at the CERN SPS/H4 beamline facility with a pion beam of momentum 150 GeV/c. In this test beam, the pulse height distribution from the detector, currents from the individual GEM foils and count rates from the detectors are measured. The details of the spark identification, the value of the spark probability, and its variation as a function of gain will be presented in this section. The spark probability measurement of a DM triple GEM detector has been done by the CBM collaboration and reported earlier [27]. A comparison of spark probability results, obtained with double mask and single mask triple GEM chambers are discussed qualitatively at the end of this section.

4.8.0.1 Description of the GEM module

A SM triple GEM detector having the dimension of 10 cm $\times$ 10 cm, is used during the beam test. The GEM foils with a hole diameter of 70 μm and a pitch of 140 μm are obtained from CERN. The drift gap, 2 transfer gaps, and the induction gap are kept at 3 mm, 2 mm and 2 mm respectively (3-2-2-2 configuration). A protection resistance of 10 MΩ is employed to the top plane

of each GEM foil and also to the drift plane. Fig. 4.52 shows the schematic diagram of the GEM module used in the test beam campaign. The read-out plane consists of 512 pads, each of 4 mm $\times$ 4 mm size. All the readout pads have been routed to 4 connectors of 128 pins each. Even though the read-out plane was segmented for the module, in this study, the signals obtained from all the 128 pads are summed by a sum-up board and a single output has been fed to a charge sensitive preamplifier. (The sum-up board is a specially designed board having connections from 128 pins to a single LEMO. Signals coming from any of the 128 pads will reach a single preamplifier via the LEMO connector.)

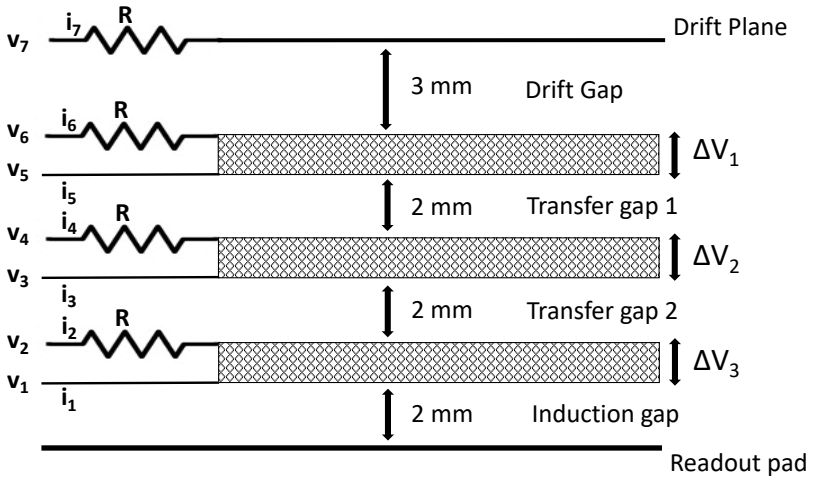

Figure 4.52: Arrangement of GEM foils, voltage and current distribution in different planes of the chamber.

The analog signals from the preamplifiers are put into the linear Fan-in-Fan-out (FIFO) module that gives four identical analog signals at the output which are exactly the same as the input signal. For data acquisition, PXI LabView is used [28]. Signals from one output of the linear FIFO are put to the PXI LabView scope card for ADC spectra. Signals from another output are fed to a NIM discriminator. The threshold to the signal is set at 10 mV in the discriminator to eliminate the noise. The discriminated signals are counted using a PXI LabView scalar. The counts from the pad plane of the GEM detector are sampled for 100 ms binning.

The GEM module is operated throughout the experiment with a premixed Ar/CO_2 gas mixture in the 70/30 volume ratio. The HV to the different GEM planes is applied by a seven-channel HVG210 power supply made by LNF-INFN [29]. This module allows powering and controlling the applied voltages of a triple GEM detector. The module communicates with the peripherals via the CAN bus. The HVG210 power supply comprises seven almost identical channels, each of them being able to produce a specified voltage level with a current reading and current limiting option. The currents of all channels are recorded and used to determine the occurrence of a spark. The applied voltages and measured currents on each channel from the bottom plane of the lowest GEM foil up to the drift plane are named as V_1 to V_7 and i_1 to i_7, respectively. The details of the electric fields in the drift, transfer, and induction gap for a particular voltage configuration are summarised in Table 4.5 [30].

Table 4.5: Typical potential differences and fields on the various gaps of the triple GEM chamber, operated with Ar/CO_2 in a 70/30 mixing ratio.

Gap Name	Gap width (mm)	Potential difference (V)	Electric field (kV/cm)
Drift	3	400	1.33
Transfer 1	2	395	1.98
Transfer 2	2	395	1.98
Induction	2	390	1.95

4.8.0.2 Experimental setup

The experimental setup used in the test beam campaign is shown in Fig. 4.53. Two crossed finger scintillators (Scintillator 1 and Scintillator 2, both having dimensions 5 cm $\times$ 5 cm) are placed to monitor the incoming particle rate at a distance of 80 cm from the beam pipe end. The coincidence of those two scintillators (crossed area of 5 cm $\times$ 5 cm) is used as a beam counter. The SM triple GEM detector under test is placed at a distance of 168 cm from the beam pipe end, as shown in Fig. 4.53. An iron block of length 20 cm is employed to

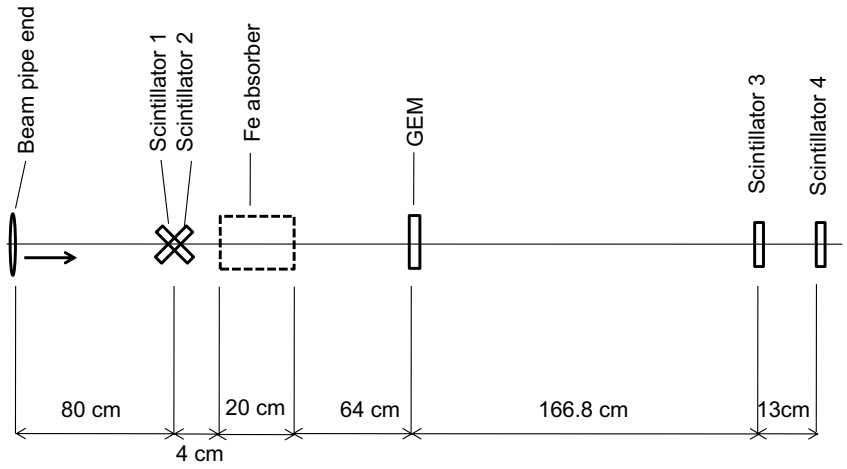

Figure 4.53: A schematic of the experimental setup.

generate a particle shower. The particle shower is identified by the coincidence between the signals from the first two finger scintillators and no signal from the last two scintillators (Scintillator 3 and Scintillator 4, having dimensions 10 cm $\times$ 20 cm and 20 cm $\times$ 30 cm, respectively). The distance between the iron block and the GEM module is 64 cm as shown in Fig. 4.53. The centres of

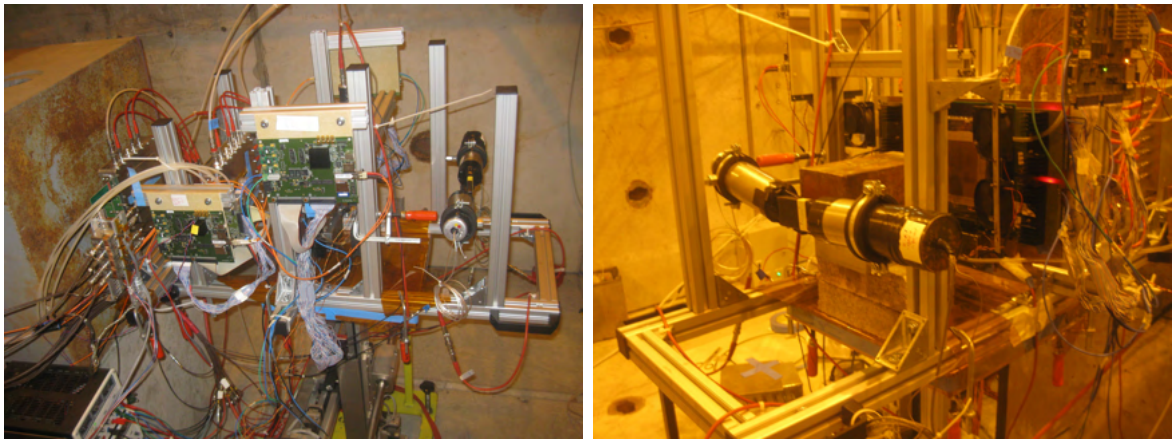

Figure 4.54: The setup for the spark probability measurement of the SM triple GEM chamber with the pion beam at the CERN SPS accelerator facility. Left: setup for the pion beam, Right: setup for the shower.

the 4 scintillators (Scintillator 1, 2, 3, 4), the iron block and the GEM module are mechanically aligned with the centre of the beam pipe. In Fig. 4.54, the arrangement of the setup at the CERN SPS accelerator facility is shown for

the pion beam setup (left) and for the shower setup (right) with the 20 cm iron slab inserted in between the finger scintillators and GEM detector.

The FLUKA simulation package is used to calculate the number of particles reaching the detector surface after the shower production by the iron slab [31, 32, 33]. From the FLUKA simulation, the numbers of pions, neutrons, muons, protons, kaons and electrons reaching the GEM plane are found to be 2.4, 0.2, 0.009, 0.1, 0.3, and 10 respectively, per primary pion beam of energy 150 GeV/c. The particle distribution on the GEM plane, as obtained from the FLUKA

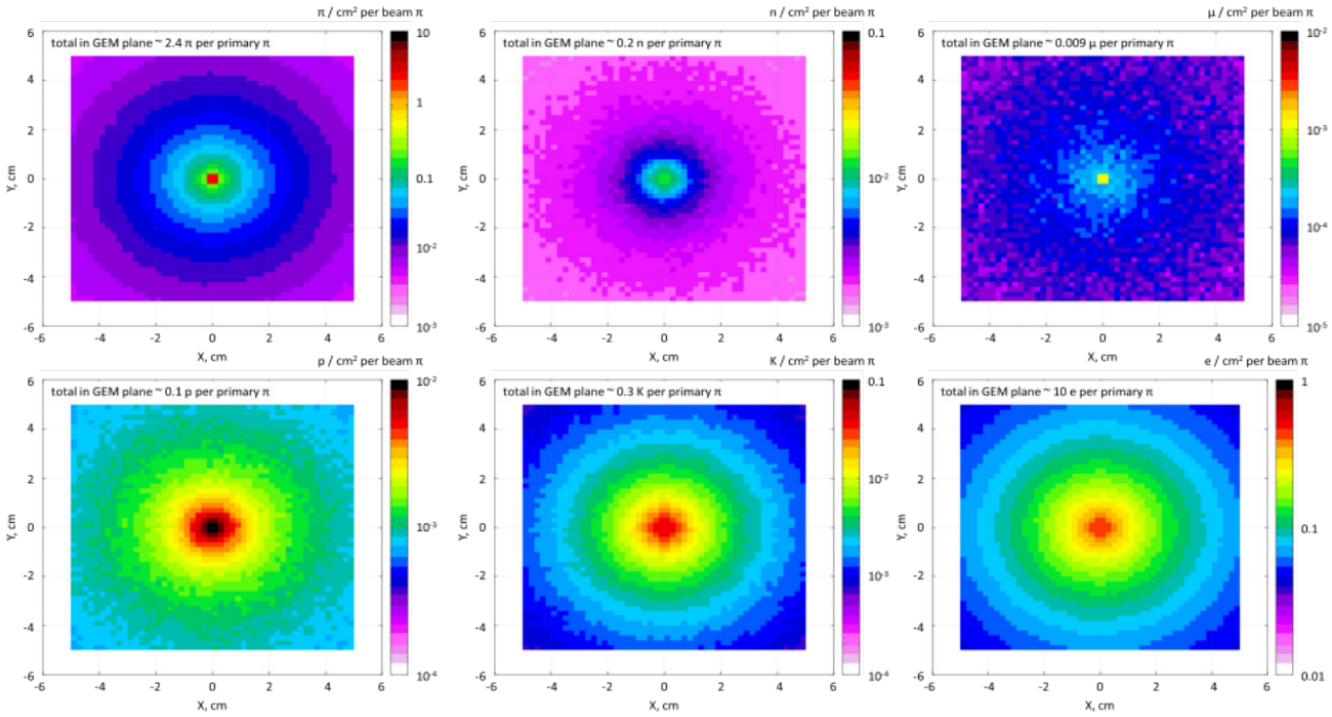

Figure 4.55: Particle flux at the GEM plane during the shower from FLUKA simulation induced by a 150 GeV/c pion beam on 20 cm thick iron slab. The figures are generated by Dr. Anna Senger, FAIR, Germany.

simulation, is shown in Fig. 4.55. In this study, in order to measure spark probability, pion beam of rates 8, 27, 43, 48, 150 and 170 kHz are used whereas to produce a shower, pion beam of rates 6, 50 and 120 kHz are employed to hit a 20 cm thick iron block. The pion beam hit the GEM detector on an area of $\sim$ 10 mm^2, whereas in this setup during the shower, for each pion beam the

number of secondary particles hitting the whole GEM plane of area 100 cm^2 is 13.009 (sum of the numbers of secondary pions, neutrons, muons, protons, kaons, and electrons reaching GEM plane per primary pion).

The voltages and currents from all seven channels of the HVG210, counts from the scintillators, GEM detector and the pulse height of the GEM detector signals are measured.

4.8.0.3 Results

In this test beam, the currents in all the channels from the top and bottom planes of three GEM foils and the drift planes are measured. The data for the ADC spectra are stored for all voltage settings. The data for counts from the GEM detector and the scintillators are also stored.

4.8.0.4 ADC spectra

The ADC spectra of the detected particles are studied to investigate the performance of the chamber. The ADC distribution for a pion beam of a typical average rate of 27 kHz is shown in Fig. 4.56. The energy distribution of the minimum ionizing particle is expected to follow the Landau distribution [34], as observed from the ADC distribution for pion (Fig. 4.56) with a GEM voltage setting of ΔV_1=390 V, ΔV_2=385 V and ΔV_3=380 V and corresponding gain $\sim$ 80000. The Most Probable Value (MPV) of the distribution is found to be at $\sim$ 51 ADC channel and a small saturation peak is observed at the 700 ADC channel.

The ADC distribution for heavily ionizing particles produced after the shower is shown in Fig. 4.57 with GEM voltage configurations of ΔV_1=390 V, ΔV_2=385 V and ΔV_3=380 V and the corresponding gain is $\sim$ 80000. The MPV of the distribution is found at $\sim$ 51 ADC channel and a large saturation peak is observed. However, it is somehow unexpected that the MPV is the same both for the heavily ionizing and minimum ionizing particles. The mean of the

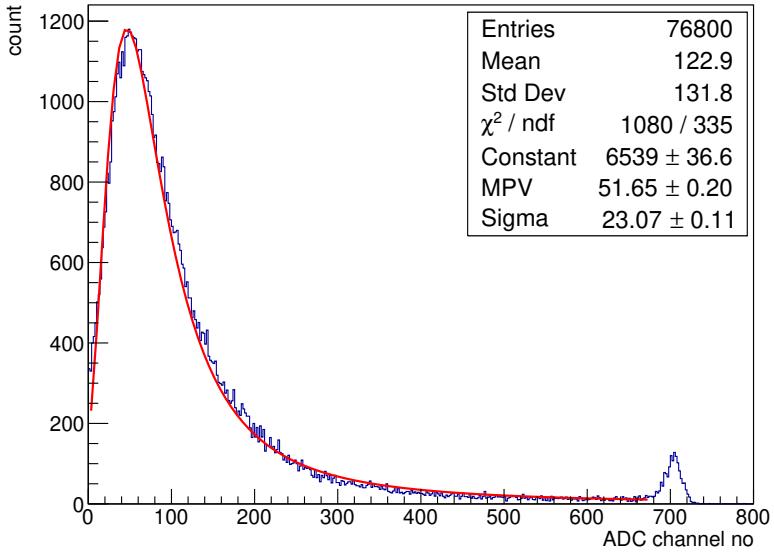

Figure 4.56: ADC distribution for the pion of average rate 27 kHz with ΔV_1=390 V, ΔV_2=385 V and ΔV_3=380 V.

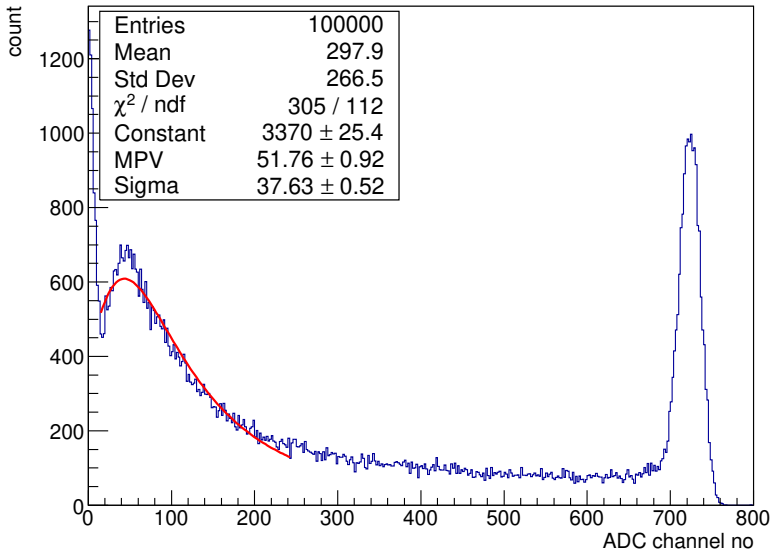

Figure 4.57: ADC distribution for shower environment with ΔV_1=390 V, ΔV_2=385 V and ΔV_3=380 V.

distribution for the pion beam and the shower, at the same voltage settings, are found to be at 122.9 and 297.9 ADC values respectively. The average energy

distribution of the particles produced in the shower is higher. For the shower, the mean value is increased only by a factor of ~ 2.5, which is also somehow surprising taking into account the steep increase of the Bethe-Bloch formula towards small velocities. The large saturation peak for the shower environment reflects the existence of heavily ionizing particles in the shower. In this work PXI, LabView based scope card is used to store the ADC spectra. It digitises the difference between the maximum and minimum edges of a signal and takes that number as the amplitude of the signal. For saturated signal also, although the maximum edge is more or less fixed but both the edges (maximum and minimum) can fluctuate a bit. Accordingly, the digitised value also fluctuates. This is the reason for the broadening of the saturation peak in both Fig. 4.56 and Fig. 4.57. From the scope data, it can be inferred that the detectors were in good condition during the beam-time.

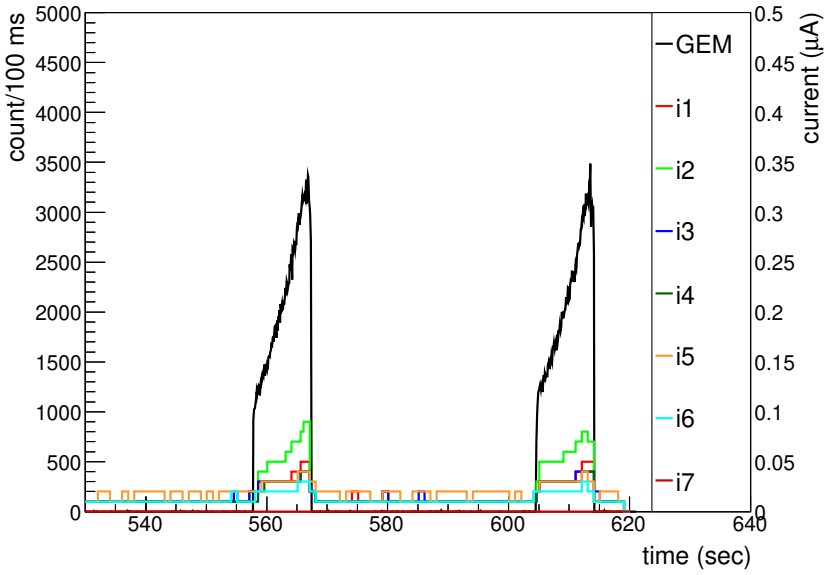

Figure 4.58: Currents and the GEM counting rate for the Pion beam of rate 27 kHz. The GEM count rate is plotted in the units of counts/100 ms. The different currents i1 to i7 correspond to V1 to V7.

4.8.0.5 Measurement of current

In this study, currents from the drift plane and both the top and bottom planes of each of the GEM foils are recorded using the HVG210 [29] high voltage power supply module. The counts from the GEM detector as well as from the scintillators are sampled for 100 ms binning. The variation in the current along with the count rate from the GEM module is shown as a function of time in Fig. 4.58 and Fig. 4.59.

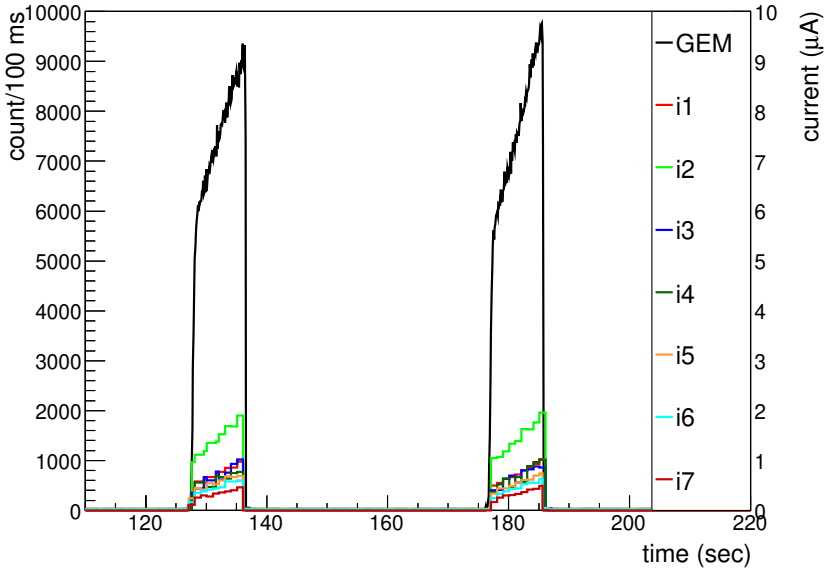

Figure 4.59: Current and the GEM counting rate during Shower: Beam rate is 120 kHz. The GEM count rate is plotted in the units of counts/100 ms. The different currents i1 to i7 correspond to V1 to V7.

Fig. 4.58 shows the variation of the currents and the GEM count rate during and in between the spills of the pion beam of an average rate 27 kHz with GEM voltage settings of ΔV_1=390 V, ΔV_2=385 V and ΔV_3=380 V and the corresponding gain is $\sim$ 80000. In Fig. 4.59, the variation in the currents and GEM count rate is shown for the shower produced by a pion beam of an average rate of 120 kHz hitting the 20 cm iron slab. In this case the GEM voltage settings are ΔV_1=385 V, ΔV_2=380 V and ΔV_3=375 V and the corresponding gain is $\sim$ 60000. The spill structure of the SPS beam increases with time,

reaches a maximum and then drops immediately to 0, as obtained from both the GEM detector and beam counter. The duration of the spill in the SPS beam is ∼10 s and the off spill time is ∼ 40 s. From Fig. 4.58 and Fig. 4.59, the maximum absolute increase in the current is observed in i2, i.e. on top of the third GEM-foil, where the maximum number of ions reach.

4.8.0.6 Measurement of spark probability

The most important goal of this beam time is the measurement of spark probability. The spark probability is defined as the ratio of the number of sparks that occurred in the detector and the total number of particles incident on it [35, 36, 37]. In this study, two different methods are used to identify a spark in the GEM module, as previously done for the DM detector [27]. The first method identifies a spark if there is a sudden drop in the GEM counting rate. The second one determines a spark by the sudden jump in the current obtained from the top of each GEM foil.

During a spark, the sudden drop of the electric field in the GEM hole reduces the gain of the detector, and as a result, the count rate of the chamber decreases. That is why it is a beneficial method to calculate the number of sparks that occurred in the GEM module during the spill. To identify a spark during a spill, the ratio of the counts from the GEM module and beam counter is used. If the ratio drops below 65% of its average value, then it is considered as a spark. Different threshold values between 50% to 70% are tested, but no significant change in the result is observed. Above 70%, the spark counts increase drastically because then all the small fluctuations in the GEM count rate are considered as a spark, and below 50% the spark count comes to be zero. The above-mentioned definition is used for the identification of spark in the analysis. In Fig. 4.60, the black line shows the count registered on the GEM module during a spill and a sudden drop in the count rate indicates the occurrence of a spark in the chamber. Fig. 4.61 shows that sometimes more than one sparks are observed in the module during a spill.

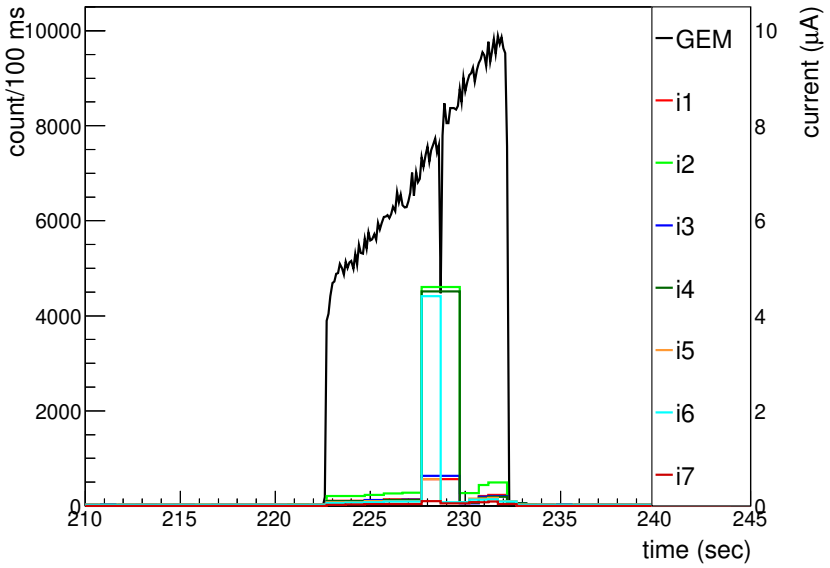

Figure 4.60: Identification of spark from the drop in the GEM counting rate during a spill. In parallel, the currents on all GEM electrodes are registered and displayed. The time axis is shown in the unit of second. i1 to i7 shown in different colours, are the currents corresponding to V1 to V7. The GEM count rate, shown in black, is in the unit of counts/100 ms.

Measuring the currents from each layer of the GEM foil is another method of determining a spark in the module. The current will jump whenever there is a spark. In Fig. 4.60 and Fig. 4.61, the sudden jump in the current in the top layers of the GEM foil is observed when there is a drop in the GEM counting rate. The threshold for the current is set to 2 μA to define a spark, but the identification of the spark is more accurate if the first method is used i.e. from the drop in the GEM counting rate. This is because of the sampling rate for the current monitoring is less than the sampling rate for the count rate data storing. If Fig. 4.61 is considered, then the number of sparks is two if counted from the drop in the GEM counting rate; but it is coming to be one if counted from the jump in the current. That is why, for our analysis, the spark probability is calculated from the drop in the counting rate of the GEM module during a spill. However, from the current jump, it can be known in which foil actually the spark took place.

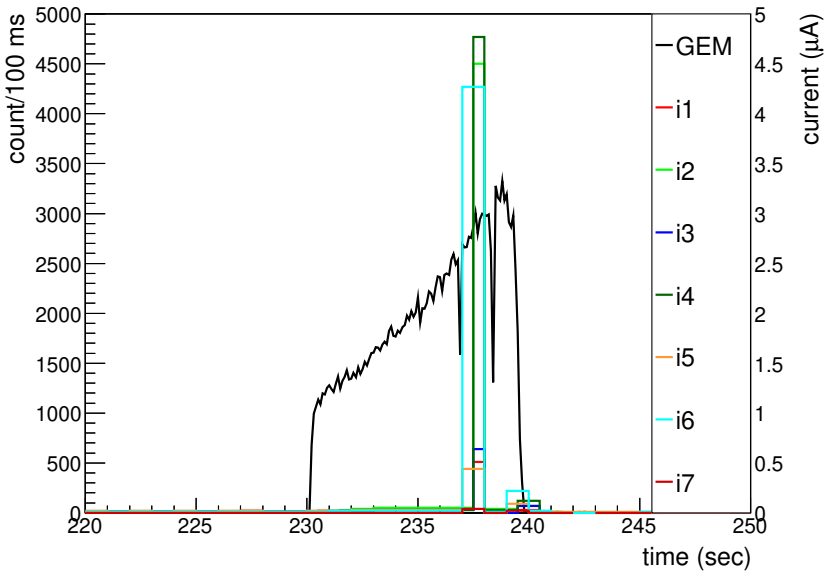

Figure 4.61: Example of the spill where two sparks are observed. The time axis is shown in the unit of second. i1 to i7, shown in different colours, are the currents corresponding to V1 to V7. The GEM count rate, shown in black, is in the unit of counts/100 ms.

The calculated spark probability as a function of the gain of the module is shown in Fig. 4.62. The gain of the module is measured by using a 5.9 keV Fe^{55} X-ray source. During the beam time, the gain of the detector is found to be within the range of $\sim$ 40000 to 130000 for the operational global GEM voltage ($\Delta V_1 + \Delta V_2 + \Delta V_3$) settings of 1120 V to 1185 V. In this operational global voltage range of 1120 V to 1185 V and the corresponding gain between 40000 to 130000, taking 30 primary electrons per incident pion (minimum ionising particle) in the 3 mm drift gap, the total number of electrons reaching readout will be 1.2×10^6 to 3.9×10^6 respectively. This corresponds to a total charge between 192 fC to 624 fC respectively. In this study, the spark probability of the SM triple GEM detector in the "3-2-2-2 configuration" is found to be $\sim 10^{-7}$ for a 150 GeV/c pion beam of rate 150 kHz with a gas gain between 40000 and 80000.

To calculate the spark probability of the GEM module in the shower environment, pion beam of rates 6, 50 and 120 kHz have been employed to a 20 cm thick

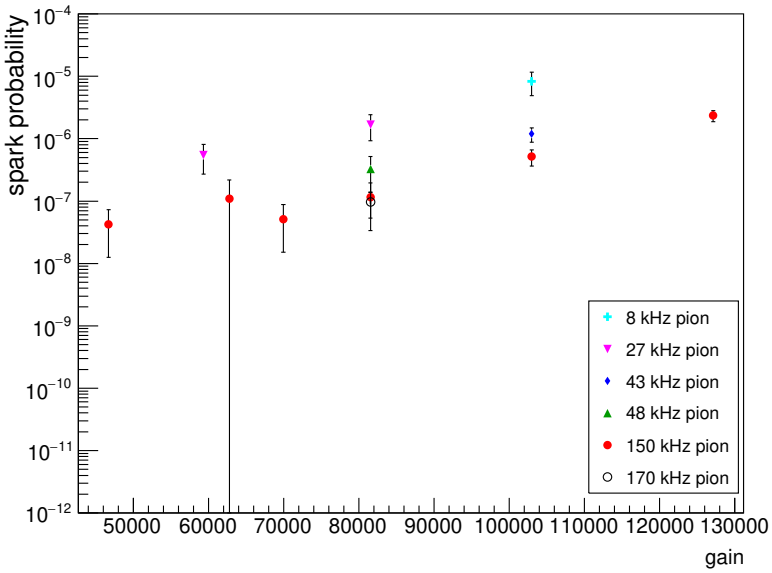

Figure 4.62: Spark probability of the detector as a function of the gain.

iron slab. The voltage settings of the detector were ΔV_1=385 V, ΔV_2=380 V and ΔV_3=375 V respectively and the gain is $\sim$ 60000. The total integrated number of pions incidents on the iron slab for these three rates were 3.32×10^5, 2.40×10^6 and 1.10×10^6 respectively. No spark is detected in these settings using both the methods i.e. drop in the GEM counting rate and jump in the current. Though, during the shower, the number of secondary particles on the detector surface (13.009 secondary particles reached the detector plane per pion beam) increases as it is seen from the FLUKA simulation, still no spark has been identified. The particle density per unit surface area of the GEM detector is much smaller for the secondary particles produced in the shower than that for the pion beam. In these measurements, the particles hitting per unit area of the GEM detector for the pion beams of rate 8, 27, 43, 48, 150 and 170 kHz are $\sim$ 0.8, 2.7, 4.3, 4.8, 15 and 17 kHz/mm^2 respectively and that for shower produced by pion beam of rate 6, 50 and 120 kHz are $\sim$ 0.008, 0.065 and 0.16 kHz/mm^2 respectively. That is the probable reason for not getting any spark in the shower setup.

The efficiency of the chamber is also calculated for different particle rates by taking the ratio of the three-fold (3F) signal from the two finger scintillators and the GEM chamber and dividing it by the two-fold (2F) signal obtained from the two finger scintillators. The variation of the efficiency of the chamber as a function of the global GEM voltage, i.e (ΔV_1+ΔV_2+ΔV_3), is shown in Fig. 4.63. For this pion and muon beams are used. It is observed that, with

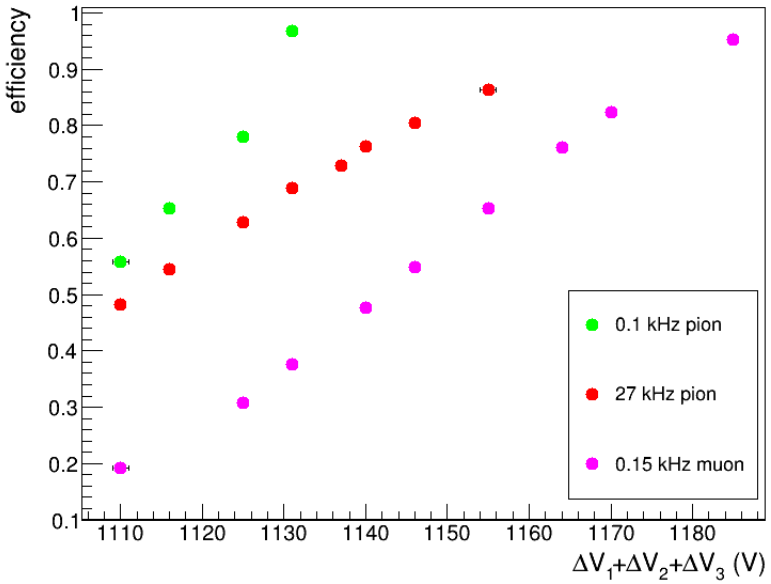

Figure 4.63: Efficiency (3F/2F) as a function of the sum of the voltages across the GEM foil for different particle rates.

increasing particle rates, the efficiency of the chamber decreases and that is mainly due to the presence of the protection resistance of 10 MΩ. With increasing particle rates, the current at the top of the GEM foil increases and as a result, the potential drop across the protection resistance increases with increasing particle rates. The potential drop across the protection resistance effectively reduces the ΔV across the GEM foil and thus the gain of the chamber decreases and the efficiency of the chamber decreases.

The comparison between the spark probability measurement for the DM triple GEM detector, as reported earlier [27], and the present measurement for the SM triple GEM detector are the followings:

The drift gap of the DM GEM chamber was 2 mm. In the case of the DM triple GEM detector, the spark probability was measured mostly for the shower induced by a pion beam with a 10 cm thick iron absorber and also for a pure pion beam. In this operational global voltage range, the gain of the detector was measured to vary between 20,000 and 50,000. 11 MΩ protection resistors were employed in all seven channels. In this study, the spark probability was found to be $\sim 10^{-7}$ for the 150 GeV/c pion beam and also for the shower. On the other hand, the drift gap of the SM GEM detector was 3 mm. The spark probability was measured mainly for pion beam of different rates and shower produced by pion beams of rates of 6, 50 and 120 kHz after hitting an iron slab of thickness 20 cm. The detector was operated at a gain between 40000 and 130000. A protection resistance of 10 MΩ has been employed only to the top plane of each GEM foil and to the drift plane. In this case, the spark probability is $\sim 10^{-7}$ for a 150 GeV/c pion beam of rate 150 kHz with a gain between 40000 and 80000. No spark has been observed during the shower.

In this test beam, the SM triple GEM detector was operated at a very high gain. Actually, in CBM-MuCh the GEM chambers will be operated at a gain $\sim$ 5000-8000. Extrapolating the value of the spark probability for a 150 GeV/c pion beam of rate 150 kHz is coming $\sim 10^{-9}$ at gain $\sim$ 5000-8000. The value of the spark probability, obtained from this beam test, is a little bit high for the operation of the CBM muon chambers at a gain of $\sim$ 5000-8000.

4.9 Summary

A systematic study of the characteristics of triple GEM detector prototypes is carried out. Four important aspects of triple GEM detectors such as uniformity, stability, charging-up and spark probability are addressed.

The efficiency of the SM triple GEM chamber is measured using cosmic ray muons. An efficiency of >90% is obtained with a ΔV of 390 V onwards across each of the GEM foils. The time resolution of the SM triple GEM chamber is

measured using 661 keV gamma from the ^{137}Cs source. The best time resolution is obtained at a ΔV of 390 V across each of the GEM foils and the value is 44.08 $\pm$ 9.91 ns. The probable reason behind observing the relatively higher timer resolution is due to the time walk effect.

The uniformity study over the active area of a DM chamber with a ΔV of 385.9 V across each GEM foil and using Ar/CO_2 gas mixture in the 70/30 volume ratio shows a 10 % variation in the gain and a 20 % variation in the count rate and energy resolution. The uniformity of a SM triple GEM chamber is investigated with and without considering the effect of charging-up of the GEM foil. Similar behaviour in the uniformity of the performance is observed with and without considering the charging-up effect of the GEM foils.

The long-term stability in terms of gain and energy resolution of the DM chamber is investigated with ΔV of 383.7 V, 359 V and 331 V across each GEM foil, when operated with Ar/CO_2 gas mixture in 70/30, 80/20 and 90/10 volume ratio respectively. No degradation is observed in gain and energy resolution other than a fluctuation of $\sim$10% after accumulating a total charge of 6.0 mC/mm^2, 0.6 mC/mm^2 and 1.8 mC/mm^2 for Ar/CO_2 gas mixtures in 70/30, 80/20 and 90/10 volume ratios respectively. In the case of the SM triple GEM chamber, the long-term stability study with Ar/CO_2 gas mixture in the 70/30 volume ratio is carried at the ΔV of 404 V across each of the GEM foils. No significant degradation is observed in the normalised gain and normalised energy resolution other than a variation of $\sim$5% after accumulating a total charge of 0.85 mC/mm^2.

A detailed study of the effect of charging-up phenomena on the SM and DM triple GEM detector prototype is performed. The findings are summarised in Table 4.6. In Fig. 4.64, the variation in the charging-up time of the SM and DM triple GEM chamber is plotted as a function of measured gain of the chamber with different irradiation rates. It is observed that with increasing gain, the charging-up time of the chamber is shifting toward lower values.

Table 4.6: Summary of charging-up time for different radiation flux and gain of the SM and DM triple GEM chambers.

GEM foil	ΔV (V)	Electric fields (kV/cm)	Flux (kHz/mm^2)	Saturated gain	Charging-up time (h)
DM	390	Drift field: 2.3	$\sim$ 0.08	$\sim$ 4900	2.376 ($\pm$ 0.020)
		Transfer fields: 3.5	$\sim$ 0.20	$\sim$ 5100	1.524 ($\pm$ 0.008)
		Induction field: 3.5	$\sim$ 3.20	$\sim$ 5500	1.395 ($\pm$ 0.004)
SM	402.7	Drift field: 2.4 Transfer fields: 3.6 Induction field: 3.6	$\sim$ 4.8	$\sim$ 9000	0.594 $\pm$ 0.001
	409	Drift field: 2.4	$\sim$ 0.04	$\sim$ 13000	0.268 ($\pm$ 0.003)
		Transfer fields: 3.6	$\sim$ 0.14	$\sim$ 11800	0.297 ($\pm$ 0.001)
		Induction field: 3.6	$\sim$ 0.42	$\sim$ 12600	0.280 ($\pm$ 0.002)
			$\sim$ 7.78	$\sim$ 12200	0.228 ($\pm$ 0.001)
	410	Drift field: 2.4	$\sim$ 0.04	$\sim$ 13800	0.285 ($\pm$ 0.005)
		Transfer fields: 3.7	$\sim$ 0.14	$\sim$ 13700	0.351 ($\pm$ 0.003)
		Induction field: 3.7	$\sim$ 0.42	$\sim$ 13500	0.407 ($\pm$ 0.002)
			$\sim$ 7.78	$\sim$ 13400	0.335 ($\pm$ 0.002)
	411	Drift field: 2.4	$\sim$ 0.14	$\sim$ 14500	0.190 ($\pm$ 0.002)
		Transfer fields: 3.7	$\sim$ 0.42	$\sim$ 14700	0.436 ($\pm$ 0.002)
		Induction field: 3.7	$\sim$ 7.78	$\sim$ 14000	0.186 ($\pm$ 0.001)

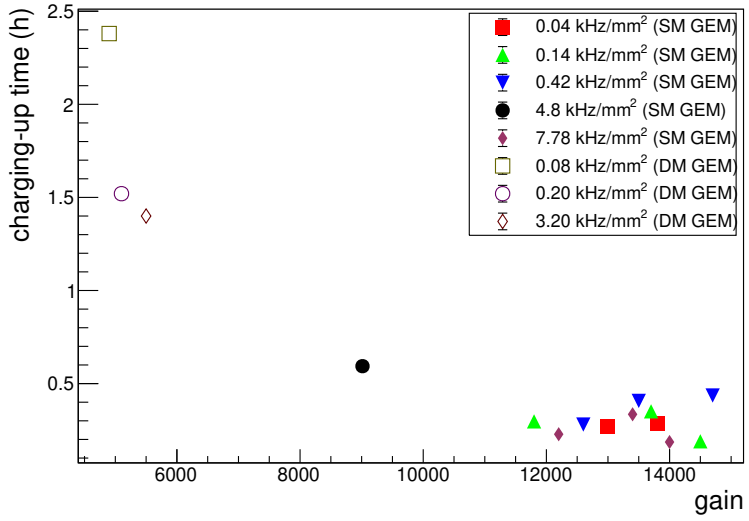

Figure 4.64: Charging-up time as a function of the measured gain of the SM and DM triple GEM chambers.

The spark probability of a SM triple GEM chamber prototype is measured at the CERN SPS/H4 beam-line facility. The chamber is tested with 150 GeV/c pion beam. An iron block of thickness 20 cm is placed in the beam-line and before the GEM chamber under testing to create a shower. The spark in the chamber is identified by looking for the drop in the GEM counting rate as compared to the beam counters. It is observed that, for a gain between 40,000 to 80,000, the spark probability is $\sim 10^{-7}$ for the pion beam of momentum 150 GeV/c and rate of $\sim$150 kHz. No spark is observed for the shower produced by the pion beam due to the relatively smaller particle flux, as compared to the pion beam setup.

References

[1] S. Chattopadhyay *et al.*, Technical Design Report for the CBM : Muon Chambers (MuCh); GSI, 2015; https://repository.gsi.de/record/161297

[2] R. P. Adak *et al.*, Nucl. Instr. Meth. Phys. Res. A 846, 29 (2017)

[3] You Wen-Hao *et al.*, Chinese Physics C Vol. 39, No. 4, 046001 (2015)

[4] CDT CASCADE Detector Technologies GmbH, Hans-Bunte-Str. 8-10, 69123 Heidelberg, Germany; www.n-cdt.com

[5] S. Roy *et al.*, Nucl. Instr. Meth. Phys. Res. A 936, 485 (2019)

[6] A. Kumar *et al.*, 2021 JINST 16 P09002

[7] M. C. Altunbas *et al.,* Nucl. Instr. Meth. Phys. Res. A 515, 249 (2003)

[8] S. Chatterjee *et al.,* Nucl. Instr. Meth. Phys. Res. A 1014, 165749 (2021)

[9] S. Chatterjee *et al.,* JINST 15, T09011 (2020)

[10] D. Nag *et al.,* ADNHEAP 2017 Springer Pros. in Phys. 201, 211

[11] S. Chatterjee *et al.,* arXiv:2206.04051

[12] S. Chatterjee *et al.*, Nucl. Instr. Meth. Phys. Res. A 936, 491 (2019)

[13] M. Gola *et al.*, Nucl. Instr. Meth. Phys. Res. A 951, 162967 (2020)

[14] Y. Huang *et al.*, Chinese Physics C Vol. 40, No. 4, 046001 (2016)

[15] B. Azmoun *et al.*, IEEE Nuclear Science Symposium Conference Record, VOL. 6, pages 3847 - 3851, (2006)

[16] M. V. Nemallapudi, Master's Thesis at University of Arkansas. 2012 https://scholarworks.uark.edu/etd/533/

[17] M. Alfonsi, Nucl. Instr. Meth. Phys. Res. A 671, 6 (2012)

[18] P. M. M. Correia *et al.*, JINST 9 (2014)

[19] Philip Hauer *et al.*, Nucl. Instr. Meth. Phys. Res. A 976, 164205 (2020)

[20] V. Tikhonov *et al.*, Nucl. Instr. Meth. Phys. Res. A 478, 452 (2002)

[21] M. C. Altunbas *et al.*, Nucl. Instr. Meth. Phys. Res. A 515, 249 (2003)

[22] CERN ROOT; https://root.cern/

[23] S. Chatterjee *et al.,* Nucl. Instr. Meth. Phys. Res. A 1014, 165749 (2021)

[24] S. Chatterjee *et al.*, J. Phys.: Conf. Ser. 1498, 012037 (2020)

[25] M. Kalliokoski *et al.,* Physics Procedia 37, 464 (2012)

[26] https://www.emsdiasum.com/microscopy/technical/datasheet/77708.aspx

[27] S. Biswas *et al.*, Nucl. Instr. Meth. Phys. Res. A 800, 93 (2015)

[28] LABVIEW; http://www.ni.com/labview/whatsnew/

[29] G. Corradi, *et al.*, Nucl. Instr. Meth. Phys. Res. A 572, 96 (2007)

[30] S. Biswas *et al.*, Journal of Instrumentation 8, C12002 (2013)

[31] FLUKA simulation package; http://www.fluka.org/fluka.php

[32] A. Senger, CBM Progress Report, 2011

[33] G. Battistoni, *et al.*, AIP Conference Proceedings 896 (2007) 31, Proc. of Hadronic Shower Simulation Work-shop 2006

[34] https://meroli.web.cern.ch/Lecture_landau_ionizing_particle.html

[35] S. Bachmann, *et al.*, Nucl. Instr. Meth. Phys. Res. A 470 (2001) 548

[36] G. Bencivenni, *et al.*, Nucl. Instr. Meth. Phys. Res. A 494, 156 (2002)

[37] M. Alfonsi, *et al.*, Nucl. Instr. Meth. Phys. Res. A 518, 106 (2004)

Chapter 5

GEM chambers at mini-CBM beam time campaign

5.1 Overview

The mini-CBM (mCBM) campaign [1] is the precursor of the CBM experiment [2, 3] at the existing SIS18 facility in GSI [4] Germany and consists of all the detector sub-systems which are planned to be a part of the CBM experiment. The mCBM campaign is a part of the FAIR [5] Phase 0 program which is launched to investigate the performance of different detector sub-systems under CBM like environments. The proposed aims of the mCBM campaign are the following:

- Understanding the performance of the detector sub-systems in a high rate nucleus-nucleus collision environment
- Implementation of free-streaming data acquisition including data transfer and handling
- Implementation and tuning of online track and event reconstruction as well as event selection algorithms
- Understanding of detector control systems

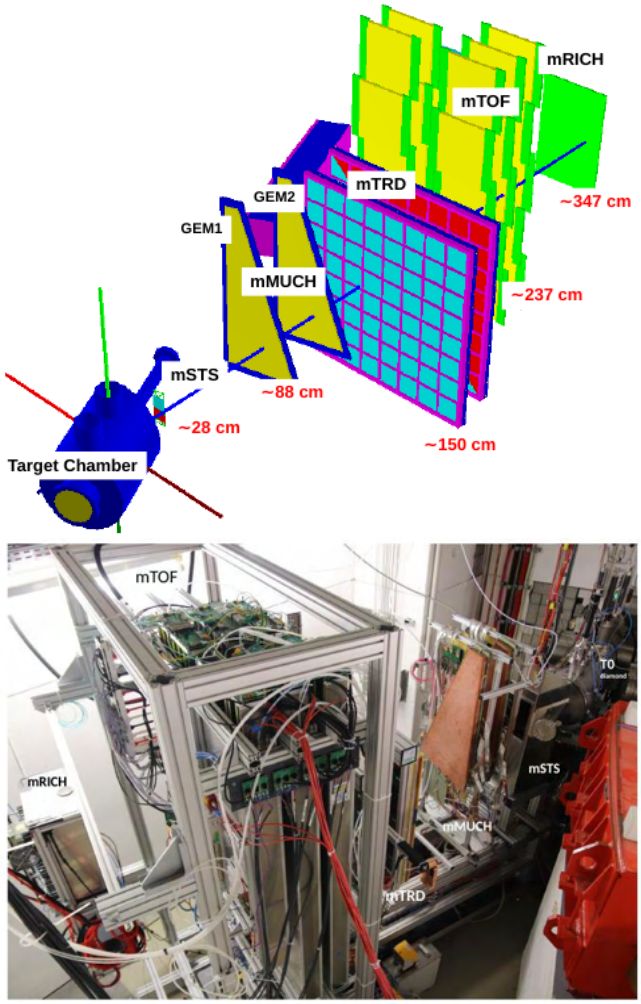

Figure 5.1: Schematic of the mCBM experimental setup (top). Detectors are placed at 25° from the beam axis. The detector sub-systems, placed downstream of the target chamber, are the following: mSTS - mini-Silicon Tracking Station, mMUCH - mini-Muon Chamber System, mTRD - mini-Transition Radiation Detector, mTOF - mini-Time Of Flight, mRICH - mini-Ring Imaging Cherenkov. The view from the mCBM cave is shown in the bottom figure.

Along with all other detectors, two real size (Module 1: Length: $\sim$ 80 cm, Module 2: Length: $\sim$ 100.5 cm) SM triple GEM detector modules are installed and commissioned at the mCBM experiment as a part of the mini-MUCH (mMUCH) setup [6]. The schematic of the mCBM experimental setup is shown in Fig. 5.1 (top). The GEM modules which are placed in the mCBM cave at GSI are shown in Fig. 5.2.

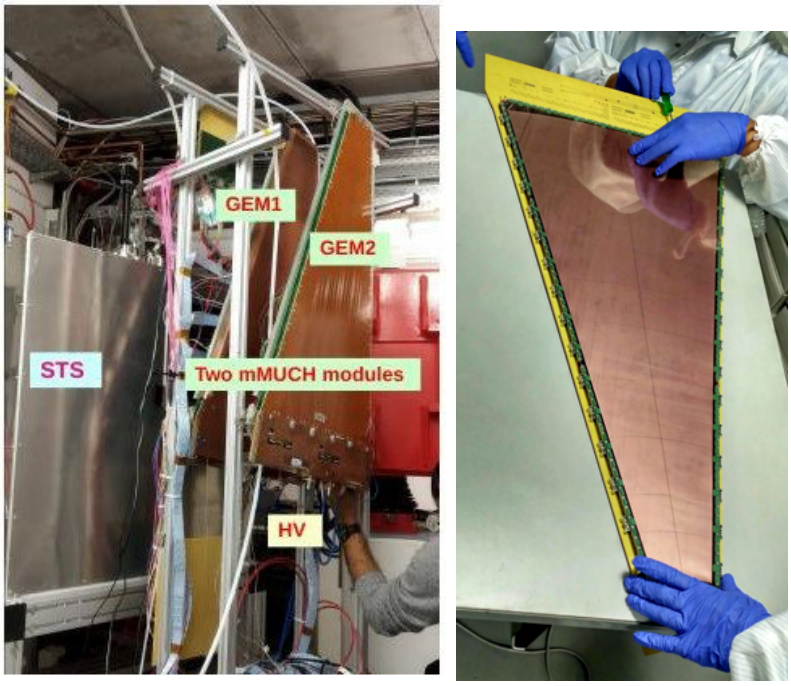

Figure 5.2: Left: Photograph of the experimental setup showing different detector sub-systems installed at the SIS18 facility of GSI for the mCBM campaign. Right: Real size trapezoidal GEM module used as a mMUCH chamber.

The detector performance is studied for a ^{40}Ar beam with beam kinetic energy of 1.7 A GeV on a 2.5 mm thick ^{197}Au target at an average intensity of $\sim 5 \times 10^6$ per spill. The data is analyzed using the CBMROOT analysis framework [7]. The noisy channels of the Front End Boards (FEB) are masked to observe a clear spill structure. In Fig. 5.3, the spill structure as recorded by the GEM chambers is shown along with that of T0 detector.

The gain and time resolution of the chambers are calculated after performing the clustering and hit reconstruction with the data taken by the mMUCH setup and the free-streaming CBM DAQ system. The variation of time resolution of the GEM1 chamber is shown in Fig. 5.4. The mean time resolution is found to be $\sim$ 19 ns with a variation of $\sim$ 5 ns over the scanned area of the chamber. The variation of the gain of the GEM1 chamber is shown in Fig. 5.5. The gain is found to be varied $\sim$ 15 % over the scanned area of the chamber. The spatial resolution correlation among the chambers is also studied. The details of the test setup, data analysis techniques and results are discussed in Ref. [6].

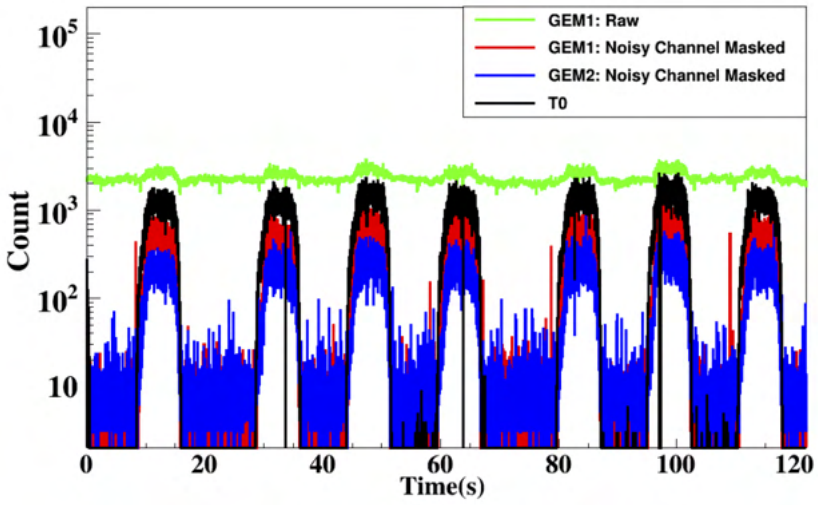

Figure 5.3: Spill structure of GEM1, GEM2 and TO detectors. The noisy channels are masked in the FEBs to see the clear spill structure.

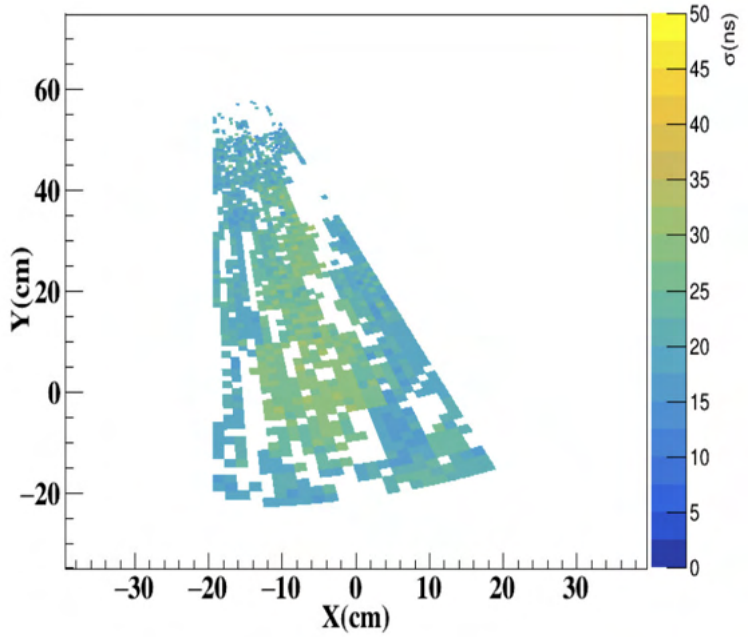

Figure 5.4: Time resolution map of GEM1 chamber. The plot is taken from Ref. [6].

5.2 Summary

Two large size SM triple GEM modules have been tested in the mCBM campaign [1] at the SIS-18 facility in GSI [4], as a part of the FAIR [5] Phase 0 program. The chambers are tested with the ^{40}Ar beam of kinetic energy 1.7 A GeV

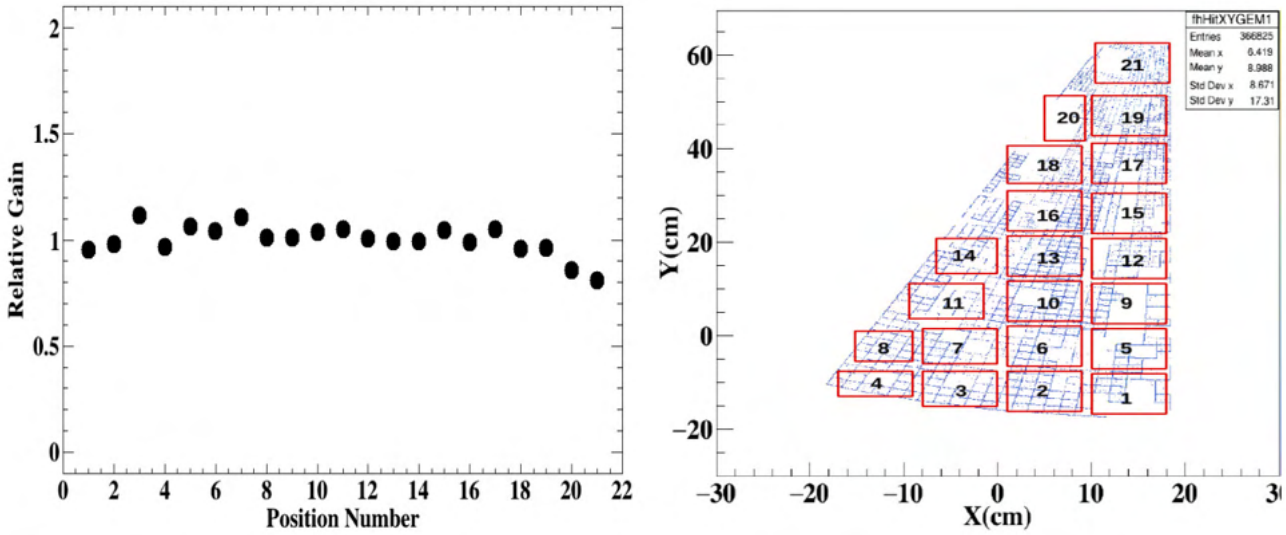

Figure 5.5: Gain map of GEM1 chamber. The active area of the chamber is divided into 21 smaller areas as shown in the right figure. The left figure indicates the relative gain values at the different areas of the chamber. The plots are taken from Ref. [6].

on a 2.5 mm thick ^{197}Au target. The uniformity in gain and time resolution of the chambers is studied. Spatial correlation between the GEM chambers is also investigated [6]. No significant deterioration is observed in their expected performance under the realistic experimental scenario in the nucleus-nucleus collision system.

The triple GEM detector, as described here, is found to be stable under high radiation. This makes it a suitable candidate as a tracking device in the CBM-MuCh setup as well as for any high-rate experiment.

References

[1] mCBM@SIS18, The CBM Collaboration; http://dx.doi.org/10.15120/GSI-2019-00977

[2] The CBM experiment; https://www.cbm.gsi.de/

[3] P. Senger and N. Herrmann, Nucl.Phys.News 28 (2018) 2, 23

[4] SIS18 accelerator facility at GSI; https://www.gsi.de/en/work/accelerator_operations/accelerators/heavy_ion_synchrotron_sis18

[5] The Facility for Antiproton and Ion Research FAIR; https://fair-center.eu/

[6] A. Kumar et al., 2021 JINST 16 P09002

[7] The CbmRoot Framework; http://computing.gitpages.cbm.gsi.de/cbmroot/

Chapter 6

Summary & outlook

Heavy-Ion (HI) experiments are aimed to explore the properties of a new state of matter, expected to be created after the collision of nuclei at relativistic speeds, known as the Quark Gluon Plasma (QGP). The Compressed Baryonic Matter (CBM) experiment at the future Facility for Antiproton and Ion Research (FAIR), Germany will explore the QCD phase diagram at low temperature and moderate to high baryon density regime. The foreseen energy domain of FAIR (SIS100) will provide the unique possibility to investigate nuclear matter at extremely high densities very similar to the core of the neutron stars. The foreseen high interaction rates at CBM will also provide a unique facility to study the rare probes with better precession. The expected peak interaction rate is $\sim$ 10 MHz. Such unprecedented interaction rates will require detectors which can handle high particle fluxes. The Muon Chamber (MuCh) sub-system at CBM will dedicatedly be used for the tracking and identification of muon pairs coming from the decay of Low Mass Vector Mesons (LMVM) and J/ψ's. In order to handle the expected large particle fluxes ($\sim$ 0.5 MHz/cm^2), Gas Electron Multiplier (GEM) detectors will be used in the first two stations of MuCh. Moreover, Resistive plate Chambers (RPC) is one of the options for the last two stations due to the relatively lower particle fluxes ($\sim$ 30 kHz/cm^2). The motivation of this thesis work was to study of the feasibility of di-muon detection at CBM SIS100 energies using Monte Carlo (MC) based simulations

and to understand the performance of triple GEM chamber prototypes under high irradiation environment.

The thesis was structured in the following way.

The first chapter (Chapter 1) gave a brief introduction to the High Energy Physics (HEP) experiments, their goals and the challenges. After the brief discussion about the HEP experiments, the uniqueness and opportunities of the CBM experiment were discussed. The physics goals and the potential observables of the CBM experiment were discussed afterwards. A brief summary of the different ongoing or planned fixed target Heavy-Ion (HI) experimental facilities was given at the end of Chapter 1.

In Chapter 2, the feasibility study of di-muon detection at CBM SIS100 energies was discussed. This chapter included the following investigation:

Optimisation of the MuCh geometry configuration:

The MuCh detector sub-system consists of several hadron absorbers and the triplet of tracking detectors, as placed in between the absorbers. The first absorber was of 58 cm thickness and was made of Concrete and Graphite. The rest of the absorbers were made of iron with thicknesses of 20 cm, 20 cm, 30 cm and 100 cm. The 100 cm thick iron absorber would only be used for the J/ψ measurement setup of MuCh.

The optimisation study of the MuCh absorber configuration was carried out by studying the ω ($\rightarrow \mu^+\mu^-$) reconstruction at $\sqrt{s_{NN}} = 4.1$ GeV central Au+Au collision with different absorber thickness configurations. These studies revealed that the reduction of the thickness of the iron absorbers, of the order of a few centimetres, would degrade the performance of di-muon measurements at SIS100 energies. It could be anticipated that a surface tolerance of the order of a few millimetres might preserve the feasibility of di-muon detection.

After studying the effect of absorber thicknesses on the reconstruction performance of ω ($\rightarrow \mu^+\mu^-$), the effect of the MuCh 5^{th} absorber on the J/ψ ($\rightarrow \mu^+ \mu^-$) reconstruction was investigated for a central Au+Au collision

system at $\sqrt{s_{NN}}$ = 4.54 GeV. The realistic design of the MuCh 5^{th} absorber was implemented as suggested by the MuCh mechanical team. To mimic the situation of non-uniform iron plates, several vertical gaps were implemented between the consecutive iron plates used in the MuCh 5^{th} absorber. From this study, it was concluded that the reconstruction performance of J/ψ ($\rightarrow \mu^+\mu^-$) would rather be insensitive to the foreseen vertical gaps of realistic size, between the absorber plates.

After optimizing the MuCh absorber configuration, the reconstruction performance was investigated with the realistic design of the MuCh detector subsystem for different collision energies foreseen at CBM SIS100.

Reconstruction of freeze-out cocktail:

The reconstruction of the freeze-out cocktail in the di-muon channel was performed for the Au+Au collision system at $\sqrt{s_{NN}}$ = 2.9, 4.1 and 4.9 GeV. The di-muon combinatorial background was calculated using Super Event (SE) technique. The signal to background (S/B) ratio was investigated for the mentioned energies. It was observed that the S/B values were less than 1 and therefore the estimation of the di-muon combinatorial background was very crucial. Four different techniques of background estimation namely the super event technique, mixed event technique, event by event analysis and like-sign method were also investigated and discussed in Chapter 2.

The reconstruction of J/ψ ($\rightarrow \mu^+\mu^-$) was carried out for central Au+Au and Ni+Ni collision systems at $\sqrt{s_{NN}}$ = 4.54 and 5.47 GeV. The efficiency$\times$acceptance correction was performed in order to compare the reconstructed spectra with the input spectra. This study concluded that the reconstruction of J/ψ ($\rightarrow \mu^+\mu^-$) was feasible with the model predicted multiplicities and the MuCh detector sub-system.

After discussing the feasibility of di-muon detection using the MuCh detector sub-system at CBM SIS100 energies, the focus was shifted towards the R&D

of the triple GEM chambers where the primary goal was to understand the behaviour of the chamber under high irradiation.

The historical development of advanced gaseous detectors was discussed in Chapter 3 with the introduction to the GEM detector and its applications.

Chapter 4 presented the results of detailed R&D on triple GEM prototypes with Ar/CO_2 gas mixtures and an Fe^{55} X-ray source of 5.9 keV energy. This chapter included the following investigations:

Basic characterisation of triple GEM chambers:

This section presented the steps for calculating the gain and energy resolution of the GEM prototypes. The variation of gain and energy resolution was studied for different voltages applied across the GEM foil. The efficiency and time resolution measurement of the chamber was also discussed in this section.

Effect of environmental parameters on the gain and energy resolution:

The performance of any gaseous detector depends on the variation of the ambient environmental parameters. In this section, the correlation of gain and energy resolution of the GEM chamber was discussed with the ambient temperature, pressure and humidity variation. The procedure to nullify the effects of environmental parameter variation on the performance of the chamber was also discussed in this section.

Uniformity in performance in terms of gain, energy resolution and count rate:

Uniformity in performance is an essential criterion for any tracking device. Since GEM is proposed as the tracking device in the CBM-MuCh detector subsystem, it is very important to investigate the uniformity in performance in terms of gain, energy resolution and count rate of the GEM prototypes. For the Double Mask (DM) triple GEM chamber, over the scanned area, a 10% fluctuation in gain and a 20% fluctuation in energy resolution and count rate were observed. For the Single Mask (SM) triple GEM chamber, the variation in

gain and count rate was found to be 10% and the variation in energy resolution was 15%. The observed variation in the performance of the chamber could be attributed to the intrinsic inhomogeneity of the GEM geometry and the gap between the respective GEM foils.

The Real size GEM chambers, tested at the mini-CBM (mCBM) beam time campaign also showed a variation of $\sim$ 15 % in the measured gain value over the active area of the chamber. The details were discussed in Chapter 5.

Charging-up effect:

The presence of the dielectric (Kapton) medium inside the active area of the chamber changes its behaviour when exposed to external irradiation. The dielectric media gets charged up due to the accumulation of the charges on the surface of the dielectric and as a result, the gain of the chamber increases initially and then reaches a constant value asymptotically. The dependence of the charging-up effect with irradiation rates and with the gain of the chamber has been investigated. It was observed that with increasing charge density, the charging-up time shifts toward smaller values. The typical charging-up time was found to be 0.2-0.4 hours at a typical gas gain of $\sim 10^4$. The effect of dielectric polarisation on the gain of the chamber was also investigated for different irradiation rates and at the different gains of the chambers.

Long-term stability study:

The long-term stability of the GEM prototypes was carried out using the Fe^{55} X-ray source of 5.9 keV energy. The novelty of this work was that the same source was used to irradiate the chamber and also to measure the X-ray spectra. The DM triple GEM chamber showed only a fluctuation of $\sim$ 20% in normalised gain and normalised energy resolution after an accumulation of $\sim$ 6 mC/mm^2 charge. For the SM triple GEM chamber, a fluctuation of $\sim$ 5 % was observed after an accumulation of $\sim$ 0.8 mC/mm^2 of charge.

The probable reason behind the observation of larger variation in the normalised gain for the higher accumulated charge per unit area was due to the effect of the

environment parameters which cannot be entirely excluded by performing the T/p normalisation. The detector was irradiated continuously with 5.9 keV X-ray from the Fe^{55} source for long durations with Ar/CO_2 gas mixtures. Over this long period, some sudden changes in the environmental parameter affect the normalisation of the data. To nullify such effects, a better idea would be to use two chambers in the same gas line and use one chamber as the reference chamber and the other be the irradiating chamber. In this way, the normalisation can be performed with respect to the reference chamber and any other environmental effects can be eliminated from the data obtained from the chamber.

The typical accumulated charge per unit area for MIP in 10 CBM years is ~ 0.76 mC/mm^2. Thus with the investigated limit of accumulated charge using the Fe^{55} X-ray source at the laboratory, it can be concluded that the detector can be used safely for around 10 CBM years.

Measurement of spark probability at CERN SPS beam line facility:

The spark probability of a SM triple GEM chamber was measured at the CERN SPS/H4 beam line facility with a pion beam of momentum 150 GeV/c and also in the shower environment with the inclusion of iron block in front of the detector. The spark in the chamber was identified by looking for the drop in the GEM counting rate as compared to the beam counters. It was observed that for a gain between 40,000 to 80,000, the spark probability was $\sim 10^{-7}$ for the pion beam of momentum 150 GeV/c and at a rate of $\sim$ 150 kHz. In this test beam experiment, no spark was observed for the shower produced by the pion beam due to the relatively smaller particle flux as compared to the pion beam setup.

The performance of the real-size GEM chambers at the mCBM beam time campaign was discussed in Chapter 5. The mCBM at the existing SIS18 beam line facility is the precursor of the main CBM experiment. Real-size GEM chambers were tested in the nucleus+nucleus collision environment and satisfactory performance was observed under the realistic experimental scenario in the nucleus-nucleus collision system.

The results obtained from the works presented in this thesis can conclude that the GEM detector can be used as the tracking device in the first two stations of CBM-MuCh and also the measurement of muon pairs coming from the decay of LMVM and J/ψ is found to be feasible at SIS100 energies with the MuCh detector sub-system.

As a continuation of the presented work, the following studies might be taken as a future work plan by the interested groups;

- The charging-up effect of GEM foils is mainly attributed to the accumulation of charges on the Kapton surface which dynamically changes the electric field strength inside the GEM holes and as a result the gain of the chamber changes. In this thesis, the charging-up effect is investigated for triple GEM chambers with different irradiation rates and at the different gains of the chambers. However, it is very difficult to decouple the effect of charging up for the individual GEM foils. Therefore, it would be really interesting to study the effect of charging up on the individual foils and compare it with the observed effect in the triple GEM prototypes. Also, it would be quite interesting to implement the observed phenomena of the charging-up effect in the GEM foil in the simulation and compare the simulated results with the measured data.

- The simulation performed for the course of this thesis was done on the event-by-event method. However, in the real experiment due to the foreseen high interaction rates, the data will be taken in the free streaming mode. Therefore in the final data, no event information would be available. Several investigations are ongoing to do the reconstruction of muon pairs in a time-based mode. A similar attempt was also made as a parallel work of this thesis and the outcomes were reported in V. Singhal, S. Chatterjee *et al.*, 2021 JINST 16 P08043. The detailed investigation of the time-based reconstruction and its comparison with the well-known event by event reconstruction would be really interesting. It would also

be important to investigate in the context of CBM and also for upcoming future experiments where free streaming data acquisition will be used.

Journal pre-prints

Nuclear Inst. and Methods in Physics Research, A 1014 (2021) 165749

Contents lists available at ScienceDirect

Nuclear Inst. and Methods in Physics Research, A

journal homepage: www.elsevier.com/locate/nima

Study of charging-up effect for a single mask triple GEM detector

S. Chatterjee *, A. Sen, S. Das, S.K. Ghosh, S. Biswas

Department of Physics and Centre for Astroparticle Physics and Space Science (CAPSS), Bose Institute, EN-80, Sector V, Kolkata 700091, India

ARTICLE INFO

Keywords:
Gas electron multiplier (GEM)
Single mask foil
High voltage (HV)
Charging-up
Polarisation
Gain

ABSTRACT

With the advancement of the accelerator systems and the requirements of high luminosity particle beams to reach different physics goals, detectors with good position resolution and high rate handling capability have become essential for designing any High Energy Physics (HEP) experiments. The Gas Electron Multiplier (GEM) detectors are widely used in many HEP experiments as a tracking device because of their good spatial resolution and rate handling capability.

The presence of the dielectric medium inside the active volume of the GEM detector changes its behaviour when exposed to external radiation. This mechanism is commonly referred as the charging-up effect. In this article, the effect of the charging-up phenomenon and the initial polarisation effect of the dielectric on the gain of the chamber are reported for a single mask triple GEM chamber with Ar/CO_2 gas mixture.

1. Introduction

Gas Electron Multiplier (GEM) detector, introduced by Fabio Sauli in 1997 [1], is used in many HEP experiments [2] for its high rate handling capability (~1MHz/mm^2) [1] and good position resolution (~ 70 μm) [3]. The micro pattern structure of the foil is utilised to achieve good position resolution, to reduce the ion backflow in case it is used in a drift chamber and also to handle high rates [4–8]. A standard GEM foil consists of a 50 μm Kapton foil with 5 μm copper cladding on both sides. A large number of holes are etched into the Copper cladded Kapton foil using the photolithographic technique [9]. Depending on the etching technique, the GEM foils are classified as a double mask or single mask type. The single mask technique is developed mainly due to the requirement of the large area GEM chambers where the alignment of the two masks (on the top and bottom side of the copper cladded Kapton foil) is not possible. However, the holes obtained with the single mask technique is asymmetrically bi-conical in shape as compared to the holes obtained with the double mask technique [10]. Different studies are performed to understand the effect of the variation of hole geometry on the final performance of the chamber [11–13]. The dielectric medium (Kapton) present in the active volume of the detector, changes the behaviour of the chamber when exposed to external radiation. As a result, the gain of the chamber increases initially and then reaches a constant value asymptotically. This increase in gain is due to the charging-up of the dielectric medium. Many different groups have reported on the studies to understand the effect of this charging-up phenomenon in GEM detectors [14–16]. The charging-up effect for a double mask triple GEM prototype (10 cm × 10 cm) is reported in Ref. [17]. In the present work, the effect of charging-up on a single mask triple GEM chamber of dimension 10 cm × 10 cm, operated with Ar/CO_2 gas mixture in 70/30 volume ratio is investigated with Fe^{55} X-ray source and reported in this article. The effect of initial polarisation of the dielectric is also investigated for different gain of the chamber with different irradiation rates. The details of the GEM prototype and experimental setup are discussed in Section 2 and the results are reported in Section 3.

2. Detector description and experimental setup

The single mask triple GEM detector prototype consisting of 10 cm × 10 cm standard stretched foils, obtained from CERN is assembled in the clean room of the RD51 laboratory [18]. The drift gap, transfer gap 1, transfer gap 2 and the induction gap of the chamber is kept at 3, 2, 2, 2 mm respectively [19]. A voltage divider resistive chain is used to power the chamber as shown in Fig. 1. A low pass filter is placed between the HV module and resistor chain as shown in Fig. 1 to bypass the ac components present in the HV line. The chamber has an XY printed board (256 X-tracks, 256 Y-tracks) on the base plate and that works as the readout plane. Each of 256 X-tracks and 256 Y-tracks is connected to two 128 pin connectors. However, for the purpose of this work individual track readout is not used. Instead of that, a sum-up board (provided by CERN) is used for each 128 pin connector. A total of 4 sum-up boards are used in this prototype. The signal from one of the sum-up boards is put to a charge sensitive preamplifier (VV50-2) having gain 2 mV/fC and shaping time 300 ns [20]. The output signal from the preamplifier is fed to a linear Fan-in-Fan-out (linear FIFO) module. One analog signal from the linear FIFO is put to a Single Channel Analyser

* Corresponding author.
E-mail address: sayakchatterjee@jcbose.ac.in (S. Chatterjee).

https://doi.org/10.1016/j.nima.2021.165749
Received 30 June 2021; Received in revised form 9 August 2021; Accepted 15 August 2021
Available online 18 August 2021

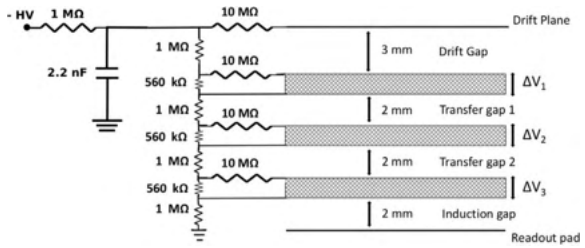

Fig. 1. Schematic of the HV distribution through the resistive chain to different planes of the single mask triple GEM detector. A low pass HV filter is used between the HV line and resistive chain.

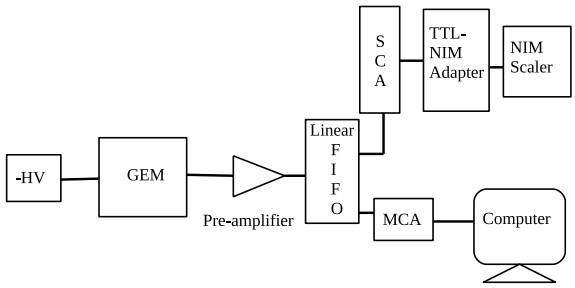

Fig. 2. Schematic of the electronic circuit used for data acquisition.

(SCA) to measure the rate of the incident particle. The SCA is operated in integral mode and the lower level in the SCA is used as the threshold to the signal. The threshold is set at 0.9 V to reject the noise. The discriminated signal from the SCA, which is TTL in nature, is put to a TTL-NIM adapter and the output NIM signal is counted using a scaler. Another output of the linear FIFO is fed to a Multi-Channel Analyser (MCA) to obtain the energy spectra. The schematic of the electronic circuit is shown in Fig. 2. For the entire study, the chamber is operated with pre-mixed Ar/CO_2 gas in a 70/30 volume ratio. A constant gas flow rate of ~3.5 l/hr is maintained using a Vögtlin gas flow meter. Collimators are used to irradiate the chamber with different X-ray flux coming from the Fe^{55} source. The ambient temperature, pressure and relative humidity are monitored continuously using a data logger, built-in house [21].

3. Results

The effect of charging-up of the dielectric inside the active volume of the chamber on its performance is studied. The Fe^{55} energy spectra obtained from the MCA is analysed and the gain is calculated in the same way as mentioned in Ref. [17]. In Fig. 3, the typical Fe^{55} spectrum is shown for the single mask triple GEM chamber at - 5100 V which corresponds to ΔV of 410 V across each of the GEM foils. To measure the initial polarisation effect of the dielectric, the recording of the spectra is started as soon as the HV reached its specific set value and the source is placed at a particular position of the chamber. The same Fe^{55} source is used to irradiate the chamber as well as to record the X-ray spectra. To see the effect of HV and irradiation rates on the initial polarisation of the dielectric, X-ray spectra with different HV and collimator settings are recorded for 20 seconds without any interval between two consecutive measurements. The details of the HV settings used for the study of initial polarisation effect, their corresponding ΔV across each GEM foils, average gain and the electric field strengths in the drift, transfer and induction gaps are listed in Table 1.

Due to the initial polarisation effect, the decrease in gain for the first few minutes as reported in Ref. [17], is also observed in this study. In Fig. 4, the variation of the gain as a function of time is shown for a particle flux of ~ 0.14 kHz/mm^2 at a HV of - 5100 V. The variation in ambient temperature (T) to pressure (p) ratio for the first 20 min

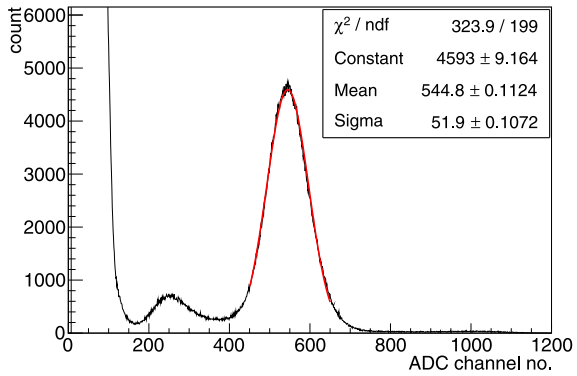

Fig. 3. Typical Fe^{55} spectra at - 5100 V. The ΔV across each of the GEM foil is 410 V. The corresponding drift field, transfer fields and induction field are ~ 2.4 kV/cm, ~ 3.7 kV/cm and ~ 3.7 kV/cm respectively.

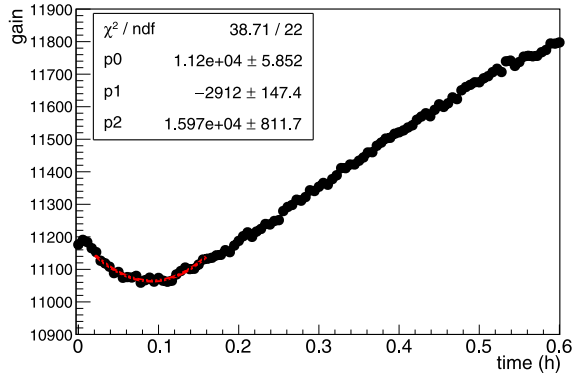

Fig. 4. Variation of the gain as a function of time at a HV of - 5100 V. The initial decrease in gain due to the polarisation effect is fitted with a 2nd degree polynomial.

Table 1
Potential difference across each GEM foil, average gain and fields on the various gaps of the triple GEM chamber for different HV settings. The gain values are measured with an irradiation rate of ~ 0.14 kHz/mm^2.

HV (V)	ΔV (V)	Gain	Drift field (kV/cm)	Transfer field (kV/cm)	Induction field (kV/cm)
- 5085	409	~ 12950	~ 2.4	~ 3.6	~ 3.6
- 5100	410	~ 13600	~ 2.4	~ 3.7	~ 3.7
- 5115	411	~ 14300	~ 2.4	~ 3.7	~ 3.7

is below 1% for all the measurements. Though the variation of gain in any gaseous detector with temperature and pressure is a well known phenomenon [22] but since the variation in temperature to pressure ratio is small, no T/p normalisation is performed for this initial period. To identify the time up to which the gain decreases initially, the gain is fitted with a 2nd degree polynomial using the chi-square minimisation technique, as available in ROOT [23]. From the fitting parameters, the ratio $p1/2p2$ gives the minimum. The fitted curve with the respective chi-square value is shown in Fig. 4. The same technique is repeated for different gain and rate configurations to find out the time up to which the gain reduces due to the initial polarisation of the dielectric and then again starts to increase due to the charging-up effect.

In Table 2, the time (hour) up to which the initial gain decreases due to the initial polarisation effect is listed for different ΔV and irradiation rates.

In Fig. 5, the variation in the time of the initial decrease of gain for different irradiation rates is shown. The data points are fitted with a linear function. It is observed that the time up to which the gain decreases initially due to the polarisation effect is anti-correlated with the voltage across the GEM foils. An effect of the irradiation rates

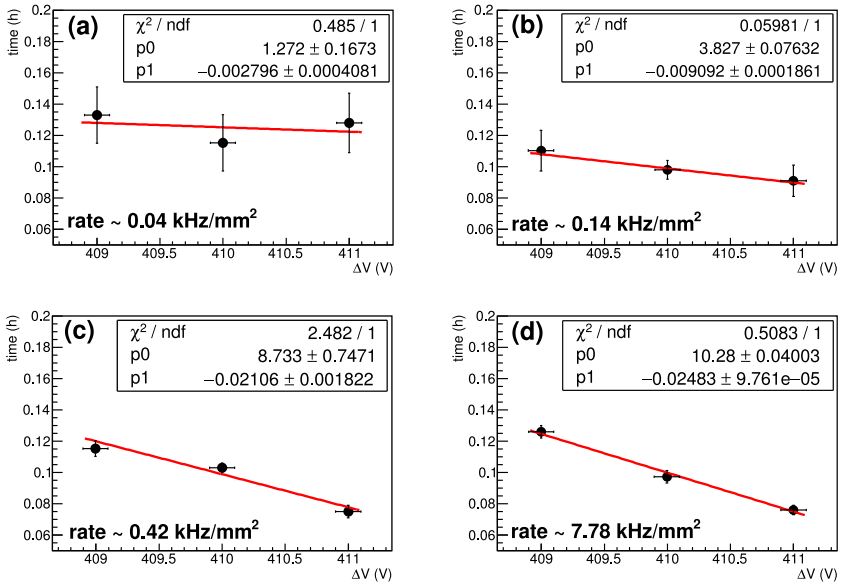

Fig. 5. Variation of the initial gain decrease time as a function of voltage across the GEM foils (ΔV) for different irradiation rates.

Table 2
Variation of time in hour up to which the initial gain decreases with different ΔV and irradiation rates.

ΔV	time (h)			
(V)	rate ~ 0.04 (kHz/mm²)	rate ~ 0.14 (kHz/mm²)	rate ~ 0.42 (kHz/mm²)	rate ~ 7.78 (kHz/mm²)
409	0.133 (± 0.018)	0.110 (± 0.013)	0.115 (± 0.005)	0.126 (± 0.004)
410	0.115 (± 0.018)	0.098 (± 0.006)	0.103 (± 0.003)	0.097 (± 0.004)
411	0.128 (± 0.019)	0.091 (± 0.010)	0.075 (± 0.004)	0.076 (± 0.003)

on the polarisation effect is also observed. As shown in Fig. 6, the rate of decrease of time with ΔV increases with the increasing rate of irradiation.

To observe the effect of charging-up phenomenon, the HV is switched on for around ~ 60 min before starting the measurement to ensure that the polarisation of the dielectric in the GEM foil is over. After that, the measurement is started as soon as the Fe^{55} X-ray source is placed on the chamber. The spectra for 60 s are stored at an interval of 120 s and analysed to obtain the gain of the chamber. Ambient temperature, pressure and humidity are also monitored continuously. To nullify the effect of temperature and pressure on the gain of the chamber, the gain is normalised with T/p and then fitted with the exponential function as discussed in Ref. [17],

$$G = p_0(1 - p_1 e^{-t/p_2}) \quad (1)$$

where G is the normalised gain, p_0 and p_1 are the constants, t is the measured time in hour and p_2 is the time constant of the charging-up effect. In Fig. 7, the variation of normalised gain as a function of time (hour) at a HV of - 5085 V is shown for different irradiation rates as listed in Table 3. In the case of Fig. 7(c), the small jumps in the normalised gain around 0.9 h and 2.2 h are due to some sudden change in the ambient T/p value as recorded by the data logger. The details of the charging-up time, irradiation rates and saturated gain are listed in Table 3.

The charging-up time for different X-ray flux is shown in Fig. 8. The charging up time varies between 0.2 - 0.4 h depending on the rate of irradiation as shown in Fig. 8. In Fig. 9, the variation of gain

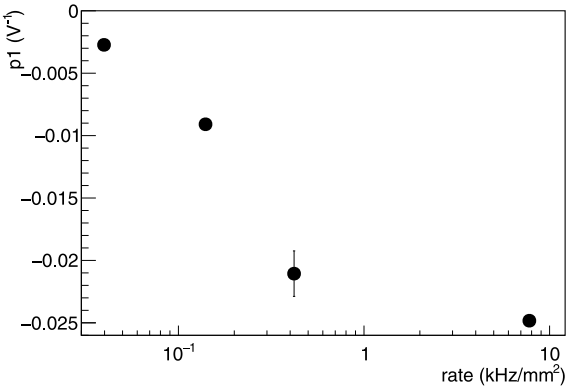

Fig. 6. Variation of the slope (p1) as a function of irradiation rates.

Table 3
Saturated gain and charging-up time for different irradiation rates.

ΔV (V)	rate (kHz/mm²)	Saturated gain	Charging-up time (h)
409	~ 0.04	~ 13000	0.268 (±0.003)
	~ 0.14	~ 11800	0.297 (±0.001)
	~ 0.42	~ 12600	0.280 (±0.002)
	~ 7.78	~ 12200	0.228 (±0.001)
410	~ 0.04	~ 13800	0.285 (±0.005)
	~ 0.14	~ 13700	0.351 (±0.003)
	~ 0.42	~ 13500	0.407 (±0.002)
	~ 7.78	~ 13400	0.335 (±0.002)
411	~ 0.14	~ 14500	0.190 (±0.002)
	~ 0.42	~ 14700	0.436 (±0.002)
	~ 7.78	~ 14000	0.186 (±0.001)

as a function of time (hour) is shown to illustrate both the effects of polarisation and charging-up of the dielectric medium on the gain of the chamber. It is visible in Fig. 9 that initially, the gain decreases due to the initial polarisation effect of the dielectric for around 0.1 h. After that due to the charging-up effect, the gain starts to increase and saturates after around 1.0 h.

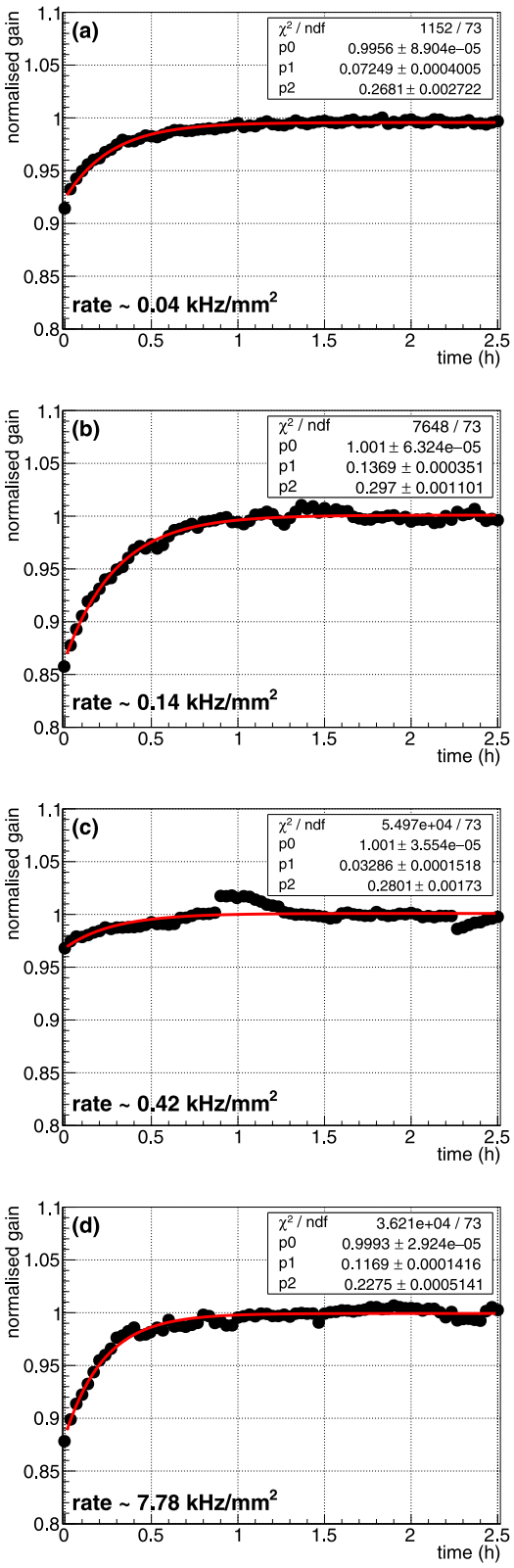

Fig. 7. Variation of normalised gain as function of time (hour) for different irradiation rates. All the measurements are carried out at a HV of - 5085 V ($\Delta V = 409V$).

4. Summary and outlook

The effect of charging-up phenomena and initial polarisation of the dielectric inside the active volume of the 10 cm × 10 cm single mask triple GEM prototype is investigated with Fe^{55} X-ray source at different gains and irradiation rates. The chamber is operated with Ar/CO_2 gas mixture in the 70/30 volume ratio. The effect of initial polarisation of the dielectric is investigated for four different irradiation rates and with three different voltage settings. To quantify the effect of rate and ΔV across the GEM foils on the polarisation effect, the initial decrease of the gain of the chamber is fitted with a 2nd degree polynomial and then from the fitting parameters, the time up to which the gain is decreasing initially is found out. It is observed that this time decreases with increasing ΔV across the GEM foils. A correlation is also observed between the irradiation rates and the effect of the initial polarisation of the dielectric. At a given ΔV, with increasing particle flux, the time required to reach the minimum gain value reduces. After the initial polarisation effect, the gain of the chamber increases due to the modification of the electric field lines inside the GEM holes, *i.e* the charging-up effect. In order to quantify the effect of the rate on the charging-up effect, the T/p normalised gain is fitted with Eq. (1) and $p2$ gives the charging-up time taking analogy from the charging-up mechanism in RC networks [24]. The charging-up time is found to be between 0.2–0.4 h.

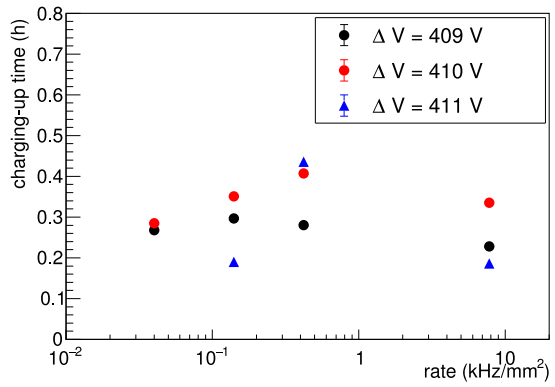

Fig. 8. Charging-up time as a function of rate for different voltage settings.

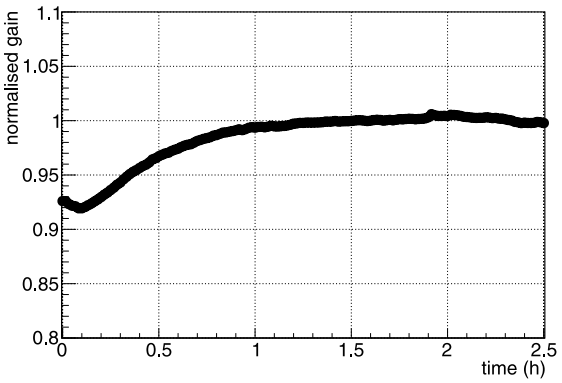

Fig. 9. Variation of normalised gain as a function of time (in hour) at a HV of -5085 V and particle flux ~ 7.78 kHz/mm^2. The measurement is started as soon as the HV reached to its specific value and the source placed on the chamber.

Declaration of competing interest

The authors declare that they have no known competing financial interests or personal relationships that could have appeared to influence the work reported in this paper.

Acknowledgments

The authors would like to thank the RD51 collaboration for the support in building and initial testing of the chamber in the RD51

laboratory at CERN. We would also like to thank Mr. Subrata Das for helping in building of the collimators used in this study. We would like to thank Dr. L. Ropelewski, Dr. E. Oliveri of CERN and Prof. Sibaji Raha, Prof. Rajarshi Ray and Dr. Sidharth K. Prasad of Bose Institute for valuable discussions and suggestions in the course of the study. This work is partially supported by the research grant SR/MF/PS-01/2014-BI from DST, Govt. of India, and the research grant of CBM-MuCh project from BI-IFCC, DST, Govt. of India. S. Biswas acknowledges the support of the DST-SERB Ramanujan Fellowship, India (D.O.No. SR/S2/RJN-02/2012).

References

[1] F. Sauli, Nucl. Instrum. Methods Phys. Res. A 386 (1997) 531.
[2] A.F. Buzulutskov, Instrum. Exp. Tech. 50 (2007) 287.
[3] B. Ketzer, et al., Nucl. Instrum. Methods A 535 (2004) 314.
[4] D. Abbaneo, et al., Nucl. Instrum. Methods A 718 (2013) 383.
[5] B. Ketzer, Nucl. Instrum. Methods A 732 (2013) 237.
[6] T. Balog, J. Phys. Conf. Ser. 503 (2014) 012019.
[7] S. Biswas, et al., Nucl. Instrum. Methods A 800 (2015) 93.
[8] S. Chatterjee, et al., Nucl. Instrum. Methods A 977 (2020) 164334.
[9] Oliveira, et al., United States Patent, Patent No.: US 8, 597, 490 B2.
[10] S. Duarte Pinto, et al., J. Instrum. 4 (2009) P12009.
[11] A. Karadzhinova, et al., J. Instrum. 10 (2015) P12014.
[12] S. Das, Nucl. Instrum. Methods Phys. Res. A 824 (2016) 518.
[13] A. Shah, et al., Nucl. Instrum. Methods Phys. Res. A 936 (2019) 459.
[14] P. Hauer, et al., Nucl. Instrum. Methods Phys. Res. A 976 (2020) 164205.
[15] B. Azmoun, et al., IEEE Nucl. Sci. Symp. Conf. Rec. 6 (2006) 3847.
[16] M. Alfonsi, Nucl. Instrum. Methods Phys. Res. A 671 (2012) 6.
[17] S. Chatterjee, et al., J. Instrum. 15 (2020) T09011.
[18] http://rd51-public.web.cern.ch/rd51-public/.
[19] R.P. Adak, et al., J. Instrum. 11 (2016) T10001.
[20] CDT CASCADE Detector Technologies GmbH, Germany, www.n-cdt.com.
[21] S. Sahu, et al., J. Instrum. 12 (2017) C05006.
[22] M.C. Altunbas, et al., Nucl. Instrum. Methods Phys. Res. A 515 (2003) 249.
[23] https://root.cern/.
[24] V. Tikhonov, et al., Nucl. Instrum. Methods Phys. Res. A 478 (2002) 452.

Journal of Instrumentation

Study of charging up effect in a triple GEM detector

To cite this article: S. Chatterjee *et al* 2020 *JINST* **15** T09011

Jinst

PUBLISHED BY IOP PUBLISHING FOR SISSA MEDIALAB

RECEIVED: *July 23, 2020*
ACCEPTED: *August 18, 2020*
PUBLISHED: *September 30, 2020*

TECHNICAL REPORT

Study of charging up effect in a triple GEM detector

S. Chatterjee,[a,1] **A. Sen,**[a] **S. Roy,**[a] **K. Nivedita G,**[b] **A. Paul,**[c] **S. Das**[a] **and S. Biswas**[a]

[a] *Department of Physics and Centre for Astroparticle Physics and Space Science (CAPSS), Bose Institute, EN-80, Sector-V, Bidhannagar, Kolkata 700091, India*

[b] *IISER, Maruthamala PO, Vithura, Thiruvananthapuram, Kerala 695551, India*

[c] *Department of Physics, University of Calcutta, 92, APC Road, Kolkata 700009, India*

E-mail: sayakchatterjee@jcbose.ac.in

ABSTRACT: The advancement of Micro Pattern Gaseous Detector technology offers us different kinds of detectors with good spatial resolution and high rate capability and the Gas Electron Multiplier (GEM) detector is one of them. Typically GEM is made up of a thin polyimide foil having a thickness of 50 micrometers with 5 micrometers copper cladding on top and bottom sides. The presence of polyimide changes the gain of the detector under the influence of external radiation and the phenomenon is referred to as the charging up effect. The charging up effect is investigated with a double mask triple GEM detector prototype with Ar/CO_2 gas mixture in 70/30 ratio under continuous irradiation from a strong Fe^{55} X-ray source. The detailed method of measurements and the test results are presented in this article.

KEYWORDS: Electron multipliers (gas); Gaseous detectors; Gaseous imaging and tracking detectors; Micropattern gaseous detectors (MSGC, GEM, THGEM, RETHGEM, MHSP, MICROPIC, MICROMEGAS, InGrid, etc)

ARXIV EPRINT: 2007.11444

[1] Corresponding author.

https://doi.org/10.1088/1748-0221/15/09/T09011

2020 JINST 15 T09011

Contents

2020 JINST 15 T09011

1 Introduction

Gas Electron Multiplier (GEM) is one of the most advanced detectors of the Micro Pattern Gas Detector (MPGD) group [1, 2]. GEM is widely used in many High Energy Physics (HEP) experiments as a tracking device because of its good position resolution due to its micro pattern structure [3–6]. The high rate handling capability of the GEM detector makes it a suitable candidate for the experiments where large particle flux is expected [7]. GEM is made up of a thin Kapton foil of thickness 50 µm with 5 µm copper cladding on sides of the foil. A large number of holes are etched on the Kapton using the photolithographic technique [8].

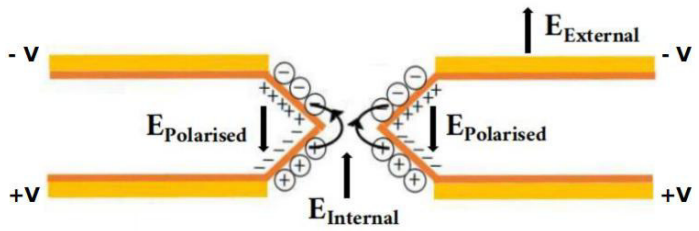

Figure 1. Schematic representation of the Charging up effect inside a GEM hole. $E_{Polarised}$ indicates the electric field generated due to the dielectric polarisation. $E_{External}$ indicates the electric field generated due to the external high voltage and $E_{Internal}$ indicates the electric field generated due to the accumulation of the charges on the Kapton wall.

The holes in a standard GEM foil have an outer and inner diameter of 70 µm and 50 µm respectively. The distance between the centers of two neighboring holes, that is the pitch, is 140 µm. To create an electric field inside the holes, an external high voltage (HV) is applied between the copper layers. The holes in the GEM foil act as the multiplication region for the incoming electrons. As shown in figure 1 usually voltage is applied in such a way that the top of the GEM foil is at negative potential compared to the bottom plane and the electrons move downwards. The electrode placed above the top layer of GEM foil is called the drift electrode or drift plane and the gap between the drift plane and top of the GEM foil is called the drift region. An incoming

charged particle produces primary electrons mainly in the drift region. These primary electrons are focussed towards the GEM holes by the electric field. The high electric field inside the holes enforces the electrons to multiply by an avalanche. Several GEM layers can be used in cascade mode to attain high gain without increasing the biasing voltage and consequently the discharge probability of the chamber [9–11].

The presence of the Kapton foil inside the active part of the detector changes its behavior when exposed to external radiation. Due to the high electric field ($\sim$ kV/cm) inside the GEM holes, the incoming electrons get sufficient kinetic energy to start an avalanche of further ionization. Due to the dielectric properties of the polyimide (Kapton), they get polarised by the external electric field. During this multiplication process, the electrons and ions may diffuse to the polyimide surface and due to the polarisation of the polyimide by the external HV, the ions or electrons can be captured on the wall of the Kapton foil. This phenomenon is illustrated in figure 1. Due to the high resistivity of the Kapton, the charges remain there for a rather long time. As a result of sufficient accumulation of charge on the wall, the electric field configuration inside the hole changes dynamically and this phenomenon is known as the charging up effect. The accumulated charges on the surface of the Kapton foil increase the field inside the holes and as a result, the gain of the chamber increases with time. Many studies have reported that the charging up effect is responsible for a time-dependent change in gain, which asymptotically reaches a constant value [12–15]. In this article, a systematic investigation of the charging up process with different irradiation rates in a triple GEM detector prototype built using double mask foils operated with Ar/CO_2 gas mixture in the 70/30 volume ratio is reported. A strong Fe^{55} source is used to irradiate as well as to record the 5.9 keV X-ray spectra from the chamber. The details of the detector setup are described in section 2 and the results are discussed in section 3.

2 Detector description and experimental setup

In this study, a triple GEM detector prototype, consisting of 10 cm $\times$ 10 cm double mask GEM foils, obtained from CERN is used. The drift, transfer, and induction gaps of the chamber are kept at 3 mm, 2 mm, and 2 mm respectively (3-2-2-2 configuration).

The HV to the drift plane and individual GEM planes are applied through a voltage dividing resistor chain. 10 MΩ protection resistors are applied to the drift plane and top of each GEM foil. A schematic of the resistor chain and different gaps of the chamber is shown in figure, 2. The readout of the chamber is made up of nine pads of dimension 9 mm $\times$ 9 mm each. The signals in this study are taken from all the pads added by a sum up board and a single input is fed to a charge sensitive preamplifier (VV50-2) [16]. The gain of the preamplifier is 2 mV/fC with a shaping time of 300 ns. A NIM based data acquisition system is used to process the signals from the preamplifier. The output signal from the preamplifier is fed to a linear Fan-in-Fan-out (linear FIFO) module. One analog signal from the linear FIFO is put to a Single Channel Analyser (SCA) to measure the rate of the incident particle. The SCA is operated in integral mode and the lower level in the SCA is used as the threshold to the signal. The threshold is set at 0.1 V to reject the noise. The discriminated signal from the SCA, which is TTL in nature, is put to a TTL-NIM adapter and the output NIM signal is counted using a NIM scaler. The count rate of the detector in Hz is then calculated. Another output of the linear FIFO is fed to a Multi-Channel Analyser (MCA) to obtain the energy spectra. A schematic representation of the electronics set-up is shown in figure 3.

2020 JINST 15 T09011

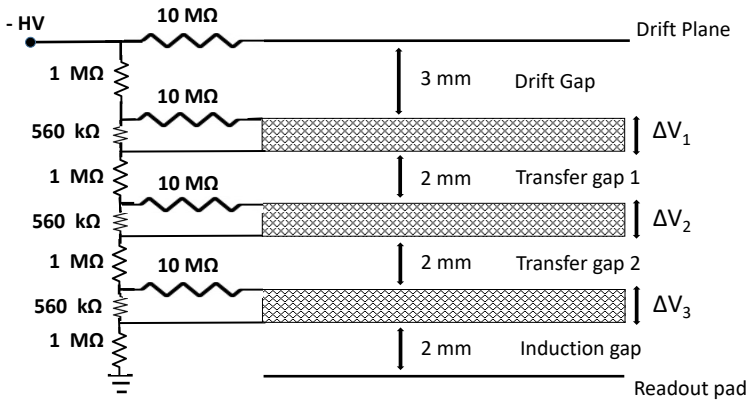

Figure 2. Schematic of the HV distribution of the triple GEM chamber. The drift gap, transfer gap and induction gaps are kept at 3 mm, 2 mm, and 2 mm respectively.

Pre-mixed Ar/CO_2 gas in a 70/30 volume ratio is used for the whole study. A constant gas flow rate of 3.5 l/hr is maintained using a Vögtlin gas flow meter. Perspex, aluminium and G-10 collimators having different hole diameters are used to irradiate the chamber with different X-ray flux coming from the Fe^{55} source. The ambient temperature, pressure, and relative humidity are monitored continuously using a data logger, built-in house [17].

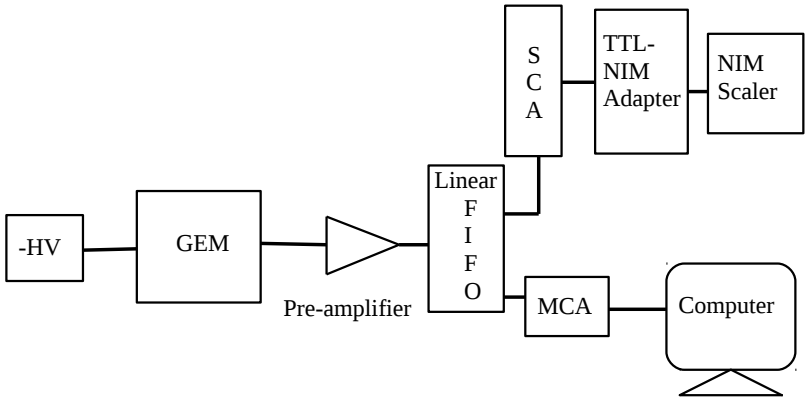

Figure 3. Schematic representation of the electronics setup.

3 Results

The 5.9 keV peak of the Fe^{55} energy spectrum obtained from the MCA is fitted with a Gaussian distribution to obtain the gain of the chamber. A typical Fe^{55} energy spectrum at −4.2 kV is shown in figure 4. The applied HV of −4.2 kV corresponds to ΔV of ~ 390 V across each GEM foil and the drift field, transfer field, and induction field of 2.3 kV/cm, 3.5 kV/cm, and 3.5 kV/cm respectively.

The amount of the input charge is calculated by assuming the full energy deposition of the 5.9 keV X-ray in the 3 mm drift gap of the chamber. The number of primary electrons for Ar/CO_2

2020 JINST 15 T09011

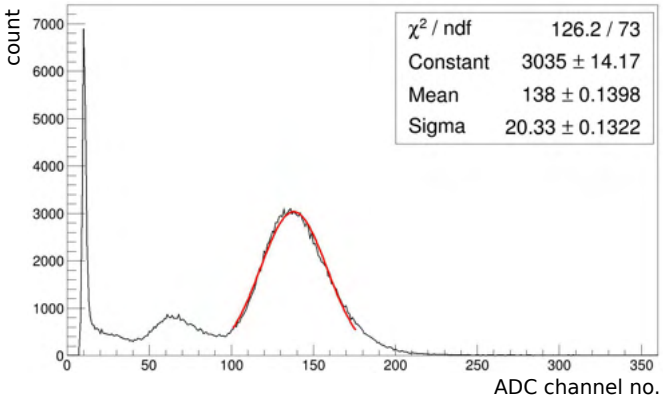

Figure 4. Typical Fe^{55} spectra obtained at a HV of −4.2 kV and irradiated with 10 kHz X-ray on 50 mm^2 area. The Main peak is fitted with a Gaussian distribution (red line) to calculate the gain of the chamber.

in the 70/30 ratio is 212. The ratio of the output charge to the input charge gives the gain of the chamber. The details of the gain calculation and long-term behavior of the chamber were reported earlier [18, 20]. The variation of the gain as a function of time for three different rates of the incoming X-rays, 1 kHz, 10 kHz, and 90 kHz respectively along with the ratio of ambient temperature (T) to pressure (p) are shown in the top (a), middle (b) and bottom (c) plot of figure 5. Using collimators, X-rays of rates 1 kHz, 10 kHz, and 90 kHz are made to fall on 13 mm^2, 50 mm^2 and 28 mm^2 area of the chamber, which implies particle flux of 0.08 kHz/mm^2, 0.2 kHz/mm^2 and 3.2 kHz/mm^2 respectively. All the measurements are carried out at an HV of −4.2 kV.

Since it is well known that the gain of any gaseous detector depends on temperature and pressure [21], that is why the variation in T/p is plotted along with the gain as a function of time. The HV is kept OFF for 180 minutes, 60 minutes, and 8 minutes before the measurement is started with 1 kHz, 10 kHz, and 90 kHz X-ray rates respectively. In all three cases, the data taking starts immediately after the HV is switched ON and the source is placed on the active area of the detector. The energy spectra are stored at an interval of 10 minutes for 1 kHz and 10 kHz rates and 3 minutes for 90 kHz X-ray rates respectively. The same Fe^{55} source is used to irradiate the chamber as well as to obtain the spectra. From figure 5, it is evident that the gain decreases for the first few minutes and then increases for a few hours of operation and reaches a saturation asymptotically. The decrease in the initial gain may be due to the loss of the primary electrons(/ions) which are stuck on the polarised dielectric (Kapton) surface. Since the polarisation of the dielectric medium itself takes some finite time that is why whenever the HV and irradiation started simultaneously, an initial decrease in gain is observed. Afterward, the gain increases sharply for the first few hours due to the lensing effect created by the accumulated charges on the wall of the Kapton foil because this effect increases the electric field strength inside the GEM hole. The absolute gain values after saturation are not the same for all the cases due to the different source positions. The variation in gain over the active area of the particular chamber is reported earlier [19] and it was found that there was a variation of ∼10% (RMS). For all the measurements, the gain shows a saturation followed by an initial increase. The gain is normalised further to eliminate the T/p dependence on the gain. For the T/p normalisation, data obtained after ∼360 minutes of operation (i.e. the saturated gain value)

2020 JINST 15 T09011

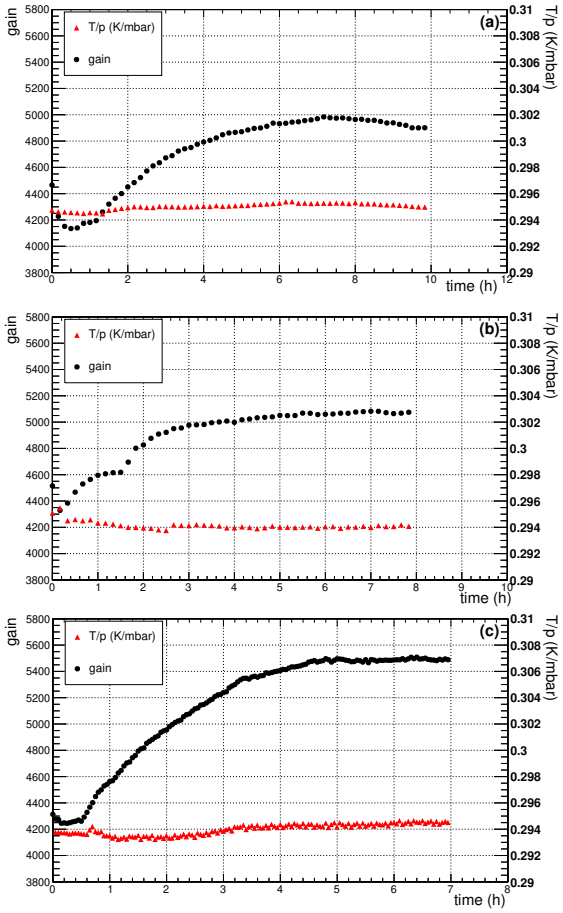

Figure 5. Variation of gain and T/p as a function of time. The top (a), middle (b) and bottom (c) plots are for 1 kHz, 10 kHz and 90 kHz X-rays irradiation rates falling on 13 mm^2 (0.08 kHz/mm^2), 50 mm^2 (0.2 kHz/mm^2) and 28 mm^2 (3.2 kHz/mm^2) area of the GEM chamber respectively. All the measurement are carried out at a HV of −4.2 kV and three different positions on the active area of the chamber.

is used where only the T/p effect is dominant on the gain variation. The method of normalisation is discussed in ref. [18]. The normalised gain is fitted with an exponential function of the form [22]

$$G = p_0 \left(1 - p_1 e^{(-t/p_2)}\right) \tag{3.1}$$

where G is the normalised gain, p_0 & p_1 are the constants, t is the measurement time in hours, and p_2 is the time constant of the charging-up effect, taking analogy from the charging up mechanism of any RC network [23].

The fitted normalised gain is shown in figure 6 for the 1 kHz (top), 10 kHz (middle) and 90 kHz (bottom) X-ray irradiation rates. For the fitting, the first ∼20 minutes are excluded because that includes both the effect of dielectric polarisation and charging up. After that, the charging up effect is dominant and is fitted with equation (3.1) to get an idea about the time constant of the charging up effect. In figure 5(b), a small change is visible in the trend of increasing gain from

2020 JINST 15 T09011

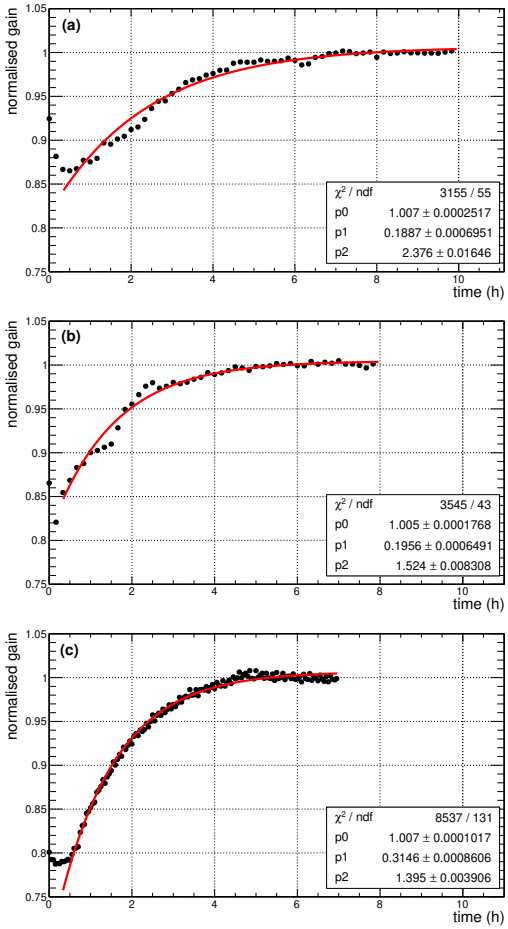

Figure 6. Variation of the normalised gain as a function of time. The top (a), middle (b) and bottom (c) plots are for 1 kHz, 10 kHz and 90 kHz X-rays irradiation rates falling on 13 mm^2 (0.08 kHz/mm^2), 50 mm^2 (0.2 kHz/mm^2), 28 mm^2 (3.2 kHz/mm^2) area of the GEM chamber respectively.

1–2 hours along the time axis and that is due to the two opposite effects namely charging-up and T/p variation. The charging-up process will tend to increase the gain and decrease in T/p will tend to reduce the gain. As a result of these two competing processes, the slope of the curve changes, and that is also reflected in figure 6(b). This competing effect between the charging-up and T/p is distinct in figure 7 where 1 kHz X-rays irradiation 13 mm^2 area of the GEM chamber. For this measurement, the high voltage is switched ON, the source is placed on the detector, and data-taking is started. Before that, the HV is kept OFF for ~ 60 minutes. The first three points in figure 7(a) show a decreasing trend in the gain which is a combined effect of T/p and dielectric polarisation. After that, though the T/p value shows a decreasing trend, there is no visible decrease in the gain. That is due to the two competing processes, the effect of the decreasing T/p and charging-up on the gain is anti-correlated. Then after ~1.5 hr, the gain increases because of the charging-up and T/p variation. The corresponding normalised gain variation is shown in figure 7(b).

To identify whether the decrease in the gain at the first few minutes is due to dielectric polarisation or not, a different measurement is performed by keeping the HV ON for ~24 hours

2020 JINST 15 T09011

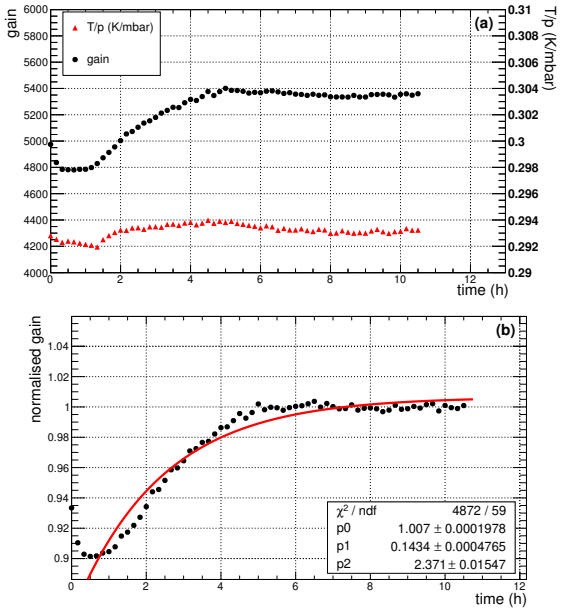

Figure 7. Variation of gain, T/p (a) and normalised gain (b) as a function of time for 1 kHz X-rays irradiating 13 mm^2 (0.08 kHz/mm^2) area of the GEM chamber. The measurement has been carried out at an HV of −4.2 kV. The HV was kept OFF for ∼ 60 minutes before taking the first measurement with the Fe^{55} X-ray source.

before the first measurement. The HV is kept at −4.1 kV which corresponds to $\Delta V \sim 382$ V across each GEM foil and drift field, transfer field, and induction field of 2.3 kV/cm, 3.4 kV/cm and 3.4 kV/cm respectively. The chamber is irradiated with 1 kHz X-ray falling on 13 mm^2 area of the chamber. Once the source is placed, the measurement is started immediately. The variation of gain, T/p, and normalised gain is shown as a function of time in figure 8(a) and 8(b) respectively. The data is stored at an interval of 10 minutes. It is evident from the plot that there is no decrease in gain is observed at the beginning.

Since the charging-up process is due to the accumulation of the charges on the GEM holes therefore the charging-up process depends on the flux of incident radiation. More the flux of the incident particle faster will be the charging-up effect and the same behavior also appears from this study. From figure 6, for 1 kHz, 10 kHz, and 90 kHz operations, the time constant of the charging-up effect is found to be 2.376 ± 0.02 hours, 1.524 ± 0.008 and 1.395 ± 0.004 hours respectively. The time constant of charging-up effect obtained from figure 7(b), agrees well with 6(a). From figure 8(b), the time constant of the charging-up effect is found to be 3.294 ± 0.018 for 1 kHz X-ray. The time constant of charging-up effect obtained from 8(b) can not be compared with figure 6(a) and figure 7(b) because the HV is different. The residual voltage dependence on the charging-up effect is also seen in ref. [22].

4 Summary and outlook

The charging-up effect of a double mask triple GEM prototype is studied using different irradiation rates from a Fe^{55} X-ray source. The chamber is operated with Ar/CO_2 gas mixture in a 70/30

2020 JINST 15 T09011

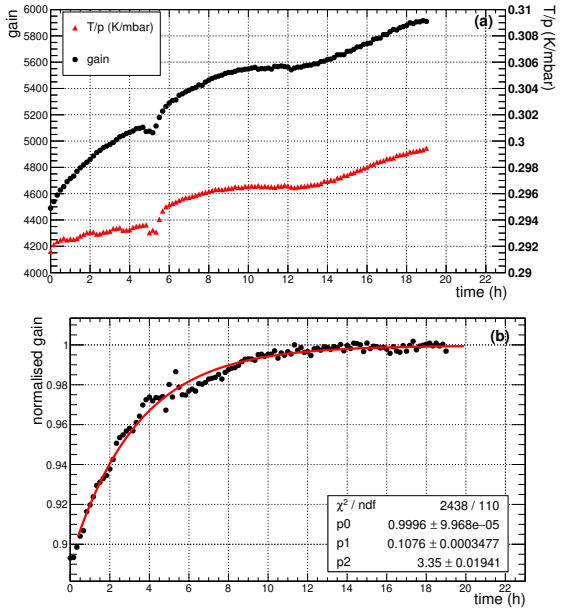

Figure 8. Variation of gain, T/p (a) and normalised gain (b) as a function of time for 1 kHz X-rays irradiating 13 mm^2 (0.08 kHz/mm^2) area of the GEM chamber. The measurement is carried out at HV of −4.1 kV. The HV is kept ON for 24 hours before taking the first measurement with the Fe^{55} X-ray source.

volume ratio. The HV is kept OFF for a few minutes to several hours before starting the respective measurements. The data is stored just after the HV is ON and the source is placed on the chamber to see the effect of dielectric polarisation on the gain of the chamber. It is observed that the gain initially decreases and then increases to reach a saturation value. To ensure the decrease in the gain of the chamber during the first few minutes is due to dielectric polarisation, a different set of measurements is performed where the HV is kept ON for ∼24 hours before the data taking. No initial decrease in gain is observed in that case as shown in figure 8 because the dielectric (i.e. Kapton) is already polarised due to the application of HV beforehand. With different particle fluxes, the time constant of the charging up effect is investigated. It is found that the charging-up time decreases with increasing particle flux. Though the time constant value is decreasing with increasing particle flux, the exact scaling of the time constant with particle flux is not possible because we are observing an overall effect due to the three GEM foils and it is very difficult to disentangle the effects of each GEM foil on the final results. Also since the charging up time depends on the GEM hole geometry, properties of the Kapton foil, charge density in the GEM holes, etc., therefore we can only conclude that the time constant of the charging up effect decreases with increasing particle flux. The two competing effects of T/p variation and charging-up on the gain the chamber is studied by recording the 5.9 keV Fe^{55} X-ray spectra and as expected it is coming to be anti-correlated as shown in figure 7. The dependence of the charging-up process on the gain of the detector, electric field strengths of different layers, used gas mixture, and also on the different kinds of GEM foils is under investigation.

2020 JINST 15 T09011

Acknowledgments

The authors would like to thank the RD51 collaboration for the support in building and initial testing of the chamber in the RD51 laboratory at CERN. We would like to thank Dr. A. Sharma, Dr. L. Ropelewski, Dr. E. Oliveri and Dr. Chilo Garabatos of CERN and Dr. C.J. Schmidt and Mr. Jörg Hehner of GSI Detector Laboratory and Prof. Sanjay K. Ghosh, Prof. Sibaji Raha, Prof. Rajarshi Ray and Dr. Sidharth K. Prasad of Bose Institute for valuable discussions and suggestions in the course of the study. This work is partially supported by the research grant SR/MF/PS-01/2014-BI from DST, Govt. of India, and the research grant of CBM-MuCh project from BI-IFCC, DST, Govt. of India. S. Biswas acknowledges the support of DST-SERB Ramanujan Fellowship (D.O. No. SR/S2/RJN-02/2012) and Intramural Research Grant provided by Bose Institute.

References

[1] F. Sauli, *GEM: A new concept for electron amplification in gas detectors*, *Nucl. Instrum. Meth. A* **386** (1997) 531.

[2] F. Sauli, *The gas electron multiplier (GEM): Operating principles and applications*, *Nucl. Instrum. Meth. A* **805** (2016) 2.

[3] C. Altunbas et al., *Construction, test and commissioning of the triple-GEM tracking detector for COMPASS*, *Nucl. Instrum. Meth. A* **490** (2002) 177.

[4] M.G. Bagliesi et al., *The TOTEM T2 telescope based on triple-GEM chambers*, *Nucl. Instrum. Meth. A* **617** (2010) 134.

[5] B. Ketzer, *A Time Projection Chamber for High-Rate Experiments: Towards an Upgrade of the ALICE TPC*, *Nucl. Instrum. Meth. A* **732** (2013) 237 [arXiv:1303.6694].

[6] D. Abbaneo et al., *GEM based detector for future upgrade of the CMS forward muon system*, *Nucl. Instrum. Meth. A* **718** (2013) 383.

[7] T. Balog, *Overview of the CBM detector system*, *J. Phys. Conf. Ser.* **503** (2014) 012019.

[8] R. De Oliveira and S. Duarte Pinto, *Method of manufacturing a gas electron multiplier*, U.S. Patent 8,597,490 B2 (2013).

[9] S. Bachmann et al., *Performance of GEM detectors in high intensity particle beams*, *Nucl. Instrum. Meth. A* **470** (2001) 548.

[10] S. Biswas et al., *Measurement of the spark probability of a GEM detector for the CBM muon chamber (MuCh)*, *Nucl. Instrum. Meth. A* **800** (2015) 93 [arXiv:1504.00001].

[11] S. Chatterjee et al., *Spark probability measurement of a single mask triple GEM detector*, *Nucl. Instrum. Meth. A* **977** (2020) 164334.

[12] B. Azmoun et al., *A study of gain stability and charging effects in GEM foils*, in proceedings of the *2006 IEEE Nuclear Science Symposium Conference Record*, San Diego, CA, U.S.A., 29 October–1 November 2006, pp. 3847–3851.

[13] M.V. Nemallapudi, *Gain of a Single Gas Electron Multiplier*, MSc Thesis, University of Arkansas, Fayetteville Arkansas U.S.A. (2012) and online at https://scholarworks.uark.edu/etd/533/.

[14] M. Alfonsi et al., *Simulation of the dielectric charging-up effect in a GEM detector*, *Nucl. Instrum. Meth. A* **671** (2012) 6.

2020 JINST 15 T09011

[15] CERN RD-51 collaboration, *A dynamic method for charging-up calculations: the case of GEM*, 2014 *JINST* **9** P07025 [arXiv:1401.4009].

[16] CDT CASCADE Detector Technologies GmbH, Hans-Bunte-Str. 8–10, Heidelberg 69123, Germany https://n-cdt.com/.

[17] S. Sahu et al., *Design and fabrication of data logger to measure the ambient parameters in gas detector R&D*, 2017 *JINST* **12** C05006.

[18] S. Roy et al., *Stability study of gain and energy resolution for GEM detector*, *Nucl. Instrum. Meth. A* **936** (2019) 485 [arXiv:1804.02819].

[19] S. Chatterjee et al., *Study of uniformity of characteristics over the surface for triple GEM detector*, *Nucl. Instrum. Meth. A* **936** (2019) 491 [arXiv:1807.04961].

[20] S. Chatterjee et al., *Long term stability study of triple GEM detector using different Argon based gas mixtures: an update*, *J. Phys. Conf. Ser.* **1498** (2020) 012037.

[21] M.C. Altunbas et al., *Aging measurements with the gas electron multiplier (GEM)*, *Nucl. Instrum. Meth. A* **515** (2003) 249.

[22] P. Hauer et al., *Measurements of the Charging-Up Effect in Gas Electron Multipliers*, *Nucl. Instrum. Meth. A* **976** (2020) 164205 [arXiv:1911.01848].

[23] V. Tikhonov and R. Veenhof, *GEM simulation methods development*, *Nucl. Instrum. Meth. A* **478** (2002) 452.

2020 JINST 15 T09011

Nuclear Inst. and Methods in Physics Research, A 977 (2020) 164334

Contents lists available at ScienceDirect

Nuclear Inst. and Methods in Physics Research, A

journal homepage: www.elsevier.com/locate/nima

Spark probability measurement of a single mask triple GEM detector

S. Chatterjee [a], U. Frankenfeld [b], C. Garabatos [b], J. Hehner [b], T. Morhardt [b], C.J. Schmidt [b], H.R. Schmidt [c,b], A. Lymanets [b], S. Biswas [a,b,1,*]

[a] Department of Physics and Centre for Astroparticle Physics and Space Science (CAPSS), Bose Institute, EN-80, Sector V, Kolkata 700091, India
[b] GSI Helmholtzzentrum für Schwerionenforschung GmbH, Planckstrasse 1, D-64291 Darmstadt, Germany
[c] Physikalisches Institut - Eberhard Karls Universität Tübingen, Auf der Morgenstelle 14, D-72076 Tübingen, Germany

ARTICLE INFO

Keywords:
GEM
Single mask foil
Pion beam
Shower
Gain
Spark probability

ABSTRACT

Triple Gas Electron Multiplier (GEM) detectors will be used as a tracking device in the first two stations of CBM MUon CHamber (MUCH), where the maximum particle rate is expected to reach ~1 MHz/cm^2 for central Au-Au collisions at 8 AGeV. Therefore, the stable operation of the detector is very important. Discharge probability has been measured of a single mask triple GEM detector at the CERN SPS/H4 beam-line facility with a pion beam of ~150 GeV/c and also in an environment of highly ionizing shower particles. The spark probability as a function of gain has been studied for different particle rates. The details of the experimental setup, method of spark identification and results are presented in this paper.

1. Introduction

The Compressed Baryonic Matter (CBM) [1] experiment at the future Facility for Antiproton and Ion Research (FAIR) [2] in Darmstadt, Germany, will explore the QCD phase diagram at low temperature and moderate to high baryonic density regime [3]. The decay of charmonium (J/ψ), low mass vector mesons ρ^0, ω^0, ϕ^0 in the muonic decay channel, i.e., $\mu^+\mu^-$ will be used as a probe to get an idea about the in-medium modifications of the particles [4]. They will carry the information about the medium formation, the transition from the hadronic phase to the QGP phase and chiral symmetry restoration.

The MUon CHamber (MUCH) at CBM will be used dedicatedly for muon tracking [5]. Since the product of multiplicity and branching ratio for the muonic decay mode is very small ($\sim 10^{-3} - 10^{-8}$), therefore it is necessary to go up in interaction rate to get a signal, well separated from the background. This is only possible with the application of advanced instrumentation, including fast detectors with very high rate handling capability and good position resolution. MUCH will consist of five absorber layers of thickness 60, 20, 20, 30, 100 cm respectively. The first absorber will be made up of 60 cm carbon. The rest of the absorbers will be made up of iron. In between the absorbers (termed as stations), three active detector layers will be placed. To handle high rate, the triple GEM [6] detector technology has been chosen for the first two stations, and RPC or straw-tube will be used for the rest of the stations in the MUCH detector system [7–15].

From simulation it has been found that the particle rate in the first four stations will be 0.8 MHz/cm^2, 0.1 MHz/cm^2, 15 kHz/cm^2, 5.6 kHz/cm^2 respectively for central Au-Au collisions at 8 AGeV [16]. To operate the detectors for a long period without any discharge is an essential criterion for MUCH.

GEM is made up of a thin kapton foil of thickness 50 μm with 5 μm copper cladding on both sides of the foil. A large number of holes are etched on the kapton using the photolithographic technique [17]. Depending on the photolithographic technique used, the GEM foils can be divided into two types namely single mask and double mask GEM foils. In double mask technology for etching, the exposure of the metallized polymer foils, coated with a photosensitive resin, to ultraviolet light through masks from both sides of the sheet is required [18]. On the other hand, in single mask technology, following the masking, the metal and kapton are etched from one side [19,20]. The foil is first chemically etched to remove about half of the metal, opening the holes on the bottom side; a second kapton etching allows one to realise quasi-conical holes [21].

The spark probability measurement of a double mask triple GEM detector has been done and reported earlier [22]. Since the CBM GEM detectors will be of single mask type because of its large size, it is very important to measure the spark probability of a single mask GEM detector.

The main goal of this study is to measure the spark probability of a single mask triple GEM detector with a high momentum pion beam and also for a heavy shower environment. A single mask triple GEM detector has been tested at the CERN SPS/H4 beamline facility with a pion beam of ~150 GeV/c. In this test beam, the pulse height

* Corresponding author at: Department of Physics and Centre for Astroparticle Physics and Space Science (CAPSS), Bose Institute, EN-80, Sector V, Kolkata 700091, India.
E-mail address: S.Biswas@gsi.de (S. Biswas).
[1] I would like to happily state that all the authors have equal credit for the work.

https://doi.org/10.1016/j.nima.2020.164334
Received 26 April 2020; Received in revised form 1 July 2020; Accepted 2 July 2020
Available online 6 July 2020

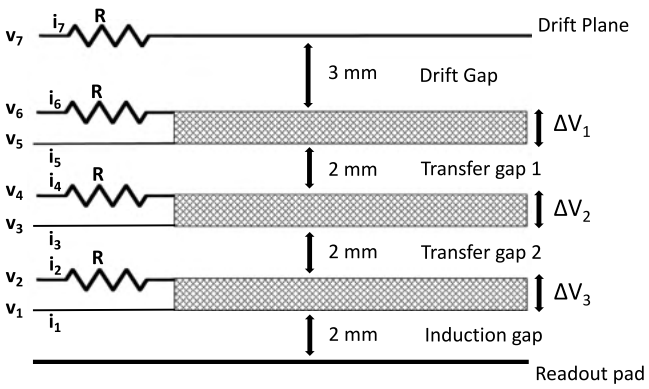

Fig. 1. Arrangement of GEM foils, voltage and current distribution in different planes of the chamber.

distribution from the detector, currents from the GEM foils and count rates from the detectors have been measured. The details of the spark identification, the value of spark probability, and its variation as a function of gain will be presented in this article.

2. Description of the GEM module

A single mask triple GEM detector having the dimension of (10 × 10) cm^2 has been used during the beam test. The GEM foils with hole diameter of 70 μm, and pitch of 140 μm have been obtained from CERN. The drift gap, 2 transfer gaps, and induction gap have been kept at 3 mm, 2 mm, and 2 mm, respectively (3-2-2-2 configuration). A protection resistance of 10 MΩ has been employed to the top plane of each GEM foil and to the drift plane. Fig. 1 shows the schematic diagram of the GEM module, used in the test beam campaign. The read-out plane consist of 512 pads of (4 × 4) mm^2 size. All the readout pads have been routed to 4 connectors of 128 pins each. Even though the read-out plane was segmented for the module, in this study the signals obtained from all the 128 pads are summed by a sum-up board and a single output has been fed to a charge sensitive preamplifier. (The sum-up board is a specially designed board having connection from 128 pin to a single LEMO. Signals coming from any of the 128 pads will reach to a single preamplifier via the LEMO connector.)

The analog signals from the preamplifiers have been put to the linear Fan-in-Fan-out (FIFO) module that gives four identical analog signal at the output exactly same as the input signal. For data acquisition, PXI LabView has been used [23]. Signals from one output of the linear FIFO have been put to PXI LabView scope card for ADC spectra. Signals from another output have been fed to a NIM discriminator. The threshold to the signal has been set at 10 mV in the discriminator to eliminate noise. The discriminated signals have been counted using a PXI LabView scalar. The counts from the pad plane of the GEM detector are sampled for 100 ms binning.

The GEM module has been operated throughout the experiment with a Ar/CO_2 gas mixture in the 70/30 volume ratio. The high voltages (HV) to the different GEM planes have been applied by a seven-channel HVG210 power supply made by LNF-INFN [24]. This module allows for powering and controlling the applied voltages of a triple GEM detector. The module communicates with peripherals via CAN bus. The HVG210 power supply comprises seven almost identical channels, each of them being able to produce a specified voltage level with a current reading and current limiting option. The currents of all channels were recorded and used to determine the occurrence of a spark. The applied voltages and measured currents on each channel from the lower plane of lowest GEM foil up to the drift plane are named as V_1 to V_7 and i_1 to i_7, respectively. The details of the electric field in the drift, transfer, and induction gap for a particular voltage configuration are summarised in Table 1 [9].

Table 1
Typical potential differences and fields on the various gaps of a triple GEM chamber, operated with Argon and CO_2 in a 70/30 mixing ratio.

Gap name	Gap width (mm)	Potential difference (V)	Field (kV/cm)
Drift	3	400	1.33
Transfer 1	2	395	1.98
Transfer 2	2	395	1.98
Induction	2	390	1.95

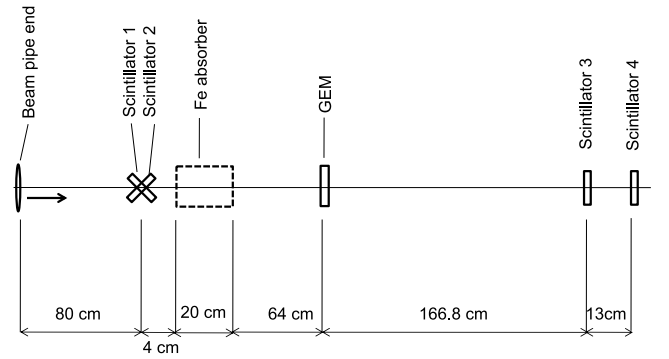

Fig. 2. A sketch of the experimental setup.

3. Experimental setup

The arrangement of the experimental setup used in the test beam campaign is shown in Fig. 2. Two crossed finger scintillators (Scintillator 1 and Scintillator 2, both having dimension (5 × 5) cm^2) have been placed to monitor the incoming particle rate at a distance of 80 cm from the beam pipe end. The coincidence of those two scintillators (crossed area (5 × 5) cm^2) have been used as a beam counter. The single mask triple GEM detector under test has been placed at a distance of 168 cm from the beam pipe end as shown in Fig. 2. An iron block of length 20 cm has been employed to generate a particle shower. The particle shower has been identified by the coincidence between the signals from the first two finger scintillators and no signal from the last two scintillators (Scintillator 3 and Scintillator 4, having dimension (10 × 20) cm^2 and (20 × 30) cm^2, respectively). The distance between the iron block and the GEM module was 64 cm as shown in Fig. 2. The centres of the 4 scintillators (Scintillator 1, 2, 3, 4), the iron block and the GEM module have been mechanically aligned with the centre of the beam pipe. FLUKA simulation package has been used to calculate the number of particles reaching on the detector surface after the shower production by the iron slab [25–27]. From the FLUKA simulation the number of pion, neutron, muon, proton, kaon, and electron reaching on the GEM plane was found to be 2.4, 0.2, 0.009, 0.1, 0.3, 10, respectively, per primary pion of energy 150 GeV/c. In this study, to measure spark probability pion beam of rates 8, 27, 43, 48, 150 and 170 kHz have been used where as to produce shower, pion beam of rates 6, 50 and 120 kHz have been employed to hit a 20 cm thick iron block. The pion beam hit the GEM detector in an area of ~10 mm^2, where as in this set-up during shower, for each pion beam the number of secondary particles hitting the whole GEM plane of 100 cm^2 is 13.009 (sum of the numbers of secondary pion, neutron, muon, proton, kaon, and electron reaching GEM plane per primary pion).

The voltages and currents from all seven channels of the HVG210, counts from the scintillators, GEM detector and the pulse height of the GEM detector signals have been measured. In Section 4, we shall discuss the relevance of those measurements for the investigation of the spark probability of the module.

4. Results

In this test beam, the current in all the channels from the top and bottom plane of three GEM foils and the drift planes have been

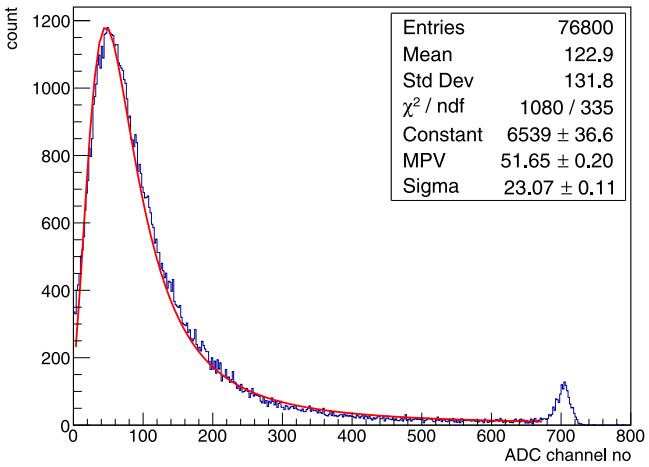

Fig. 3. (Colour online) ADC distribution for the pion of average rate 27 kHz with ΔV_1 = 390 V, ΔV_2 = 385 V and ΔV_3 = 380 V and corresponding gain ~80 000.

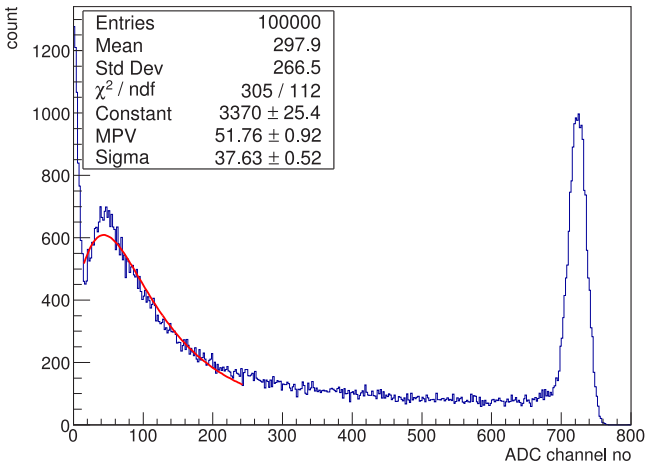

Fig. 4. (Colour online) ADC distribution for shower environment with ΔV_1 = 390 V, ΔV_2 = 385 V and ΔV_3 = 380 V and corresponding gain ~80 000.

measured. The data for the ADC spectra have been stored for all voltage settings. The data for counts from the GEM detector and from the scintillators have been also stored.

4.1. ADC spectra

The ADC spectra of the detected particles have been studied. The ADC distribution for a pion beam of a typical average rate 27 kHz is shown in Fig. 3. The energy distribution of the minimum ionizing particle is expected to follow the Landau distribution [28], as observed from the ADC distribution for pion (Fig. 3) with a GEM voltage settings of ΔV_1 = 390 V, ΔV_2 = 385 V and ΔV_3 = 380 V and corresponding gain ~80 000. The Most Probable Value (MPV) of the distribution has been found at ~51 ADC channel and a small saturation peak has been observed at 700 ADC channel.

The ADC distribution for the heavily ionizing particles produced after the shower is shown in Fig. 4 with GEM voltage configuration of ΔV_1 = 390 V, ΔV_2 = 385 V and ΔV_3 = 380 V and corresponding gain ~80 000. The MPV of the distribution has also been found at ~51 ADC channel and a large saturation peak has been observed. Although it is somehow unexpected that the MPV is the same both for the heavily ionizing and minimum ionizing particles. The mean of the distribution for the pion beam and for shower, at the same voltage settings have been found to be at 122.9 and 297.9 ADC value, respectively. The

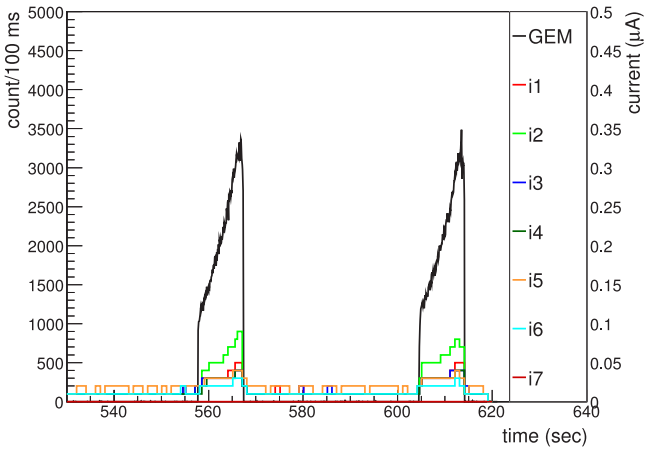

Fig. 5. (Colour online) Currents and the GEM counting rate: Pion beam 27 kHz. The GEM count rate is plotted in the units of counts/100 ms. The different currents i1 to i7 correspond to V1 to V7.

average energy distribution by the particles produced in the shower is higher. For shower the mean value has increased only by a factor of ~2.5, which is also somehow surprising taking into account the steep increase of the Bethe-Bloch formula towards small velocities. The large saturation peak for the shower environment reflects the existence of heavily ionizing particles in the shower. In this work PXI LabView based scope card has been used to store the ADC spectra. It digitizes the difference of the maximum and minimum edge of a signal and takes the number as the amplitude of the signal. For saturated signal also, although the maximum edge is more or less fixed but both the edges (maximum and minimum) can fluctuate a bit. Accordingly the digitized value also fluctuates. This is the reason for the broadening of the saturation peak in both Figs. 3 and 4. From the scope data, it can be inferred that the detectors were in good condition during the beam time.

4.2. Measurement of current

In this study, the currents from the drift plane, top and bottom plane of each of the GEM foils have been recorded using the HVG210 [24] high voltage power supply module. The counts from the GEM detector as well as from the scintillators are sampled for 100 ms binning. The variation in the current along with the count rate from the GEM module is shown as a function of time in Figs. 5 and 6.

Fig. 5 shows the variation of the currents and the GEM count rate during and in between the spills of the pion beam of average rate ~27 kHz with GEM voltage settings of ΔV_1 = 390 V, ΔV_2 = 385 V and ΔV_3 = 380 V and corresponding gain ~80 000. In Fig. 6, the variation in the currents and GEM count rate are shown for the shower produced by a pion beam of an average rate of 120 kHz hitting the 20 cm iron slab. The GEM voltage settings were ΔV_1 = 385 V, ΔV_2 = 380 V and ΔV_3 = 375 V and corresponding gain was ~60 000. The spill structure of the SPS beam increases with time reaches a maximum and then drops immediately to 0 as obtained from both the GEM detector and beam counter. The duration of the spill in the SPS beam is ~10 s and the off spill time is ~40 s. From Figs. 5 and 6, the maximum absolute increase in current is observed in i2 i.e. on the top of the third GEM-foil, where the maximum number of ions reach.

4.3. Measurement of spark probability

The most important goal of this beam time was the measurement of spark probability. The spark probability is defined as the ratio of the number of sparks occurred in the detector and the total number of

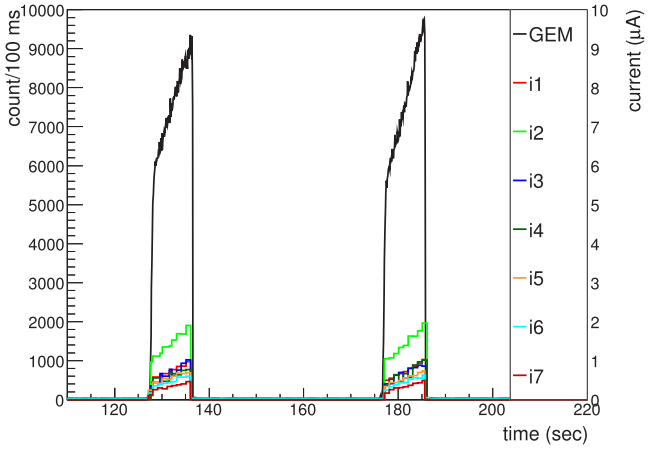

Fig. 6. (Colour online) Current and the GEM counting rate during Shower: Beam rate 120 kHz. The GEM count rate is plotted in the units of counts/100 ms. The different currents i1 to i7 correspond to V1 to V7.

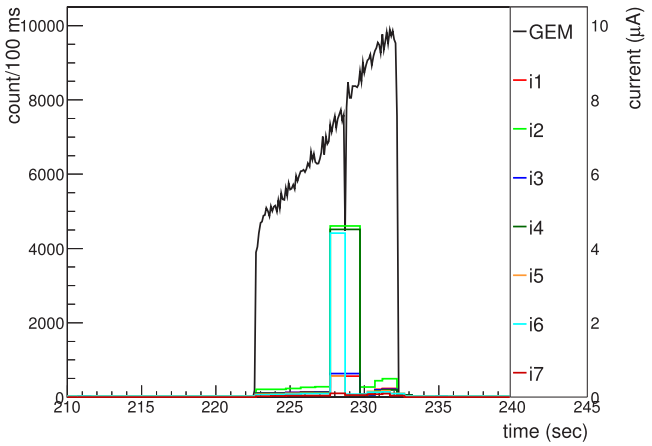

Fig. 7. (Colour online) Identification of spark from the drop in the GEM counting rate during a spill. In parallel, the currents on all GEM electrodes were registered and are displayed. The time axis is shown in the unit of second. i1 to i7 shown in different colours are the currents correspond to V1 to V7. The count rate, shown in black is in the unit of counts/100 ms.

particles incident on it [29–31]. In this study, two different methods have been used to identify a spark in the GEM module as previously done for the double mask detector [22]. The first method identifies a spark if there is a sudden drop in the GEM counting rate. The second one determines a spark by the sudden jump in the current obtained from the top of each GEM foil.

During a spark, the sudden drop of the electric field in the GEM hole reduces the gain of the detector, and as a result, the count rate of the chamber decreases. That is why it is a beneficial method to calculate the number of sparks that occurred in the GEM module during the spill. To identify a spark, the ratio of the counts from the GEM module and beam counter has been used. If the ratio drops below 65% of its average value, then it is considered as a spark. Different threshold values between 50% to 70% have been tested, but no significant change in the result is observed. Above 70%, the spark counts increase drastically because then all the small fluctuations in the count rate are considered as a spark, and below 50% the spark count is coming to be zero. The above-mentioned definition has been used for the identification of spark in the analysis. In Fig. 7, the black line shows the count registered on the GEM module during a spill and a sudden drop in the count rate indicates the occurrence of spark in the chamber. Fig. 8 shows that sometimes more than one spark is observed in the module during a spill.

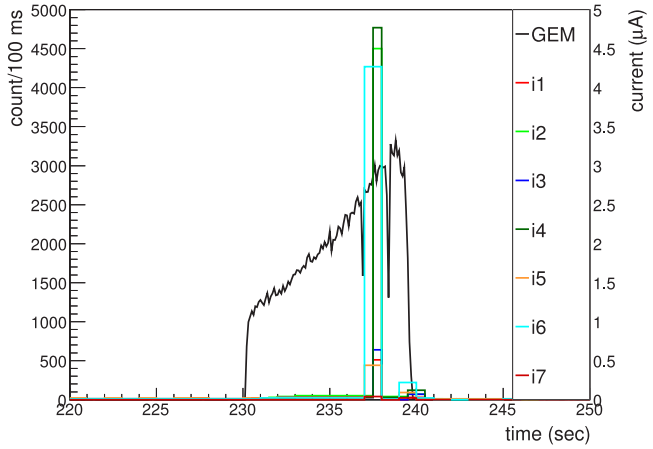

Fig. 8. (Colour online) Example of the spill where two sparks are observed. The time axis is shown in the unit of second. i1 to i7 shown in different colours are the currents correspond to V1 to V7. The count rate, shown in black is in the unit of counts/100 ms.

Measuring the currents from each layer of the GEM foil is another method of determining spark in the module. The current will increase particularly at the top of each GEM foil whenever there is a spark. In Figs. 7 and 8 the sudden jump in the current in the top layers of the GEM foil is observed when there is a drop in the GEM counting rate. The threshold for the current is set to 2 μA to define a spark, but the identification of the spark is more accurate if we use the first method i.e. from the drop in the GEM counting rate because of the sampling rate for the current monitoring is less than the sampling rate for the count data monitoring. If we consider Fig. 8, then the number of sparks is two if we count from the drop in the GEM counting rate, but it is coming to be one if we count the spark from the jump in the current. That is why, for our analysis, the spark probability is calculated from the drop in the counting rate of the GEM module during a spill.

The calculated spark probability as a function of the gain of the module is shown in Fig. 9. The gain of the module has been measured using a 5.9 keV Fe^{55} X-ray source. During the beam time, the gain of the detector is found to be within the range of ∼40 000 to 130 000 for the operational global GEM voltage ($\Delta V_1 + \Delta V_2 + \Delta V_3$) settings of 1120 V to 1185 V. In this operational global voltage range of 1120 V to 1185 V and corresponding gain between 40 000 to 130 000, taking 30 primary electrons per incident pion (minimum ionizing particle) in the 3 mm drift gap the total number of electrons reaching readout will be 1.2×10^6 to 3.9×10^6, respectively. This corresponds to a total charge between 192 fC to 624 fC, respectively. The spark probability of the single mask triple GEM detector in "3-2-2-2 configuration" has been found to be $\sim 10^{-7}$ for a 150 GeV/c pion beam of rate 150 kHz with a gas gain between 40 000 and 80 000.

To calculate the spark probability of the GEM module in the shower environment, pion beam of rates 120, 50 and 6 kHz have been employed to a 20 cm thick iron slab. The voltage settings of the detector were $\Delta V_1 = 385$ V, $\Delta V_2 = 380$ V and $\Delta V_3 = 375$ V respectively and the gain was ∼60 000. Total integrated number of pions incident on the iron slab for these three rates were 1.10×10^6, 2.40×10^6 and 3.32×10^5, respectively. No spark has been detected in these settings using both the methods i.e. drop in GEM counting rate and jump in current. Though during the shower, the number of secondary particles on the detector surface (13.009 secondary particles reached the detector plane per pion) increases as we have seen from the FLUKA simulation, but still, no spark has been identified.

5. Summary and outlook

The spark probability of a single mask triple GEM detector in "3-2-2-2 configuration" has been measured with mostly pure pion beam

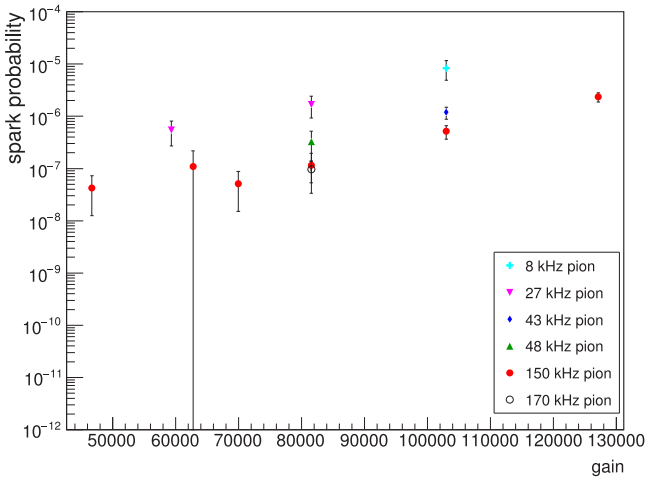

Fig. 9. (Colour online) Spark probability of the detector as a function of the gain.

and also for a shower produced by pion beam with a 20 cm thick iron block. Two different methods have been used to identify sparks in the chamber. In the first method the spark is identified by sudden drop in the GEM counting rate whereas in the second method it is done by the sudden jump in the current obtained from the top of each GEM foil. The variation of the spark probability as a function of the gain has been presented for the pion beam. For the pion beam the spark probability increases exponentially with the gain. The spark probability of the detector has been found to be $\sim 10^{-7}$ for 150 GeV/c pion beam of rate 150 kHz with a gain between 40 000 and 80 000. No spark has been observed for shower produced by pion beams of rates of 120, 50 and 6 kHz after striking an iron slab of thickness 20 cm. The pion beam hit the chamber in an area of ~10 mm^2, where as in this set-up during shower, for each pion beam the number of secondary particles hitting the whole GEM plane of 100 cm^2 is 13.009. Consequently the particle density per unit surface area of the GEM detector is much smaller for the secondary particles produced in shower than that for the pion beam. In these measurements the particles hitting per unit area of the GEM detector for the pion beams of rate 8, 27, 43, 48, 150 and 170 kHz are ~0.8, 2.7, 4.3, 4.8, 15 and 17 kHz/mm^2, respectively and for that for shower produced by pion beam of rate 6, 50 and 120 kHz are ~0.008, 0.065 and 0.16 kHz/mm^2, respectively. That is the probable reason of not getting any spark in the shower set-up.

The comparison between the spark probability measurement for the double mask triple GEM detector as reported earlier [22] and the present measurement for the single mask triple GEM detector are the followings. The drift gap of the double mask GEM chamber was 2 mm. In case of double mask triple GEM detector the spark probability was measured mostly for shower induced by a pion beam with a 10 cm thick iron absorber and also for a pure pion beam. In this operational global voltage range the gain of the detector was measured to vary between 20,000 and 50,000. 11 MΩ protection resistors were employed in all the seven channels. In this study the spark probability was found to be $\sim 10^{-7}$ for 150 GeV/c pion beam and also for shower. On the other hand, the drift gap of the single mask GEM detector was 3 mm and the spark probability was measured mainly for pure pion beam of different rates and for shower produced by pion beams of rates of 120, 50 and 6 kHz after hitting an iron slab of thickness 20 cm. The detector was operated at gain between 40 000 and 130 000. A protection resistance of 10 MΩ has been employed only to the top plane of each GEM foil and to the drift plane. In this case the spark probability has been found to be $\sim 10^{-7}$ for 150 GeV/c pion beam of rate 150 kHz with a gain between 40 000 and 80 000. No spark has been observed during the shower.

In this test beam the single mask triple GEM detector was operated at very high gain. Actually in CBM-MUCH the GEM chambers will be operated at a gain ~5000–8000. Extrapolating the value of spark probability for 150 GeV/c pion beam of rate 150 kHz it is coming $\sim 10^{-9}$ at gain ~5000–8000. The value of the spark probability obtained from this beam test is little bit high for the operation of the CBM muon chambers at gain ~5000–8000. As an outlook, the measurements will be repeated in future and also at operational gain, with different electric fields in the Drift, Transfer and Induction gaps and with different value of current limiting protection resistor and will be communicated at a later stage.

Declaration of competing interest

The authors declare that they have no known competing financial interests or personal relationships that could have appeared to influence the work reported in this paper.

Acknowledgements

We are grateful to Dr. Anna Senger of GSI for the FLUKA simulation results. We would like to thank Jorrit C. L. Widder for his effort during the SPS test beam. We are thankful to Prof. Dr. Peter Senger of GSI and Dr. Subhasis Chattopadhyay of VECC, Kolkata for their support in course of this work. We are also grateful to Dr. Leszek Ropelewski and Dr. Serge Duarte Pinto of RD51 for their valuable suggestions. S. Biswas acknowledges Dr. Ingo Fröhlich of University of Frankfurt, Prof. Dr. Peter Fischer of Institut für Technische Informatik der Universität Heidelberg and the support of DST-SERB Ramanujan Fellowship (D.O. No. SR/S2/RJN-02/2012). S. Chatterjee acknowledges his Institutional Fellowship research grant of Bose Institute. S. Chatterjee and S. Biswas would like to thank Ms. Shreya Roy, Prof. Sanjay K. Ghosh, Prof. Sibaji Raha, Prof. Rajarshi Ray, Prof. Supriya Das and Dr. Sidharth K. Prasad of Bose Institute for valuable discussions during the data analysis.

References

[1] http://www.fair-center.eu/for-users/experiments/cbm.html.
[2] http://www.fair-center.eu/.
[3] The CBM Physics Book, 2010.
[4] A. Prakash, et al., arXiv:1102.0882 [nucl-ex].
[5] T. Balog, J. Phys. Conf. Ser. 503 (2014) 012019.
[6] F. Sauli, Nucl. Instrum. Methods Phys. Res. A 386 (1997) 531.
[7] S. Biswas, et al., Nucl. Instrum. Methods Phys. Res. A 718 (2013) 403, arXiv:1408.0075.
[8] S. Biswas, et al., Nucl. Instrum. Methods Phys. Res. A 824 (2016) 504, arXiv:1505.07767.
[9] S. Biswas, et al., J. Instrum. 8 (2013) C12002, arXiv:1310.0642.
[10] S. Chatterjee, et al., Nucl. Instrum. Methods Phys. Res. A 936 (2019) 491.
[11] R.P. Adak, et al., J. Instrum. 11 (2016) T10001.
[12] R.P. Adak, et al., Nucl. Instrum. Methods Phys. Res. A 846 (2017) 29, arXiv:1604.02899v2.
[13] S. Roy, et al., Nucl. Instrum. Methods Phys. Res. A 936 (2019) 485.
[14] S. Chakraborty, et al., Nucl. Instrum. Methods Phys. Res. A 936 (2019) 424.
[15] S. Roy, et al., Nucl. Instrum. Methods Phys. Res. A 936 (2019) 488.
[16] E. Nandy, et al., Springer Proc. Phys. 201 (2018) 157–165.
[17] Oliveira, et al., United States Patent, Patent No.: US 8, 597, 490 B2, Dec. 3, 2013.
[18] C. Altunbas, et al., Nucl. Instrum. Methods A 490 (2002) 177.
[19] M. Villa, et al., Nucl. Instrum. Methods A 628 (2011) 182.
[20] M. Alfonsi, et al., Nucl. Instrum. Methods A 617 (2010) 151.
[21] F. Sauli, Nucl. Instrum. Methods Phys. Res. A 805 (2016) 2.
[22] S. Biswas, et al., Nucl. Instrum. Methods Phys. Res. A 800 (2015) 93, arXiv:1504.00001.
[23] http://www.ni.com/labview/whatsnew/.
[24] G. Corradi, et al., Nucl. Instrum. Methods Phys. Res. A 572 (2007) 96.
[25] http://www.fluka.org/fluka.php.
[26] A. Senger, CBM Progress Report, 2011.
[27] G. Battistoni, et al., AIP Conf. Proc. 896 (2007) 31, Proc. of Hadronic Shower Simulation Work-shop 2006.
[28] https://meroli.web.cern.ch/Lecture_landau_ionizing_particle.html.
[29] S. Bachmann, et al., Nucl. Instrum. Methods Phys. Res. A 470 (2001) 548.
[30] G. Bencivenni, et al., Nucl. Instrum. Methods Phys. Res. A 494 (2002) 156.
[31] M. Alfonsi, et al., Nucl. Instrum. Methods Phys. Res. A 518 (2004) 106.

Long term stability study of triple GEM detector using different Argon based gas mixtures: an update

Journal of Physics: Conference Series **1498** (2020) 012037 doi:10.1088/1742-6596/1498/1/012037

Long term stability study of triple GEM detector using different Argon based gas mixtures: an update

S Chatterjee, S Roy, A Sen, S Chakraborty[1], S Biswas, S Das, S K Ghosh, S K Prasad and S Raha

Department of Physics and Centre for Astroparticle Physics and Space Science (CAPSS), Bose Institute, EN-80, Sector V, Kolkata 700091, India

E-mail: sayakchatterjee@jcbose.ac.in

Abstract. The long-term stability in terms of gain and energy resolution of a prototype triple Gas Electron Multiplier (GEM) detector has been investigated with high rate X-ray irradiation. Premixed Ar/CO_2 (80:20) and (90:10) gases have been used for this stability study. A strong Fe^{55} X-ray source is used to irradiate the chamber. The uniqueness of this work is that the same source has been used to irradiate the GEM prototype and also to monitor the spectra. This arrangement is important since it reduces the mechanical complexity of using an X-ray generator as well as the cost of the setup. A small area of the chamber is exposed continuously to the X-ray for the entire duration of the operation. The effect of temperature and pressure on the gain and energy resolution is monitored. The result of the long-term stability test for a triple GEM detector using Ar/CO_2 (70:30) gas mixture has been reported earlier [1]. The results with Ar/CO_2 (80:20) and (90:10) gas mixtures for the same chamber are presented in this article.

1. Introduction

Gas Electron Multiplier detectors are being used in many High Energy Physics experiments as tracking devices for their high rate capability [2][3][4]. The Compressed Baryonic Matter (CBM) [5] experiment at the future Facility for Antiproton and Ion Research (FAIR) [6], Darmstadt, Germany will use the triple GEM detector as a tracking device in the MUon CHamber (MUCH) [7][8][9][10] to track the di-muon pairs originating from the decay of low mass vector mesons, which will give us the information about the fireball created after the collision. Triple GEM detectors will be used in the first two stations of MUCH because the rate will be very high ($\sim$1.0 MHz/cm^2 for the first station [11]) there. The motivation of this particular work is to understand how the chamber behaves under continuous high irradiation [1][12][13]. The stability study in terms of gain and energy resolution of a triple GEM detector has been carried out with Ar/CO_2 (80:20) and (90:10) gas mixtures and results are presented in this paper.

2. Experimental details

A double mask triple GEM detector prototype obtained from CERN, having dimensions 10 cm$\times$10 cm, has been used for this study. The drift, transfer and induction gaps of the detector are kept at 3 mm, 2 mm, 2 mm, respectively. The high voltage is distributed between

[1] Present address: Nuclear Power Corporation of India Limited, Kakrapar, Gujrat, India

the drift plane and individual GEM foils using a voltage divider resistor chain. The signal is collected using a sum up board from all the segmented readout pads, each of dimensions 9 mm × 9 mm. It is fed to a charge sensitive preamplifier (VV50-2) having a gain of 2 mV/fC and shaping time of 300 ns [14]. The output of the preamplifier is fed to the linear Fan In Fan Out (FIFO) module. One output of the linear FIFO is fed to a Single Channel Analyzer (SCA) for rate measurement and the other output is fed to a Multi-Channel Analyzer (MCA) to obtain the energy spectrum. The SCA is operated in integral mode and the threshold is set at 0.1 V to reject noise. The output of the SCA is fed to the TTL-NIM adapter to convert the TTL signal to NIM signal and then counted by a NIM scaler.
Premixed Ar/CO_2 (80:20) and (90:10) gases have been used at a constant flow rate for this study. $\Delta V \sim$ 326 V and 300 V across each GEM foil were maintained throughout the experiment for (80:20) and (90:10) gas mixtures, respectively. A perspex collimator having an area of $\sim$13 mm^2 has been used to irradiate the chamber at a rate of $\sim$250 kHz. The results obtained for the (80:20) and (90:10) gas mixture are given in the next section.

3. Results

The gain and energy resolution have been calculated from the Fe^{55} 5.9 keV peak and then normalization is done using T/p correction as reported earlier [1]. The stability test of the detector has been carried out for $\sim$30 hours and $\sim$140 hours with Ar/CO_2 (80:20) and (90:10) gas mixtures, respectively.

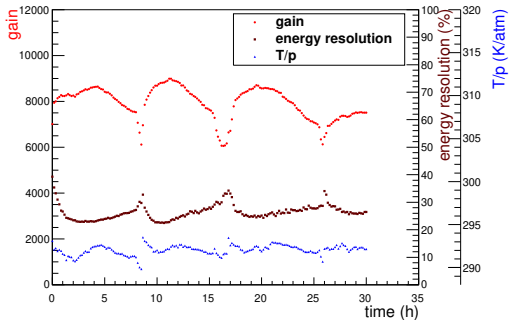

Figure 1. Variation of gain, energy resolution and T/p as a function of time for Ar/CO_2 (80:20) gas mixture.

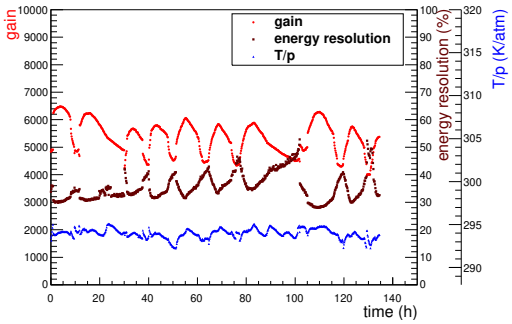

Figure 2. Variation of gain, energy resolution, and T/p as a function of time for Ar/CO_2 (90:10) gas mixture.

Figure 1 and 2 show the variation of gain and the energy resolution of the prototype as a function of time along with the ratio of ambient temperature (T=t+273) and pressure (p) for (80:20) and (90:10) gas mixtures, respectively. Figure 3 and 4 show the variation of normalized gain and normalized energy resolution as a function of the charge accumulated per unit area for (80:20) and (90:10) gas mixtures, respectively. Figure 5 and 6 show the variation in the normalized gain and energy resolution for the (80:20) gas mixture and figure 7 and 8 show that for the (90:10) gas mixture, respectively.
The variation in the normalized gain and energy resolution has been found to be $\sim$10% for both the (80:20) and (90:10) gas mixtures as shown in figure 5, 6, 7 and 8.

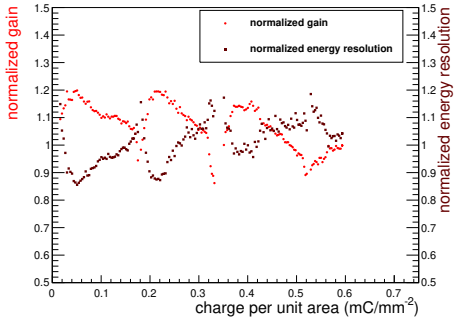

Figure 3. Variation of normalized gain and normalized energy resolution as a function of the total charge accumulated per unit area for Ar/CO_2 (80:20) gas mixture

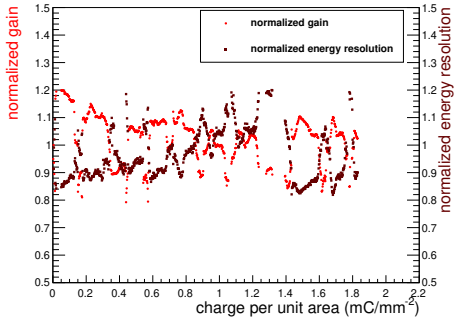

Figure 4. Variation of normalized gain and normalized energy resolution as a function of the total charge accumulated per unit area for Ar/CO_2 (90:10) gas mixture

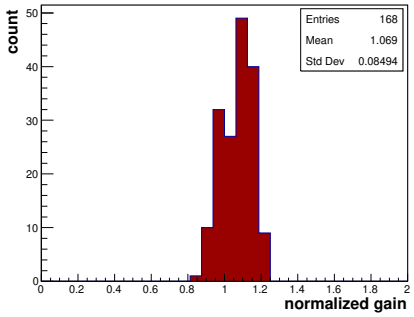

Figure 5. Distribution of normalized gain for Ar/CO_2 (80:20) gas mixture

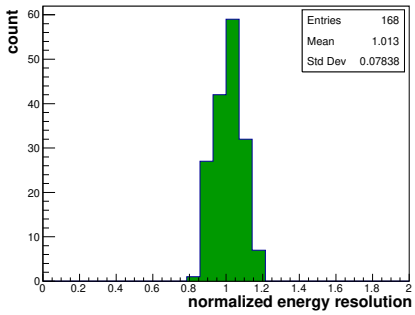

Figure 6. Distribution of normalized energy resolution for Ar/CO_2 (80:20) gas mixture

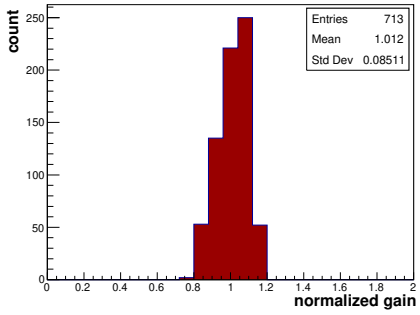

Figure 7. Distribution of normalized gain for Ar/CO_2 (90:10) gas mixture

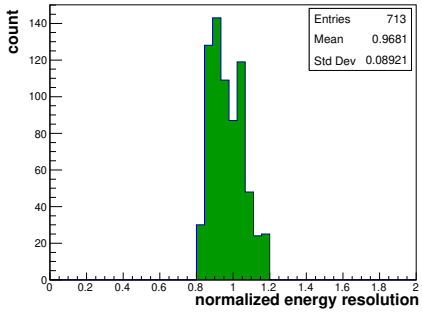

Figure 8. Distribution of normalized energy resolution for Ar/CO_2 (90:10) gas mixture

4. Conclusions

A systematic study on the stability of gain and energy resolution of a prototype triple GEM detector in long term operation under a high rate of X-ray irradiation has been carried out with Ar/CO_2 (80:20) and (90:10) gas mixtures. For this study, the same Fe^{55} source is used to irradiate the chamber as well as to measure the gain and energy resolution at an interval of 10 minutes. Using a collimator, the chamber is irradiated with a particle rate of $\sim$20 kHz/mm^2 for $\sim$30 hours with Ar/CO_2 (80:20) gas mixture and for $\sim$140 hours with Ar/CO_2 (90:10) gas mixture which are equivalent to a charge accumulation of 0.6 mC/mm^2 and 1.8 mC/mm^2, respectively. No degradation is observed in gain and energy resolution other than a fluctuation of $\sim$10% after the long exposure to X-ray.

Acknowledgments

The authors would like to thank the RD51 collaboration for all kinds of support. We would like to thank Dr. A. Sharma, Dr. L. Ropelewski and Dr. E. Oliveri of CERN and Dr. C. J. Schmidt and Mr. J. Hehner of GSI Detector Laboratory for valuable discussions and suggestions in the course of the study. This work is partially supported by the research grant SR/MF/PS-01/2014-BI from Department of Science and Technology, Govt. of India and the research grant of CBM-MUCH project from BI-IFCC, Department of Science and Technology, Govt. of India. S. Biswas acknowledges the support of DST- SERB Ramanujan Fellowship (D.O. No. SR/S2/RJN-02/2012). Special thanks to Ms. Aayushi Paul for her contribution.

References

[1] Roy S et al 2019 *Nucl. Instrum. Methods* A **936** 485
[2] Sauli F 1997 *Nucl. Instrum. Methods* A **386** 531
[3] Aggarwal M M 2018 *Nucl. Instrum. Methods* A **903** 215
[4] Patra R N 2017 *Nucl. Instrum. Methods* A **862** 25
[5] http://www.fair-center.eu/for-users/experiments/cbm.html
[6] http://www.fair-center.eu/
[7] Dubey A K et al 2013 *Nucl. Instrum. Methods* A **718** 418
[8] Adak R P et al 2017 *Nucl. Instrum. Methods* A **846** 29
[9] Biswas S et al 2013 *Journal of Instrumentation* **8** C12002
[10] Biswas S et al 2013 *Nucl. Instrum. Methods* A **718** 403
[11] Technical Design Report for the CBM, November 2014
[12] Adak R P et al 2016 *Journal of Instrumentation* **11** T10001
[13] Biswas S et al 2016 *Nucl. Instrum. Methods* A **824** 504
[14] CDT CASCADE Detector Technologies GmbH, www.n-cdt.com.

Nuclear Inst. and Methods in Physics Research, A 936 (2019) 491–492

Contents lists available at ScienceDirect

Nuclear Inst. and Methods in Physics Research, A

journal homepage: www.elsevier.com/locate/nima

Study of uniformity of characteristics over the surface for triple GEM detector

S. Chatterjee, S. Chakraborty, S. Roy *, S. Biswas, S. Das, S.K. Ghosh, S.K. Prasad, S. Raha

Department of Physics and Centre for Astroparticle Physics and Space Science (CAPSS), Bose Institute, EN-80, Sector V, Kolkata 700091, India

ARTICLE INFO

Keywords:
GEM
Gas detector
Uniformity
Gain
Energy resolution
Rate

ABSTRACT

A study of the uniformity of gain, energy resolution and count rate over the active area of a triple GEM detector has been performed using a strong Fe^{55} X-ray source with premixed gas of Argon and CO_2 in 70/30 ratio and conventional NIM electronics. The details of the experimental setup and the results we found are presented in this article.

Contents

1. Introduction

Triple GEM chambers [1,2] will be used in CBM experiment [3] at FAIR [4] for muon tracking (Muon Chamber: MUCH). Keeping this in mind, we carried out a study of the uniformity of gain, energy resolution and count rate over the surface of a standard 10 cm × 10 cm triple GEM detector, using a Fe^{55} X-ray source. For this study, the detector was filled with an Argon and CO_2 gas mixture in 70/30-volume ratio. A low noise charge sensitive preamplifier and conventional NIM electronics was used. The above-mentioned characteristics for the GEM detector were measured on a grid of 5 × 4 positions in the centre. Uniformity study using a collimated source of low activity is reported in Ref [5]. The novelty of the present work is that high radiation (~300 kHz) is used for the measurement of gain and energy resolution and that the radiation is not collimated to a point but a patch of ~50 mm^2 was exposed.

2. Detector descriptions and experimental set-up

In this study, a GEM detector prototype manufactured at CERN, consisting of three 10 cm × 10 cm double mask foils was used [5]. The drift, transfer and induction gaps of the detector are kept fixed at 3 mm, 2 mm and 2 mm respectively. The high voltages (HV) to the drift plane and individual GEM planes were applied through a voltage dividing resistor chain. The readout plane consists of 9 readout pads each of area 9 mm × 9 mm. So the active area of the prototype reduces to about 3 cm × 3 cm in the central region. In this study we used the signal given by the sum of all the pads, performed through a summing board, and a single input was fed to a charge sensitive preamplifier (VV50-2) [6]. The gain of the preamplifier is 2 mV/fC with a shaping time of 300 ns. The preamplifier output was fed to a linear Fan-in-Fan-out (FIFO) module and used both for measuring the rate as well as for spectroscopy. The analog signal from the linear FIFO was connected to a Single Channel Analyser (SCA) to measure the rate of the incident particles. The SCA was operated in integral mode and the lower level in the SCA was used as the threshold to the signal. The threshold was set at 0.1 V to reject the noise. 0.1 V corresponds 3σ of typical noise level. At HV of −4150 V with 0.1 V threshold the noise rate was found to be 45 Hz. The discriminated signal from the SCA, which is TTL in nature, was put to a TTL-NIM adapter and the output NIM signal was counted using a NIM scaler. The signal count rate of the detector in Hz is then calculated. Another output of the linear FIFO was fed to a Multi Channel Analyser (MCA) to obtain the energy spectrum. A schematic representation of the set-up is shown

* Corresponding author.
E-mail addresses: shreyaroy@jcbose.ac.in (S. Roy), saikat.biswas@cern.ch, saikat@jcbose.ac.in (S. Biswas).

https://doi.org/10.1016/j.nima.2018.08.068
Received 12 June 2018; Received in revised form 21 August 2018; Accepted 21 August 2018
Available online 23 August 2018

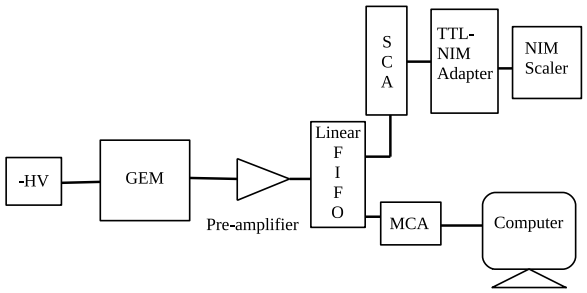

Fig. 1. Schematic representation of the electronics setup.

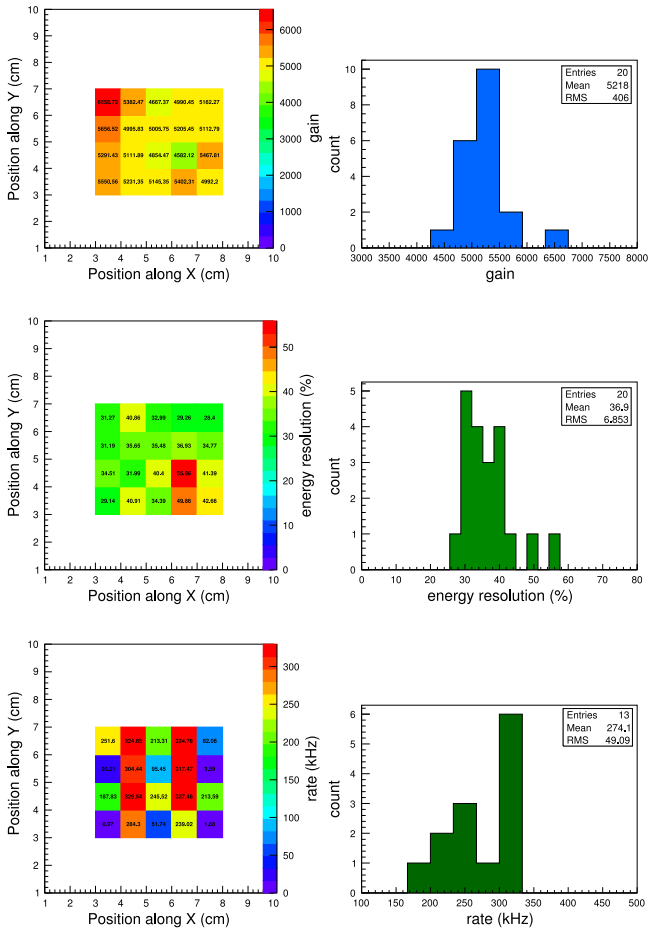

Fig. 2. Gain (top), energy resolution (middle), count rate (bottom) at 20 different places on the detector and their distribution.

in Fig. 1. Pre-mixed Ar/CO_2 in 70/30 volume ratio was used for the whole study. A constant gas flow rate of 3.4 l/h was maintained using a Vögtlin gas flow meter. For all measurements a circular collimator of diameter 8 mm was used to expose the X-ray from Fe^{55} source. Initially the gain, energy resolution and count rate are measured from the energy spectrum and the scaler count for the Fe^{55} X-ray source, varying the ΔV, as described in detail in Ref. [7]. Here ΔV is the potential difference across a single GEM foil. ΔV were same for all three GEM foils. Since the experiment was performed with a radiation source which emits a constant number of particles, a plateau in the count rate is reached at the highest efficiency of the chamber.

The uniformity investigation of the detector described here was carried out at an applied HV of −4150 V corresponding to a ΔV ~385.9 V across each GEM foil. The active area of the chamber was divided in 100 zones of 1 cm^2 and the above three parameters are measured in a grid of 5 × 4 positions in the centre of the detector i.e. in 20 zones. For each position, spectra and counts are recorded for 1 min.

3. Results

The gain of the detector is calculate as ratio of the 5.9 keV peak of Fe^{55} X-ray spectrum (fitted with a Gaussian) converted in charge using the gain on the ADC and preamplifier and the average number of electron produced in the gas (212 for Ar/CO_2 70/30 mixture) whereas the energy resolution is defined as the FWHM of that Gaussian function.

Fig. 2 shows the measured values of the gain, energy resolution and count rate at different places of the detector (left panel) as well as the distribution of these three parameters (right panel). For some zones where there is no readout pad corresponding the source position the count rate was found to be as low as 100 kHz. So for the distribution of the count rate a lower cut of 150 kHz was used.

4. Conclusions

The characteristics of the GEM detector will not be the same over it's active area. It is to be mentioned here that a gain variation up to a few percent is possible due to the intrinsic inhomogeneity in the geometry of the GEM holes and the gaps between the GEM foils. In this study the gain, energy resolution and count rate were measured at 20 places on the active area of the triple GEM detector prototype moving a Fe^{55} X-ray source manually to check the uniformity. For each measurement an area of ~50 mm^2 was exposed by 5.9 keV X-ray. Over the measured area the gain fluctuation was found to be ~10% while the fluctuation of energy resolution and count rate is ~20%. The fluctuations in gain and energy resolution reported in Ref [5] are 8.8% and 6.7% respectively. However, they have used a collimated source of low activity.

Acknowledgements

The authors would like to thank Dr. Christian J. Schmidt and Mr. Jörg Hehner of GSI Detector Laboratory for valuable discussions and suggestions in the course of the study and providing some components. This work is partially supported by the research grant SR/MF/PS-01/2014-BI from DST, Govt. of India and the research grant of CBM-MUCH project from BI-IFCC, DST, Govt. of India. S. Biswas acknowledges the support of DST-SERB Ramanujan Fellowship, India (D.O. No. SR/S2/RJN-02/2012).

References

[1] F. Sauli, Nucl. Instrum. Methods A 386 (1997) 531.
[2] C. Altunbas, Nucl. Instrum. Methods A 490 (2002) 177.
[3] http://www.fair-center.eu/for-users/experiments/cbm.html.
[4] http://www.fair-center.eu/.
[5] R. Patra, et al., Nucl. Instrum. Methods A 862 (2017) 25.
[6] CDT CASCADE Detector Technologies GmbH, Hans-Bunte-Str. 8-10, 69123 Heidelberg, Germany, www.n-cdt.com.
[7] S. Roy, et al., Stability study of gain and energy resolution for GEM detector, In this proceedings, arXiv:1804.02819.